Super-resolution imaging of cell-surface Sonic hedgehog multimolecular signalling complexes

Mirella Koleva

Department of Chemistry, Imperial College London

Thesis submitted for the degree of

Doctor of Philosophy

2 October 2013

To my parents

Abstract

Sonic hedgehog is a fascinating protein with great responsibility over the formation and upkeep of our bodies. It is widely studied, not least because dysregulation of the Shh signalling pathway leads to repercussions on human health, such as contraction of cancer. Gaining an understanding of its signalling mechanism is central to inventing preventative measures and treatments against this disease. This thesis focuses on the study of the spatial organisation of Shh multimolecular signalling complexes on the surface of producing cells, and those dispatched in the vicinity of those cells, using high-resolution optical imaging beyond the diffraction limit. With unprecedented resolution, the differences in organisation of Shh pre- and post-release from the surface were characterised, and the influence of the lipid modifications of Shh, namely cholesterol and palmitate, investigated. The main findings were that both lipid adducts are necessary for large-scale multimerisation, but not for the formation of small, sub-diffraction limit oligomers. Together with data I collected about the profile of the clusters' size distributions, I find that electrostatic interactions between the molecules may be the engine driving the multimerisation process. Furthermore, the role of lipid modifications may, at least in part, be to retain Shh on the surface while multimerisation proceeding according to the law of mass action builds upon the small oligomer nucleation sites prepared presumably by the electrostatic interactions in the first place. Other, more indirect lines of evidence again based on the profile of the multimer size distribution insinuated that Shh complexes may not undergo any proteolytic modifications prior to release – contrary to some reports in the literature. The results presented in this thesis are the fruits of a completely fresh and innovative approach to examining Shh, which for the first time delivers concrete dimensional details about the elusive structure of the Shh multimer.

Statement of originality

I hereby certify that the work presented in this thesis is entirely my own unless otherwise stated. Work done by others is clearly acknowledged and referenced. The material has not previously been submitted for any other thesis or degree at this or any other university.

Mirella Koleva
02 October 2013

Acknowledgements

First and foremost, I would like to express my thanks to my supervisors for offering me to study this topic, after an unexpected turn of events precluded me from working on my original project of choice. In many ways, the present project has been even more interesting, albeit more challenging, requiring me to be an expert simultaneously in two burgeoning research fields – super-resolution microscopy and hedgehog multimerisation. I am very grateful to Tony and Mark (not in any particular order) for their continuous guidance, support and for challenging my thinking – all of which helped to make me a better researcher.

I would like to thank Dr Niall Adams from the Statistics Section of the Department of Mathematics in Imperial College, who kindly helped me with the statistical analysis of the data in Chapter 7, Dr Martin Spitaler for always being so well-disposed and amenable to discussion, and Mr Stephen Rothery for generally being extremely helpful, and for his invaluable practical experience with microscopes. Finally, I would like to thank Dr Sunil Kumar for checking periodically on the progress of my writing, making wise suggestions, being a good 'bad influence' (despite what he says), and for providing continuous entertainment during the Summer of the Thesis!

Table of contents

Abbreviations

aa
: Amino acid(s)

ADAM
: A disintegrin and metalloprotease

AOTF
: Acousto-optic tunable filter

APC
: Angled physical contact

APS
: Ammonium persulphate

Arg
: Arginine

AU
: Airy unit

BFP
: Back focal plane

Boc
: Brother of Cdo

BSA
: Bovine serum albumin

cAMP
: Cyclic AMP

CCD
: Charge-coupled device

cDNA
: Complementary deoxyribonucleic acid

Cdo
: Cell adhesion molecule downregulated by oncogenes

CDS
: Correlated dual sampling

CMLE
: Classical maximum likelihood estimation method

CMOS
: Complementary metal-oxide semiconductor

COS-7
: African green monkey kidney cell line (CV-1 in origin, and carrying the SV40 genetic material)

CW
: Cardin-Weintraub

Cys
: Cysteine

DFT
: Discrete Fourier transform

DH
: Double helix

Dhh
: Desert hedgehog

DIC
: Differential interference contrast

Disp
: Dispatched

DM
: Dichroic mirror

DMEM
: Dulbecco's modified Eagle's growth medium

DNA
: Deoxyribonucleic acid

*d*STORM
: Direct stochastic optical reconstruction microscopy

ECM
: Extracellular matrix

EDTA
: Ethylenediaminetetraacetic acid

EGFP
: Enhanced green fluorescent protein

EM
: Electron-multiplying

EMCCD
: Electron-multiplier charge-coupled device

ER
: Endoplasmic reticulum

ERAD
: Endoplasmic reticulum-associated degradation

F-actin
: Filamentous actin

FAP
: Fluorogen-activating protein

FC
: Fibre connector

FCS
: Foetal calf serum

FDA
: Floating diffusion amplifier

FFT
: Fast Fourier transform

FN3
: Fibronectin type III

FP
: Fluorescent protein

FPALM
Fluorescence photoactivation localisation microscopy
FRET
Förster resonance energy transfer
FWHM
Full-width at half-maximum
G-actin
Globular actin
GAG
Glycosaminoglycan
GAM
Goat anti-mouse
GAR
Goat anti-rabbit
Gas1
Growth arrest specific 1
GFP
Green fluorescent protein
Gli
Glioma-associated oncogene transcription factor
Gln
Glutamine
GlOx
Glucose oxidase
Glu
Glutamic acid
Gly
Glycine
GPCR
G protein-coupled receptor
GPI
Glycosylphosphatidylinositol
GSD
Ground-state depletion
HEK293
Human embryonic kidney cell line
Hh
Hedgehog
Hhip / Hhip1
Hedgehog interacting protein
HRP
Horseradish peroxidase
HS
Heparan sulphate
HSC
Hedgehog signalling complex
HSPG
Heparan sulphate proteoglycan
IFT
Intraflagellar transport proteins
Ihh
Indian hedgehog
iPALM
Interferometric photoactivation localisation microscopy
LED
Light-emitting diode
Lys
Lysine
mAb
Monoclonal antibody
MEA
Beta-mercaptoethylamine
MES
2-(N-morpholino)ethanesulfonic acid
mRNA
Messenger ribonucleic acid
NA
Numerical aperture
NVP
Nodal vesicular particle
OTF
Optical transfer function
pAb
Polyclonal antibody
PAGE
Polyacrylamide gel electrophoresis
PALM
Photoactivation localisation microscopy
PBS
Phosphate buffered saline
PBST
Phosphate buffered saline and Tween-20
PEP
Pauli exclusion principle
PFA
Paraformaldehyde
PKA
Protein kinase A
PMT
Photomultiplier tube
PSF
Point-spread function
Ptc
Patched
PVDF
Polyvinylidene difluoride
Q-Q plot
Quantile-quantile plot

RESOLFT
Reversible saturable optically linear fluorescence transitions
RMS
Root-mean-square
RNA
Ribonucleic acid
ROI
Region of interest
sCMOS
Scientific complementary metal-oxide semiconductor
SDS
Sodium dodecyl sulphate
Ser
Serine
Shh
Sonic hedgehog
Shh::EGFP
Enhanced green fluorescent protein fused to Sonic hedgehog
Shh-C24S
Non-palmitoylated Sonic hedgehog
Shh-FL
Full-length Sonic hedgehog
Shh-N
Non-cholesteroylated Sonic hedgehog
Shh-NC24S
Sonic hedgehog lacking lipid modifications
SIM
Structured illumination microscopy
SMLM
Single-molecule localisation microscopy
Smo
Smoothened
SNR
Signal-to-noise ratio
SPDM
Spectral precision distance microscopy
SPEM
Saturated pattern excitation microscopy
SSD
Sterol-sensing domain
SSIM
Saturated structured illumination microscopy
STAM
Saturated transient absorption microscopy
STED
Stimulated emission depletion
STORM
Stochastic optical reconstruction microscopy
TDM
Transition dipole moment
TEMED
Tetramethylethylenediamine
TG
Transglutaminase
Thr
Threonine
TIRF
Total internal reflection fluorescence
Tyr
Tyrosine
UV
Ultraviolet

List of figures

List of tables

1. Introduction

The hedgehog (Hh) family of proteins plays a pivotal regulatory role in the development, maturation and maintenance of most multicellular organisms. During embryogenesis, it is concerned with orchestrating the differentiation of cells into tissues which perform different functions by providing them with positional information by means of a spatially varying concentration gradient. In adult life, Hh family members are involved in the constant regeneration of certain epithelial tissues and repair in response to injury, by means of stem cell-like progenitor cells. Hh signalling perpetuates homeostasis of the taste buds [Miura *et al.*, 2001], gut [van den Brink *et al.*, 2007], lungs [Watkins *et al.*, 2003], hair follicles [St-Jacques *et al.*, 1998] and blood-brain barrier [Amankulor *et al.*, 2009][Alvarez *et al.*, 2011]. Hh pathway activation also assists the healing of broken bones [Miyaji *et al.*, 2003], damaged lung [Watkins *et al.*, 2003] and brain tissue [Amankulor *et al.*, 2009].

Dysregulation of the Hh pathway has been associated with numerous pathological conditions. Insufficient levels of Hh signalling during development cause congenital malformations, including cyclopia [Ryan *et al.*, 2012], whereas overexpression of Hh in later life can contribute to oncogenesis [Eaton, 2006], such as skin, brain, gastrointestinal, prostate, pancreatic, stomach, oesophagus, breast, small-cell and non-small-cell lung cancer [Zarogoulidis *et al.*, 2013][Thayer *et al.*, 2003][Berman *et al.*, 2003]. In the past few years, pharmaceuticals designed to tackle specifically the altered genetics of tumorous formations have been approved as a preferred method of treatment, since they offer increased chances of patient survival over the standard, highly toxic, chemotherapy treatment. As a result, there is an increased interest from a clinical standpoint in elucidating the mechanisms of tumour evolution and cell maintenance, and the signalling pathways implicated in it. The Notch, Wingless and Shh signalling cascades are all implicated in organogenesis and maintenance of progenitor cells, and are thus of heightened interest to oncologists. Inhibitors of these pathways are already under study as therapeutic agents; however, due to cancer's evolvement of resistance to these molecules, amongst other reasons, more needs to be understood about the mechanisms of regulation in order to prevent relapses of the disease [Zarogoulidis *et al.*, 2013].

Hh was discovered by Christiane Nüsslein-Volhard and Eric Wieschaus in 1980 in a genetic mutation experiment in the fruit fly *Drosophila melanogaster* [Nüsslein-Volhard *et al.*, 1980]. It was identified as a gene important for the correct segmentation of the fly embryo. Mutating the gene caused the disappearance of correct segmentation polarity in the fly embryo, which was instead replaced with a uniform cover of denticles – not unlike a hedgehog. Later work discovered that vertebrates harbour three *Hh* orthologues: 1) Sonic hedgehog (*Shh*), 2)

Desert hedgehog (*Dhh*), and 3) Indian hedgehog (*Ihh*). In terms of genetic sequence, *Dhh* is the most similar to *Drosophila Hh*. The Dhh and Ihh proteins are highly specialised, with Ihh being expressed in bones and cartilage and Dhh concerned with the development of the peripheral nervous system and reproductive organs. Shh is much more widespread and presides in the nervous system and many epithelial tissues [Ingham *et al.*, 2001].

Motivated by the strong involvement of Shh deregulation in the contraction of cancer, numerous research groups have made it their aim to identify methods to manipulate the signalling pathway and, in the majority of cases, focus on diminishing the signalling potential of the Hh family. In order to do this, however, more needs to be understood first about its signalling mechanism. To date, it is known that, in order to reach target cells, Hh traverses the intercellular environment in the form of a multimeric macromolecule. The mechanism through which it assembles, however, is currently unknown and the subject of considerable controversy. Conventional biochemical techniques have so far been unable to provide an unequivocal answer to this question. The problem therefore clearly necessitates a novel approach.

Imaging the multimerisation process on the molecular scale would be ideal. In fact, conventional fluorescence imaging techniques have proven, in the past few decades, to be extremely valuable for biological studies. For many years, however, their resolution had been hampered by the ostensibly insurmountable tendency of light to diffract. This physical phenomenon limits the achievable resolution to 200 nm at best, which is more than ten times the size of a single protein molecule. Fortunately, less than a decade ago, a family of fluorescence imaging techniques, known under the collective name of single-molecule localisation microscopy, which can overcome this fundamental resolution limit became available to the wider research community. In this work, I focus namely on implementing a sub-type of this family of imaging techniques, called STORM, in order to attempt to understand better the Shh multimerisation mechanism.

2. Background and Theory

2. 1. The Mammalian Shh Signalling Pathway

2. 1. 1. The canonical pathway

Shh is a morphogen which operates in a dose-dependent manner through a carefully controlled concentration gradient. The response elicited in receiving cells in the presence of Shh differs depending on the relative abundance of Shh, how sustained the signalling is, as well as on the cells' relative position to the Shh-producing cells [Mukhopadhyay *et al.*, 2013]. In brief, Shh signalling functions through regulating the processing status (*i.e.* activity) and stability of the family of Glioma-associated oncogene (Gli) transcription factors, which are composed of the three isoforms: Gli1, Gli2 and Gli3 [Palm *et al.*, 2013]. Some of the transcriptional targets of the mammalian Shh pathway are the negative regulators, *Ptc1*, *Ptc2* and *Hhip1*, one of the Gli proteins themselves: *Gli1* [Mukhopadhyay *et al.*, 2013] and *missing in metastasis* (*MIM*) [Chen *et al.*, 2007].

Shh signalling begins its course by translation of the *Shh* gene into a 45-kDa preprotein. This precursor form is composed of two domains: an amino-terminal (N-terminal) signalling domain that takes part in signal transduction, and a carboxy-terminal (C-terminal) intein-like autocatalytic domain. In addition, the N terminus of the preprotein contains a signal sequence which directs the molecule to the endoplasmic reticulum (ER) for post-translational processing. In humans, the precursor undergoes cleavage between residues Gly^{197} and Cys^{198}, assisted by the C-terminal domain which acts as a cholesterol transferase, adjoining a cholesteryl moiety onto the newly exposed glycine [Porter *et al.*, 1996]. More specifically, as shown in **Fig. 2.1.1.1.**, the nucleophilic 3β-hydroxyl group of cholesterol attacks the thioester intermediate formed after autocleavage of the C terminus, resulting in change of the linkage to an ester bond [Resh, 2013]. The N terminus is also modified with a lipid adduct. First, the signal sequence is removed and palmitic acid, donated by palmitoyl-CoA, is covalently attached to the α-amino group of Cys^{24} *via* an amide bond by Hedgehog acyl transferase (Hhat), a transmembrane protein of the membrane-bound *O*-acyl transferase (MBOAT) family, which is embedded in the ER membrane [Dierker *et al.*, 2009a][Resh, 2013]. Intriguingly, nearly all other known palmitoylated proteins undergo S-acylation, *i.e.* targeting of the thiol side chain instead [Ohlig *et al.*, 2011][Buglino *et al.*, 2008][Pepinsky *et al.*, 1998].

The resulting processed protein is thought to be the most potent and physiologically relevant form of Shh [Dierker *et al.*, 2009b]. The molecule then passes through the secretory pathway [Resh, 2013] and is displaced from the cell interior upon binding to Dispatched (Disp)

[Ma *et al.*, 2002], a 12-pass transmembrane protein with a sterol-sensing domain [Burke *et al.*, 1999]. Once Shh has travelled to the external membrane leaflet, it is thought to localise into specialised membrane microdomains, called lipid rafts [Rietveld *et al.*, 1999]. Lipid rafts have a higher degree of order, compared to the bulk of the membrane, and are enriched in cholesterol, glycosphingolipids and phospholipids acylated with saturated fatty acids [Resh, 2013].

At this stage, an unknown process takes place which facilitates the distribution of Shh to receiving cells, several cell diameters from the site of production. Heparan sulphate proteoglycans (HSPGs) are thought to assist in the dispersal. These molecules have already been established as vital participants in various other signalling events, often acting as ligand co-receptors

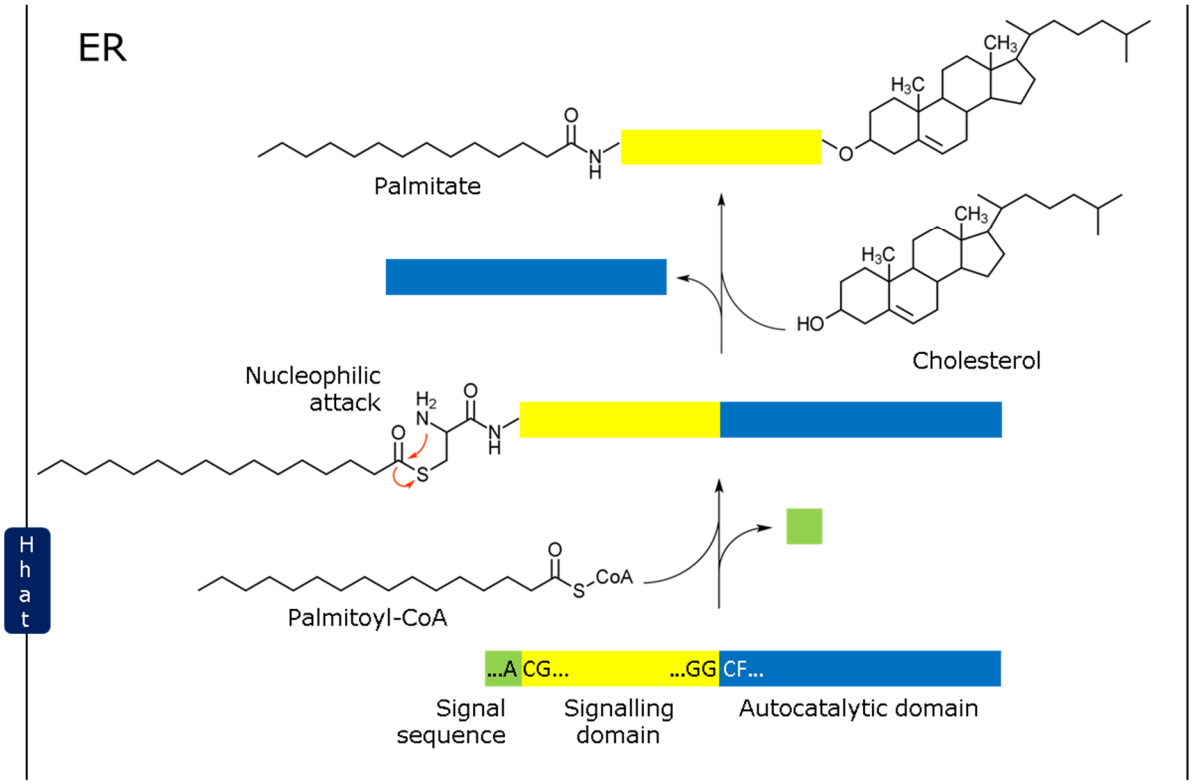

Figure 2.1.1.1. Biogenesis and post-translational modification of human Shh in the endoplasmic reticulum. Human Sonic hedgehog (Shh) is synthesised as a tripartite protein, consisting of a signal sequence (residues 1-23), followed by the signalling domain (residues 24-197) and concluding with the autocatalytic domain (residues 198-462). By virtue of the signal sequence, the preprotein is translocated to the endoplasmic reticulum (ER) lumen, whereby a post-translational sequence of events takes place. First, the signal peptide is cleaved, whereupon Hedgehog acyltransferase (Hhat) palmitoylates the exposed cysteine residue on the N terminus (left-hand side of the molecule in the figure). Palmitic acid is provided by a palmitoyl-CoA donor. The covalent bond formed between Shh and palmitate is initially a thioester bond which, after a spontaneous internal nucleophile attack, is transformed into irreversible amide linkage. Subsequently, cholesterol catalyses the autoprocessing of the C terminus (right-hand side of the molecule) and the covalent addition of cholesterol onto the C terminus.

[Eaton, 2006]. Moreover, HSPGs have been reported to be essential for Hh signal reception and modulation of its trafficking, and to take part in morphogen-Ihog (a Hh co-receptor, discussed further below) interactions in *Drosophila* [Gallet *et al.*, 2008][McLellan *et al.*, 2006]. A discussion devoted to the nature of HSPGs, including their role in Shh intercellular transit, can be found in section 3. 1. 5. of the next chapter.

Patched (Ptc) functions as the main Shh receptor. Its binding affinity for the Shh ligand is in the low nanomolar range – that is, relatively high [Marigo *et al.*, 1996] (**Fig. 2.1.1.2**). Ptc comprises 12 transmembrane domains and two large extracellular loops. The primary sequence and topology of Ptc most closely resembles the resistance-nodulation-division (RND) family of bacterial transporters. The vast majority of these transporters occur in bacteria, where they serve to pump lipophilic toxins and heavy metals out of the cell by setting up a proton gradient. Although proton gradients are scarcely found in the vicinity of eukaryotic cells' membranes, interestingly, mutation of highly conserved RND-domain amino acids in Ptc which are vital for RND transporter activity strongly attenuates Ptc function [Peart *et al.*, 2002].

Ptc, like many cholesterol-binding proteins, contains a ~180 amino acid-long sterol-sensing domain (SSD). Mutating key conserved amino acids in the SSD compromises the ability of Ptc to regulate Shh target gene expression, without altering its ability to bind the Shh ligand. Apart from the role of Ptc as a Shh signal transducer, the molecule also acts to downregulate the extracellular Shh gradient by sequestering it in a manner independent of its signal-transducing properties. Ptc therefore does not only function as an inhibitor of the Shh pathway activation but also acts to restrict Shh's range of movement [Chen *et al.*, 1996]. Mammals have two Ptc genes: *Ptc1* and *Ptc2*; *Ptc2* encodes a protein slightly smaller than *Ptc1*, but with similar tertiary structure and domains. The proteins seem to display some degree of overlap in their expression,

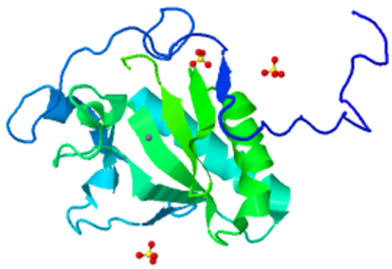

Figure 2.1.1.2. Crystal structure of the signalling domain of human Shh. The N-terminal side of the signalling domain is the protruding string of peptides seen on the right. The red and yellow ball-and-stick structures are sulphate ions on residues № 701, 702 and 705; these act as chemical ligands, interacting with the zinc ion (grey sphere in the centre) on residue 200 to form a coordination site for binding to the Sonic hedgehog receptor, Patched. Figure obtained from the Protein Data Bank (PDB ID: 3M1N); crystallographic data provided by [Pepinsky *et al.*, 2000].

although there also appear to be distinct areas with mutually exclusive expression. *Ptc1* and *Ptc2* transcription is controlled by the Gli transcription factors, and both are upregulated in response to Shh [Goodrich *et al.*, 1996].

Upon Shh binding to Ptc, the latter releases its repression on Smoothened (Smo), a 7-pass transmembrane GPCR protein from the frizzled family, whereupon Smo relocates into the membrane of the primary cilium (discussed further below), enabling the progression of downstream signalling (**Fig. 2.1.1.3**). It is not well understood how Ptc exercises its inhibition on Smo. One theory suggests that Ptc regulates Smo's access to lipophilic ligands which affect its trafficking and activity. Given that Ptc has been found to recruit Lipophorin sterols from endosomes, this hints at a possible involvement of inhibitory Lipophorin lipids in the modulation of Smo activity [Khaliullina *et al.*, 2009]. Alternatively, Ptc may repress Smo *via* secretion of provitamin D3. Activation of Smo, on the other hand, may be effected indirectly by oxysterols [Bürglin, 2008].

The primary cilium is a finger-like organ projecting from the surface of the cell, composed of fibrillar bundles of tubulin stemming from a basal body in the base of the cilium. This organelle was until recently thought to be vestigial. In stark contrast to its assumed idleness, the primary cilium has numerous functions, including serving as a sensory antenna in several different types of cells, and is absolutely required for Shh signalling in vertebrates [Mukhopadhyay, 2013]. It has been shown that Smo must localise to the primary cilium in order to signal effectively [Corbit *et al.*, 2005][Eaton, 2006]. The primary cilium encapsulates the hedgehog signalling complex (HSC), a molecular complex of downstream effectors, and serves as a platform for its formation. Amongst other molecules, the HSC comprises Suppressor or Fused (Sufu), which downregulates the pathway in a cilium-independent manner [Chen *et al.*, 2009]. Sufu mediates the processing and stabilisation of Gli2/3 and may act in some way to regulate the passage of Gli into the nucleus. Signalling between Smo and the Gli homologues is mediated by the kinase Kif7 [Liem *et al.*, 2009]. Kif7, itself a scaffolding protein and also part of HSC, supports the integration into the complex of the additional kinases, consisting of Protein kinase A (PKA), GSK3 and CK1. The last three are all responsible for phosphorylating and thus priming the transcription factors for proteolysis by the proteasome in the absence of Shh [Milenković *et al.*, 2010][Robbins *et al.*, 2012]. PKA is activated by cyclic adenosine monophosphate (cAMP) in the absence of Shh and operates in the base of the cilium. The transduction mechanism between Smo and cAMP has not been demystified yet, although there is some evidence that the missing link might be the rhodopsin-family GPCR, Gpr161 [Mukhopadhyay *et al.*, 2013].

Smo thus transduces the Shh signal by manipulating the processing state of the Gli transcription factors indirectly *via* the HSC. When Smo is in its active conformation, Gli1 and Gli2 are stabilised in their full-length form and subsequently converted into their active form. Converse-

ly, when Smo is inactive, all three Gli transcription factors are truncated into a repressor form [Mukhopadhyay *et al.*, 2013].

As a curious aside, loss-of-function mutation of the intraflagellar transport (IFT) proteins responsible for the correct architecture and function of the cilium causes dysfunctional Shh signalling. Depletion of retrograde IFTs results in the mislocalisation of Smo and additionally prevents the generation of both the activator and repressor forms of Gli [May *et al*, 2005]. On the other hand, depletion of anterograde IFTs results in full-length, neutral Gli and a constitutive activation of the pathway [Eggenschwiler *et al.*, 2007]. This highlights the important intervention of IFTs in Shh signalling.

Signal transduction is modulated by additional Shh-binding proteins which act as co-

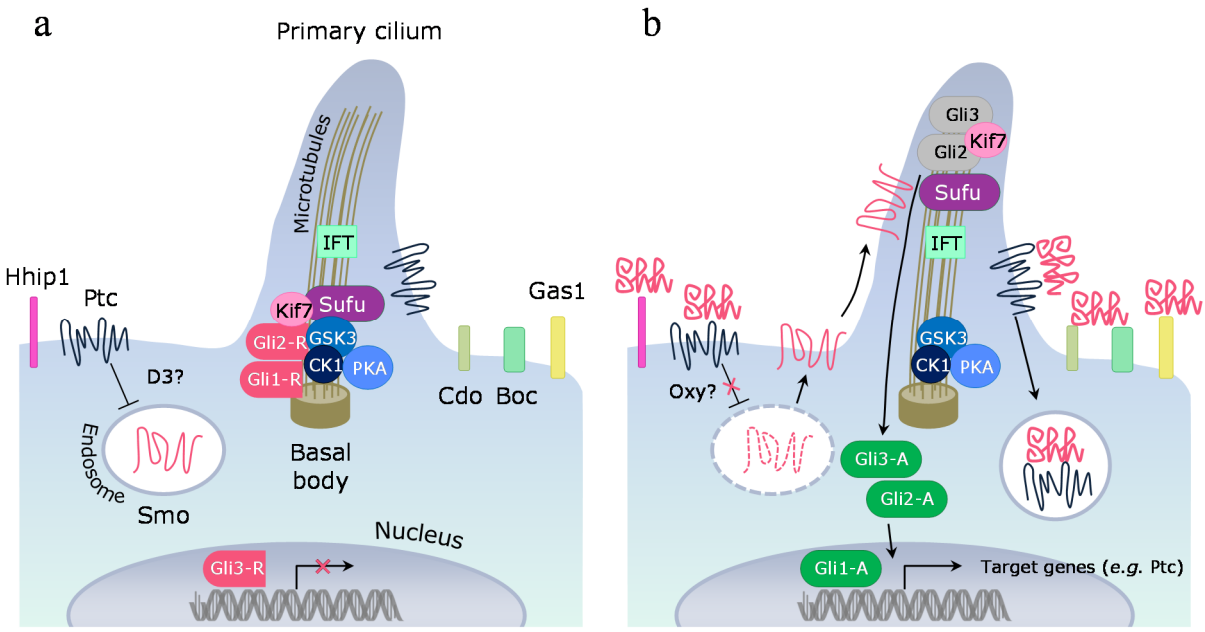

Figure 2.1.1.3. The canonical mammalian Shh signalling pathway – signal transduction at the receiving cell. (a) In the absence of Shh signalling, Ptc inhibits trafficking of Smo to the ciliary membrane, presumably though vitamin D3 secretion. As a result, PKA, CK1, GSK3 and Kif7 kinases are free to act at the base of the cilium and promote the formation of the repressor form of the Gli transcription factors, which move into the nucleus to repress target gene transcription. (b) In the presence of Shh, the morphogen binds to Ptc and abrogates repression of Smo through a mechanism possibly involving oxysterol (Oxy) activity. Smo arrests the proteolytic processing of Gli, permitting full-length Gli to accumulate and translocate to the tip of the cilium. The latter are then transformed into transcriptional activators and begin to initiate transcription of target genes in the nucleus. The presence of IFT proteins is required for Shh signalling; they are implicated in both repression and activation of Gli. Hhip1 competes with Ptc for removing Shh from the cell surface and acts as a pathway inhibitor. Cdo, Boc and Gas1, on the other hand, enhance Shh signalling.

receptors. Many of the co-receptors are highly conserved across mammals and Drosophila, despite their differential regulation in different animals. Discovered in Drosophila, Interference hedgehog (Ihog) was the first identified Hh co-receptor. Ihog is a positive regulator of Hh signalling, since deliberately compromising Ihog function leads to diminished Hh signalling. It is a single-pass transmembrane protein, characterized by a small non-conserved intracellular domain and an extracellular domain comprised of four immunoglobulin-like domains and two fibronectin type III (FN3) domains. Ihog binds to both Hh and Ptc via the FN3 domains, whereby the first domain associates with Hh and the second with Ptc. Vertebrates have two homologues of Ihog: cell adhesion molecule down-regulated by oncogenes (Cdo) and brother of Cdo (Boc). Removing one or the other co-receptor from the signalling cascade causes mildly abnormal phenotypes in mice, indicative of disruption in Shh signalling. Loss of both Cdo and Boc, however, results in more severely affected phenotypes, exhibiting evident Shh loss of function. This perhaps hints at a redundancy in the co-receptors' role [Beachy *et al.*, 2010]. Other membrane-surface proteins that Shh binds are the hedgehog interacting protein (Hhip1) and the GPI-anchored protein growth arrest specific 1 (Gas1) [Stebel *et al.*, 2000]. Hhip1 is known to antagonise Shh signalling, whereas Gas1 is a positive regulator. Despite upregulating the pathway, Gas1 is down-regulated by Shh [Allen *et al.*, 2007]. In *Drosophila*, Hhip1's orthologue Hhip competes with Ptc in clearing Hh from the extracellular environment; this could be a means of restricting the spread of Hh in a manner analogous to Ptc [Chuang *et al.*, 1999].

2. 1. 2. Non-canonical signalling pathways

Shortly after its discovery, a link between Shh and a series of signalling components, including the Gli transcription factors, was made. The causal sequence of interactions between these molecules was eventually revealed and set out in the signalling pathway just described in the previous section. Since then, however, it has come into view that Shh can signal also *via* Gli-independent mechanisms. The former sequence of signalling events has therefore been termed the 'canonical' signalling cascade, whereas the latter has acquired the label 'non-canonical'.

The non-canonical signalling mechanism, as already mentioned, is Gli independent, and unifies under its umbrella term two distinct nexuses: type I, which does not require Smo, and type II, which initially imitates canonical signalling until the Smo agonist, whereupon the pathway diverges. Type I signalling is anti-apoptotic. Type II non-canonical Shh signalling regulates the actin cytoskeleton by means of the small GTPases RhoA and Rac1 [Liem *et al.*, 2009]. Other components involved in the pathway depend on the context; in fibroblasts, PI3K and G_i proteins are involved, whereas in neurons either Tiam1 or Src-family kinases Src and Fyn take part.

On the whole, Shh signalling is now recognised to act through several context-dependent signalling mechanisms that have the ability to interact dynamically [Robbins *et al.*, 2012].

2. 2. Microscopy

2. 2. 1. Cell fixation

In order to obtain images faithful to real life, microscopy should ideally be carried out on live specimens. Unfortunately this comes at the cost of facing a multitude of problems. Cell movement and maintenance of cells in a physiologically 'comfortable' state is unwieldy and difficult.

As an alternative to live-cell imaging, various chemical treatment protocols have been developed, ensuring that specimens retain their three-dimensional structure after death. This is achieved with a choice of fixatives. Fixation causes cell metabolism to cease and enables preservation of microstructures down to a certain scale, whilst destroying other material (such as enzymes) which falls below this scale threshold [Pawley, 2006]. No one fixation method is flawless, since all lead to shrinkage of the sample, though this undesired effect is mitigated to some extent in the horizontal plane by the adherence of the cell to the substratum. Therefore the true cell dimensions are usually maintained better in the plane of the image (*x*-*y*) than in the *z* direction.

The perfect fixative would permeate the cell swiftly and preserve the ultrastructure before the cell has time to react and produce artefacts. As already mentioned, an ideal fixing agent has not yet been discovered, and in practice one has to select a fixative best suited to the experimental investigation at hand. Although there exist other types of fixatives, this section shall discuss solely chemical fixatives – in particular formaldehyde and methanol – since they were used in the experiments in this work.

Chemical fixatives can be delineated into two distinct categories: coagulating and cross-linking. The former type encompasses substances such as ethanol, methanol and acetone, and tends to effect a rapid change in the cell's hydration state, resulting in either coagulation or extraction of proteins from the cell. Coagulating fixatives are ubiquitous and easy to apply, and therefore enjoy some popularity. In spite of this, they carry some disadvantages, as they tend to precipitate proteins and have been found to cause considerable shrinkage of the cell (a 50% reduction in size, [Pawley, 2006]).

Cross-linking fixatives include formaldehyde and glutaraldehyde. A common disadvantage to all aldehydes is that they induce blebbing in the cell membrane. Each compound

forms covalent cross-links with its own specific active chemical groups. Glutaraldehyde is disfavoured by the fluorescence microscopy community because of its propensity for introducing unwanted fluorescence into the sample (although that can be quenched post-fixation with sodium borohydride, $NaBH_4$), and, more importantly, is known to destroy antibody binding sites. Due to its double reactivity (it has two reactive groups per molecule, unlike formaldehyde, which has only one), it is capable of cross-linking proteins on the surface of the cell very rapidly. However, because of its size, glutaraldehyde permeates the cell relatively slowly (ten times slower), compared to formaldehyde.

Formaldehyde, HCHO, is a gas. When dissolved in water, it forms a complex with water, called methylene glycol (**Fig. 2.2.1**). Formaldehyde reacts with nitrogen atoms. It cross-links proteins by forming a meshwork of methylene bridges (CH_2) between reactive groups (**Fig. 2.2.1**), if they are sufficiently close. Groups that react with formaldehyde are: amino, amido, guanidine, thiol, phenol, imidazolyl and indolyl, amongst others. This chemical can therefore cross-link nucleic acids (DNA and RNA). Carbohydrates and lipids become trapped under a web of cross-linked proteins, but since they do not contain nitrogen groups, they themselves do not

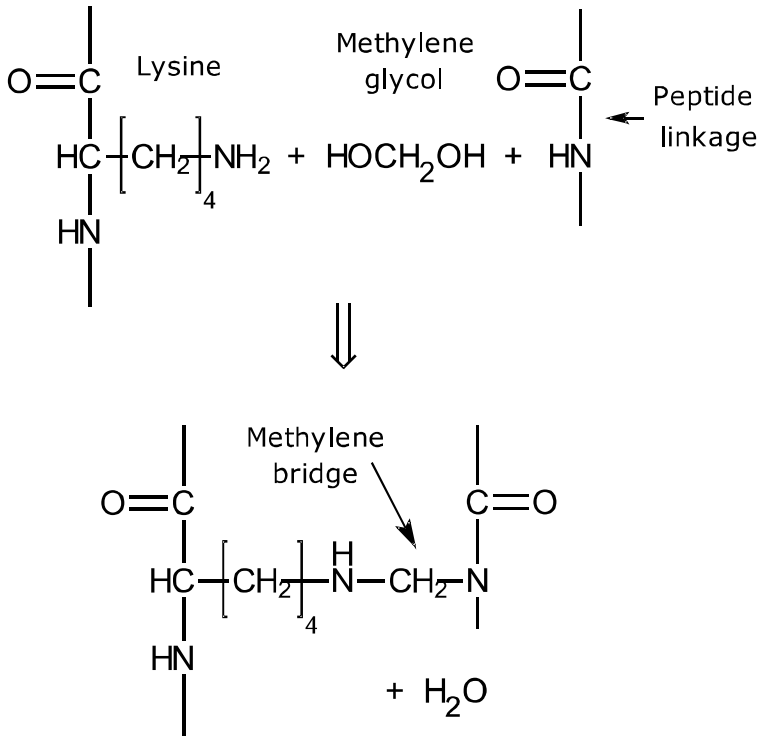

Figure 2.2.1. Formaldehyde cross-linking. Example of a lysine residue being cross-linked to the peptide linkage of a protein. At room temperature and pressure, formaldehyde is a gaseous substance. Methylene glycol is the complex formed by formaldehyde when it dissolves in water. If nitrogen atoms from two different molecules are positioned sufficiently close to each other, methylene glycol will link them together *via* a methylene bridge in a condensation reaction, whereby water is released as a by-product.

become part of the polymer. Labile structures, such as filamentous actin, are not preserved well with formaldehyde at physiological pH [Kiernan, 2000].

2. 2. 2. The photophysical phenomenon of fluorescence

Luminescence is a broad term encompassing any form of light emission in a substance, resulting from radiative relaxation of excited electronic states [Lakowicz, 2006]. This optical phenomenon is subcategorised into fluorescence and phosphorescence (**Fig. 2.2.2**).

Each electronic energy level is spread into a manifold of states, arising from the different possible vibrational energy levels that the fluorophore can assume. Following absorption of an excitation photon, the fluorophore transcends into a higher excited singlet state – *e.g.* S_1 or S_2. The absorption process occurs on a timescale of 10^{-15} s. In the majority of cases, the fluorophore rapidly relaxes to the lowest vibrational level of S_1 through a process called internal conversion within a typical timeframe of 10^{-13} s. A 'fluorescent' photon is emitted upon return of the fluorescent molecule from the lowest vibrational S_1 state (the excited state's thermal equilibrium) to the ground state, an event lasting typically 1-5 ns. This time interval is also known as the lifetime of the fluorophore. Typically, the fluorophore will return to a higher ground-state (S_0) vibrational level, which quickly undergoes thermal equilibration (dissipation of excess

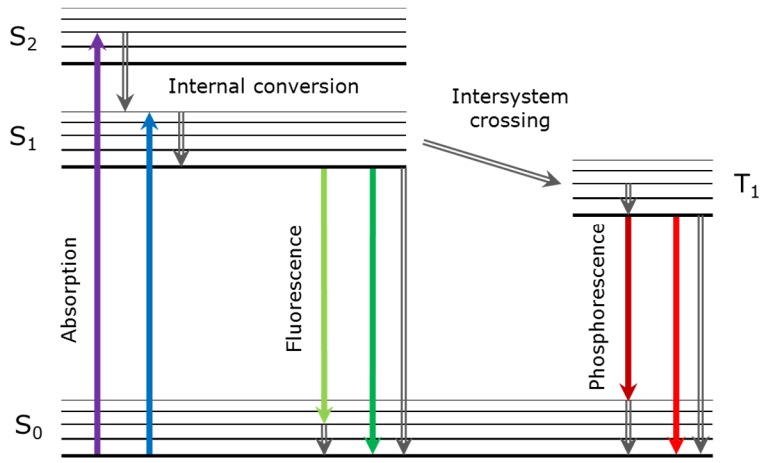

Figure 2.2.2. Jabłoński diagram. This diagram shows the radiative (coloured arrows) and non-radiative (hollow grey arrows) electronic transitions in a fluorescent molecule. Each electronic state (S_0, S_1, S_2 and T_1) is subdivided into a 'manifold' of states (grouped horizontal lines) corresponding to different vibrational energies of the molecule. After absorbing a photon of a frequency corresponding to the difference in energies between two singlet states S, the molecule either relaxes back to the least energetic singlet state (S_0) emitting a fluorescent photon in the process, or with a small probability enters a state with a different spin multiplicity (*i.e.* a triplet state, T_1), whereby after a short delay it emits a photon *via* a process termed phosphorescence.

energy through heat) and causes the fluorophore to rest in its lowest energy state.

On rare occasions, fluorophores in the S_1 state enter the first triplet state (right-hand side of **Fig. 2.2.2**). This event is called intersystem crossing. The process of crossing back to the singlet ground state by emitting a 'phosphorescent' photon is called phosphorescence. Phosphorescence lifetimes are relatively slow transitions occurring on a timescale of milliseconds to seconds. In general, the wavelength of phosphorescence is red-shifted compared to that of fluorescence. An explanation for the difference in rates of fluorescence and phosphorescence is given in Appendix A.

Table 2.2.1. Timescales of various photophysical processes experienced in a typical fluorophore. h is Planck's constant; ν_{ex} is the frequency of an excitation photon; ν_{em} is the frequency of an emission photon; Q represents heat.

Process	*Transition*	*Timescale (seconds)*
Absorption	$S_0 + h\nu_{ex} \rightarrow S_1$	10^{-15}
Internal conversion	$S_1^* \rightarrow S_1 + Q$	10^{-13}
	$S_0^* \rightarrow S_0 + Q$	
	$T_1^* \rightarrow T_1 + Q$	
Fluorescence	$S_1 \rightarrow S_0 + h\nu_{em}$	10^{-9}
Non-radiative relaxation	$S_1 \rightarrow S_0^* + Q$	10^{-9}
Intersystem crossing	$S_1 \rightarrow T_1^* + Q$	10^{-7}
Phosphorescence	$T_1 \rightarrow S_0 + h\nu_{em}$	10^{-3}–1

Excitation light is normally of higher energy than emission light. This is termed the Stokes shift and originates from the tendency of the fluorophore to rapidly decay to the lowest vibrational state of S_1, after excitation and before fluorescence is emitted. Furthermore, additional Stoke shift effects, as well as other photophysical interactions, can manifest themselves upon interaction of the fluorophore with the solvent, or with other fluorophores and non-fluorescent compounds [Lakowicz, 2006].

2. 2. 3. Conventional fluorescence microscopy techniques

A microscope is an instrument which serves three functions. 1) It magnifies the object of inter-

est, 2) provides resolution, *i.e.* enables one to distinguish one object from another, and 3) provides contrast – that is, the ability to discern an object against the background.

2. 2. 3. 1. The Widefield Microscope

The widefield microscope is one of the most basic and common types of microscope. A schematic of an inverted widefield microscope is shown in **Fig. 2.2.3.1.1**. Typically, a broadband incoherent light source serves to illuminate the sample, although, more rarely, a laser is used. A field diaphragm and a condenser diaphragm control the intensity and illumination area. Before illuminating the specimen, the broadband source is usually restricted to a narrow range of wavelengths by passing it through an excitation filter. Next, the light is reflected by a dichroic mirror through the objective and onto the specimen. Fluorescence is excited and emitted in all directions, however the objective captures only a fraction of the total emitted light, depending on the

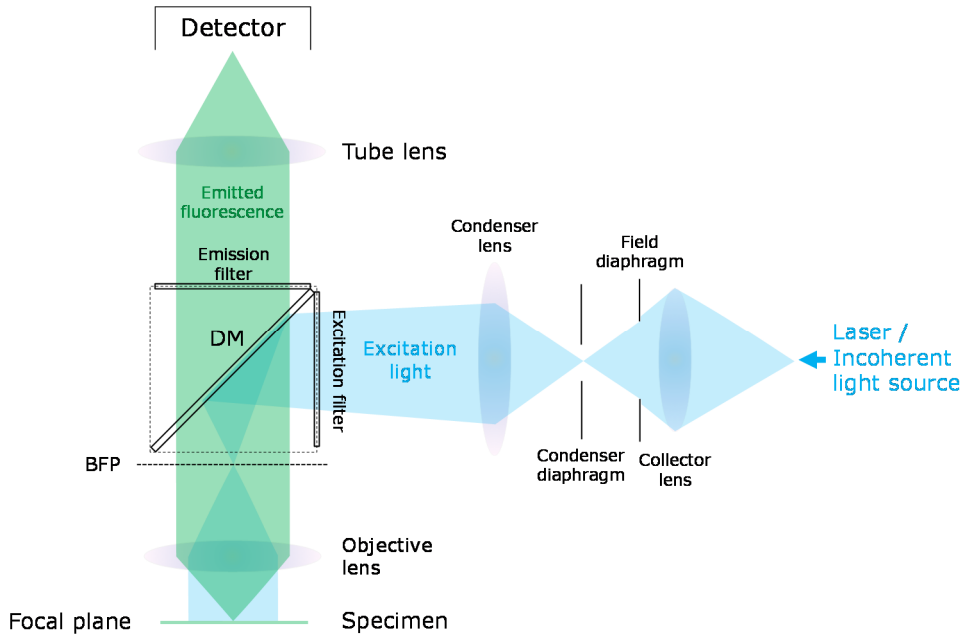

Figure 2.2.3.1.1. The inverted widefield microscope. Incoherent light, for example from an LED or a mercury lamp, or coherent light from a laser enters the microscope, passes through a band-pass excitation filter to select a narrow excitation bandwidth, whereupon it is reflected through the objective onto the specimen with a dichroic mirror (DM). Fluorescence is excited from the specimen and is partially collected by the objective. Stray excitation light is separated from the fluorescence by the DM. Further down the detection path a band-pass or long-pass emission filter also rejects any remaining excitation light, while at the same time letting fluorescence light through to the detector.

conical angle of acceptance of the objective. The excited fluorescence passes back through the objective and is directed through the dichroic mirror towards the detector. Prior to entering the detector, the emission light is 'cleaned' from any scattered light that may have found its way into the detection path. Widefield microscopes usually employ charge-coupled devices (CCDs) or complementary metal-oxide semiconductor (CMOS) cameras as detectors.

The objective lens is designed for use with fixed object and image distances; only in this optical arrangement are optical aberrations, such as spherical and chromatic, fully corrected in the image plane. In addition to an objective lens, the optical path of a microscope will also include a tube lens. Rather than using a single lens to form an image, whereby the magnification of an object will inconveniently vary with the distance of the object from the lens, a microscope employs two lenses to obtain quantitative measurements in a sample with a certain depth. In order to achieve such a depth-invariant system, known as a 'telecentric' system, the objective and tube lens are separated by a distance equal to the sum of their focal lengths. The resultant constant magnification is then the ratio of their respective focal lengths: $M = f_{tube} / f_{objective}$ [Pawley, 2006]. Telecentric systems, from a metrological perspective, also have the important property of being space invariant and linear. Space invariance means that the transverse and axial magnifications, as well as the PSF profile of the system (explained further below), are location independent.

Widefield microscopes collect light in parallel and employ high quantum-efficiency charge-coupled device detectors, making them both fast and sensitive [Parton *et al.*, 2006]. The widefield microscope, however, suffers from an inherent loss in *z*-resolution, named 'the missing cone problem' (**Fig. 2.2.3.1.2**). The so-called 'missing cones' are areas of very low contrast which prevent the viewer from experiencing the full resolution of the microscope. This causes small detail in the transverse, and particularly in the axial direction, to be virtually invisible. This effect stems from the fact that the objective's aperture is finite and therefore so is the depth of field [Macias-Garza *et al.*, 1988]. As a consequence of the non-infinitesimal depth of field of the microscope, imaging a plane of an extended object will produce an in-focus image of that plane, together with contributions from those immediately above and below it. The loss of contrast itself is due to the out-of-focus light from planes other than the one being imaged that mask the signal of interest and so reduce the signal-to-background ratio.

The size of the point-spread function (PSF), *i.e.* the image of a point source in the far field (some distance away much greater than the wavelength of light), dictates the resolution capability of the microscope. The axial extent of a widefield PSF should, in principle, be infinite (not permitting any resolution in *z*) and the light should be evenly distributed among the different planes. This is not the case in reality because apertures beyond the entrance pupil cause vignetting of the PSF (clipping of the peripheral edges). As a result, the axial PSF of the widefield mi-

croscope is finite but relatively large, so that imaging an object not confined to a single plane will incur poor contrast in the focal plane. This problem cannot be resolved simply by increasing the numerical aperture (*NA*) of the objective in order to see even smaller detail, because the depth of field scales as $1/NA^2$, meaning that even more out-of-focus light is gathered from lateral directions, resulting in an even larger blur contribution.

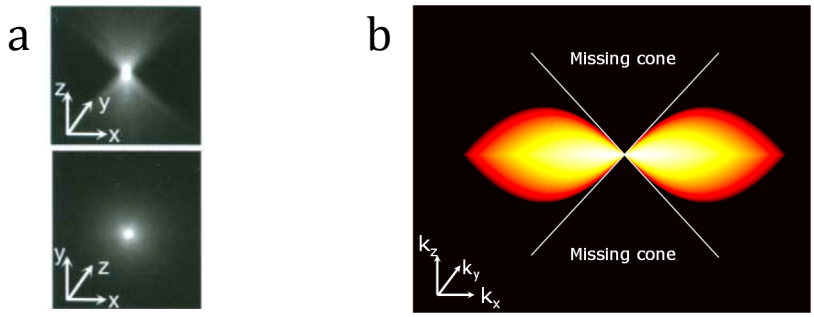

Figure 2.2.3.1.2. The widefield microscope point-spread function (PSF) and the 'missing cone' of spatial frequencies. (a) Light gathered from a point-like, self-luminous object by a lens system and focused into an image distributes itself into a shape called the 'point-spread function' (PSF). (b) Converting the PSF into reciprocal (Fourier) space allows easy examination of the size of the details transmitted by the system, which are represented by the spatial frequencies k_x, k_y and k_z. Fourier transforming the PSF yields a toroid. An axial cross-section thereof is represented here with a colour heat map, where the 'heat' is proportional to the degree of transmittance of the different details, whose fineness increases with distance from the centre of the image. There are two 'cones' of missing spatial frequencies arranged symmetrically around the origin and extending along the *z*-axis. The missing cones thus signify a complete absence in distance discrimination in the axial direction. Panel (a) reproduced with permission from Elsevier from [Parton *et al.*, 2006]; panel (b) reproduced with permission from the author from [Poher, 2008].

2. 2. 3. 2. The Confocal Microscope

The invention of the confocal microscope is usually accredited to Marvin Lee Minsky, with the filing of his patent in 1957. However, Hiroto Naora published a paper describing the confocal principle [Naora, 1951] six years in advance of this date, making him the true inventor of the technique [Cremer *et al.*, 2013].

As already mentioned in the previous section, widefield microscopes are intended to

image objects in the objective's plane of focus. In reality, however, other light sources anywhere within the objective's conical angle of acceptance, as well as above and below the focal plane, will also contribute light to the image plane, effectively obscuring the object of interest through a loss in contrast. The confocal microscope overcomes this limitation through selectively blocking out-of-focus light from the planes adjacent to the plane of focus, as well as in a transverse direction, to some extent.

The basic layout of a point-scanning confocal microscope is displayed in **Fig. 2.2.3.2**. The beam from a laser excitation source is focused into a pinhole, which effectively behaves as a point source. The light is then collimated and consecutively reflected by a dichroic mirror (DM) and a pair of scanning mirrors (discussed further below), whereupon it is transmitted through the objective lens and focused onto the fluorescently labelled specimen. The captured fluorescence light retraces the path of the excitation beam up to the DM, whereupon it is transmitted through the DM and focused into a pinhole in front of the detector [Pawley, 2006].

The ability of a confocal microscope to discriminate features laterally is a consequence of the relationship between lateral displacement in the object and image planes. For instance, light emitted a distance Δx from the focus within the focal plane will be projected at $M\Delta x$ from the detector pinhole (where M is the magnification of the system), thereby increasing the chance of it not being detected.

A more important and valuable property of the confocal microscope, however, is its axial discrimination ability. Fluorophores situated in front of and behind the focal plane would be excited by the incoming laser beam. They are then brought into focus either just short of or further than the plane of the detection pinhole aperture, meaning that most of this light is excluded and that only objects in focus are allowed to reach the detector (**Fig. 2.2.3.2**). The objective forms an image of the detection pinhole (and illumination pinhole, since it is located in a conjugate plane to its detection counterpart) on the object. The detection pinhole therefore determines the volume element of the sample that is observable [Pawley, 2006]. Under certain circumstances (well focused beam, small confocal aperture), the thickness of the observable slice may be less than 500 nm. For its superior resolution capabilities therefore, compared to the widefield microscope, confocal microscopy presents an attractive candidate for examining relatively thick specimens, such as biological cells.

By virtue of the pinhole, the PSF of a confocal microscope acquires a smaller spatial extent equal to about the square of a widefield microscope's PSF; (it would be exactly square, if the excitation and emission wavelengths were the same). Since the presence of the pinhole in the microscope determines both the illumination and emission profile of the PSF, the resultant PSF is the product of the two PSFs (or, equivalently, convolution of the two toroids with missing cones, **Fig. 2.2.3.1.2** right, meaning that the central void is consequently filled in), thus drastic-

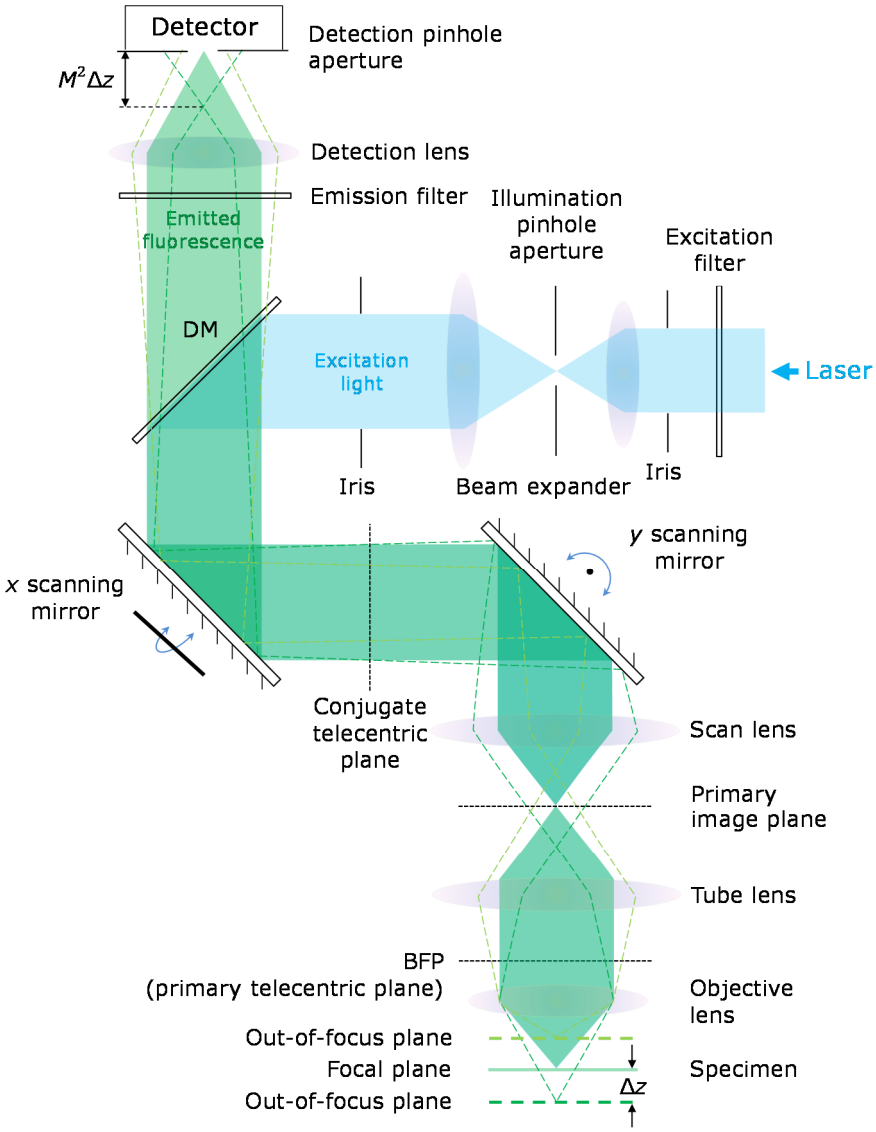

Figure 2.2.3.2. Point-scanning laser confocal microscope. Laser illumination (right) enters the system and is reflected by a dichroic mirror (DM), followed by two scanning mirrors. Next, the beam is imaged by means of a relay lens system onto the pupil of the objective lens. The objective focuses the beam into a diffraction-limited spot onto the specimen. Since only one spot is visible at any one time, the beam needs to be scanned across the specimen in a raster pattern using the two scanning mirrors which can pivot in orthogonal directions around the point on which they are mounted. Fluorescence arising in the focal plane as a result of excitation of the sample retraces the optical path of the excitation beam up to the DM, where it is passed into a side port housing the detector. Immediately before the detector is a pinhole aperture which passes all of the in-focus light. Note that fluorescence arising outside the focal plane (dark green and light green dotted lines) follows a slightly different optical path, converging to a focus some distance away from the pinhole and thus causing it to be greatly attenuated at the detection plane. The amount of attenuation of out-of-focus light – and therefore the thickness of the optical section imaged – depends on the diameter of the pinhole. To reach a compromise between contrast, resolution and signal-to-noise ratio, the pinhole is usually set to the size of an Airy disc. More details on the choice of pinhole diameter are given in section 2. 2. 2. 3. 3.

cally improving axial resolution.

A point-scanning confocal microscope observes only one point of the sample at a time. In order to build up a 2D or 3D image of the sample, either the beam must be scanned across the sample (beam scanning), or the stage must move the object across the stationary beam (object scanning). In a telecentric system, there is a strict relationship between the angle of a scanning beam and the point where it is focused. Thus, different areas of the specimen can be probed by changing the angle of the scanning beam. To effect this change in angle, 'scanning mirrors' are introduced into the set-up. One mirror can be mounted so as to tilt around a single axis of rotation, thereby providing scanning ability in one dimension only. To enable scanning along the *x* as well as *y* direction, the second mirror is installed to move in an orthogonal direction. The image of one mirror is then formed on the next, and an intermediate optical system involving a scan lens is used to form an image of the last scanning mirror onto the back focal plane (BFP; also known as entrance aperture and Fourier plane) of the objective.

The 3D structure of a microscopic specimen can be obtained by incrementing the focal plane of the microscope vertically though the specimen using a *z*-stepper motor [Macias-Garza *et al.*, 1988]. This method is called 'optical serial sectioning'. The point-scanning laser confocal microscope (**Fig. 2.2.3.2**) thus builds up an image of the specimen by scanning the laser beam across the specimen, line by line, by deflecting it in the *x* and *y* direction using galvanometric scanners, and moving the focus vertically to image different planes. A photomultiplier tube (PMT) detects the emitted fluorescence from the scanned specimen details pixel by pixel. The laser beam itself is focused to a diffraction-limited spot on the specimen, thereby necessitating the acquisition of several hundreds of thousands, to a million spots, to reconstruct a single image. The sequential nature of acquisition of the image is inherently slower than widefield acquisition, and necessitates a low pixel dwell time (on the order of microseconds) to constrain the imaging rate within a reasonable time window. This requirement demands certain specifics from both the detector and light source. The detector must have a very fast response time; a PMT is therefore suitable for this purpose. One of the disadvantages of PMTs, however, is their low quantum efficiency (~10%), compared to charge-coupled devices (CCDs), which typically have quantum efficiencies in excess of 70%. Since fewer photons contribute to the image, PMTs generate an image with reduced quality due to the increased statistical noise. To comply with the need for a short excitation timescale, a bright illumination source is necessary – hence a laser is often used for this purpose. Unfortunately, lasers fluctuate in intensity on the microsecond scale (this topic is revisited in section 2. 2. 9. 1. 1.), therefore they also contribute to the elevated statistical noise. This handicap can be mitigated to some extent by averaging frames or decreasing the scan rate – both at the expense of speed. Increasing the PMT gain does not make an improvement as it merely introduces more noise. One method of circumventing the slow acquisi-

tion speed of point-scanning laser confocal microscopes is to use a spinning disc microscope. The latter has multiple pinholes (~1000) which can gather information from the specimen in parallel, thus reducing the time required to build up the image. However, the confocality of these instruments is reduced, due to the crosstalk that occurs between the pinholes.

In summary, the main advantage of confocal microscopes over widefield microscopes is that the former perform better when imaging thick (several μm) and/or scattering specimens with high background fluorescence, such as biological cells.

2. 2. 3. 3. Resolution and sampling considerations

2. 2. 3. 3. 1. Definition of resolution

The resolution of an optical microscope is defined as the shortest distance between two points at which they remain discernible as two separate entities. The optical resolution of the system (**Table 2.2.3.3.1.1**) can be estimated using one of several theories put forward by Abbe, Rayleigh, Sparrow and others, that are based on different arbitrary criteria (**Fig. 2.2.3.3.1**). The Abbe limit [Abbe, 1873] is based on the highest spatial frequency which can be transmitted through the microscope objective and is therefore perhaps the most physically relevant resolution criterion. The Rayleigh resolution limit is defined as the distance required to separate two point sources in order for the first minimum of the PSF diffraction pattern of one source to coincide with the PSF maximum of the other. This distance is in fact one-half of an Airy disc, the lateral extent of the central peak of the PSF. The Sparrow criterion declares two point sources to be just resolved if the individual PSFs overlap so that an intensity minimum in the composite PSF between their actual positions is just discernible [Sparrow, 1916]. The expressions for each of these resolution limits, with relevance to conventional (widefield) microscopy in the lateral as well as axial direction, are given in the table below.

Table 2.2.3.3.1.1. Widefield microscope resolution, as defined by three common resolution criteria. n, refractive index of the immersion fluid; NA, numerical aperture; λ, wavelength of light. These expressions are approximations for low NA.

	Abbe	*Rayleigh*	*Sparrow*
Lateral resolution	$0.50n\frac{\lambda}{NA}$	$0.61n\frac{\lambda}{NA}$	$0.47n\frac{\lambda}{NA}$
Axial resolution	$2n\frac{\lambda}{NA^2}$	$2n\frac{\lambda}{NA^2}$	$1.65n\frac{\lambda}{NA^2}$

The numerical aperture, is defined as follows:

$$NA = n \sin \alpha, \qquad \textbf{Eq. 2.2.3.3.1}$$

with α being the half-angle of the objective aperture.

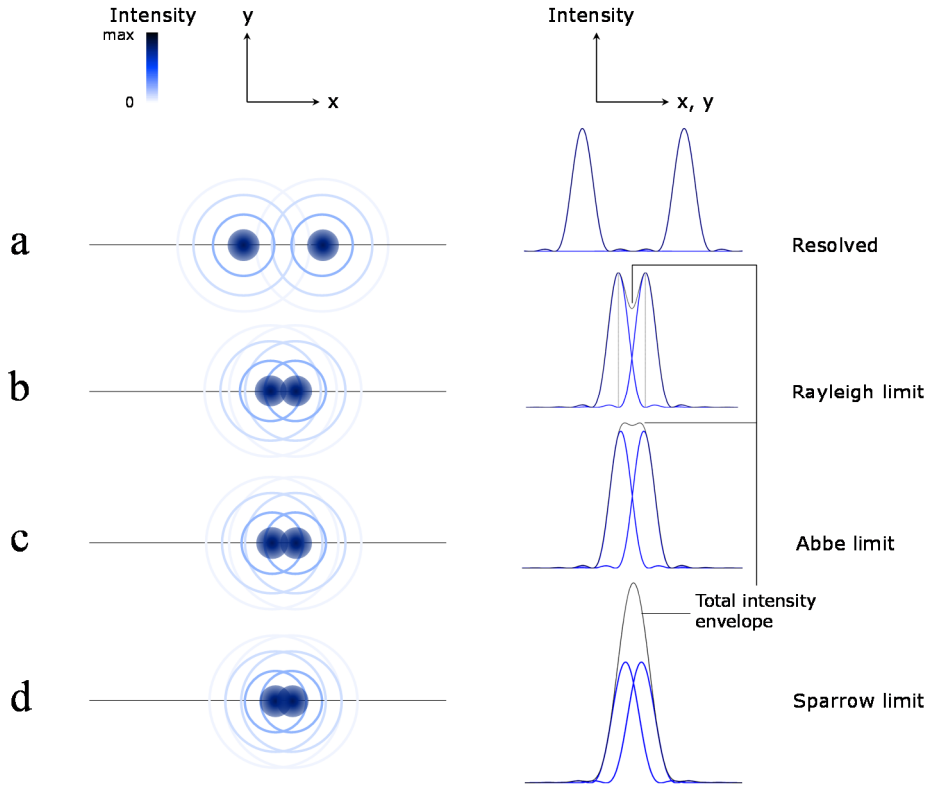

Figure 2.2.3.3.1. The resolution limit and its many definitions. (a) Two point sources can be distinguished as two separate entities when they are situated a sufficient distance apart. The exact cut-off distance is somewhat arbitrarily defined in several different ways. The Rayleigh criterion (b), for example, is defined as the separation at which the first minimum of one PSF coincides with the central maximum of the other. (c) The Abbe limit is the smallest feature that can be transmitted by an ideal wide-field microscope. It is not defined in terms of the relative position of two adjacent point sources, but is shown here pictorially merely to enable comparison with the other resolution criteria. (d) The limit of resolution can be defined with respect to the ability to discern contrast, *i.e.* when a dip in intensity between two point sources is just possible to make out (the Sparrow criterion). The example in (d), therefore, is just unresolved according to the Sparrow limit.

Resolution is also frequently expressed as FWHM, as shown in the table below.

Table 2.2.3.3.1.2. Widefield and confocal microscope resolution expressed in terms of FWHM. *PH* is the object-side pinhole diameter, in μm. The pinhole is a diaphragm of variable diameter. The expression for the axial resolution of the confocal microscope given here is for a pinhole of diameter 1 Airy unit. All of the data in this table apply to a fluorescent point object and are appropriate for high-*NA* objective lenses [Wilhelm *et al.*, 2008][Li *et al.*, 2000].

	Optical slice thickness	*FWHM lateral resolution*	*FWHM axial resolution*
Widefield	Undefined	$0.51\frac{\lambda_{em}}{NA}$	$1.67n\frac{\lambda_{em}}{NA^2}$
Confocal	$\sqrt{\left[\frac{0.88\cdot\lambda_{em}}{\left(n-\sqrt{n^2-NA^2}\right)}\right]^2+\left(\frac{\sqrt{2}\cdot n\cdot PH}{NA}\right)}$	$0.51\frac{\lambda_{exc}}{NA}$	$\frac{0.88\cdot\lambda_{exc}}{\left(n-\sqrt{n^2-NA^2}\right)}$

The lateral and axial resolution in both widefield and confocal microscopes are unequal, with the lateral always being finer. The *z*-elongated geometry is due to the asymmetry in the light wavefront as it emerges from the objective. The reason for the square, rather than linear, dependence of the *z*-resolution on the *NA* is connected to the factors determining the rejection of out-of-focus light. In a widefield microscope, this is caused by vignetting – that is, the blocking of light incident outside the aperture of the optical components. In a confocal microscope, this is effected through the pinhole in a controlled manner. The amount of blur allowed into the imaging plane depends on the area covered by the oncoming light (incident on the aperture) relative to the aperture size. Since the acceptance angle of the objective governs the angle at which light spreads before and beyond the focus, then it must determine the diameter of the spot superimposed on the aperture. The area of the spot will therefore depend on the square of the acceptance angle – hence NA^2 [Walker *et al.*, 2008].

2. 2. 3. 3. 2. The Nyquist-Shannon sampling theorem

Acquiring data with a microscope essentially constitutes an analogue-to-digital conversion: the smoothly varying signal from the sample is digitised into a number of equidistant, discrete steps. This periodic sampling tactic can be applied to measure either spatially or temporally varying signals.

Owing to the limit imposed on the fineness of detail that the microscope optics can re-

solve, there is a set of optimal sampling frequencies that can be applied whilst acquiring the data that guarantee no loss of information. The Nyquist theorem states that, for a signal with a defined maximal frequency, it is possible to reconstruct the signal perfectly, only if it is sampled at no less than twice the maximum frequency of the signal:

$$f_{x,y/z}^{Nyq} = \frac{f_s}{2} \geq f_{x,y/z}^{max}, \qquad \textbf{Eq. 2.2.3.3.2}$$

where $f_{x,y/z}^{max}$ signifies the maximum frequency of the signal in the *x*-*y* plane or in the *z*-direction, and f_s is the sampling frequency that one is trying to determine.

In the current context, optimal sampling is achieved by optimising the pixels' (voxels') size. The sampling frequency therefore advises on the correct sampling density (sampling per unit distance) that is required for optimum information collection. In order to obtain this figure, the relationship between the pixel (voxel) size and its projection in the object plane must be established. This is because the smallest detail within the specimen in the image plane is the PSF; sampling must therefore be carried out on the scale of the PSF, in order to capture all available information. Observing this rule is especially important for deconvolving data (section 2. 2. 9. further below), since excessively coarse sampling that records several PSFs per sample would not allow them to be disentangled. In addition, undersampling can introduce aliasing artefacts. Due to the inevitable diffraction of light, however, sampling at a higher rate will in most cases not produce any additional benefits – on the contrary, as the extra data will use up additional data storage space, take longer to acquire, and in the meantime more than the strictly necessary fluorophore bleaching could be incurred. Oversampling in the plane transverse to the optic axis will also increase the shot noise, due to the low photon count collected by the small pixels.

When choosing the correct sampling rate, most of the resolution criteria outlined in section 2. 2. 3. 3. 1. are not appropriate as they are not completely correct for this purpose and can lead to undersampling. Instead, the sampling frequency should be determined by the maximum spatial frequency transmitted by the microscope, which is mathematically related to the PSF.

The maximum spatial frequency transmitted by a widefield and a confocal microscope has been calculated by C. J. R. Sheppard [Sheppard *et al.*, 1977][Sheppard, 1986a][Sheppard, 1986b]. Conversion from frequency to distance, d, can be made using the relationship $f_s = d^{-1}$. In order to just satisfy the Nyquist criterion, the periodic sampling distance should at least be halved: $f_{Nyq} = (2d)^{-1}$. In this case, for a widefield microscope, the critical sampling distances, as communicated in the publications by Sheppard listed above, are:

$$d_{x,y} = \frac{\lambda_{em}}{4n \sin \alpha} \qquad d_z = \frac{\lambda_{em}}{2n(1 - \cos \alpha)}.$$

It is immediately obvious that $d_{x,y}$ is one-half the Abbe resolution limit (**Table 2.2.3.3.1.1**) as expected, since it indicates the highest spatial frequency passed by the microscope objective. d_z is in fact also one-half of the axial Abbe limit, although it is less trivial to recognise this; the expression above can be converted to the form given in **Table 2.2.3.3.1.1** by employing trigonometric identities.

In the case of a confocal microscope, the PSF is the product of the excitation and emission PSF, therefore it is twice as small as the widefield PSF. Hence, the critical sampling distances for a confocal microscope are one-half as small as those for the widefield:

$$\Delta d_{x,y}^{Nyq} = \frac{\lambda_{ex}}{8n \sin \alpha} \qquad \Delta d_z^{Nyq} = \frac{\lambda_{ex}}{4n(1 - \cos \alpha)}.$$

Note that it is the excitation wavelength that is relevant here.

Contrast is improved as a result of the broader bandwidth being passed by the confocal microscope. It should be emphasised, however, that doubling the bandwidth does not imply a doubling in the resolution. If the FWHM is used as a measure of resolution, then the confocal microscope improves resolution only by a factor of ~1.4 ($\sqrt{2}$) [Walker *et al.*, 2008]. Although capable of transmitting details twice as fine as the widefield microscope, the confocal attenuates high frequencies relatively strongly. The widefield also attenuates high frequencies near the cut-off, but to a lesser degree, as shown in **Fig. 2.2.3.3.2**.

2. 2. 2. 3. 3. Choice of pinhole diameter for confocal microscopy

With pinhole sizes less than 1 Airy unit (abbreviated as AU and equivalent to 1 Airy disc) in the object plane, the signal strength decreases drastically (**Fig. 2.2.3.3.3**). Due to the diminished SNR, the probability of resolving closely spaced objects plummets – hence a pinhole size of 1 AU is usually selected:

$$1 \text{ AU} = 1.22 \frac{\lambda_{exc}}{NA}.$$

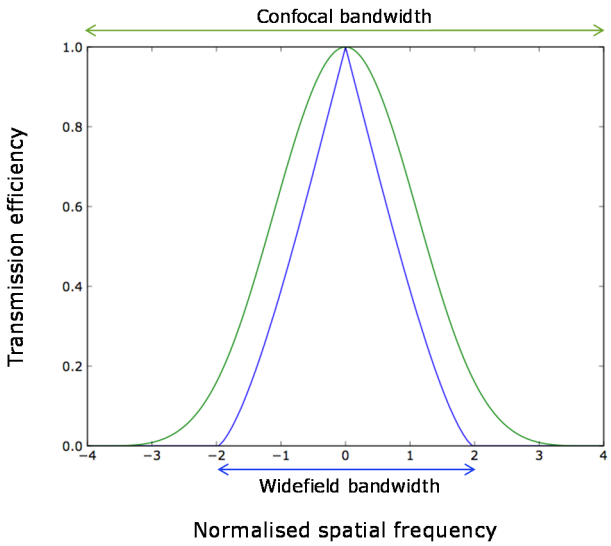

Figure 2.2.3.3.2. The optical transfer function (OTF) of ideal widefield and confocal microscopes. This graph shows the relative theoretical efficiency with which different spatial frequencies are transmitted by each microscope. Spatial frequencies are normalised with respect to wavelength and *NA*. The higher the spatial frequency, the smaller the detail. In theory, the confocal microscope should have twice the resolution of the widefield; however, due to strong attenuation of high frequencies, its resolution gain in practice is only about 1.4 times. Figure kindly provided by Prof. Mark Neil.

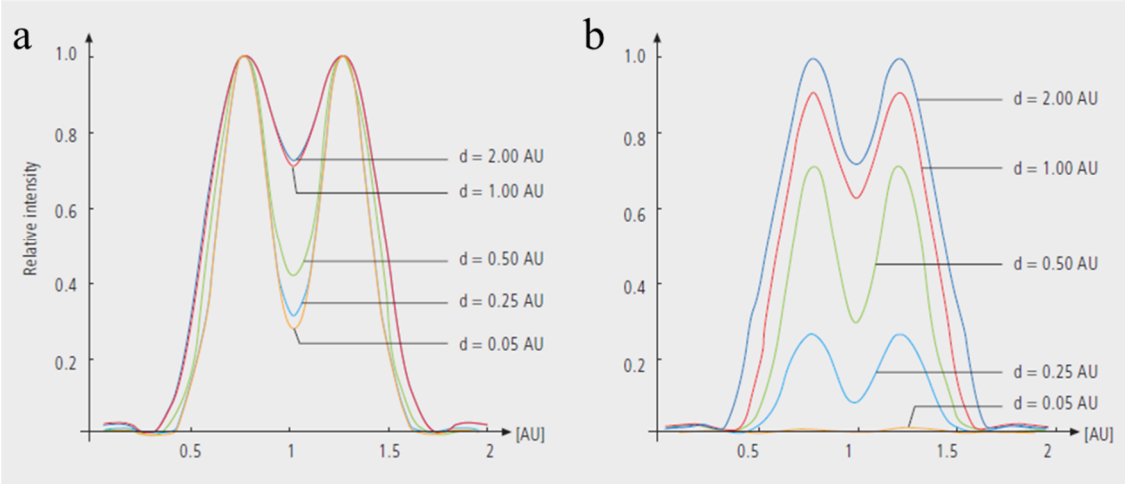

Figure 2.2.3.3.3. Impact of pinhole diameter on resolution *versus* noise trade-off. Plotted is the combined intensity of the PSFs of two point sources spaced ~0.5 Airy units (AU) apart in a direction transverse to the optic axis; (a) normalised with respect to maximum intensity, (b) non-normalised. (a) Constricting the pinhole leads to an improvement in resolution, as illustrated by the deepening dip in the middle of the graph and the narrowing of the individual PSF profiles. A pinhole diameter of 1 AU just selects the central maximum of each PSF, losing only a minimal amount of light from the side lobes, and leads to a modest gain in resolution. (b) Constricting the pinhole, however, also causes the detected signal intensity to decline sharply. For weak signals, such as are encountered in fluorescence imaging, a loss in intensity is associated with a drastic rise in shot noise (not shown in figure). Thus a pinhole diameter of 1 AU usually offers the best compromise between attaining as high resolution as possible, whilst keeping the noise from scrambling the signal by maintaining a high signal-to-noise ratio as well. Figure reproduced with permission from Carl Zeiss Ltd. from [Wilhelm *et al.*, 2008].

2. 2. 4. Total internal reflection (TIRF) microscopy

2. 2. 4. 1. Prerequisite conditions for TIRF

Total internal reflection fluorescence microscopy is an axial super-resolution technique with surface-selective properties. TIRF microscopy makes use of near-field excitation with an evanescent wave to reduce the excited volume to a thin slice (typically <100 nm) immediately above the coverslip surface. The technique can be implemented using two different geometries: one relying on a prism for excitation beam delivery, with the objective serving to collect the emitted fluorescence from the sample, and one where the objective doubles as illumination light distributor, obviating the need for a prism. The following explains the underlying principles of TIRF with an objective-type configuration, as opposed to prism-type, since that was the method I implemented in my imaging system.

Total internal reflection is a phenomenon, whereby light arriving at a sufficiently shallow angle at the boundary between two materials with successively lower refractive indices is totally reflected back into the first medium (**Fig. 2.2.4.1.1**). The critical angle, θ_C, *i.e.* the minimal angle of incidence at which TIR is incipient, is dependent upon the relative magnitude of the refractive indices of the two materials. If the first medium's refractive index is n_1 and the second n_2, then the critical angle, measured from the normal to the interface, is given by

$$\theta_C = \sin^{-1}\left(\frac{n_2}{n_1}\right). \qquad \textbf{Eq. 2.2.4.1.1}$$

Eq. 2.2.4.1.1 is a special case of Snell's law (**Fig. 2.2.4.1.2**). The latter determines in which direction light will bend as it passes through media of different refractive indices. At supercritical angles, all of the incident light is reflected at the boundary. Despite this, a so-called evanescent wave propagates into the medium beyond the interface. An evanescent wave is a form of light which does not propagate with sinusoidal intensity, but instead decays exponentially within a distance of less than a single wavelength [Axelrod, 2013].

The phenomenon of the evanescent wave arises out of geometrical considerations and the law of conservation of energy, expressed in terms of Maxwell's equations and the electromagnetic wave equation. Obliged to comply with these constraints, light cannot propagate and is forcibly extinguished. The following paragraph explains this from a rigorous mathematical standpoint, and derives an expression for the penetration depth of the evanescent field.

Firstly, for the sake of simplicity, the problem is examined in two dimensions, and the plane of incidence is taken to be the *x*-*z* plane (**Fig. 2.2.4.1.2**). Again, for explanatory convenience, if light is represented as a plane wave (*i.e.* with planar wavefronts), then the wavevector

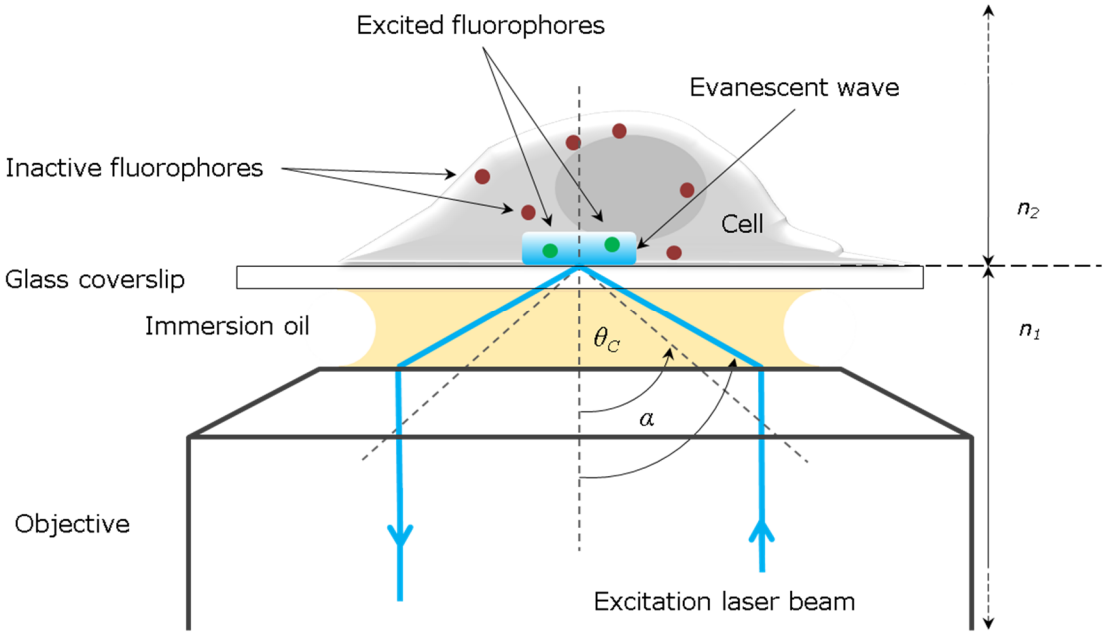

Figure 2.2.4.1.1. The total internal reflection (TIR) configuration. Total internal reflection fluorescence (TIRF) microscopy is relegated to imaging the specimen slice closest to the coverslip, and attenuates background signal from fluorophores situated deeper into the specimen. It requires a special set of conditions to operate. In order for TIR to occur at the coverslip-sample interface, the embedding medium must have a lower refractive index than that of the objective immersion fluid, *i.e.* $n_2 < n_1$. In addition, the objective must have a sufficiently high numerical aperture in order to be able to transmit oblique rays pitched above the critical angle, θ_C. θ_C itself depends on the ratio between n_1 and n_2. With respect to the delivery of excitation light at the sample, the TIR configuration involves passing the collimated beam through one half of the objective; the beam's displacement from the optic axis at the BFP dictates the angle at which the emergent beam strikes the coverslip-specimen plane of contact.

describing its propagation is given thus:

$$\boldsymbol{k_m} = k_{mx}\hat{\boldsymbol{x}} + k_{mz}\hat{\boldsymbol{z}}, \qquad \textbf{Eq. 2.2.4.1.2}$$

where the wave's amplitude in each dimension reads

$$k_m = \frac{2\pi}{\lambda_m} = \frac{n_m \omega}{c} = \sqrt{k_{mx}^2 + k_{mz}^2}\,. \qquad \textbf{Eq. 2.2.4.1.3}$$

m indicates the identity of the medium (m =1 or 2 in this case), n_m is its corresponding refractive index, ω is the angular frequency of the wave, or its colour (which is invariant), and c is the speed of light in vacuum [Axelrod, 2013]. In a given medium m, k_m is always conserved.

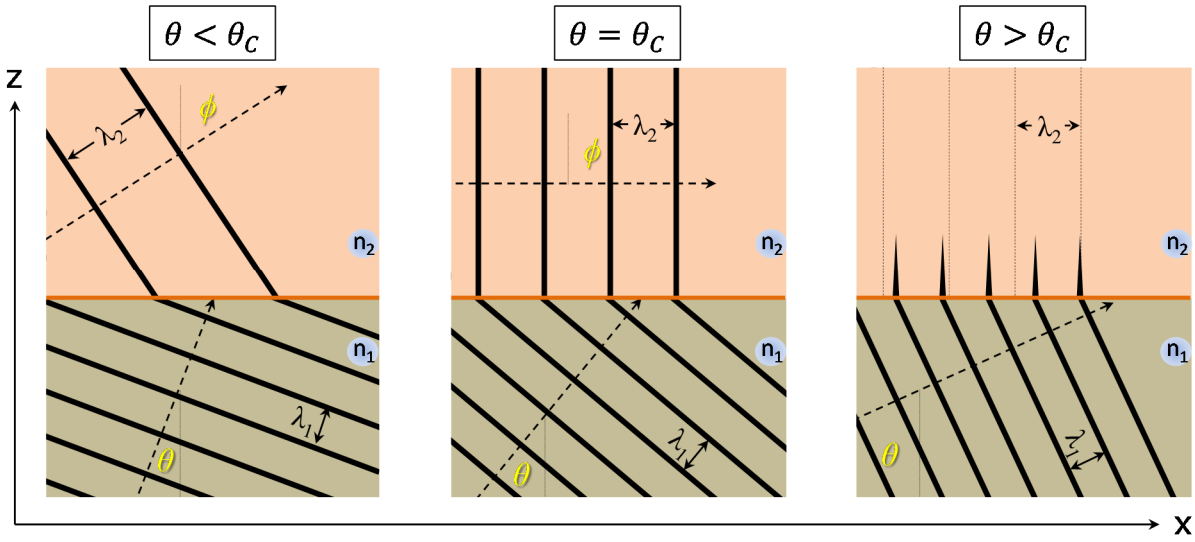

Figure 2.2.4.1.2. Snell's law of refraction at a surface and generation of an evanescent wave at supercritical angles. When light energy propagating through a transparent medium with a high index of refraction, n_1, impinges on a planar interface with a medium with lower index of refraction, n_2, the direction of light in the new medium will bend (refract) according to Snell's law: $n_1 \sin\theta = n_2 \sin\phi$. This behaviour is a consequence of avoiding discontinuities at the boundary, forcing the projection of the wavelengths along the surface to match on either side. At subcritical angles of incidence ($\theta < \theta_C$, measured from the normal to the surface), most of the light is transmitted into the medium with the lower refractive index. At $\theta = \theta_C$ (**Eq. 2.2.4.1.1**), the refracted light will propagate parallel to the surface. For supercritical angles ($\theta > \theta_C$), however, all of the light will be totally internally reflected into the medium with higher refractive index – except for a small proportion of the incident light, which will penetrate the surface and travel parallel to it. The vertical dashed lines represent the wavefronts of the wave with the shortest wavelength that could be supported by medium n_2 (same wavelength as in the $\theta = \theta_C$ case). However, due to the large angle of incidence, the wavefronts in medium n_2 are forced even closer together than this shortest allowed distance – hence the wave must disappear. The amplitude of this field, unlike that produced at $\theta = \theta_C$, therefore decays exponentially with depth z (short spikes) and is capable of exciting only fluorophores that might be present in the vicinity of the surface [Axelrod, 2008].

If k_{mx} is somehow made greater than k_m, then k_{mz} will have to become imaginary, in order to satisfy the conserved relationship in **Eq. 2.2.4.1.3**. Such a situation is possible if the wavefronts in the x direction in medium 1 are 'squeezed' very close together, so that their wavelength becomes shorter than the natural wavelength of the medium beyond the interface (medium 2), which is $\lambda_2 = 2\pi/k_2$. This situation is realised for supercritical angles (**Fig. 2.2.4.1.2**, $\theta > \theta_C$ condition). The wavelength of light travelling in medium m is $\lambda_m = \lambda_0/n_m$, where λ_0 is the wavelength of the incident light in vacuum. The component in the x-direction will therefore be $\lambda_{mx} = \lambda_0/(n_m \sin\theta)$. Observing the boundary conditions, *i.e.* the fact that wavelengths must

match at either side of the interface, it follows that $\lambda_{1x} = \lambda_{2x}$.

The spatial variation of the plane wave's electric field in the z direction can be written as

$$E_{mz} = e^{ik_{mz}z}. \qquad \textbf{Eq. 2.2.4.1.4}$$

It is easy to see then that if k_{2z} is imaginary, the field in medium 2 will decay exponentially. This field is perceived by an observer as the intensity:

$$I_{2z} = |E_{2z}|^2 = \left|e^{-|k_{2z}|z}\right|^2 = e^{-2|k_{2z}|z} = e^{-\frac{z}{d}}, \qquad \textbf{Eq. 2.2.4.1.5}$$

where d is the characteristic penetration depth of the evanescent field, or the distance over which it decays in intensity by a factor or $1/e$. The penetration depth therefore has a dependence on $|k_{2z}|$ as shown below:

$$d = \frac{1}{2|k_{2z}|}. \qquad \textbf{Eq. 2.2.4.1.6}$$

Bearing in mind **Eq. 2.2.4.1.3** for medium 2, **Eq. 2.2.4.1.1**, and the boundary conditions (or, equivalently, Snell's law) for the x-component of the wavelength to calculate $|k_{2z}|$, one arrives at the following expression for d:

$$d = \frac{\lambda_0}{4\pi n_1}\left(\sin^2\theta - \sin^2\theta_C\right)^{-\frac{1}{2}}. \qquad \textbf{Eq. 2.2.4.1.7}$$

The penetration depth is independent of the polarisation of the incident light and can take on a range of different values, depending on the wavelength used, the refractive indices of the immersion medium and mounting medium, and the angle of incidence. Typically, d varies between about λ_0 for incidence angles just greater than θ_C, to a tenth of this value for easily attainable supercritical incidence angles and the most commonly encountered refractive indices [Axelrod, 2013].

2. 2. 4. 2. Polarisation effects

2. 2. 4. 2. 1. Asymmetry in the behaviour of *s*- and *p*-polarised evanescent waves

In the context of a TIRF microscope, the polarisation of light entering medium n_2 will depend on

the polarisation of the laser and the spatial orientation of this polarisation with respect to the plane of incidence. The latter is defined by the propagation vector of the incident beam and the normal to the TIR plane. If the laser light is linearly polarised perpendicularly to the incidence plane, then the vibration of the electric field is said to be *s*-polarised (*s* stands for *senkrecht*, German for 'perpendicular'), and the evanescent wave's vibration in medium n_2 will be confined in the *x*-*y* plane. By contrast, light linearly polarised parallel to the plane of incidence (*p*-polarised light), upon traversing the boundary into the less dense medium, n_2, will begin to 'cartwheel' along the surface with a spatial periodicity of $\lambda_{exc}/n_1 \sin\theta$, where λ_{exc} is the wavelength of the laser source [Axelrod *et al.*, 1983][Leake *et al.*, 2006][Axelrod, 2008]. The elliptically *p*-polarised wave will therefore contain both axial and transverse components from the incident wave.

This carries implications about the manner and efficiency of excitation of the fluorophore dipoles. The absorption dipole moment, $\boldsymbol{\mu}$, of a fluorescent molecule is the orientation along which light must be absorbed in order for the fluorophore to transcend to an excited state. When $\boldsymbol{\mu}$ and the electric field vector of the excitation light are aligned, the excitation efficiency is maximal and fluorescence emission strength is at its peak (**Fig. 2.2.4.2.1**); this is because the electric field vibration must push the charges along the orientation of $\boldsymbol{\mu}$. When the vectors are mutually orthogonal, no light absorption, and therefore no fluorescence emission, can occur.

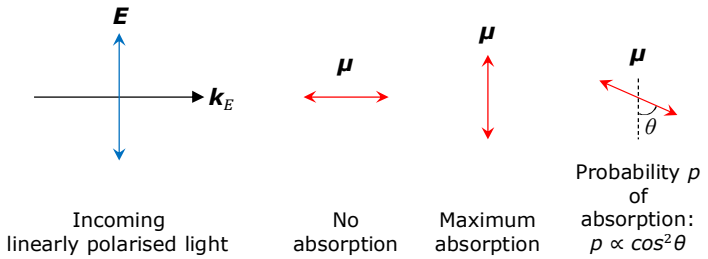

Figure 2.2.4.2.1. Probability of excitation of fluorophores with linearly polarised light. Illuminating an ensemble of randomly oriented fluorophores with linearly polarised light excites the fluorophores selectively. The fluorophore absorption dipole moment, $\boldsymbol{\mu}$, must be oriented parallel to the electric field vector, $\boldsymbol{E}$, of the incident light, in order for absorption to take place. A fluorophore with a dipole moment oriented perpendicularly to the incoming polarised light will not be excited. Some of the fluorophores with oblique orientations will become excited, others will not; the probability of absorption is proportional to the cosine squared of the angle θ between direction of light polarisation and $\boldsymbol{\mu}$.

2. 2. 4. 2. 2. Intensity increase of the evanescent wave at the substrate-specimen boundary

Upon encountering the lower refractive index, n_2, an abrupt rise in intensity occurs at the TIRF interface (*i.e.* at $z = 0$) [Lakowicz, 1992] (**Fig. 2.2.4.2.2**). This is a consequence of the standing-

wave interference between the incident and reflected beam. Due to the heterogeneity in the response of *s*- and *p*-polarised light at the interface, the intensity step at the boundary is different.

By considering the amplitude and polarisation of the incident electric field, the evanescent intensity increase of *p*- and *s*-polarised light at $z = 0$ (the TIR plane) and at a particular supercritical incidence angle is given by the formulae:

$$I_p = I_{p0} \frac{(4\cos^2\theta)(2\sin^2\theta - n^2)}{n^4\cos^2\theta + \sin^2\theta - n^2} \qquad \textbf{Eq. 2.2.4.2.2a}$$

$$I_s = I_{s0} \frac{4\cos^2\theta}{1-\left(\frac{n_2}{n_1}\right)^2}, \qquad \textbf{Eq. 2.2.4.2.2b}$$

where I_{p0} is the *p*-polarised intensity component of the incident light, I_{s0} is the *s*-polarised intensity component, and n_1 and n_2 are as defined previously. For subcritical angles, the plot can be extended without discontinuities at the critical angle using Fresnel coefficients whilst observing the separate boundary conditions of the electric and magnetic field across the TIRF interface [Lakowicz, 1992].

With the refractive indices and *s*-polarised light that have been used throughout this thesis, at the maximum acceptance angle of the objective, α, the intensity increase at the TIRF interface is about 1.51 fold (**Fig. 2.2.4.2.2**). This information has been used in Chapter 8, where the maximum acceptance angle was sought in order to decrease the penetration depth as much as possible to avoid exciting fluorescence from the cytoplasmic part of the cell.

2. 2. 5. Super-resolution imaging

The quest to demolish the fundamental resolution barrier of optical microscopy began in the 1990s, with the concept of stimulated emission depletion (STED) microscopy, which was developed by Stefan Hell [Hell *et al.*, 1994] and first realised in 1999 [Klar *et al.*, 1999]. The approach is based on shrinking the excitation volume produced by a laser-scanning microscope. In the meantime, a family of two other axial super-resolution techniques, namely 4Pi [Hell, 1992] and I^{5}M [Gustafsson *et al.*, 1995] were conceived, which rely on the coherent addition of spherical wavefronts from the specimen, captured by two carefully aligned, opposing high-*NA* objectives, in order to compress the effective PSF in the *z* direction. Around this time, a different approach named structured illumination microscopy (SIM) was also being launched [Heintzmann *et al.*, 1999][Gustafsson *et al.*, 1999]. Other super-resolution techniques, unrelated to the STED and

SIM principles and united under the umbrella term 'single-molecule stochastic localisation microscopy', emerged almost simultaneously in 2006: photoactivation localisation microscopy (PALM) [Betzig *et al.*, 2006], fluorescence photoactivation localisation microscopy (FPALM) [Hess *et al.*, 2006] and stochastic optical reconstruction microscopy (STORM) [Rust *et al.*, 2006]. A brief overview of these methods will be given in this section; however, it will be emphasised on the STORM modality, since it is the technique used in later chapters of this work.

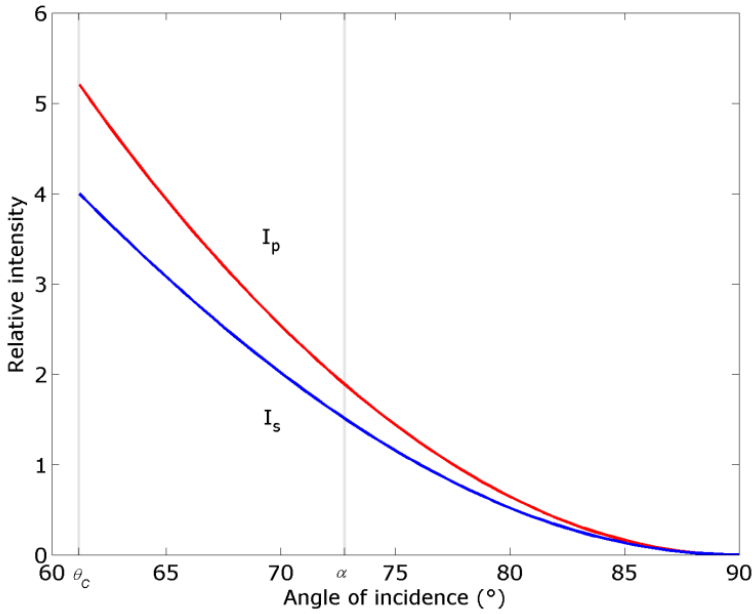

Figure 2.2.4.2.2. The intensity of the evanescent wave is a function of the incidence angle and polarisation. The quantity plotted on the ordinate is the relative intensity of TIRF illumination with respect to the incident intensity, which is taken to be unity for convenience. For *s*-polarised light, at θ_C, the critical angle, the intensity at the TIRF interface is 4 times greater than the incident intensity. At the maximum acceptance angle, α, of the TIRF objective used in this thesis, the intensity of *s*-polarised light at the coverslip-specimen interface is approximately 1.51 times greater than the intensity of the incident beam.

2. 2. 5. 1. Stimulated emission depletion (STED) microscopy

STED is a 'deterministic' technique, in the sense that it builds up the super-resolution image through sequential scanning of the sample. STED employs two lasers in order to slim down the diffraction-limited PSF formed by the illumination beam in the sample plane. As with a confocal

microscope, one laser delivers a diffraction-limited excitation beam matched to the absorption spectrum of the fluorophore in use. The second beam, termed the 'STED beam' is red-shifted to approximately the emission wavelength of the fluorophore. The latter beam is shaped in the form of a torus (for example, with an optical vortex), with the excitation beam arranged coaxially and coinciding with the zero-intensity centre of the STED beam (**Fig. 2.2.5.1**). Thus, only fluorophores residing in the centre of the torus can be excited, whereas those towards the periphery undergo stimulated emission which de-excites them back to the ground state , leaving them invisible. Spontaneous emission (the fluorescence one is interested in) can then be separated from stimulated emission with careful choice of filters [Hell, 2007].

The fluorophores respond non-linearly to depletion from the STED beam. In fact, there exists an intensity threshold at which stimulated emission just outcompetes fluorescence. Increasing the STED beam intensity thus shrinks the excitation radius, and the effective illumination PSF can be reduced virtually indefinitely in this manner. If I_s stands for the depletion intensity threshold, the resolution as a function of STED intensity varies as follows:

$$r \approx \frac{\lambda}{2 \cdot NA \cdot \sqrt{1+\frac{I_{max}}{I_s}}},$$

where $\lambda/2NA$ is the Abbe resolution limit and I_{max} denotes the maximum intensity of the STED beam [Westphal *et al.*, 2005].

To date, a lateral resolution as low as 15–20 nm has been achieved with STED in helping to discern endosomal and nuclear protein patterns [Donnert *et al.*, 2006]. In addition, STED has also been applied to studying SNARE proteins in the plasma membrane [Sieber *et al.*, 2006], protein distributions at neuronal synapses [Willig *et al.*, 2006], and at neuromuscular junctions [Kittel *et al.*, 2006]. Two-colour STED [Donnert *et al.*, 2007], *in vivo* STED [Schröder *et al.*, 2009] and live-cell STED [Hein *et al.*, 2008] have also been realised. Nevertheless, STED microscopy is limited to a specific subset of fluorescent dyes whose excitation spectrum does not overlap with the STED wavelength – otherwise the latter will excite, instead of suppress, fluorescence. In addition, the dyes must be considerably photostable to withstand the high intensities required to achieve high resolution.

Other techniques related to STED are ground-state depletion (GSD) and saturated pattern excitation microscopy (SPEM). GSD makes use of a PSF-engineered scanning beam to transfer fluorophores from the singlet ground state to the dark triplet state, whereas SPEM exploits the saturable property of the fluorophores to produce higher spatial frequency harmonics in the fluorescence emission pattern [Hell, 2007][Cremer *et al.*, 2013].

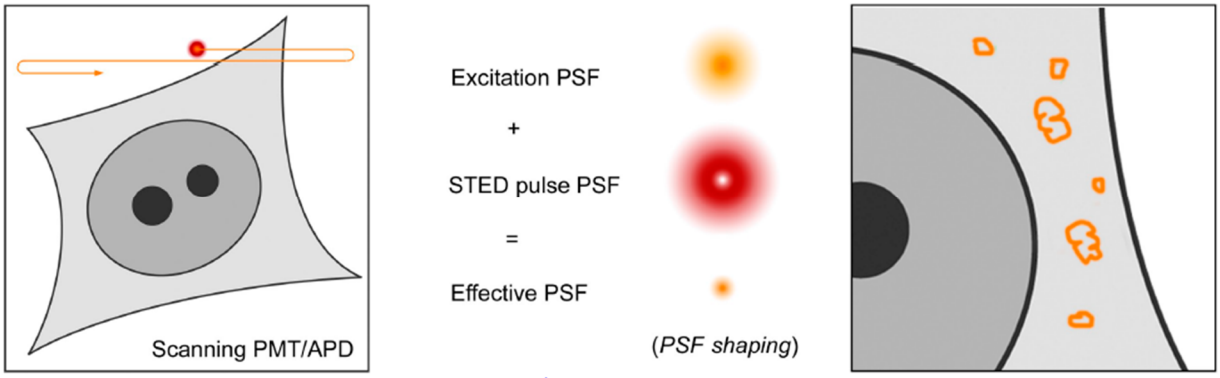

Figure 2.2.5.1. Principle of stimulated emission depletion (STED) microscopy. An excitation laser beam is combined coaxially with a spatially modulated beam of much longer wavelength, called the STED beam. The excitation beam is able to excite fluorescence from molecules only in the zero-intensity centre of the STED beam. Fluorescence from fluorophores surrounding this region is suppressed through stimulated emission. In this way, the effective PSF is reduced and the resultant resolution increased. Diagram reproduced from [Schermelleh et al., 2010] with permission from, and copyright to, Rockefeller University Press.

2. 2. 5. 2. Structured illumination microscopy (SIM)

Unlike STED, SIM is a widefield technique which illuminates the entire sample at once. This approach was invented by Rainer Heintzmann, Christoph Cremer and Mats Gustafsson [Heintzmann *et al.*, 1999][Gustafsson, 1999][Gustafsson, 2000]. It is based on the idea that illumination of a predetermined sinusoidal pattern can be 'convolved', or combined, with sub-resolution features in the sample to produce an interference (Moiré) pattern containing coarser spatial details which can be captured by the objective. The illumination pattern of light is created by shining light through a 'grating' (**Fig. 2.2.5.2**). Three to five images are collected with the grating superimposed at different phase angles over the sample, and another three to four at different orientations, in order to ensure a nearly isotropic resolution gain.

After collecting the desired information encoded on the carrier wave of the illumination pattern, specialised software separates the two signals in the Fourier domain, retains the one of interest and transforms it back into real space.

Due to the need to shift the illumination pattern multiple times to scan the sample, this imaging scheme has a relatively low temporal resolution. In terms of spatial resolution, it can achieve an improvement of up to a factor of 2, compared to a confocal microscope. A subtype of SIM, called saturated structured illumination microscopy (SSIM), can accomplish even better resolution. SSIM introduces nonlinearities in the excitation pattern which permit even higher-order frequencies to be recorded in reciprocal space. Lateral discrimination down to 50 nm has

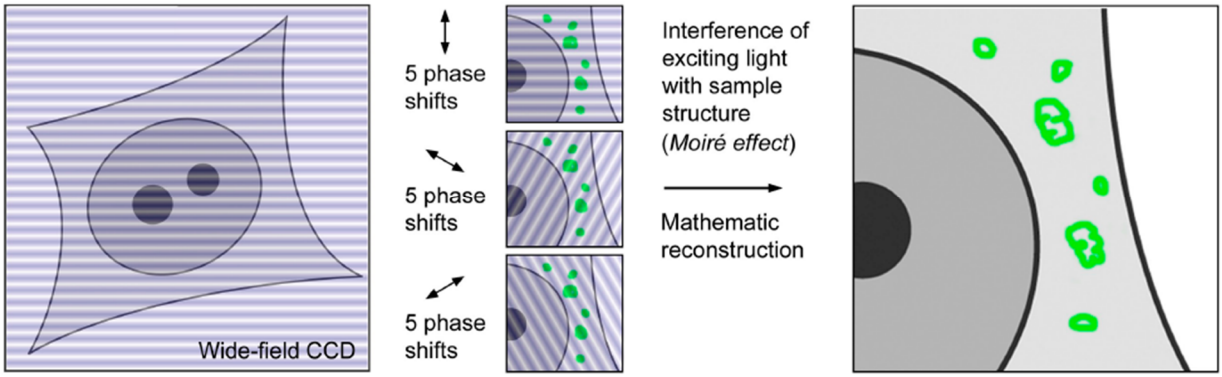

Figure 2.2.5.2. Principle of structured illumination microscopy (SIM). The specimen is illuminated with a well-defined sinusoidal pattern which is rotated and translated over the specimen several times. An interference pattern, called Moiré fringes, is produced upon interaction of the illumination with the sample. Otherwise unresolvable features can be deduced from the fringes and computationally restored. Diagram reproduced from [Schermelleh *et al.*, 2010] with permission from, and copyright to, Rockefeller University Press.

been successfully attained [Gustafsson, 2005]. However, similar to STED, SSIM requires progressively higher illumination intensities in order to achieve ever higher resolution, and can therefore incur radiation damage on the sample.

Nevertheless, to date, SIM has enjoyed extensive application to various biological problems – including imaging in fixed cells of mitochondria [Hirvonen *et al.*, 2009], the immune synapse of natural killer cells [Brown *et al.*, 2011], and tubulin and kinesin dynamics in live cells [Kner *et al.*, 2009].

2. 2. 5. 3. Single-molecule localisation microscopy (SMLM)

2. 2. 5. 3. 1. 2D STORM and PALM

SMLM, akin to SIM, is an ensemble imaging technique, in the sense that it makes use of the wide-field configuration to collect information from the sample in no particular order. SMLM consists of two closely related modalities: PALM and STORM (**Fig. 2.2.5.3**), which are both based on the premise that spatial separation of the fluorescent emitters to a density of no more than one molecule per diffraction-limited area can bring the effective resolution into the nanoscale. This is because isolating the fluorophores allows their locations to be very precisely determined by pin-pointing the centre of their PSFs.

A convenient and fairly accurate closed-form expression of the localisation error is pre-

sented here:

$$\Delta r_{rms} = \sqrt{\frac{s^2+\frac{a^2}{12}}{N} + \frac{8\pi s^4 b^2}{a^2 N^2}} \propto \frac{s}{\sqrt{N}}, \qquad \textbf{Eq. 2.2.5.3}$$

where s is the standard deviation of the PSF, a represents the size of the pixels and b is the background noise in photons per pixel [Thompson *et al.*, 2002]. The first term is a contribution from the photon-counting noise and becomes dominant at high photon numbers; the second is the background level which prevails at low photon numbers. The simplified expression on the right-hand side above is roughly true when the background is negligible. The resolution improvement factor, $\sqrt{N}$, is derived from photon statistics. Since single molecules emit relatively few photons, their emission conforms to a Poisson distribution. The standard deviation of a Poisson distribution equates precisely to the square-root of the total number of photons detected. Thus the confidence (*i.e.* precision) with which the centre position of the molecule can be determined rises

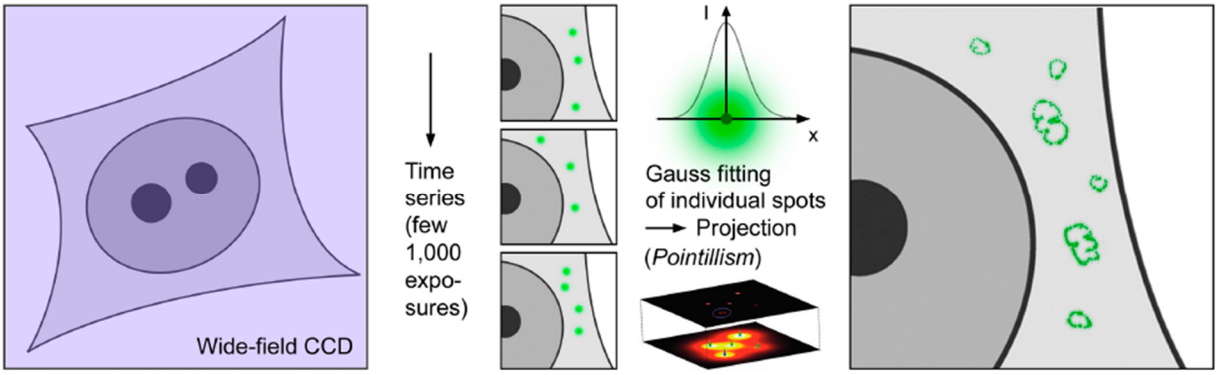

Figure 2.2.5.3. Principle of single-molecule localisation microscopy (SMLM), comprising stochastic optical reconstruction microscopy (STORM) and photoactivation localisation microscopy (PALM). STORM utilises a combination of high-intensity laser illumination and a redox chemical imaging buffer to switch reversibly stochastic subsets of the fluorophore population between a bright and a dark state and image them individually multiple times over several activation cycles. PALM operates on a similar principle, though instead activating the fluorophores with UV light and deactivating them permanently *via* photobleaching, thus imaging each fluorophore subset only once. By careful tuning of the laser intensity (and buffer reagents, in the case of STORM), the majority of the fluorophores can be maintained in the dark state, leaving visible only an optically resolvable subset of fluorophores. The isolated molecules are then fitted with a PSF (or more often with a 2D Gaussian function approximating a PSF) which permits to determine their centre positions very accurately. Iterating the process allows the eventual localisation of the entire fluorophore population. Subsequently, all of the localised molecules are integrated into a single image – the super-resolution reconstruction. Diagram reproduced from [Schermelleh *et al.*, 2010] with permission from, and copyright to, Rockefeller University Press.

with the brightness of the molecule and results in a concomitant rise in resolution. The boost in the effective root-mean-square resolution that SMLM can afford, Δr_{rms}, is therefore roughly proportional to the square-root of the total number of photons, *N*, emitted by the molecule. To maximise the amount of useful photons collected, as opposed to those originating from the background, STORM and PALM are often carried out in the TIRF configuration.

Since biological samples contain a fairly dense distribution of fluorophores, sparsity is achieved through temporal separation: small subsets of the probes are activated stochastically, imaged, then either bleached (PALM) or returned to a stable dark state (STORM). It is worth drawing attention to the fact that separating individual fluorophores can also be executed through exploiting a mixed population of fluorophores with different spectral signatures – as was proposed in 1997 in a technique called spectral precision distance microscopy (SPDM) [Heintzmann *et al.*, 1997].

Originally, PALM was conducted with specially designed photoactivatable fluorescent proteins, whereas STORM was performed with reversibly switchable small organic dyes (immersed in an oxygen-scavenging buffer necessary for controlled switching). Through the years, the defining characteristics of PALM and STORM have become increasingly blurred with the implementation of photoconvertible proteins, such as Dronpa, which can interconvert from the dark to the bright state multiple times, and the recent addition of commercial photoactivatable dyes manufactured by Abberior, which undergo only one switching cycle before being permanently bleached.

STORM originally made use of a pair of cyanine dyes, Cy3 and Cy5 [Rust *et al.*, 2006]. Cy5 acted as a fluorescence 'reporter', whose signal was actually detected, whereas the Cy3 served as a silent 'activator', accelerating the rate of conversion of the reporter back into the fluorescent state. It should also be remarked that the switching on and off was effected, respectively, with two distinct wavelengths. Here, a subtle distinction can be made between fluorophores which are both imaged and turned off with the same wavelength (negative switches, such as the Cy3-Cy5 dye pair) and those which are turned on and imaged with the same wavelength (positive switches, such as the photoswitchable protein Padron). The complexity of this approach – in particular, the need to devise and execute special protocols for labelling antibodies with those dyes in the correct ratio, and simultaneously comply with the proximity requirement of the cyanine dyes which controls the fluorescence recovery rate, seemed daunting at first. However, the discovery that acceptable switching could be performed with single dyes (Cy5 and Alexa Fluor® 647 [Heilemann *et al.*, 2008]), without the needed for an activator dye, was welcomed by the imaging community and led to numerous research groups embracing this novel, simplified version of STORM. The scheme was named 'direct' STORM, or *d*STORM. In contrast to the parent technique, *d*STORM requires substantial laser intensities (~1,000 times greater than used in

conventional STORM) to revert the dyes to the dark state. *d*STORM has now become the standard version of STORM, and for this reason in this thesis it will henceforth be referred to simply as 'STORM', omitting the '*d*'.

The advent of multicolour PALM [Shroff *et al.*, 2007] and STORM [Bates *et al.*, 2007] opened new avenues for the stochastic localisation techniques. In 2008, acquiring a sufficiently large set of images to achieve the highest resolution (~20 nm) typically required several minutes; however, a temporal resolution of several tens of seconds was possible – at a trade-off for lower spatial resolution (~60 nm) [Shroff *et al.*, 2008]. By 2011, video-rate imaging had been realised for the first time, with resolution of ~25 nm in 2D and frame rates of 0.5 s, or ~30 nm transverse / ~50 nm axial resolution in volumetric 3D imaging at 1-2 Hz frame rates [Jones *et al.*, 2011].

The characteristic advantages and limitations of all the main families of super-resolution techniques listed so far – with the SMLM varieties of STORM and PALM evaluated separately – are laid out in **Table 2.2.5.3** below.

Table 2.2.5.3. Advantages and disadvantages of different super-resolution techniques. Comparison of stimulated emission depletion (STED), structured illumination microscopy (SIM) and single-molecule localisation microscopy (SMLM), comprising the modalities stochastic optical reconstruction microscopy (STORM) and photoactivated localisation microscopy (PALM).

Technique	*Advantage*	*Disadvantage*
STED	• Resolution limit of 15 nm. • Relatively rapid acquisition (approximately the same as a confocal microscope); • No need for post-processing of the data to extract super-resolution image → fewer artefacts.	• Rapid sample bleaching and/or photodestruction, due to requirement for a very high-intensity STED beam; • Requires ultra-photostable dyes with strictly defined spectral characteristics.
SIM	• Conventional dyes or FPs can be used, as long as they are reasonably photostable.	• Only a two-fold improvement in resolution, compared to standard fluorescence techniques (*i.e.* ~100 nm); • Complex and time-consuming

		acquisition and data post-processing → artefacts such as aliasing possible.
STORM	• Localisation precision limit of 10 nm; • Ordinary dyes can be used; • Does not require FP fusion with protein of interest.	• Live-cell imaging possible, but complicated due to redox buffer requirements for photoswitching; • Complex and time-consuming acquisition and data post-processing → pointillism-related artefacts possible.
PALM	• Localisation precision limit of 10 nm.	• Complex and time-consuming acquisition and data post-processing → pointillism-related artefacts possible; • Actual resolution may be worse than for STORM, due to FPs having, on average, a 10-fold lower photon emission rate.

2. 2. 5. 3. 2. Methods for 3D STORM and PALM

In order to gain 3D information, one strategy involves encoding 3D information in the *x*-*y* plane. With the aid of a cylindrical, astigmatic lens, the relative depth of the particle can be encoded in the deliberate introduction of asymmetry (ellipticity) in the image [Kao et al., 1994]. Thus, if the particle is above the focal plane, its image is stretched in one lateral dimension, whereas if it is below that reference point, the image is stretched in the orthogonal lateral direction. Resolution of ~30 nm in *x* and *y*, and ~60 nm in *z* has been achieved with this technique [Huang et al., 2008]. One disadvantage of using astigmatism is that the resolution is nearly always slightly compromised in one lateral direction by the artificial widening of the PSF in that direction. The depth range over which the astigmatic lens can provide reliable *z* information is limited by the threshold of detection, as the signal is gradually dissipated with vertical distance from the focal plane. Remodelling the PSF in the shape of two twisting lobes along the optic axis in the manner

of a double helix (DH) is yet another variant of the same fundamental principle [Pavani et al., 2008]. The angular orientation of the lobes informs on the depth, whereas the midpoint between the lobes corresponds to the (*x*, *y*) coordinates of the particle. The positional accuracy of DH-PSF systems are 14 nm in the *x*-*y* plane and 37 nm in the *z*, and the axial range of operation is 5-6 μm.

Another approach is to infer the axial position by comparing two slices of the object taken at different depths to the expected form of the PSF. Thus, the specimen is imaged simultaneously in two different planes along the *z*-axis and the *z*-position of the particle deduced, based on the amount of defocus observed in each image [Juette et al., 2008]. This method is termed 'biplane FPALM' and is capable of attaining a resolution of 30 nm in the *x*-*y* plane and 75 nm in the *z* consistently throughout the sample. It has a depth range of several micrometres.

Interferometric PALM (iPALM) is yet another way of deriving axial information. Analogous to DIC and phase contrast, which exploit interferometry albeit qualitatively, iPALM measures the phase of the interference using a set-up with two opposing objectives and multiple detectors [Shtengel *et al.*, 2009]. With iPALM a resolution of sub-20 nm in all directions is possible.

2. 2. 5. 3. 3. STORM imaging probes

2. 2. 5. 3. 3. 1. Fluorescent proteins (FPs)

Currently, there are two major classes of fluorescent probes suitable for STORM imaging. One class is derived from an array of fluorescent proteins isolated from marine animals, such as the coral family *Pectiniidae* and the jellyfish *Aequorea victoria*. Dronpa is an example of a photoswitchable protein modified from a naturally occurring fluorescent coral protein, whereas photoswitchable GFP is a mutant of a native version famously isolated from jellyfish.

Virtually all proteins employed in PALM imaging have been modified to enhance their fluorescent properties. Switching from one state to the other is associated with a change in absorbed wavelengths and fluorescence quantum yield. The bright 'on' state and dark 'off' state are often thermally and photochemically intercovertible. Reversible conversion has been shown to occur *via cis-trans* photoisomerisation, where the chromophore tripeptide is in the *cis* conformation when in the 'on' state. Photoswitching may also involve protein side-chain rearrangements [Warren *et al.*, 2013]. Spectroscopic contrast is also thought to be generated by photoinduced protonation (switching on) and deprotonation (switching off the fluorophore) of the phenolic oxygen of the chromophore [Imamoto *et al.*, 1997].

2. 2. 5. 3. 3. 2. Small synthetic, organic dyes

The second type of probes consists of synthetically engineered organic dyes. These fluorescent markers are around 10 times brighter than FPs and can be subdivided into several categories, based on the precursor that they are derived from: rhodamine, fluorescein, coumarin, cyanine, oxazine, thiazine and others. Alexa Fluor® 488, Alexa Fluor® 555 and ATTO 565 (related to Rhodamine 630 [Sauer *et al.*, 2011]) are all rhodamine derivatives, and have been utilised throughout this work. Their chemical structure is displayed in **Fig. 2.2.5.3.3.2.1**. Concentrating therefore on the specific behaviour of rhodamine derivatives, the following passage will lay out the photoswitching strategies for these dyes in more detail.

In order to be able to reduce the fraction of fluorophores in the 'on' state to enable the acquisition of single-molecule images on the detector, most of the fluorophore population labelling the sample needs to be switched to a dark state. The longer the dark state, the higher the fraction of dark molecules. The triplet-state lifetimes of rhodamine derivatives are relatively short: typically 5-6 μs. This is not long enough for the purposes of STORM imaging; one aims therefore to convert the dye to an alternative, much longer-lived dark state – such as a stable radical ion. The triplet state can be depopulated *via* an electron transfer reaction with a reducing or oxidising agent to form radical anions or cations. Rhodamine-based dyes tend to form anions much more easily than cations; for this reason, usually a reducing agent, such as β-mercaptoethylamine (MEA; also known as cysteamine) is used to stimulate the conversion.

When the fluorophore enters the triplet state, a chemical reaction catalysed by excitation light, whereby a primary thiol compound, *e.g.* MEA, reacts with the probe, results in inactivation of the fluorescent chromophore group by breaking of chemical bonds – more specifically,

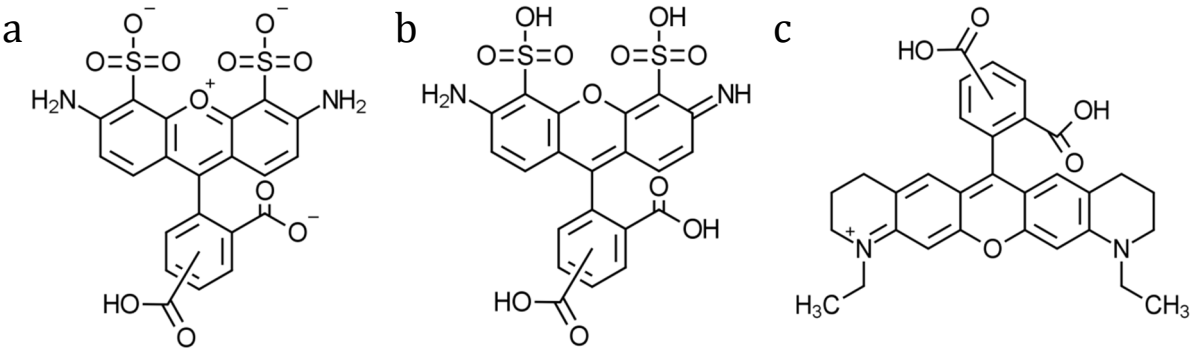

Figure 2.2.5.3.3.2.1. Chemical structure of organic fluorescent dyes. (a) Alexa Fluor® 488, (b) Alexa Fluor® 555 and (c) ATTO 565. Structures for (a) and (b) obtained from [http://www.ebi.ac.uk, The European Bioinformatics Institute]; (c) obtained from [www.atto-tec.com, ATTO-TEC GmbH].

by photocycloreversion (photoinduced ring-opening) [Sauer *et al.*, 2011]. In the presence of a reducing thiol, the radical-ion dark state of rhodamine dyes can be extended by 3-6 orders of magnitude, compared to the triplet lifetimes [van de Linde *et al.*, 2011]. Light-driven reduction of the dye is more efficient when the oxygen concentration is reduced. In order to sequester free oxygen in the sample, a combination of the enzyme glucose oxidase (GlOx) and a substrate, glucose, is employed (**Fig. 2.2.5.3.3.2.2**) [Aitken *et al.*, 2008].

Once in the triplet state, the fluorophore is faced with two different fates (**Fig. 2.2.5.3.3.2.3**). The triplet state can either react with molecular oxygen – a very potent triplet-state quencher – to repopulate the singlet ground state or react with the reducing agent to form a semi-reduced radical anion: the long-lived, metastable dark state. The dye radical can then react spontaneously with oxygen to repopulate the singlet ground state. Radicals have one unpaired electron in an open-shell configuration. Although generally short-lived due to their high reactivity, some organic radicals are relatively stable because of the delocalisation of the unpaired electron in a conjugated π system.

The probability of transition to the dark state for rhodamine dyes is only 0.1%. For this reason, this class of dye requires irradiation with relatively high excitation intensities (on the order of kW/cm^2) to populate the triplet state efficiently. More information on the quantum-mechanical significance of this state is given in Appendix A. It is important to understand the quantum mechanical behaviour of the dye molecules because it offers an explanation for why the bright and dark states have different durations and rates of interconversion.

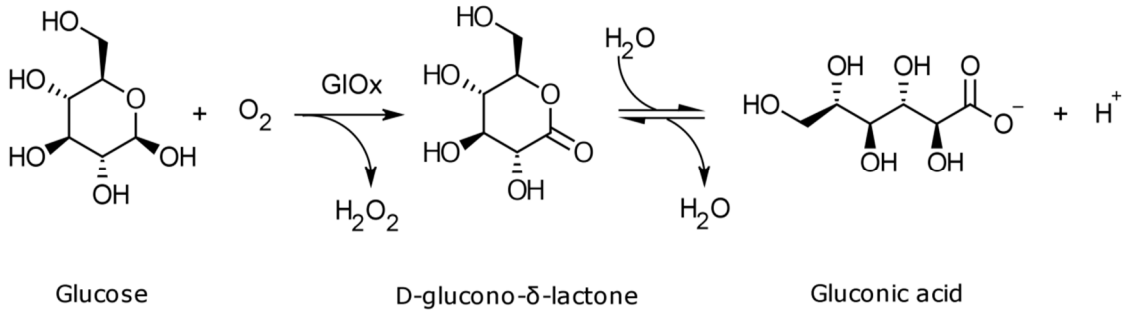

Figure 2.2.5.3.3.2.2. The oxygen scavenging reaction of the enzyme glucose oxidase (GlOx). The rate of switching between the metastable fluorescent and dark states can be controlled through manipulation of the probe's photochemical properties. The long-lived dark state of the radical ion can be extended by preventing molecular oxygen from interacting with it and returning it to the ground state. Glucose oxidase sequesters oxygen through catalysing the oxidation of glucose into D-glucono-δ-lactone, which is subsequently hydrolysed to gluconic acid.

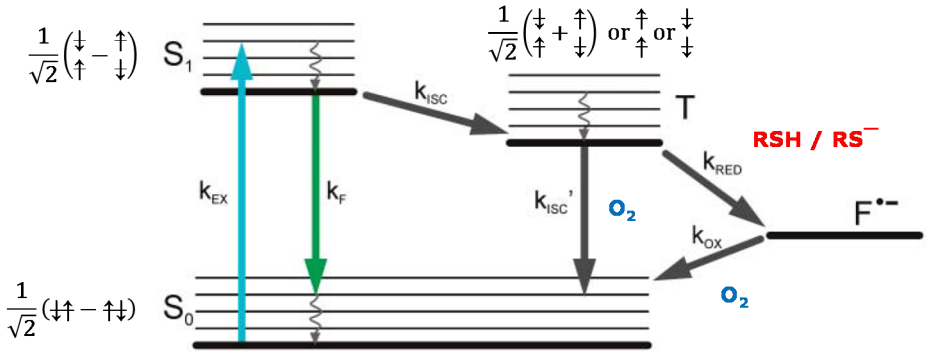

Figure 2.2.5.3.3.2.3. Jabłoński diagram of the photoswitching scheme of rhodamine-derived dyes. Upon excitation (blue arrow) the fluorophore cycles between the singlet ground state (S_0) and the first excited singlet state (S_1), emitting fluorescent photons with each relaxation to the lower energetic state (green arrow). Occasionally, depending on the intersystem crossing rate, k_{ISC}, the molecule will enter a transient, dark triplet state, T. This dark state is usually short-lived, lasting less than 10 µs for rhodamine dyes. Reducing and oxidising agents in the embedding medium have the capacity to perform electron transfer reactions on the dye molecule. Thus, in the presence of a primary thiol compound (RSH / RS^-), the molecule converts to a stable, dark radical ion state. For rhodamine dyes, this is often an anion. The molecule can be restored from the dark states (T, $F^{\bullet-}$) back to the fluorescent state *via* interaction with molecular oxygen. Quantum mechanical states of the fluorophore's valence electrons are also indicated. For the nomenclature, the reader is referred to Appendix A. Figure adapted from [van de Linde *et al.*, 2009] with permission from The Royal Society of Chemistry (RSC) on behalf of the Centre National de la Recherche Scientifique (CNRS) and the RSC.

From a super-resolution standpoint, the capability of custom-engineering the duration of the dark and bright states of the synthetic molecular probe is highly desirable. Judicious optimisation of these parameters with respect to the imaging conditions and instrument set-up during recording holds numerous advantages: maximised signal-to-noise ratio (SNR), for example, leads to superior localisation precision, whereas regulation of the fraction of fluorophores in the 'on' state ensures that the sparsity condition at the heart of the stochastic super-resolution techniques is fulfilled. In this vein, adjusting the fluorophore population density to an average of just one molecule per diffraction-limited area streamlines the data gathering efficiency, minimising both the total number of frames required for reconstruction and the overall output file size. The reduced imaging time in turn translates into a lower degree of photodamage of the specimen and less chance of photobleaching the fluorescent probes. Finally, engineering the fluorescent states gives the microscopist freedom to decide whether to make a compromise be-

tween localisation accuracy and speed of acquisition in situations where the acquisition time is the limiting factor – such as in live-cell imaging.

To summarise, the desirable traits of fluorophores for STORM and PALM alike are high quantum yield, photostability, and extinction coefficient (absorbing probability), as well as a high contrast ratio (the ratio of photons emitted in the bright state, compared to the number emitted in the dark state). Dense labelling of the specimen also ensures that the resolution is not limited by failure in satisfying the Nyquist criterion (**Eq. 2.2.3.3.2**). However, it should be emphasised that the presence of too many fluorophores per diffraction-limited volume can lead to problems with achieving the sparsity prerequisite of SMLM, since the probability of adjacent fluorophores being in the 'on' state is increased.

2. 2. 6. Enhanced green fluorescent protein

The original, native green fluorescent protein (GFP) was isolated from the Pacific jellyfish *Aequorea Victoria* by Osamu Shimomura in the 1960s [Shimomura *et al.*, 1962]. A large part of marine flora and fauna is photoluminescent. The primary light sources in these organisms are either aequorin or luciferase, whose chemiluminescence is absorbed and re-emitted with a red-shift by a secondary photoprotein. GFP is such a secondary photoprotein [Phillips, 1997].

GFP is remarkable for its self-sufficiency: it does not require intervention from other molecules to fold itself and its fluorescent domain (chromophore). Courtesy of this feature, GFP has enjoyed successful recombinant expression in countless organisms, other than its native. It was not until GFP cDNA was first cloned [Prasher *et al.*, 1992] and its functional expression in non-native organisms, such as bacteria, demonstrated [Chalfie *et al.*, 1994] that its significance for cell, molecular and developmental biology became tangible.

Following translation of the gene, the maturation of the protein proceeds by autocatalytic cyclisation and oxidation of the chromophoric trio of residues, Ser^{65}-Tyr^{66}-Gly^{67}. This trio of residues is attached to the peptide backbone through the 1- and 2-positions of the ring [Tsien, 1998]. Wild-type GFP has a strong absorption peak at ~395 nm and a lower peak at ~475 nm, with an emission peak in the green at ~ 508 nm [Phillips, 1997][Garcia-Parajo *et al.*, 2000]. Mutating residues which are members of the chromophore, or those surrounding it, can improve the photostability and emission of the fluorescent protein. A widespread product of such mutation is the S65T, where Ser^{65} has been mutated to Thr. This mutant, called 'enhanced GFP', or EGFP, possesses a single excitation peak at ~475 nm, is six times brighter, and its photophysical properties exhibit a larger absorption cross-section and lack of photoisomerism, compared to wild-type GFP [Heim *et al.*, 1995][Garcia-Parajo *et al.*, 2000].

(E)GFP consists of a topless and bottomless 'barrel' comprising 11 β-sheets. The diameter of the barrel is ~4 nm and its length along the axis of symmetry is ~3 nm. Within the cylindrical case is nested the fluorescent core of the protein – part of an irregular α-helical motif which extends to form 'caps' on both ends. The highly regular structure of the β-barrel is thought to protect the chromophore heart of the protein and resist unfolding and instability threatened by heat and denaturants [Phillips, 1997]. The chromophoric structure of EGFP is displayed in **Fig. 2.2.6**.

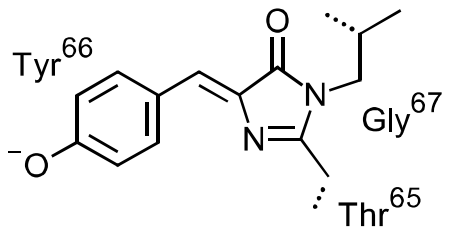

Figure 2.2.6. Chemical structure of the chromophore of enhanced green fluorescent protein (EGFP). The chromophore consists of a tripeptide of threonine, tyrosine, and glycine. Dotted lines symbolise sites of attachment to the rest of the protein.

2. 2. 7. Differential interference contrast (DIC)

Unstained biological cells are often difficult to observe using traditional bright field illumination, due to their being virtually transparent. Invented by Francis Smith in 1955, DIC improves the visibility of the cells by converting differences in optical path length through the sample into amplitude differences in the image. Visually, this is manifested as pronounced contrast improvement in the specimen (**Fig. 2.2.7**). Images produced with DIC microscopy have a characteristic shadow-cast appearance – as if the specimen were illuminated obliquely by a single light source.

The practical implementation of the DIC concept is described in the following outline. A polariser and analyser filters are inserted into the optical pathway before the condenser and after the objective, respectively. One birefringent (Nomarski) prism is situated at the front focal plane of the condenser and a second prism at the rear focal plane of the objective. Incoherent

light emanating from a white-light source, is focused onto the prism and, with the polarizer in the optical path, is linearly polarized at 45° to the optic axis of the prism. The birefringent crystal splits the oncoming beam into a pair of beams (termed the ordinary and extraordinary rays), with plane-polarisations oriented at mutually orthogonal directions and travelling parallel to each other at a separation distance slightly beneath the resolution of the microscope objective. The shear distance (the beams' separation) is typically 0.15 μm for a high-*NA* objective. The sheared pair of light rays are next refracted and relayed by the condenser lens so that they travel parallel to each other all the way to the specimen.

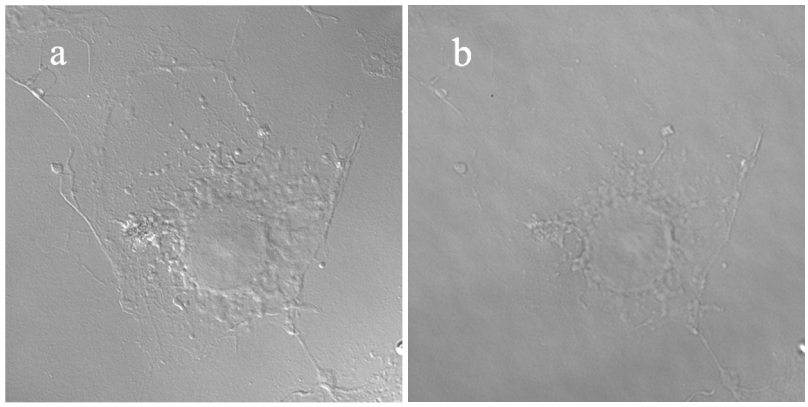

Figure 2.2.7. Comparison of the effectiveness of differential interference contrast (DIC) and bright field transmitted-light imaging techniques to provide contour definition of a biological cell. The images both show the same COS-7 cell (typical cell diameter from this cell line is ~20 μm), imaged in turn with (a) DIC and (b) bright field illumination. DIC renders the cell easily discernible, and in three-dimensional relief, by converting optical path differences into intensity differences. However, in bright field, which simply illuminates the specimen straight through, the cell is hardly visible. Clearly, DIC provides much better specimen contrast than the bright field illumination mode.

Upon encountering the specimen, one beam will become phase-shifted with respect to the other, due to the differential refractive index and/or thickness that the beams each experience individually whilst passing through the specimen. The shift in the relative phase of the beams depends on the path difference, which is the difference in the product of the local refractive index and the geometrical distance traversed by each beam.

After emerging from the specimen, the light beams are captured by the objective lens and brought into focus at the focal plane of another Nomarski compound prism which recombines the beams. Though propagating along a common path, the light beams at this point still retain their perpendicular linear polarisations. Following this, they impinge on the polariser with a polarisation plane oriented at right angles to the analyser, and simultaneously at 45° to

the beams' polarisations. Polarisation components vibrating in the same direction as the analyser polarisation will be transmitted and will form an interference pattern. The rays will interfere constructively or destructively to varying degrees, depending on the relative phase difference; this phase difference is translated onto the image as a change in intensity.

2. 2. 8. Image processing using Fourier transformation theory

Fourier transforms are a useful tool for image manipulation. They are frequently used to analyse the frequency content of signals, as well as to modify and improve images for a broad variety of purposes. Fourier transforms offer attractive advantages. They enable the conversion of data into a different domain – called 'Fourier' or 'frequency' space – which is a convenient medium for image processing, because this greatly accelerates and simplifies manipulations, such as removing noise or performing large-scale filtering, which would otherwise be much more difficult to do in the spatial domain and requires significantly greater computational effort. For example, subtracting the information from a particular location in the Fourier domain removes the equivalent information from the entire real image. Also, mathematical operations that need to be carried out are reduced from a complicated convolution to a straightforward multiplication.

Fourier transforms are an expansion of the concept of the Fourier series. The latter is based upon the idea – formally known as Fourier's theorem – that any periodic function, such as the intensity variation in space describing an object, can be decomposed into a weighted combination of sine and cosine functions with well-defined frequencies. Fourier transforms are a generalisation of the Fourier series, where the periodicity condition is relaxed, such that it is possible to describe any function of arbitrary periodicity. The Fourier transform fully encodes the image information, and the image can be reconstructed exactly [Russ, 1998].

The 1D Fourier transform for a continuous signal which varies in space, $f(x)$, can be written as follows:

$$F(k) = \int_{-\infty}^{+\infty} f(x) e^{-2\pi i k x} dx, \qquad \textbf{Eq. 2.2.8.1}$$

where k is the spatial frequency, analogous to the definition in section 2. 2. 4. 1. (**Eq. 2.2.4.1.3**). The frequency space function, $F(k)$, describes the amount of each frequency term that must be added together to form $f(x)$.

The inverse transform, or the method by which this operation is undone, is shown be-

low:

$$f(x) = \frac{1}{2\pi} \int_{-\infty}^{+\infty} F(k) e^{2\pi i k x} dk. \qquad \textbf{Eq. 2.2.8.2}$$

The functions $f(x)$ and $F(k)$ are known as a Fourier transform pair.

In silico, the above equations are discretised. This is because a computer can only handle discrete points of a finite quantity, and since a digital image is made up of pixels sampled at finite intervals. The integral from minus to plus infinity will therefore be reduced to a finite summation. The discretised equivalents of the Fourier transform pair given in **Eq. 2.2.8.1** and **Eq. 2.2.8.2**, cast in the exact form employed by the Matlab language, are:

$$F(k) = \sum_{x=1}^{N} f(x) e^{-2\pi i \frac{(x-1)}{N}(k-1)}$$

$$f(x) = \frac{1}{N} \sum_{k=1}^{N} F(k) e^{2\pi i \frac{(x-1)}{N}(k-1)},$$

where N is the size of the image in number of pixels (which are assumed to be regularly spaced) and $f(x)$ is the intensity of the image at the pixel situated at x.

For a 2D image, the 2D discrete Fourier transforms (DFTs) are expressed thus:

$$F(k_x, k_y) = \sum_{x=1}^{N} \sum_{y=1}^{M} f(x,y) e^{-2\pi i \left[\frac{(x-1)}{N}(k_x-1) + \frac{(y-1)}{M}(k_y-1)\right]}$$

$$f(x,y) = \frac{1}{MN} \sum_{x=1}^{N} \sum_{y=1}^{M} F(k_x, k_y) e^{2\pi i \left[\frac{(x-1)}{N}(k_x-1) + \frac{(y-1)}{M}(k_y-1)\right]}.$$

Since the dimensions x and y are orthogonal, then so are k_x and k_y. This implies that the transformation can be carried out in each direction separately. For example, a series of one-dimensional transforms can be performed on the individual rows of the image, whereupon one-dimensional transforms can be applied once again, this time to the columns of the image, resulting in a two-dimensional transform of the image. These operations can be implemented very efficiently in an algorithm known as the fast Fourier transform (FFT) [Russ, 1998]. In order to calculate the DFT of N points in the conventional way, the computational time would be propor-

tional to N^2. On the other hand, the FFT algorithm reduces this proportionality to just $N \log N$.

2. 2. 9. Deconvolution

Deconvolution is a signal-processing technique popularly used in many branches of science and engineering. Although it had long enjoyed widespread use in astronomy for sharpening photographs acquired with telescopes, the technique was first applied to biological fluorescence microscopy only in the 1980s [Parton *et al.*, 2006]. The term 'deconvolution' relates to undoing the blurring which occurs in the far field (distance between object and imaging plane >> λ, where λ is the wavelength of light radiated from the object), where diffraction effects cause divergence of the light rays. The imaging process inevitably leads to some loss of information. Very high spatial frequencies (corresponding to small details in the specimen) fail to be captured by the microscope objective. The cut-off frequency depends on the numerical aperture of the objective. Deconvolution is capable not only of improving the resolution by reversing this loss of detail to some extent, but can also improve the contrast of the image. Applying deconvolution to wide-field serial optical sections can yield an 'optically sectioned' result on a par with that obtained with a confocal microscope, and can even confer superior contrast [Pawley, 2006]. Although confocal microscopy eliminates light not originating from the focal plane by use of a pinhole in the imaging path, it rarely excludes all out-of-focus information, and still involves a convolution operation. Therefore confocal imaging can also benefit from deconvolution. This is possible through considering information about the imaging process itself, such as the statistics of photon capture and the detailed understanding of the weighting function that transforms the object in the image plane [Pawley 2006].

Blurring is borne out of several phenomena: 1) diffraction of light, as a consequence of its wave nature, 2) scattering of light by the specimen, 3) refractive index mismatch, imperfections in the optical components and their alignment. All of the above factors, and more, contribute to the misdirection of light in the imaging plane [Pawley, 2006].

A biological specimen can be thought of as being composed of an infinite number of points (having no size in the *x*-, *y*- and *z*-dimensions). In the detector plane, these points are each replaced with the PSF of the microscope; this modification corresponds to the mathematical operation known as convolution (**Eq. 2.2.9.1** and **Eq. 2.2.9.2**).

$$\iiint_{-\infty}^{+\infty} o(x-x', y-y', z-z') \cdot PSF(x',\, y',\, z') = i(x,y,z) \qquad \textbf{Eq. 2.2.9.1}$$

or, in symbolic notation,

$$object \otimes PSF = image. \qquad \textbf{Eq. 2.2.9.2}$$

The image formed on the detector of a microscope is therefore a convolution operation ($\otimes$) of the specimen with the microscope's own response to a point object (the PSF). The PSF can also be thought of as the three-dimensional image of a (zero-dimensional) point in space. Converting to what is known as frequency space, the convolution relationship becomes a straightforward multiplication:

$$\mathcal{F}(object) \cdot \mathcal{F}(PSF) = \mathcal{F}(image).$$

The Fourier-transformed PSF, $\mathcal{F}(PSF)$, is also known as the optical transfer function (OTF). Therefore one could, in theory, obtain the original object by dividing the Fourier-transformed image by the OTF:

$$\mathcal{F}(object) = \frac{\mathcal{F}(image)}{OTF}, \qquad \textbf{Eq. 2.2.9.3}$$

and then performing an inverse Fourier transform. **Eq. 2.2.9.3** is known as a simple linear inverse filter. This type of filter, however, performs no useful function in practice, since the presence of noise invalidates the simple relationship between image and object in the above equation. Convolution tends to attenuate high spatial frequencies more than the low frequencies, hence deconvolution aims to boost the high-frequency components to a higher degree. With the linear filter, noise, which is present at all frequencies, is boosted at every single frequency; the situation is particularly unfavourable above the cut-off frequency, where no real object data exists, yet noise is amplified. Thus, it is easy to see how noise can overwhelm and obliterate any information in an image manipulated in this way. The simple linear inverse filter, nevertheless, serves as a theoretical basis for the development of more complex filters which take into account realistic imaging conditions [Parton *et al.*, 2006].

Formulating a successful deconvolution approach begins with two assumptions: 1) linearity, *i.e.* that the sum of the individual images of two objects is the same as an image of both objects being present simultaneously, and 2) shift invariance, *i.e.* that an object will appear the same, regardless of its position within the imaged field of view. These are actually embodied in **Eq. 2.2.9.1** and **2.2.9.2**. Assumption 1) is valid if the detector and imaging mode are linear, and when self-quenching and self-absorption by the fluorophores is reduced to a minimum. The second condition is clearly untrue; however it is reasonable and acceptable for a high-quality instrument, such as a research-grade microscope.

The currently available deconvolution algorithms can be classified into 'deblurring methods' and 'image restoration methods'. The former act two-dimensionally on each individual *z*-plane; in contrast, the latter act three-dimensionally and simultaneously on the whole dataset. Deblurring methods are used for superficial, qualitative improvement on the visualisation of data and are based on subtracting out-of-focus light. Some examples include nearest-neighbour and no-neighbour deconvolution. The nearest-neighbour approach assumes that blurring at a particular plane is due to out-of-focus contributions from the planes immediately above and below it. Accordingly, the data are restored by subtracting the blurred versions of the two neighbouring planes [Pawley, 2006][Parton *et al.*, 2006]. The no-neighbours algorithm is similar to the nearest-neighbours, the only difference being that the images in the adjacent planes are assumed to be the same as the in-plane image, so that a defocused version of the image is subtracted from itself. The advantage of this class of algorithms is that they are very fast – especially the no-neighbours approach; however, they are not quantitative and are relegated for use on sparse three-dimensional objects.

A more precise and fully three-dimensional restoration method is Wiener filtering. It works by modulating the magnitude of the OTF at low OTF values, such as would be encountered near the missing cone (for the problem of the missing cone, refer to section 2. 2. 3. 1. and **Fig. 2.2.3.1.2**), with an additive correction factor. The factor can be mathematically optimised for the spectral characteristics of noise and image data. Although the Wiener filter is able to reduce the detrimental effect of noise on the deconvolved image, it is nevertheless non-optimal, not least because small modification of the OTF will have a large impact on the data in the spatial domain [Pawley, 2006].

The most accomplished methods for deconvolution to date are the non-linear constrained iterative deconvolution algorithms which have become applicable with advances in computing power. The non-linear constrained iterative procedures afford a quantitative and precise restoration, executed through attempting to reassign out-of-focus light back to its expected location of origin, as well as partially reversing aberrations arising from optical imperfections in the imaging path. This leads to an increase in the signal-to-noise ratio, contrast and effective resolution of the image. Under ideal circumstances, these approaches can even lead to super-resolution in the *z* (axial) direction through recovery of lost spatial frequencies.

The multitude of constrained iterative approaches in existence today varies in the manner in which the noise is modelled and the PSF handled. The presence of noise frequently leads to ambiguity in the restoration, *i.e.* more than one possible outcome. In order to overcome such problems, the constrained iterative approaches make a number of reasonable assumptions, *e.g.* smoothness of the object and positivity (hence the term 'constrained'). This is borne out of mathematical considerations which reject deconvolution solutions that yield negative values for

the intensity anywhere in the image, as negative intensity values carry no physical meaning. This, essentially, is the advantage of employing nonlinearity, as linear methods cannot always guarantee non-negativity [Pawley, 2006]. Thus, implicit to the positivity constraint is the fact that the object-image relationship is no longer simply proportional (*i.e.* linear). Therefore the class of constrained iterative methods is also known as 'non-linear methods'.

Achievement of super-resolution in the z dimension can also be traced to the positivity constraint: it is possible to recover some of the missing spatial frequencies in z through a systematic extrapolation. The positivity constraint is most easily implemented through an iterative approach, where the final result is not calculated in a single pass, but emerges out of a certain number of repeated steps. During each step, any negative values are set to zero; the small errors introduced in this way would be corrected in the next iteration. For a well-behaved algorithm, each new estimate should render a deconvolved image ever closer to the actual object.

The main difference between various iterative algorithms tends to be the manner of updating the estimate at each cycle. Newton iterative approaches, such as the Jansson-van Cittert algorithm, calculate the new estimate by adding a suitable weighting of the error signal, *i.e.* the difference between the blurred guess and the data. Choosing the weighting factor, however, is an *ad hoc* process.

By contrast, a different subclass of the nonlinear constrained iterative approaches, namely the maximum likelihood algorithms, is based on stringent mathematical reasoning [Pawley, 2006]. The Huygens Essential software suite, which was used in Chapter 7 of this thesis, implements the Richardson-Lucy algorithm. It works on a maximum likelihood estimation principle and assumes a Poisson noise model to mimic the noise arisen during imaging [Parton *et al.*, 2006]. This type of algorithm relies on the notion that the true object underlying the image can be found by arriving at the guess with the highest probability of giving rise to the image. This theoretical framework essentially transforms the deconvolution problem into a multi-dimensional fitting problem. Thus, the algorithm aims to find the pixel values that maximise the likelihood that the collected data would have occurred, given a specific noise model, *e.g.* Poisson noise. Imposing the nature of the noise pattern as a condition on the final result is important for the correct calculation of this probability or likelihood.

If o represents the true object, i is the image and k is the iteration number, then the following is an expression of the updating step at each iteration:

$$o^{k+1} = o^k \cdot \mathcal{F}^{-1}\left\{\mathcal{F}\left\{\frac{i}{o^k \otimes PSF}\right\} \cdot OTF^*\right\},$$

where OTF^* is the complex conjugate of the OTF [Richardson, 1972][Lucy, 1974]. Note that this algorithm uses the ratio ($i/o^k \otimes PSF$), instead of an additive error ($i - o^k \otimes PSF$).

The iterative process proceeds as follows. First, an 'initial guess' is made on the true object, based upon the raw image data. The initial guess can differ, depending on the type of constrained iterative algorithms used, and may be generated with a fast, linear inverse filter, or may simply be a smoothed version of the raw image data. For the Richardson-Lucy algorithm, this is usually either the latter, or an image with uniform intensity set to the mean intensity of the raw data [Pawley, 2006]. The next step assesses how closely the initial guess approximates the true object, by convolving the initial guess with the microscope PSF and comparing the result to the raw image data. Minimal differences in the values between the two sets of data indicate a good initial guess. An iterative process then begins, whereby a revised and improved guess, in line with the positivity constraint, is repeatedly generated, convolved with the PSF and quantitatively compared with the original data. It is very unlikely that the algorithm will ever converge on the exact solution, so the deconvolution procedure carries on indefinitely until forced to stop by some sort of stopping criterion.

After a certain number of cycles, the improvement effected on the deconvolution result is minute. In order to make a compromise between the quality of the end result and effective use of time and computing power, the number of iterations is predetermined by either of two ways. One way is to impose a limit on the number of cycles (this is typically in the range of tens to hundreds). The other is to set a lower limit on the difference found upon end-result comparison between iterations. Thus, the last 'guess', before the iterative loop is stopped, is taken to be the final deconvolution result [Parton *et al.*, 2006].

The PSF utilised in the deconvolution process can either be measured or calculated from theory. A third method for generating a PSF, called 'blind deconvolution', exists and involves estimating the PSF iteratively, in parallel with the restoration process of the image data. It is controversial whether this method should perform better or worse than the other two methods. In theory, one could defend this method by arguing that empirical PSF is flawed by the sheer scattering and refractive index mismatch in the sample; conversely, one could lay down a counterargument that withholding information about the imaging process could lead to an inferior deconvolution result. Since blind deconvolution does not feature in the Huygens Essential software package used in this work, however, the validity of this method was not examined, and the PSF utilised in deconvolution in later chapters was only either calculated or empirical.

2. 2. 9. 1. Factors affecting deconvolution quality

As already discussed in section 2. 2. 3. 3. 2., tuning the acquisition parameters for optimal sampling is very important in the first place for capturing the raw data in full, so that it can be re-

stored later with deconvolution. Failing to satisfy the Nyquist criterion would lead to restoring the image with a lower resolution than is theoretically possible. The quality of the deconvolution outcome depends on a number of factors; some are present during acquisition, others become relevant during the processing stage. Whilst acquiring the data, certain noise sources, such as detector noise (discussed in section 2. 2. 10) and laser noise (shortly to be discussed) may not be circumvented; however, it is possible to reduce optical aberrations to a minimum by preparing the sample to a high standard and making sure that it is free of dust and other contaminants.

2. 2. 9. 1. 1. Laser flicker

Intensity fluctuations due to laser flicker can have an adverse effect on the deconvolution results. Fluctuations in the laser beam brightness are a combination of two sources: 1) quantum noise, which arises from laser gain (*i.e.* unavoidable spontaneous emission occurring alongside the intended stimulated emission – the working principle of the gain medium) and resonator losses, and 2) technical noise, such as vibrations of the resonator mirrors, thermal agitation of the charge carriers in the gain medium and/or noise from the pump source [Paschotta, 2008]. The amount of noise present depends on the operation conditions; however, the noise is often lower at high pump powers, where the probability of spontaneous relaxation is reduced.

2. 2. 9. 1. 2. Typecasting

The acquired data must also be stored and handled carefully, in order to reach their full potential. Storing the image data with a sufficient precision is imperative to prevent additional noise from contaminating the deconvolution result. Compression of the data must be avoided, as this can lead to numerical truncation errors [Pawley, 2006].

Subsequently, the free parameters of the deconvolution algorithm must be appropriately selected. The parameters in question are the level of background signal, the signal-to-noise ratio (SNR) and the number of deconvolution iterations. The background level is relatively straightforward to evaluate and involves finding its average intensity. Choosing the number of iterations is more subjective, since a fundamental trade-off exists between noise and resolution. This means that increasing the resolution beyond a certain point will inevitably increase the noise in the deconvolved data. As a rule of thumb, at least 40 iterations should elapse before stopping the deconvolution process. Deconvolution carried out in this thesis was the product of 100 iter-

ations. The SNR is relatively complex to determine. The following section discusses this parameter in more depth and outlines the consequences that some inappropriate values may produce.

2. 2. 9. 1. 3. Signal-to-noise ratio (SNR)

The SNR describes the ratio between signal and noise in the raw image, and is visually interpreted as the granularity of the image. It should not be confused with the signal-to-background ratio (SBR), which is the relative strength of the signal compared to that of the background fluorescence. As an input parameter in deconvolution, the SNR controls the effective sharpness of the restored image.

Setting the signal-to-noise ratio parameter too high will lead to 'over-restoration' of the image, *i.e.* artificial shrinking of the features in the image. It can also produce ring-like structures around sharp edges (equivalent to loss of high frequencies), and attribute comet-like tails to bright objects [Pawley, 2006]. In addition, if the SNR is set excessively high, there is a risk that the noise present in the image will be amplified, or that the algorithm will not converge properly towards minimum noise. Artificial internal structure in a background scattered object may also be generated in such cases. Therefore the SNR can be perceived as an artefact limiter. On the other hand, however, if the SNR is underestimated, the noise in the image will be reduced at the expense of the final resolution of the image. This emphasises the importance of choosing a balanced and appropriate value for the SNR.

2. 2. 10. Sources and types of noise in digital detectors

Every type of detector unavoidably introduces a noise component into any measured signal. The level of noise contributed depends on the design of the detector. Below is a list of the most common types of noise in various detectors, including pixel-array and PMT detectors.

2. 2. 10. 1. Poisson noise (also known as 'shot noise' and 'photon-counting noise')

Poisson noise is not intrinsic to the detector, but is associated with the detection process. It is inextricably linked to the particle nature of light and the probabilistic quantum-mechanical processes that govern light emission. Due to this discretisation of light into photon packets and their randomised emission, there exists an uncertainty in the number of photons arriving at the detector at any particular time. The brighter the light source, *i.e.* the higher the number of emit-

ted photons per unit time, the more continuous the stream of photons and the more infinitesimal the relative fluctuations in intensity. Reducing the brightness, however, brings these quantum effects steadily into prominence. In fact, there is an inverse proportionality relationship between the magnitude of the uncertainty and the brightness of the light source. The number of photons arrived at the detector can be described by a Poisson probability distribution, with a variance equal to the mean number of photons [Pawley, 2006]. This is the dominant noise source with regard to photon-counting PMT detectors.

2. 2. 10. 2. Dark current

Dark current is caused by thermal migration of electrons in the silicon CCD chip and cosmic rays, which can manifest themselves, respectively, as a pattern or as 'hot pixels' (bright pixels in the absence of stimulation by light). The magnitude of the dark current is inversely proportional to exposure time and has an exponential dependence on the inverse of the temperature.

An effective way of combating dark current is to cool the CCD. A multi-stage Peltier element acts on the principle of the thermoelectric effect to reduce the temperature of the CCD to down to around -90°C. To preserve the low temperature, the CCD chip is usually placed in a vacuum chamber and sealed hermetically.

2. 2. 10. 3. Clock-induced charge (also known as 'spurious noise')

During the pixel-by-pixel shift of the charge towards the readout node in a CCD, there is a minute but finite possibility that impact ionisation may create additional charges, *i.e.* a noise component called clock-induced charge. Usually, the contribution of clock-induced charge is much smaller than other types of noise, and can be approximated at 0.01 electron/pixel/frame. This noise component is constant and does not vary with time.

2. 2. 10. 4. Digitisation noise

After conversion of the detected photons into electrical signals for quantitation, the analogue signal needs to be digitised in order to be understood by a computer. Detectors have a limited precision (most commonly they are 8- or 12-bit), which naturally leads to a one-half bit error;

with regard to the signal of interest, this accounts for between 0.01% and 0.2% of noise, depending on the detector.

2. 2. 10. 5. Readout noise

The most significant noise contaminant of weak signals in a CCD/EMCCD (electron-multiplier CCD) camera is usually the readout noise. Readout noise predominates in short CCD exposures, whereas dark current is dominant in long CCD exposures. It is caused by an on-chip electronic component, called the floating diffusion amplifier (FDA) which converts accumulated photoelectrons into a potential difference (voltage). A more detailed explanation of the phenomenon, and several methods to counter it, are offered below.

After an image is taken (*i.e.* oncoming light has been encoded as electronic charge on the CCD chip), the accumulated charge is transferred, pixel by pixel, into a horizontal serial register, whereupon it is fed into the FDA. As the FDA reads the charge contained within a particular pixel and transforms it into voltage, it is reset, ready to process the next pixel. The resetting itself causes some noise to be generated.

This type of noise can be tackled in several ways. Dramatic reduction can be achieved with an external correlated dual sampling (CDS) circuit, which takes two readings of the pixel – before and after transferring the charge to the readout node. Readout noise is known to be correlated with the clocking speed, *i.e.* the swiftness with which readout takes place. However, it is actually a direct consequence of thermal (Johnson) noise. The latter produces a noisy voltage proportional to the square-root of the bandwidth of the amplifier. Hence slower pixel clocking reduces readout noise.

Reducing the clocking rate, however, has a disadvantage, as this limits the camera's capacity for real-time imaging. The tendency of readout noise to overwhelm weak signals can also be mitigated by longer exposures, as the signal accumulated over time will eventually supersede the noise amplitude.

Readout noise is only applicable to pixel array cameras, such as CCDs (charge-coupled devices) and EMCCDs. This type of noise is greatly reduced in EMCCDs.

2. 2. 10. 5. 1. Fundamentals of electron multiplication gain in EMCCDs

This principle is largely based on harnessing the very same effect that produces clock-induced charge. As with a normal frame-transfer CCD, the charges accumulated in the detection area of an EMCCD are rapidly transferred underneath to the storage area, where the electrons are

ejected line by line into the horizontal serial register. Ahead of it, but before the FDA, is connected another register, termed the charge multiplication register, which multiplies the electronic signal by subjecting it to higher-than-normal voltage. In brief, the electrons are greatly accelerated across the electrodes by a voltage of 30-40 V, which occasionally leads to an impact ionisation event (with probability of 1.0-1.6% at each electrode). The repeated amplification process (usually 400 to 600 stages) achieves a high multiplication gain which dwarfs the ever-present readout noise subsequently produced by the FDA.

The multiplier gain can be expressed thus:

$$M = (1 + p)^N,$$

where p is the probability of ionisation (electron-hole pair production) at each multiplication stage, and N is the number of stages in the charge multiplication register.

The chief advantage of EMCCDs to virtually eliminate the confounding effect of amplifier readout noise on the signal, without the need to decrease the readout frequency, has made them a valuable asset for scientific low-light imaging.

2. 2. 10. 6. Excess noise (also known as 'multiplicative noise' and 'noise factor')

As a consequence of the stochastic amplification process of electric charge (the converted photonic signal) in the electron-multiplying (EM) gain register, there exists an uncertainty as to the final gain that will be imparted on the charge [Andor iXon EM+ Hardware Manual, Version 1.2]. More concretely, the passing of charge from one element to another in the EM gain register while subjected to continuous impact ionisation will only occasionally result in the production of an extra electron.

Based on the characteristics of the multiplication process, it is nevertheless possible to compute a probability distribution function for the output charge. Both theoretical and empirical analysis has ascertained this factor to be $\sqrt{2}$ for EMCCD technology. This means that, for a constant illumination intensity, the variation in the number of electrons read out from the sensor (*i.e.* the shot noise) is broadened by a factor of $\sqrt{2}$ around the mean value.

This type of noise only becomes significant for gain levels greater than 30 [Andor iXon EM+ Hardware Manual, Version 1.2].

2. 2. 10. 7. Pixel noise (also known as 'fixed-pattern noise' and 'flat-field noise')

This type of noise is due to variation in the gain and sensitivity from one pixel to another. Factors that affect its prominence include age and temperature. The severity of this effect increases in direct proportion to intensity, and at ~5,000 photons becomes of comparable magnitude to Poisson noise. For this reason, flat-field noise demands attention at high intensities and cannot be simply neglected. One means of controlling it to some extent is to use a snapshot of a uniform, white field as a normalisation factor for each pixel [Pawley, 2006].

3. Current theories on Shh multimerisation, and the relevance of the Shh lipid adducts and HSPGs

The need to reconcile the fact that Shh proteins are released from producing cells, despite the considerable hydrophobicity granted to them by the two lipid adducts, has resulted in the proposal of several considerably different Shh distribution mechanisms. Over the years, a myriad of reports investigating Shh release and conduit through the extracellular environment has accumulated, giving support to almost every one of these theories. A consensus on a single method of intercellular transport of Shh has therefore not yet been reached. The majority of this chapter will be concerned with exploring the various hypotheses and findings that have been put forward to date on this matter, including in some cases the potency of the signalling complexes. At the end of this chapter, this will be followed by a summary of the evidence for involvement of palmitate, cholesterol and HSPGs in the formation of these structures.

3. 1. Current theories on multimerisation

3. 1. 1. Homomultimers

The paradox of a heavily lipidated molecule travelling unchaperoned in the hydrophilic extracellular environment has called for seeking alternative, soluble, Shh structures. One possibility put forward is that, in order to render itself more hydrophilic, Shh sequesters its hydrophobic lipid modifications in the interior of high molecular-weight homomultimeric Shh structures [Zeng *et al.*, 2001] (**Fig. 3.1a**).

3. 1. 2. Lipoproteins

Lipoproteins are structures comprising esterified cholesterol and triglyceride, ensheathed in a monolayer of phospholipids and supported by an apolipoprotein scaffold [Eaton, 2006]. Lipoproteins were initially proposed as a carrier vehicle for Hh in *Drosophila* after they were found to co-purify together [Panáková *et al.*, 2005] (**Fig. 3.1b**). Conclusions drawn from previous research were that the *Drosophila* lipoprotein Lipophorin facilitates long-range Hh signalling, but that certain lipids contained within Lipophorin are simultaneously capable of repressing the

pathway in the absence of Hh. Recently, the lipoprotein theory was also tested in human cells (HeLa and MIA PaCa-2) [Palm *et al.*, 2013]. The main findings from exposing Shh-transfected HeLa and MIA PaCa-2 cells expressing endogenous Shh to foetal bovine serum containing human lipoproteins are that Shh associates directly with all major classes of human lipoproteins *via* its lipid modifications, implying that they facilitate Shh release. Lipoprotein-carried Shh is thought to be transported in a high molecular-weight complex, beginning from 240 kDa. Monomeric, sterol-unmodified Shh is also released according to [Palm *et al.*, 2013], albeit in a lipoprotein-independent way. The same research group's studies in the imaginal disc of *Drosophila* confirmed that lipoprotein-associated Hh is necessary, but not sufficient, to activate target gene transcription. In fact curiously, in order for full activation to occur, small amounts of the non-sterol-modified form needed to be present, along with the sterol-modified, lipoprotein-carried form.

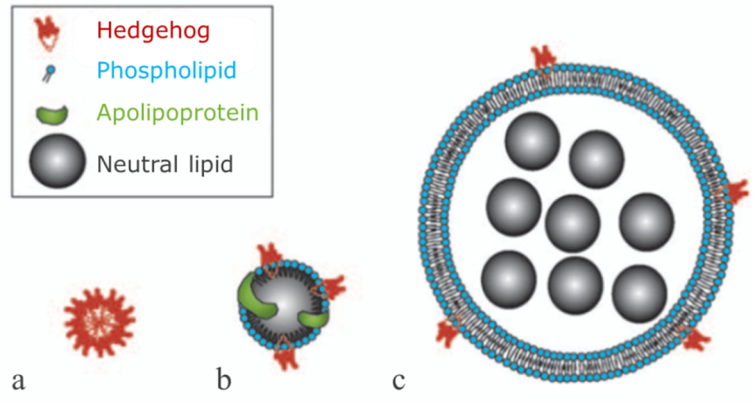

Figure 3.1. Several hypothesised structures for long-distance Shh signalling. (a) Shh homomultimer sequesters its lipid anchors internally. (b) Shh embeds itself in the phospholipid monolayer of lipoprotein particles. (c) Putative structure analogous to micelles, containing lipophilic granules, with the Shh hydrophobic moieties hidden internally. Figure adapted from [Eaton, 2006] with permission from Elsevier.

3. 1. 3. Exovesicles

Shh may spread using nodal vesicular particles (NVPs), at least in some tissues. NVPs are extracellular vesicles which manifest themselves on the surface of the ventral node during murine development [Eaton, 2006]. Electron micrographs have suggested that exovesicles may bud off from protuberances on apical microvilli [Tanaka *et al.*, 2005]. *In vivo* imaging has demonstrated

that NVPs are transported across the node by a current generated by cilia, meanwhile NVPs rupture and break down [Tanaka *et al.*, 2005]. Besides Hh, NVPs have been shown to escort retinoic acid, and electron microscopy has revealed that NVPs contain a multitude of lipophilic granules, encased in a lipid bilayer [Tanaka *et al.*, 2005] (**Fig. 3.1c**). These granules have physical characteristics not dissimilar to lipoprotein particles and have, in fact, been proposed to be the very same. This postulate is in harmony with the observation that lipoprotein particles are ideally suited for holding retinoic acid, and is further supported by the fact that lipophilic retinoids have been detected in the insect lipoprotein Lipophorin [Duncan *et al.*, 1994].

3. 1. 4. Direct cell-cell contact (juxtacrine signalling)

Although it had been demonstrated before that tissue culture cells expressing *Ptc* can endocytose Hh located on the surface of an adjacent cell [Incardona *et al.*, 2000], an until recently purely putative mode of long-range transport is the repeated transfer of Hh on filopodia from one cell to its neighbour *via* transcytosis. This has recently been backed by direct evidence [Sanders *et al.*, 2013]. Imaging Shh ligand synthesis in the chick embryo has shown that Shh in particulate form travels along long filopodia that span several cell diameters. On the responding cell, co-receptors Cdo and Boc mobilise in similar cytoplasmic extensions and intercept the signal through a momentary stabilised interaction between the filopodia.

3. 1. 5. Shh-HSPG heteromultimers and HSPG-mediated multimer formation and release

Intervention of other auxiliary molecules on the cell surface and in the extracellular matrix (ECM), in particular HSPGs, has also been considered. HSPGs are heparan sulphate (HS) glycosaminoglycan (GAG) chains attached to a protein core. Three major families of HSPGs exist: glypicans, syndecans and perlecans (**Fig. 3.1.5.1**). Each has its own distinguishing protein anchor and variable sulphated hydrocarbon chains. Syndecans (**Fig. 3.1.5.1a**) are transmembrane proteins tethered to the membrane by virtue of a hydrophobic sequence in their C-terminal domain. Glypicans have a glycosylphosphatidylinositol (GPI) anchor attached to the hydrophobic C terminus of the protein. The protein core is globular and is stabilised by disulphide bonds (**Fig. 3.1.5.1b**). Perlecans, on the other hand, are secreted HSPGs (**Fig. 3.1.5.1c**).

HSPGs were first suspected of aiding Shh multimerisation when it was discovered that that they can interact electrostatically with Hh *via* a highly conserved sequence of positively charged amino acids, called the Cardin-Weintraub (CW) motif [Bellaiche *et al.*, 1998][Rubin *et*

al., 2002][Desbordes *et al.*, 2003][Grobe *et al.*, 2005][Farshi *et al.*, 2011]. The CW motif in human Shh is the peptide $K^{32}RRXXKK^{38}$, where X indicates any amino acid. Polar contacts between basic residues R124, R154 and R156 on Shh and negatively charged sulphate amino acids have also been discovered, adding further weight to claims of involvement of HSPGs in multimerisation [Vyas *et al.*, 2008].

Which type of HSPG orchestrates Hh transport has been the subject of some debate. In *Drosophila* wing disc, the glypicans Dally and Dally-like are thought to be the culprits – although homozygous inactivation mutations of these glypicans cause a far milder impairment on the spread of Hh than heparan sulphate knockdown [Han *et al.*, 2004][Eaton, 2006]. In the brain, however, evidence is leaning towards a syndecan sub-type termed Trol [Park *et al.*, 2003].

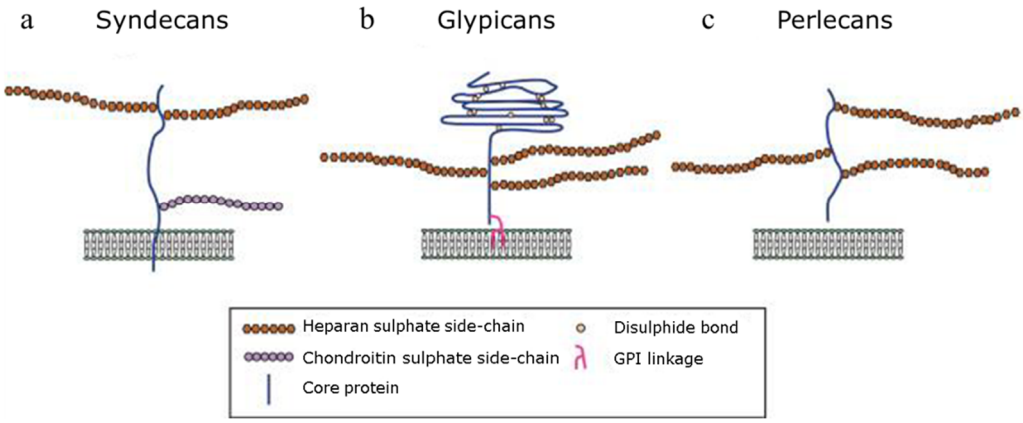

Figure 3.1.5.1. Varieties of heparan sulphate proteoglycans (HSPGs). HSPGs of different classes: syndecan, glypican or perlecan, are distinguished by the type of protein core that they possess. (a) Syndecans are transmembrane proteins. Heparan sulphate (HS) chains are attached at the distal end of the syndecan. Some syndecans have an additional chondroitin sulphate (CS) chain attached at the proximal end. (b) Glypicans attach themselves to the plasma membrane *via* a glycosylphosphatidylinositol (GPI) anchor. They are globular proteins stabilised by disulphide bonds. (c) Perlecans are secreted HSPGs. Figure reproduced from [Yan *et al.*, 2009] with permission from, and copyright to, Cold Spring Harbor Laboratory Press.

Whether HSPGs directly incorporate themselves into a high molecular-weight complex with Shh, or contribute to Shh oligomerisation and subsequent proteolytic solubilisation in a more detached manner – for example, through assisting the stabilisation of the finished multimeric products – is yet to be determined unequivocally. If HSPGs are one of the ingredients in

the Shh multimolecular complex, their presence could be vital for the generation of the correct concentration gradient.

The Grobe research group [Farshi *et al.*, 2011] has proposed an interesting model for the formation of Shh clusters with the aid of HSPGs (**Fig. 3.5.1.2**). In their model, certain HSPGs act as scaffolds with 'grooves' of a precise spacing which align Shh in such a way as to permit cross-linking by a transglutaminase enzyme. More precisely, in experiments with murine Shh transfected in Bosc cells (a cell line derived from the human embryonic kidney HEK293T cell line), it was discovered that Shh may have a preference for binding particularly sulphated HS (trisul-

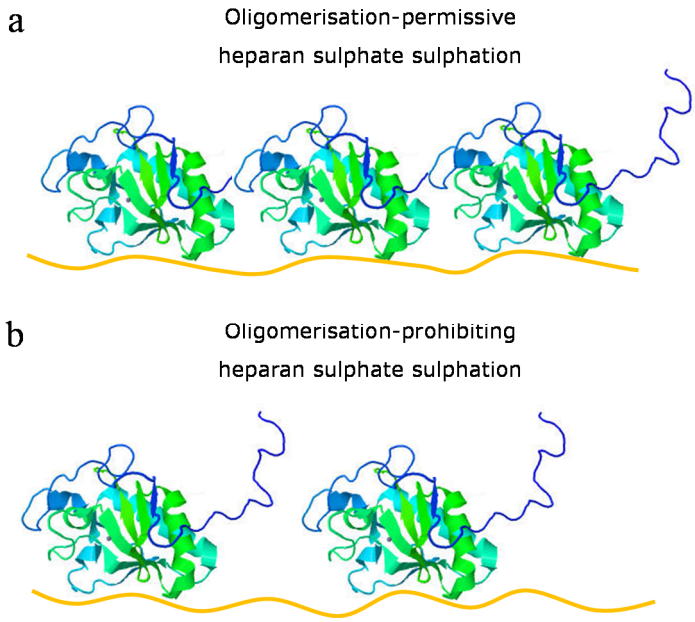

Figure 3.1.5.2. Grobe model of Shh oligomer assembly, assisted by Heparan sulphate proteoglycans (HSPGs) and transglutaminase (TG). According to the model proposed in [Dierker *et al.*, 2009b], Shh monomers on the membrane's outer leaflet initially bind to certain heparan sulphate (HS) chains of HSPGs. The orange undulating lines in the diagram represent differently sulphated HS chains. (a) HS with appropriately sulphated motifs allows proper alignment of the monomers upon HS binding, leading to the formation of a relatively unstable oligomer. In the presence of TG, the favourable positioning of Shh elicited by the HS scaffolding facilitates covalent cross-linking between the monomers, resulting in a much more robust oligomer. (b) HS with a non-permissive sulphation pattern does not allow the Shh monomers to arrange themselves in a manner conducive to intermolecular interaction, resulting in the failure to form an oligomer [Dierker *et al.*, 2009b]. Shh crystallographic structure adapted from the Protein Data Bank (PDB ID: 3M1N); crystallographic data provided by [Pepinsky *et al.*, 2000].

phated, rather than monosulphated or disulphated saccharides), and that transglutaminase may thereafter catalyse covalent *ε*-(*γ*-glutaminyl)lysyl interprotein cross-linkage to rigidify the multimeric structure and make it less amenable to proteolytic degradation. Transglutaminase has been hypothesised to bridge an unidentified lysine residue to a highly conserved N-terminal residue, Gln^{47}, on an adjacent protein. The involvement of the latter amino acid was confirmed after truncating the signalling domain beyond this amino acid inhibited the formation of multimeric structures [Dierker *et al.*, 2009b].

The same group has also identified certain members of the A Disintegrin And Metalloprotease (ADAM) family (ADAM10, ADAM12 and ADAM17) which are thought to shed the morphogen from the ectodomain by cleaving the N and C termini. The degree of Shh shedding has been found to be dependent on 2-*O*-sulphate in the HS chains [Dierker *et al.*, 2009a] (**Fig. 3.1.5.2**), where the presence of the aforementioned sulphation pattern acts to inhibit metalloprotease-mediated processing and release. The Grobe group found that expression of Shh in a cell line (pgsD-677) mutated to impair its ability to produce HS through abrogating N-acetylglucosaminyltransferase and glucuronyltransferase activities required for HS synthesis, caused dispersal mainly of the monomeric Shh form and a severe reduction in dispersal of large multimers [Ohlig *et al.*, 2011]. This constitutes substantial evidence in defence of the participation of HSPGs in Shh multimerisation, and their modulatory effects on the process – at least, *in vitro*.

The anti-Shh antibody 5E1 recognises the active conformation of Shh. It does so as it binds to an epitope overlapping partially with the zinc-coordinated Ptc receptor binding site [Bishop *et al.*, 2009][Bosanac *et al.*, 2009], (**Fig. 2.1.1.2**). A study conducted by the Grobe group employing this antibody suggests that a portion of the N terminus of Shh initially obscures the 5E1 epitope, but is removed prior to release, in order for the morphogen to become biologically active. This group found that N-terminal palmitoylation may be a prerequisite step for truncation of N-terminal peptides, which otherwise block the zinc coordination site and prevent Ptc from binding to Shh [Ohlig *et al.*, 2011]. N-palmitoylation may be necessary to bring the N terminus in close proximity with the plasma membrane to present the correct N-terminal peptide sequence to membrane-proximal ADAM sheddases, which would then cleave the beginning of the N-terminal domain, along with the attached palmitate moiety, and the cholesterol moiety on the other terminus, to solubilise the Shh multimeric complex [Ohlig *et al.*, 2011]. Presumably, the argument is that since ADAM sheddases typically process their substrates within a 1-20 residue segment from the surface of the plasma membrane, only the two ends of the Shh molecule would be truncated.

Further experiments with acylation-deficient Shh having its CW motif mutated to a loss-of-function string of alanines showed a restored binding of 5E1 to the Shh molecule [Farshi *et*

al., 2011]. This observation was somewhat imaginatively put down by the authors to flexibility of the N-terminal domain that impedes binding which, in the presence of the functional 'anchoring' CW sequence, is immobilised and confined to a locus away from the Ptc and 5E1 binding sites. Building upon further observations that monomeric and multimeric proteins display differential HS-binding capacities, this conjecture nevertheless tallies with the previously reported finding that unpalmitoylated Shh has reduced bioactivity.

3. 2. Discussion on the Shh lipid adducts and HSPGs with regard to multimerisation

Modification of proteins with lipid groups is a common phenomenon, with nearly 1,000 proteins known to date to be subjected to this process [Resh, 2013]. Different lipids confer different properties to the protein that they are modifying. As a general rule, the addition of fatty acid attachments increases affinity for membranes. Apart from membrane binding, the fatty acid palmitate is known to have diverse functions, including protein trafficking and stabilisation. Due to its long and saturated chain, it is also an excellent mediator for localisation to lipid rafts.

An important concept to consider that impacts the function of the protein is the reversibility of the modifications. For example, covalent attachment of GPI or palmitic acid *via* thioester linkage (S-palmitoylation) is transient and can be removed by phospholipases or thioesterases, respectively. In the case of the signalling molecules H-Ras and N-Ras, cyclic acylation and deacylation serves to change the localisation of the proteins, so that they may signal from two different intracellular components: the plasma membrane and the Golgi [Resh, 2013]. By contrast, Shh employs an irreversible method of palmitate attachment *via* an extremely stable amide bond (N-palmitoylation). The permanent nature of this modification raises the question of whether Hh carries the palmitate until the end of its life cycle, or whether it is removed somewhere along the course of its duty at a site different to its site of attachment. The Grobe research group has proposed that it is indeed detached from the protein, along with a sequence of N-terminal amino acids and the sterol modification, which ultimately activates the molecule prior to being deployed in the ECM [Ohlig *et al.*, 2011]. This proposal certainly attempts to resolve the paradox of the movement of a highly hydrophobic molecule in the aqueous milieu. However, there could be an alternative route to solubilisation that does not require palmitate removal. Proteins modified by myristate (another irreversible modification) are capable of burying their adduct in a hydrophobic cleft [Resh, 2013]. Although hidden from the surface, myristate is still in position to control the protein's stability and thermal resistance. The same may be true for

palmitate in Shh. Moreover, some proteins possess a so-called 'myristoyl switch', which permits the extension and retraction of the moiety, thereby permitting reversible membrane binding of these proteins. The transformation can be triggered by, amongst other stimuli, ligand binding or multimerisation [Resh, 2013]. It is therefore plausible that Hh may employ a similar mechanism, whereby palmitate is sequestered within the high molecular-weight complex in preparation for dispatch and, upon reception by the Ptc receptor, is reproduced on the outer surface.

Studies on the role of palmitic acid suggest that it is not required for Shh biological activity. A signalling activity assay involving C3H10T1/2 osteoblast precursor cells illustrated that both multimeric Shh and completely unlipidated, monomeric Shh induces differentiation of the cell line. On the other hand, Shh-C25S, a palmitoylation-deficient mouse mutant displays an ability to multimerise, but its activity is decreased, compared to the wild-type multimer. Therefore N-palmitoylation is thought to augment the potency of the signal (as already mentioned at the end of the previous section) [Kohtz *et al.*, 2001][Ohlig *et al.*, 2011].

Aside from its rare mode of palmitate modification, the Hh family currently remains the only known protein family to become covalently modified by cholesterol [Resh, 2013]. Together, these unusual properties make Hh truly unique, but also render it all the more difficult to decipher its method of migration through the ECM. The non-cholesteroylated Shh mutant [Zeng *et al.*, 2001][Lewis *et al.*, 2001][Dierker *et al.*, 2009b], has indicated that it cannot form multimeric structures under developmental conditions [Dierker *et al.*, 2009b][Ohlig *et al.*, 2011]. In addition, its biological activity is reduced, compared to the physiological multimeric complex. The reason for the superior potency of multimeric wild-type Shh has been suggested to stem from inducing clustering of the Ptc receptor, which in turn would reduce its interaction with, and therefore repression of, Smo. An alternative explanation is that the wild-type form experiences greater survivability in the extracellular environment, compared to the cholesterol-deprived monomeric form as a result of resistance to proteolytic degradation.

The cholesterol moiety has also been shown to have a regulatory influence over Shh diffusion and be equally important for long-range, as well as short-range signalling [Resh, 2013]. The manner in which cholesterol exercises its restriction on Shh spreading could be *via* interaction with receptors or ECM molecules. Recently, it has been shown that cholesterol modification is vital for the formation of the concentration gradient in *Drosophila* wing disc and for restriction of its spread: removal of this moiety leads to a movement through the ECM resembling simple diffusion [Ducuing *et al.*, 2013], (**Fig. 3.3**). In vertebrate models, more specifically the murine limb bud, this finding has been confirmed [Li *et al.*, 2006]. However, stark contradiction from other research groups, stating that cholesterol mediates long-range mobility and signalling [Lewis *et al.*, 2001][Tian *et al.*, 2005], exists but is most likely misguided. *In vivo* expression of a non-cholesteroylatable mutant truncated just before the autocatalytic domain, such as was

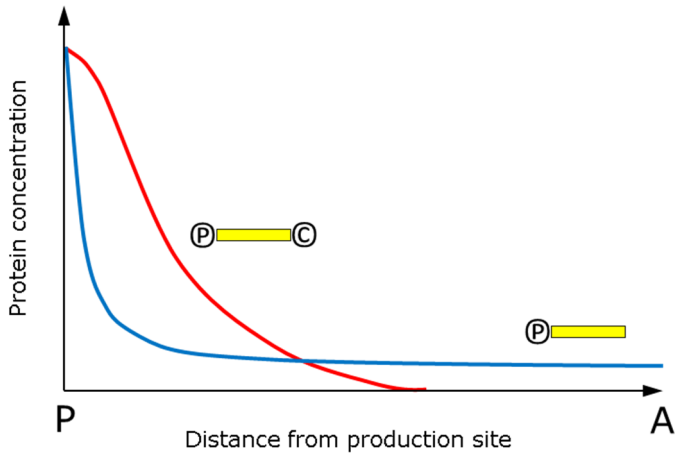

Figure 3.3. Impact of the cholesterol modification on the Shh gradient. This figure depicts the differences in spreading of the fully functional, dually lipidated form (red curve) and a non-cholesteroylated form (blue curve). This model was suggested by [Li et al., 2006] based on studies in mouse limb buds. P indicates the 'posterior' margin of the limb, where Shh synthesis and release take place, and A is the 'anterior' margin which is inhabited with Shh-receiving cells. The cholesterol moiety evidently increases the local concentration of the morphogen and apportions less of the ligand for long-range signalling.

used by those groups, results in low transcript levels, because of a nonsense-mediated RNA decay mechanism which destroys mRNAs with premature translation termination codons [Li *et al.*, 2006]. It is possible then to conceive that the reduced levels of protein production can be misinterpreted as inability of uncholesteroylated Shh to spread away from the producing cells.

Intriguingly, while Disp has been found to be absolutely required for the release of fully post-translationally modified Shh, in the murine spinal cord and limb bud Disp has been found nevertheless to be dispensable for externalisation of the sterol-unmodified mutant [Li *et al.*, 2006].

HSPGs have been found both to restrict [Han *et al.*, 2005] and to promote the diffusion of the morphogen [Kreuger *et al.*, 2004] – presumably depending on the contextual environment. If Shh interacts with glypicans, then increase in the range of spread can be achieved by cleaving the morphogen-HS complex from the lipid anchor [Kreuger *et al.*, 2004]. Alternatively, HSPGs might enable the morphogen to travel further through reducing Hh endocytosis [Franch-Marro *et al.*, 2005].

A cloud of controversy surrounds many aspects of Shh release and transportation. It ranges from disagreement on the lipidation state of the Shh produced on the cell surface and the actual physiologically relevant form of Shh, *i.e.* whether Shh is deployed solely as multimer [Farshi *et al.*, 2011], or a mixture of monomeric and oligomeric states [Palm *et al.*, 2013], to a lack of consensus on whether the precursor (full-length) protein is actually secreted externally [Tokhunts *et al.*, 2010], or whether it is degraded in the ER before it could reach the membrane [Chen *et al.*, 2011]. Indeed, different formats of the Shh signalling ligand may have evolved for the purpose of allosteric control, higher concentration of binding sites, larger binding surfaces and the nascence of new binding sites at the interface between the subunits [Farshi *et al.*, 2011][Dierker *et al.*, 2009b]. Moreover, existence of different signalling forms could have profound ramifications for the extracellular gradient profile and the binding of Shh by Ptc. Ultimately, they could present an additional form of control over target gene expression.

Non-conformity of opinions continues through the packaging and spreading to dispersal and reception. The reason for the difficulty in pin-pointing the exact mechanism of Shh release and distribution may be because the latter ultimately varies from tissue to tissue in a given organism, as well as between organisms in the Kingdom Animalia. In addition, some of these results were obtained not in animals (*in vivo*), but in tissue culture cells (*in vitro*). Working with such simple, versatile model systems, *e.g.* human embryonic kidney cells (HEK293 varieties) and similar cell lines, and artificially expressing Shh therein – although convenient, does not necessarily reflect Shh behaviour in living organisms, if not only because some of the pathway components may be missing in the selected cell line. Even so, the unwieldiness caused by the inability at present to detect very small quantities of Shh produced endogenously (even in cancer cells which over-produce it, as they depend on Shh for their survival, as has been observed in the Magee laboratory and in [Palm *et al.*, 2013]), has compelled researchers to favour studies of recombinant Shh over-expression in cell lines. Notwithstanding, certain pitfalls in this method in the specific context of Shh multimerisation studies are worth mentioning. Over-expression could cause the protein to be re-routed to a different part of the cell than the membrane so that it fails to turn up on the extracellular membrane leaflet at all. At the other extreme, if the protein is correctly transported out of the cell, the abnormally high quantity of synthesised Shh may result in the formation of larger-than-normal clusters.

Finally, some evidence suggests that lipid modifications may be responsible for weak, preliminary clustering of the Shh monomers as a prerequisite for the formation of higher molecular-weight clusters [Vyas *et al.*, 2008][Dierker *et al.*, 2009a]. Interestingly, in *Drosophila*, studies involving erasing a portion of the signalling domain (aa 115-255 of *Drosophila* Hh), but retaining sites necessary for cholesterol and palmitate attachment, have indicated that multimerisation on an optically resolvable scale cannot proceed without those amino acids [Vyas *et*

al., 2008]. In support of this, crystallographic examination has indicated that some residues (R33 and K37) located within the CW peptide may be responsible for multimerisation by electrostatic protein-protein interaction with an adjacent molecule's negatively charged hydrophobic pocket, consisting of residues D88, E89, E90, E126, D129, E130, D131, E136, E137 and D146 [Farshi *et al.*, 2011]. This suggests that the lipid modifications alone may not be sufficient for the organisation of Hh into large clusters, and the process of multimerisation may in fact be driven by interactions in the amino acid sequence of the Shh N-terminal domain [Goetz *et al.*, 2006]. On the other hand, a completely unlipidated form of Shh produced in *E. Coli* is detected exclusively in monomeric form [Ohlig *et al.*, 2011].

In brief, the purpose of the Shh multimeric complexes appears to be to stabilise the protein in the ECM, enable it to signal long-range, and to form a highly specific concentration gradient profile. Given the conflicting findings laid out in this chapter, however, clearly more information is necessary to articulate Shh's high molecular-weight packaging dependence on lipid moieties.

4. Research project question

4. 1. Hypothesis

Research on the Hh family has so far been conducted mainly with the aid of biochemical techniques. More specifically, these have included protein purification methods, such as western blotting and gel-filtration chromatography. Unfortunately, none of these provide the benefit of direct observation of the protein of interest in the convincing manner of optical imaging: in a sense, 'seeing is believing'. That is not to say that biochemical techniques cannot be trusted, but that their outcomes cannot always be interpreted unambiguously without some additional pieces of information acquired by independent means. Every experimental technique has a certain scope and I believe that biochemistry may be at its limits in providing a meaningful answer to the problem of the involvement of lipid moieties in the assembly of Shh multimolecular complexes. Evidence in support of this opinion is the state of controversy in the scientific community (outlined in the previous chapter) about almost every aspect of Shh: from the biologically relevant form [Farshi *et al.*, 2011][Tokhunts *et al.*, 2010], to the method of packaging and solubilisation [Zeng *et al.*, 2001][Tanaka *et al.*, 2005][Dierker *et al.*, 2009a][Palm *et al.*, 2013][Sanders *et al.*, 2013].

My hypothesis is that cholesterol and palmitate both play a role in determining the architecture of Shh multimeric complexes, but that they each have a distinct function.

4. 2. Aims

4. 2. 1. Development and validation of the STORM super-resolution technique

Although mainstream STORM does not yet permit single-molecule imaging in biological samples (at least not on the scale of the Shh monomer, which x-ray crystallography has shown to be ~4 nm in diameter), it presents an attractive candidate for examining the nanoscale topology of Shh. In order to test my hypothesis above, I aim therefore first to build a microscope system fit for super-resolution imaging (the first of its kind in the university). This involves selecting, aligning and installing appropriate components onto a commercial widefield microscope stand. The next step requires validating STORM in order to ensure that the results generated with it are fully reliable; this will be achieved by means of utilising a 'benchmark' structural element, such as cytoskeleton fibres, whose reconstruction in super-resolution serves as an indicator of

success or failure and can flag up potential issues with the technique.

4. 2. 2. Studying of Shh mutants with acylation and/or cholesteroylation deficiencies

In order to establish the precise impact of each lipid modification, it would be necessary to determine how the effects brought about by their separate absences, such as changes in size, shape or distribution of the multimers, compare against those in their presence. By ensuring that all other experimental factors remain the same, the differences observed (or lack thereof) can be attributed, with considerable confidence, to being a direct consequence of the relevant altered lipid modification.

For this reason, I employ a range of DNA sequences encoded in plasmids (**Fig. 4.2.2**) which I intend to transfect transiently in a versatile cell line and observe within the period of expression. The four human DNA sequences are as follows. 1) Full-length, wild-type *Shh*. 2) *Shh* with a deleted autocatalytic domain, realised by substituting cysteine 198 immediately after the end of the signalling domain for a stop codon. This should result in a palmitoylatable, but not

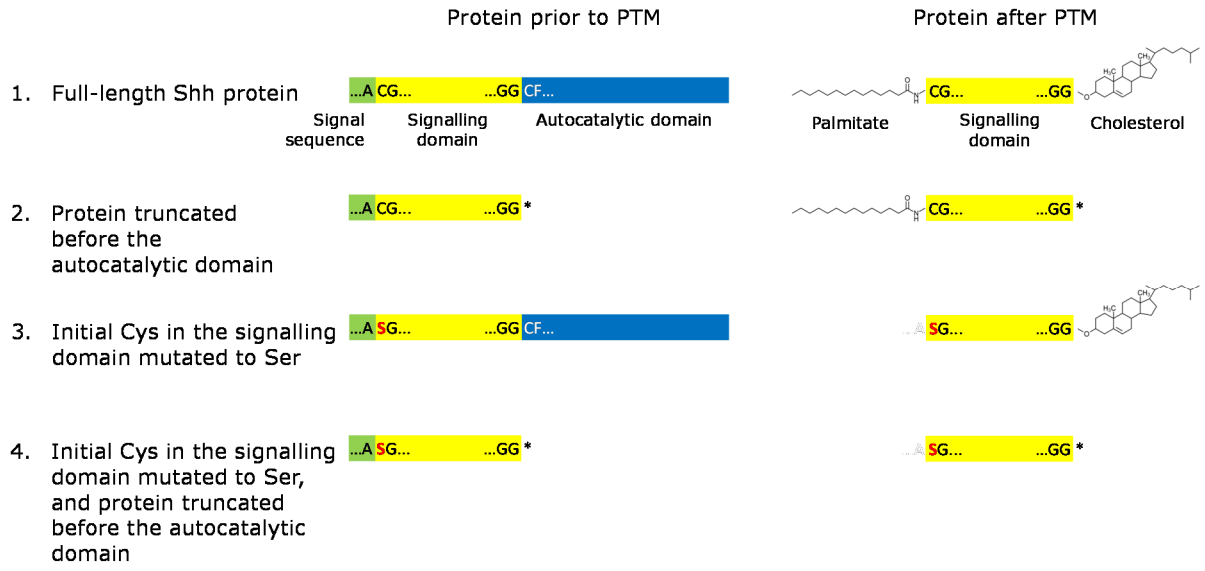

Figure 4.2.2. Expected gene products of four wild-type and mutant DNA sequences of human Shh. 1) The genetic sequence of wild-type *Shh* without any modification naturally results in the wild-type, doubly lipidated protein. 2) A mutant *Shh* DNA with a stop codon after the signalling domain should result in a palmitoylatable, but not cholesteroylatable, protein. 3) *Shh* with an acylation-incapacitating C24S mutation produces a protein lacking palmitate. 4) A combination of the gene engineering in 2) and 3) together yields a gene product that is not post-translationally modified at all. Key: PTM, post-translational modification; *, stop codon.

cholesteroylatable, protein, because the cholesterol transfer reaction cannot proceed without the facilitation of the absent Shh C-terminal domain. 3) *Shh* with a point-mutation of the guanine nucleotide in the codon coding for cysteine 24 to a cytosine, which translates as a serine residue instead of the customary cysteine. This genetic sequence yields a cholesteroylatable, but non-palmitoylatable, protein, because serine, unlike cysteine, does not contain a sulphhydryl group which is in fact needed to form a thioester intermediate before forming the stable amide linkage. 4) *Shh* combining the stop codon insertion immediately after the signalling domain, as well as the same point-mutation as in 3). It is expected that the gene product would be amenable neither to cholesteroylation, nor palmitoylation. The four DNA sequences are used in Chapter 7 and are a gift from Dr Marta Świerczyńska.

If STORM proves sufficiently trustworthy, I then aim to employ STORM to quantitate the spatial aspects of the wild-type and mutant proteins, to identify differences and speculate on the origin of those differences. In the event that STORM fails to convince of utter dependability, I plan to utilise high-resolution confocal imaging in conjunction with deconvolution, in order to supersede the diffraction limit. Finally, I aim to attempt to enumerate the Shh monomers present in individual Shh surface complexes by means of single-molecule counting.

4. 2. 3. Overview of ensuing chapters

Full details of the experimental procedures and materials are given in the next chapter. Chapter 6 is concerned with establishing and optimising the STORM technique, and attempting to quantitate full-length Shh in super-resolution. Chapter 7 focuses on quantitation using conventional confocal imaging boosted in resolution computationally with a post-acquisition deconvolution algorithm. In chapter 8, it is attempted to count individual Shh molecules within individual multimers *via* photobleaching in the TIRF mode; success in this venture is achieved by modelling the process *in silico* instead.

5. Materials and Methods

5. 1. Biological materials and methods

5. 1. 1. Buffers and solutions

Name of reagent	*Composition*
APS (ammonium persulphate) solution	10% w/v APS (Bio-Rad, Hercules, CA, USA) in ddH_2O
Bis-Tris buffer	1 M Bis-Tris solid in ddH_2O, titrated to pH 6.7 with HCl
Blocking buffer (immunostaining)	5% w/v BSA (bovine serum albumin; Sigma-Aldrich, Gillingham, UK) in PBS
Blocking buffer (western blot)	5% w/v Marvel dried skimmed milk powder, 0.02% NaN_3 in PBS, filtered
Fixative	3% w/v PFA (paraformaldehyde; Sigma-Aldrich, Gillingham, UK), 1.5% sucrose in PBS, pH 7.3
Imaging buffer	100 mM β-mercaptoethylamine (MEA; Sigma-Aldrich, Gillingham, UK), 0.5 mg/mL glucose oxidase (GlOx; Merck Chemicals Ltd., Nottingham, UK), 20% w/v D-(+)-glucose (Sigma-Aldrich, Gillingham, UK) in PBS
Lysis buffer	1% Triton X-100 (BDH Chemicals Ltd., Poole, UK), 0.1% sodium dodecyl sulphate (SDS; Merck Chemicals Ltd., Nottingham, UK), 1× cOmplete mini protease inhibitor tablet (Roche Diagnostics Ltd., Burgess Hill, UK) in 10 ml PBS, pH 7.4

PBS (phosphate buffered saline)	137 mM NaCl, 2.7 mM KCl, 10 mM Na_2HPO_4, 2 mM KH_2PO_4, pH 7.4
PBST	PBS, 0.05% v/v Tween-20 (Sigma-Aldrich, Gillingham, UK)
Running gel	24.46% ddH_2O, 48.92% v/v acrylamide-bisacrylamide mix 37.5:1 (Bio-Rad, Hercules, CA, USA), 24.46% v/v Bis-Tris, 1.96% APS solution, 0.20% TEMED (N,N,N',N'-tetramethylethylenediamine; Bio-Rad, Hercules, CA, USA)
Stacking gel	49.75% ddH_2O, 13.27% v/v acrylamide-bisacrylamide mix 37.5:1, 35.82% v/v Bis-Tris buffer, 1% v/v APS solution, 0.16% v/v TEMED
Transfer buffer (Tris-glycine-SDS)	192 mM glycine, 25 mM Tris base pH 8.3, 0.1% w/v SDS in ddH_2O

5. 1. 2. Cell culture and maintenance

Except during experiments, when cells were transferred to either 6- or 24-well plates, or MatTek™ dishes, cells were cultured in 175-cm^2 uncoated Nunc™ flasks in Dulbecco's modified Eagle's growth medium (DMEM), supplemented with 10% foetal calf serum (FCS) and 1% penicillin streptomycin antibiotics, and maintained in conditions of 37°C and 5% CO_2. They were routinely passaged upon reaching ~80% confluence with trypsin-EDTA (0.05% w/v and 0.02% w/v; PAA laboratories, Yeovil, UK). Cell lines used were HEK293 and COS-7 (both a gift from Dr Birgit Leitinger).

5. 1. 3. Western Blotting

5. 1. 3. 1. Cell culture and transfection

Cells were seeded in a 6-well plate at a density of 75,000 per well. They were then incubated at 37°C and left overnight to adhere to the substratum. On the following morning, immediately prior to transfection, the medium was changed to penicillin- and streptomycin-free medium (still supplemented with the same quantity of serum). The cells were transfected with the transfection reagent Turbofect™ (Thermo Scientific, Cramlington, UK); the transfection complex was made up in the ratio 100:1:2 µL of Opti-MEM, 1 mg/mL plasmid and Turbofect™, respectively, for every two wells. For mock transfections, the plasmid was replaced with an equal quantity of ddH_2O. Henceforth I proceeded as per the manufacturer's instructions. The transfection complex was administered evenly over the surface of each coverslip in a drop-wise fashion. Six hours post transfection, the medium was replaced with fresh, full medium, in order to reduce the cell death rate induced by the transfection reagent. After transfection, the cells were left to express the plasmid(s) over a 24-hour period at 37°C.

5. 1. 3. 2. Cell lysis

Cells were rinsed twice with ice-cold PBS and incubated on ice with 100 µL lysis buffer per well for 15 minutes. After this period, the cells were physically teased from the substratum using a cell scraper and passed three times through a 0.5-mm syringe to shear the long strands of genomic DNA. Insoluble debris was removed by centrifugation of the lysate at 16,100 × *g* for 10 minutes at 4°C. The supernatant was either used directly afterwards, or stored for future use at -80°C.

5. 1. 3. 3. Protein concentration assay

The total protein concentration of the lysates was determined using Bio-Rad's *DC* protein assay, which is a colorimetric assay of the lysate following detergent solubilisation. Samples were pipetted in duplicate in a 96-well microtitre plate, along with six protein standards varying in concentration of between 0 and 1.5 mg/mL bovine serum albumin (BSA) dissolved in lysis buffer. The samples were prepared according to the manufacturer's recommendation, and a curve of absorbance *versus* protein concentration was plotted using the protein standards. The R square value was checked on each occasion of running the assay, and if less than 0.98, the

standards were prepared once more, until a satisfactory value of R square was reached. The absorbance was measured at 700 nm with a microplate spectrophotometer (Sunrise™, Tecan Group Ltd., Männedorf, Switzerland).

5. 1. 3. 4. Protein separation by molecular weight with SDS-PAGE

Protein separation by molecular weight was achieved using sodium dodecyl sulphate polyacrylamide gel electrophoresis (SDS-PAGE). Stacking and resolving polyacrylamide gels were made with 4% and 15% polyacrylamide content, respectively. Amounts of lysates with identical protein content (usually 10 µg per sample) were made up to the same total volume using lysate buffer wherever needed, and complemented with NuPage LDS sample buffer (Invitrogen, Paisley, UK). The samples were then boiled in a heating block for 10 minutes at 90°C and subsequently loaded into the gel. 4 µL of All Blue Precision Plus molecular size marker was used as a molecular weight reference. Electrophoresis in a 2-(N-morpholino)ethanesulphonic acid (MES-SDS) running buffer (Laboratory Products Sales Inc., Rochester, NY, USA) was started and run initially at 70 V for the first 10 minutes, until the proteins passed into the separating gel, whereupon the voltage of the power source (PowerPac™, Bio-Rad, Hercules, CA, USA) was increased to 180 V for the remaining 65 minutes.

5. 1. 3. 5. Membrane transfer and immunoblotting

Separated proteins within the gel were transferred onto a polyvinylidene difluoride (PVDF) membrane (Millipore, Billerica, MA, USA) pre-activated with methanol, using semi-dry transfer apparatus (TE77X, Hoefer Inc., Holliston, MA, USA). The transfer was run for 1.5 hours at a constant current of 80 mA (~1.27 mA/cm^2). After the transfer was complete, the membrane was incubated overnight in blocking buffer at 4°C.

On the following day, the membrane was incubated with primary anti-Shh polyclonal rabbit antibody (H-160 sc-9024, #K2211, Santa Cruz Biotechnology Inc., Heidelberg, Germany) diluted 1:200 in blocking solution for 2 hours at room temperature on a rotator. Subsequently, the membrane was washed 4 × 5 minutes in PBST, whereupon it was incubated with a secondary goat anti-rabbit antibody conjugated to horseradish peroxidase (HRP) (GAR-HRP IgG H + L, #4050-05, Southern Biotech, Birmingham, AL, USA) diluted 1:20,000 in PBST for 50 minutes at room temperature on the rotator. The membrane was then washed 5 × 5 minutes in PBST. Protein bands were visualised using ECL Plus Western Blotting Detection Reagent (GE Healthcare,

Amersham, UK) imaged with Ettan DIGE Imager (GE Healthcare, Amersham, UK). The protein band detection channel included wavelengths in the range 530/40 nm, whereas the channel in which the ladder was detected had a wavelength window of 680/30 nm.

After Shh had been imaged, the membrane was washed 4 × 5 minutes and re-incubated with primary antibody – this time with monoclonal mouse anti-GAPDH (anti-GAPDH [6C5], ab8245, Abcam, Cambridge, UK), a kind gift from Ms Susann Bruche, which served as a loading control. The primary antibody was diluted 1:50,000 in blocking buffer and the membrane incubated for 30 minutes at room temperature on the rotator. Washing 4 × 5 minutes with PBST followed and a final incubation for 50 minutes with secondary goat anti-mouse HRP conjugate (GAM-HRP IgG1, #1080-05, Southern Biotech, Birmingham, AL, USA) The imaging of Shh and GAPDH was performed separately because, as the signal from the GAPDH antibody was many times stronger – even at extremely low concentrations, it was not possible to visualise both Shh and GAPDH at the same time.

5. 1. 4. Cell Immunostaining

5. 1. 4. 1. Pre-treatment of coverslips for improved adhesion

№ 1.5 coverslips (0.16–0.19 mm thick), ∅ 13 mm, were immersed in acetone for 1 hour to remove any grease films residing on the surface. They were then rinsed thoroughly from the solvent in biological-grade absolute ethanol (Merck, Darmstadt, Germany), spread on lint-free tissues to dry at room temperature and subsequently autoclaved.

5. 1. 4. 2. Cell culture and transfection

Cleaned coverglasses were inserted in the wells of 24-well plates and cells were seeded at a concentration of 60,000 per well. For super-resolution experiments, cells were seeded directly onto MatTek dishes at 300,000 per dish. Cells were then incubated at 37°C overnight and transfected as already outlined in section 5. 1. 3. 1., except that the amount of transfection complex applied was scaled relative to the area of the well. Protein expression was allowed to take place for a duration of 24 hours post transfection and prior to fixing.

5. 1. 4. 3. Fixing and permeabilisation

3% PFA fixative was prepared by dissolving 750 mg PFA into 25 ml of PBS and adding 375 mg (1.5% w/v) sucrose. The mixture was heated for 5 minutes at 65°C, then was left to cool down. 400 µL of 1 M NaOH were added and the mixture was heated again at 65°C for a further 10 minutes; at the end, the mixture was agitated to dissolve the PFA completely. Finally, through adding incremental quantities of HCl and simultaneously measuring the pH with an electronic pH meter, the pH was adjusted to 7.3. Approximately 250 µL of 1 M HCl were added in total. The mixture was then either used immediately or stored in aliquots at -20°C.

Cells were rinsed once with PBS and fixed with 3% PFA for 10 minutes at room temperature. All traces of the fixative were then removed by washing 3× with ice-cold PBS. Actin was preserved instead by subjecting cells to 100% methanol for 5 minutes at -20°C, then rinsing 3× with PBS. When full membrane permeabilisation was required, such as for staining the ER lumen, cells were additionally treated with 0.2% v/v Triton X-100 in PBS for 5 minutes at room temperature. For semi-permeabilisation (perforation of the plasma membrane, but not the ER membrane), 0.004% w/v digitonin in PBS from a 40 mg/ml stock solution prepared on the day before was incubated with the cells for 10 minutes on ice. After the time was up, cells were rinsed once with PBS and then washed 2× with PBS for a further 5 minutes on each occasion. Next, non-specific binding sites were blocked with 5% w/v BSA in PBS for 1 hour at room temperature. The blocking buffer was then replaced with a primary antibody dilution in blocking buffer. Primary antibodies used were either against Shh: H-160 and monoclonal rabbit antibody (C9C5, #2207, Cell Signaling Technology Inc., Beverly, MA, USA) at a concentration of 1:200 each; against calnexin-C: polyclonal rabbit antibody (CNX, ADI-SPA-860, Enzo Life Sciences Ltd., Exeter, UK) at a concentration of 1:100; against calnexin-N: monoclonal mouse antibody (p88, [AF18] IgG1, Enzo Life Sciences Ltd., Exeter, UK) at 1:100; against tubulin: monoclonal mouse α-tubulin (anti-tubulin IgG1, ab7291, Abcam, Cambridge, UK), at 1:200. Incubation with anti-Shh and anti-tubulin antibodies lasted 45 minutes, whereas with anti-calnexin antibodies, the total incubation time was 30 minutes.

Primary antibodies were removed by carefully replacing the solution with PBS and incubating for 5 minutes, then repeating this step a further 2 times. This was followed by incubation with either secondary antibodies or fluorescently conjugated phalloidin. For detecting the corresponding primary antibody, either goat anti-rabbit IgG H + L or goat anti-mouse IgG1 Alexa Fluor® 488 secondary antibody was used, except in the case of calnexin-C, which was detected with anti-rabbit IgG H + L Alexa Fluor® 555. The latter was also used for detecting Shh in super-resolution imaging. In all cases secondary antibodies were diluted 1:500 in blocking buffer and incubated with cells for 30 minutes at room temperature. Alexa Fluor® 568 phalloidin (Invitro-

gen, Paisley, UK) was used at a concentration of ~1:42 for direct staining of F-actin and was incubated for the same amount of time as the secondary antibodies.

Lastly, coverslips were dipped 10× in ddH_2O and MatTek dishes rinsed 3× with ddH_2O to avoid crystallisation of the PBS salts on the specimen. Residual moisture on the coverslips was removed by contacting the edge of the coverslips with a tissue, whereupon the coverslips were mounted on glass slides by embedding the face containing the specimen into an 8-µL drop of ProLong Gold antifade agent (Invitrogen, Paisley, UK).

5. 2. Physical materials and methods

5. 2. 1. Home-built total internal reflection microscope system

A Zeiss Axiovert 200 microscope (Carl Zeiss, Germany) base was fitted with a commercial total internal reflection fluorescence (TIRF) condenser kit (TILL Photonics GmbH, Germany). The complete microscope system is displayed in **Fig. 5.2.1**. A 491.5-nm (henceforth referred to as 491-nm, for brevity) and a 561-nm diode-pumped solid-state laser (Calypso™ and Jive™, respectively, Cobolt, Sweden) were used as excitation light sources. The lasers were coaxially combined using a fibre-coupled beam combiner (iFLEX-Adder™, Point Source, UK) *via* individual single laser wavelength (491 or 561 nm) optic fibres (kineFLEX™, Point Source, UK). The beam was then passed through an acousto-optic tunable filter (AOTF; AA Opto-electronic, France), followed by a mechanical safety shutter.

The microscope system was built as a joint effort between myself and the facility technician, Mr Stephen Rothery, for shared use with other researchers in the microscopy facility, and not just for this project. For this reason, components not directly associated with super-resolution were also incorporated. Single-molecule localisation super-resolution techniques usually require comparatively high illumination intensities, hence adding the AOTF does not have an apparent advantage for this technique. The AOTF was installed for fine-tuning the intensity of the laser, a feature particularly advantageous when low illumination intensities are required. The lasing process is unstable at very low intensities, making it unfeasible to control the intensity directly through the power feed of the laser. Instead, with the AOTF in place, the laser can be operated at moderate power, while the AOTF acts as a precision attenuation device.

We added an additional broadband illumination source (Polychrome IV, TILL Photonics GmbH, Uckfield, UK), specifically for reactivating fluorophores with UV light for PALM imaging, although it could be used for other purposes as well. Since the STORM modality was selected for

the work done in this thesis, the light source is not shown on **Fig. 5.2.1**; it was connected to the set-up at the TIRF condenser.

From the shutter, laser light is carried using a dual-wavelength (491-nm and 561-nm) optic fibre (kineFLEX™-duo, Point Source, UK) to a custom-made insert preceding the TIRF condenser unit. The insert contains optics intended to concentrate the laser beam into a tighter spot in the sample plane, in order to increase the effective illumination intensity at the sample and bring it within the recommended range for conducting super-resolution experiments. At this point in the optical train, the fibre tip is polished at an angle of 8° in order to minimise back-reflections that may destabilise the lasers and induce fluctuations in laser output. The fibre is therefore coupled to a fibre connector for angled physical contact (FC/APC). Beyond it, the beam encounters an aspheric collimator lens; both the lens and connector constitute a commercial package (F240APC-A, Thorlabs Ltd., United Kingdom). The beam is then passed through an achromatic doublet lens assembly (AC127-030-A, Thorlabs Ltd., United Kingdom), where the position of the doublet was chosen so that the beam was magnified by a factor of 4, according to the relationship $M = f/(f - s)$, where f is the focal length of the doublet (30.0 mm) and s is the distance between the doublet and the collimator lens. Magnifying the beam in this plane (a plane conjugate to the back focal plane, BFP) causes equivalent demagnification in the plane of the specimen, where the beam's power density increases. The illumination intensity (that is, the power per unit area) at the specimen is thus increased by a factor of 16, to an absolute intensity average of 2.33 kW/cm^2. Note that the actual power density, rather than just the power, was measured; this was achieved by measuring the illumination power at the specimen plane and dividing by the FWHM area of the laser illumination beam at the same plane. Boosting the illumination intensity was done in order to approach that reported in [Heilemann *et al.*, 2009] (3 kW/cm^2), which was used to image Alexa Fluor® 488.

After entering the TIRF condenser unit, the beam is relayed by a triangular prism *via* TIR into the microscope. The longitudinal extension of the commercial TIRF unit can be varied, thus changing the distance between the prism and the microscope objective. This distance was adjusted, according to the manufacturer's instructions, in order to focus the beam onto the BFP, and to ensure that the rays exited the objective parallel to each other. If the rays are not parallel, there is a risk that some areas in the sample will not be illuminated in TIRF, since their incidence angle would be too acute for TIR to occur. In addition, other areas with supercritical angle of illumination will experience a non-uniform penetration depth.

Inside the microscope, the beam is reflected by a dichroic mirror through the objective and onto the sample. Fluorescence emitted by the excited fluorophores in the sample is transmitted back through the objective and straight through the dichroic mirror. An emission filter is used to extinguish any remaining laser light which has made its way through the dichroic. Two

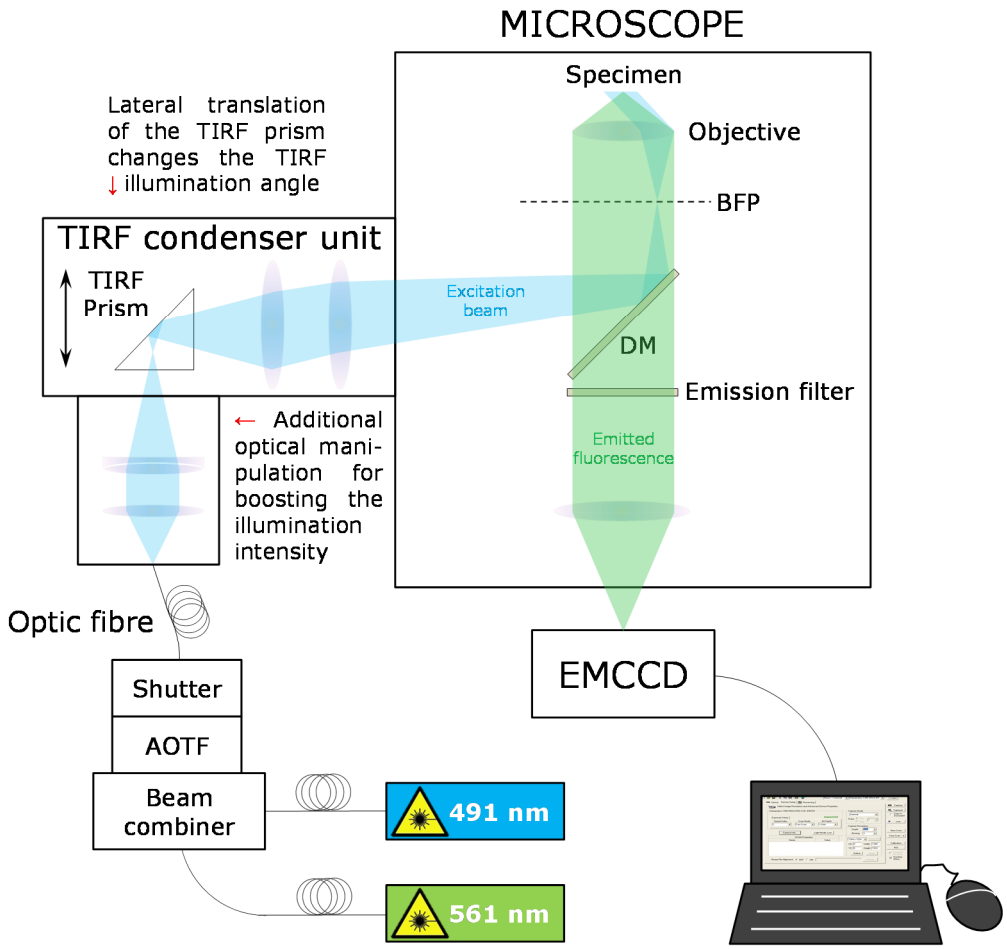

Figure 5.2.1. Total internal reflection fluorescence (TIRF) and super-resolution microscope set-up. Two 75-mW laser sources (491 nm and 561 nm) are combined using a beam combiner. The laser beams are then passed through an acousto-optic tunable filter (AOTF) which permits to fine-tune their intensity. A shutter follows immediately after, and a dual-wavelength fibre carries the light to the TIRF condenser unit. The far end of the fibre has an angled physical contact to eliminate reflections back into the lasers. Before entry into the TIRF module, additional optics magnify the beam spot by a factor of four. Inside the microscope, the laser beam is reflected from a dichroic mirror (DM) through the objective and onto the specimen. Fluorescence emitted by excited fluorophores in the specimen is captured by the objective, then passed through the DM. Most scattered or stray laser light is blocked by the emission filter; fluorescence from the specimen, on the other hand, is let through virtually unabated and is imaged onto an electron-multiplying charge-coupled device camera (EMCCD). Image data from the camera is streamed to a computer, where it is recorded using SimplePCI software.

filter cubes are installed in the microscope. One of them is a Semrock GFP 3035B (filter set 10) with a dichroic mirror (Chroma DC/z488/561rpc, Cairn Research Ltd., UK) and the original Zeiss band-pass emission filter transmitting wavelengths in the range 515-565 nm. The other cube is Zeiss TXRED 4040B (filter set 45), with entirely original components (except that the

excitation filter was removed), splitting light with a long-pass dichroic mirror at 601 nm, and a band-pass emission filter, 630/75 nm.

Inefficient reflection of laser light at the dichroic can occur, for example, at steep incidence angles, whereby the transmission profile of the dichroic experiences a shift in both wavelength and transmission efficiency. Preventing laser light from entering the imaging path to the detector can eliminate the formation of interference fringes in the image plane. The interference fringes are caused by constructive and destructive interference of the coherent laser light. In our experience, the Zeiss emission filter largely prevented the appearance of interference fringes, except occasionally at very shallow incidence angles (low TIRF penetration depths), therefore it was not found to be necessary to use a phase scrambling device to destroy the coherence.

5. 2. 2. Mechanical stabilisation

In the context of super-resolution imaging, minute displacements which are normally of no consequence to conventional microscopy begin to become significant. Lateral drift due to stage motion and axial drift caused by a change in the focus of the objective are both factors that can severely reduce the resolution achieved with PALM or STORM. The former manifests itself as elongation of all objects in the image in a well-defined direction. The latter flattens the Airy function's peak whilst widening its lateral extent, leading to a spread of the photons emanating from the molecule over a greater area. This leads to a greater uncertainty in the localisation of the molecule, hence capping the resolution potential.

Most commonly, these displacements are a consequence of a temperature gradient and undamped vibrations in the microscope system. To reduce the movement of air interacting with the sample and microscope imaging components adjacent to it, a plastic draught-proof enclosure was installed over the microscope stage and objective turret. A heater was placed inside the chamber and was set to maintain a constant temperature of 25°C. 25°C was the lowest temperature setting of the device and was chosen because it was closest to the optimal working temperature of the immersion oil, which is designed for maximal aberration correction at 23°C. Floor vibrations arising from road traffic, trains, lifts, building sway and others, as well as those induced by the microscope operator, were dampened by mounting the microscope on a vibration isolation table (Speirs Robertson Corp., USA).

Fiduciaries were not used as internal controls to correct for drift because the microspheres available for this purpose were far brighter than the signal of interest from the cells and had an overshadowing effect. Due to time restrictions, it was not possible to optimise the fiduciary protocol.

5. 2. 3. Measurement of microscope PSF using fluorescent microspheres

The PSF of a microscope can be easily measured using commercially available fluorescent microspheres. The microspheres must be smaller than the diffraction limit (for the particular *NA* and wavelength that is intended to be used), *i.e.* less than around 200 nm in diameter. They then act as point sources. The ideal size that has been empirically arrived at is 160 nm; any smaller and the signal becomes too weak, whereby the image of the microspheres becomes severely distorted by noise. Any larger and the microsphere no longer approximates a point source. In this work, the PSF measurement was carried out with 175-nm green fluorescent microspheres from the PS-Speck™ microscope point source kit (Invitrogen; Cat. no. P-7220). The spheres' excitation and emission peaks are at 505 and 515 nm, respectively, and are manufactured with a diameter tolerance of 5 nm (2.9%). The green microsphere was selected for this purpose from the kit, because its emission wavelength is closest to that of Alexa 488 (519 nm), and so the size of the PSF obtained with this method is as close as possible to what is generated by the Alexa 488 fluorophore.

The microspheres were mounted in the same embedding medium as the biological specimens of interest (ProLong Gold antifade agent) on a slide, sealed with a coverslip. This was done in order to replicate the same refraction errors occurring whilst imaging the biological specimen. A 3D *z*-stack was obtained of a field of view with several microspheres. The sampling frequency in all dimensions was set to a figure well above the Nyquist frequency (41 nm and 131 nm, compared to $f_{lateral}^{Nyq} = 89$ nm and $f_{axial}^{Nyq} = 235$ nm, respectively). This generous oversampling allowed recording information about the PSF with greater dynamic range, and therefore capturing both the bright centre and side lobes with high fidelity [Pawley, 2006]. In fact, all microscope settings mirrored those that were used to collect the biological data. To reduce the effects of noise on the quality of the extracted PSF, 9 beads spread across the field of view were averaged. In order to obtain the true microscope PSF, the physical size and shape of the microspheres was deconvolved from the images, using the suitably rearranged **Eq. 2.2.9.1 / 2.2.9.2**.

5. 2. 4. Data collection procedure for confocal microscopy

The instrument used to collect the data was a Zeiss LSM 780, with a GaAsP detector. The detector has a very high quantum efficiency (45%), compared to other PMT confocal microscope detectors, and employs a low-noise electron multiplication process. The excitation source is an Argon multiline 25-mW laser, whose 488-nm line was used for exciting Alexa Fluor® 488. The objective is a 63x Plan Apochromat lens, with a numerical aperture of 1.4.

The specimen was mounted in antifade reagent of refractive index ~1.46, matching the refractive index of the specimen (membrane refractive index varies between 1.46 and 1.6 [Parton *et al.*, 2006]). Immersion oil (Zeiss) of refractive index 1.518, matching that of the objective's optics, was applied to the objective. Indices were matched in order to reduce spherical aberration in the recorded image [Parton *et al.*, 2006].

In order to benefit from the best possible resolution of the imaging system, the Nyquist sampling rule was observed. The pixel size of the PMT and the vertical distance between optical sections were adjusted to less than one half of the expected resolvable distance in each dimension (x, y and z) – more precisely, to the values described in the previous section. More on the details of confocal microscope resolution can be found in the Background and Theory chapter in section 2. 2. 3. 3.

6. STORM imaging of cell-surface Shh complexes

The purpose of this project is to investigate the multimerisation of Shh complexes, an event which occurs on the exoplasmic surface of signal-producing cells. Little is known about the composition of these structures, their organisation and size distribution. Amongst the few known facts to date about the visual characteristics of the clusters is that they appear punctate under diffraction-limited microscopy [Incardona *et al.*, 2000][Vyas *et al.*, 2008]; in addition, FRET (Förster resonance energy transfer) studies have established that nanoscale oligomers below the resolving power of conventional optical imaging may exist [Vyas *et al.*, 2008]. FRET, however, is a 'blind' methodology which is not capable of unveiling the morphology: it is limited merely to a binary answer of whether or not molecules are spaced close enough together to suggest that they are part of a composite structure. Admittedly, the amplitude of the FRET signal can betray the relative abundance of molecules comprising clusters of different sizes, although determining the absolute abundance necessitates calibrating the signal to an individual FRET event.

In this respect, super-resolution imaging is well suited to this question as it permits direct observation of the object of interest and obtaining dimensional data. Applying it constitutes simultaneously a fresh approach to the Shh multimer problem and an innovative application of a powerful, nascent imaging technique.

6. 1. Characterisation of lateral drift in the microscope system

Stage and/or sample drift can have a substantial detrimental impact on the localisation precision (see section 5. 2. 2. of the Materials and Methods chapter). It was therefore investigated and characterised. Through trial and error, it was established that the most effective preventative measure against lateral, and in particular axial, drift was to use a heater, adjusted to a temperature of 25°C (for the choice of temperature setting, the reader is referred to section 5. 2. 2.), on the evening before the experiment. On the following day, the immersion oil was applied and the sample was set in place, followed by a further 20-minute wait for the system to equilibrate.

Due to the unavailability of larger microspheres at the time, aggregates of unsonicated 20-nm microspheres were mounted in ProLong® medium and imaged continuously over a long time period (20 minutes) with the present set-up, materials and conditions. Without being sonicated, microspheres naturally assemble into agglomerates. The agglomerate was tracked every 10 seconds over a period of 20 minutes (**Fig. 6.1**). The diameter of the imaged agglomerate was

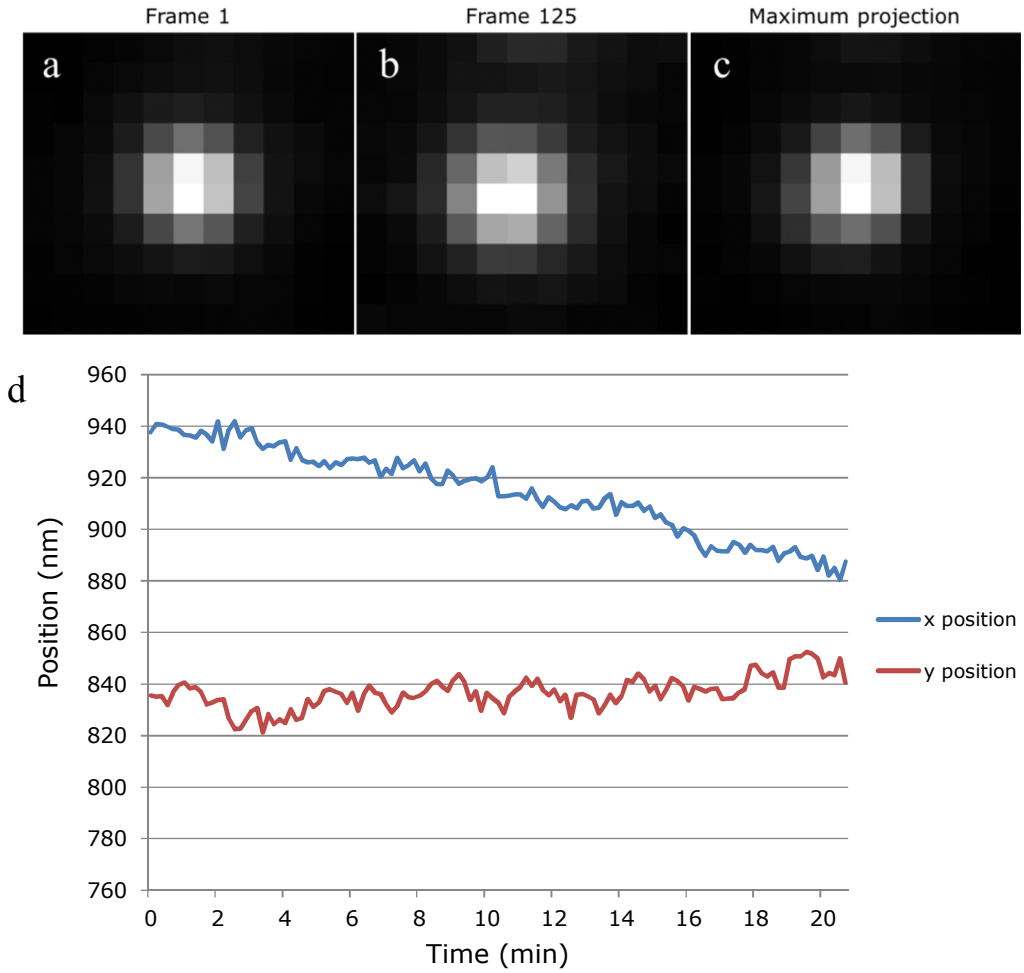

Figure 6.1. Estimation of lateral drift. The centre of an aggregate of 20-nm fluorescent microspheres measuring around 300 nm in diameter was tracked over a period of 20 minutes – more than a sufficient timeframe within which to acquire a large STORM stack. (a) The first and (b) last frame of the image sequence. (c) A maximum projection of all of the collected frames. (d) A plot of the *x* and *y* coorinates of the centre position of the aggregate. The systematic deviation of the traces announces the presence of drift in the system. A drift of about 60 nm is expected within a period of 20 minutes.

determined by measuring its full-width at half-maximum (FWHM), which was 407 nm in the *x*-direction and 370 nm in the *y*-direction, and comparing it to the FWHM expected from a point source: ~191 nm. Since the radius of the agglomerate image is equal to the square-root of the radii of the PSF and the actual agglomerate added in quadrature (as dictated by the rules of convolution), it follows that the aggregate was approximately 338 nm in diameter. Subsequently, a bleach correction macro for ImageJ, released by the European Advanced Light Microscopy Network (EAMNET), was utilised to process the amassed data and homogenise the aggregate's intensity over time. Following this, a maximum projection was performed on the whole stack (**Fig. 6.1c**). The bleaching correction was carried out in order to ensure that the result of the maxi-

mum projection is fair, and that the latter part of the stack is not under-represented due to bleaching.

To measure the *x*- and *y*-drift of the particle during the acquisition, a Matlab script was written (*x*-*y* drift estimation, Appendix B) to locate the centre of the particle in each frame using a least-squares fit to a 2D Gaussian distribution. The centre positions were then plotted as a function of time (**Fig. 6.1d**). Clearly, the drift measured was not negligible (60 nm over the course of 20 minutes) and was taken into consideration in the ensuing experiments.

6. 2. Numerical simulation of camera response and sensitivity to single molecules

At the outset, I was faced with two cameras, one of which had to be incorporated into the custom-built super-resolution microscope set-up. The available cameras were Hamamatsu EMCCD front-illuminated C9100-02 with a pixel size of 8-μm, and Hamamatsu ImageEM back-thinned and -illuminated EMCCD C9100-13 with 16-μm pixels. The effective pixel sizes after demagnification from the microscope objective (*i.e.* in the sample plane) are, respectively, 80 nm and 160 nm. According to [Thompson *et al*, 2002], the pixel size should be comparable to the standard deviation of the PSF of the molecule. According to the Nyquist criterion, the pixel size should be no larger than the Nyquist sampling distance. The two statements are, in fact, equivalent. The standard deviation of the PSF in this case is approximately 81 nm. This figure was calculated using the equation for the standard deviation of a Gaussian, s_{Airy}, most closely approximating an Airy pattern, which is derived by minimising the difference between the Airy and Gaussian functions through the least-squares criterion [Zhang *et al.*, 2006][Zhang *et al.*, 2007]:

$$s_{Airy} \approx 0.225 \cdot \frac{\lambda_{em}}{NA},$$

where λ_{em} is the emission wavelength and *NA* is the numerical aperture of the objective. This equation applies to a widefield microscope and a high-*NA* objective. The Nyquist sampling interval, calculated using Abbe's equation for lateral resolution (**Table 2.2.3.3.1.2)**, is 89.5 nm in this case. Thus, from theoretical considerations, C9100-02 (with effective pixel size of 80 nm) adhered more closely to both guidelines and should therefore be the better choice; however, in practice, other factors, such as the enhanced quantum efficiency and superior readout noise handling could tip the balance in favour of the C9100-13. With a mixture of advantages and drawbacks to each camera, it was not immediately possible to decide whether the superior sen-

sitivity, lower detection limit and higher dynamic range (~14,800 compared to ~7,000 intensity steps for C9100-02) of the C9100-13 camera would override its suboptimal pixel size.

In order to compare the performance of each camera in the scope of super-resolution, a computer simulation was written in Matlab (MathWorks, Natick, MA, USA) to test their localisation precision under the experimental conditions (Single-molecule localisation, Appendix B). Alexa Fluor® 488 was selected for the ensuing experiments due to its extremely high quantum yield, short emission wavelength, appropriateness to the laser sources and ready availability in the laboratory. The first two reasons for choosing Alexa Fluor® 488 listed above ensure a high SNR and high localisation precision, because localisation error scales inversely with the square-root of the number of photons collected (**Eq. 2.2.5.3**, Background and Theory chapter) and shorter wavelengths experience less diffraction, meaning that they produce a more tightly focused PSF.

In brief, a single Alexa Fluor® 488 molecule was modelled as a point source projected on the sensor of each camera. The position of the simulated diffraction-limited spot was shifted systematically across a single camera pixel and a simple localisation algorithm was applied to find its centre coordinates after each shift. The fluorophore was mimicked by a diffraction-limited spot: the Fourier transform of the image was calculated as the Fourier transform of a point source multiplied by the modulation transfer function (the Fourier transform of the objective pupil function). The microscope system forming the image was assumed to be free of aberrations and its resolution to be hindered solely by the diffraction limit. The numerical aperture of the objective was represented using scalar theory by the analytical expression for a low-NA objective (*i.e.* the paraxial approximation). The paraxial theory of diffraction for a converging beam begins to become invalid at NA of around 0.7 [Sheppard *et al*, 1987]. This decreased the fidelity of the simulation to the real-life situation, however, this is not expected to have a significant effect on the results of this study, since scalar theory only neglects high-order PSF lobes which are ordinarily too dim to be detected in any case. Polarisation effects were also neglected as a result. Pixel noise, a signal response inhomogeneity arising from variation in the sensitivity of the individual pixels, was also ignored. In addition, no out-of-focus positioning of the point source was simulated. Hot pixels were not incorporated in the simulation either, since these are very rare events when the cameras operate at their designated temperature, which is reached and maintained through thermoelectric cooling.

In the process of gathering a STORM image sequence, one would normally encounter fluorophore blinking at different depths in the specimen; those events which are outside the focal plane of the objective will be detected as dimmer PSFs with a further in-plane spatial reach, making them more difficult to localise accurately. Neglecting the occurrence of defocused PSFs in this case was justified however, since all imaging was carried out in the TIRF configura-

tion, which visualises fluorophores only within a thin slice much thinner that the depth of field of the objective.

A single fluorescence excitation cycle lasts on the order of a nanosecond. A typical camera frame acquired during super-resolution imaging would integrate signal over a period of time six orders of magnitude longer than that. The photon flux (number of photons per second) emitted during this time is given by the following formula [Hinterdorfer *et al.*, 2009]:

$$F = \Phi \cdot \frac{P}{E_\gamma} \cdot \sigma. \qquad \textbf{Eq. 6.1}$$

In the above equation, Φ is the quantum yield of the dye, P is the laser power density (in units of Wcm^{-2}), E_γ is the energy of one emitted photon (in joules), and σ is the absorption cross-section of the dye (in cm^2). E_γ can be calculated from the equation

$$E_\gamma = h \cdot \frac{c}{\lambda},$$

where h is Planck's constant and λ is the peak emission wavelength; the value of σ can be obtained from the Beer-Lambert law:

$$\sigma = 1000 \cdot \frac{ln(10) \cdot \epsilon}{N_A},$$

where ϵ is the molar extinction coefficient of the dye in $M^{-1}cm^{-1}$ (also called absorptivity), and N_A is Avogadro's number. σ represents the probability of the electromagnetic absorption process. The quantum yield and extinction coefficient were obtained from the Molecular Probes® handbook. The number of photons arriving at the detector depends on the camera exposure time, also known as camera integration time. Thus, the total number of photons spread over the diffraction-limited spot was set to equal the product of the flux (**Eq. 6.1**) and the exposure time.

The optical detection efficiency of the set-up, expressed predominantly with the notation found in [Kubitscheck *et al.*, 2000], is given by:

$$\eta_{total} = \eta_{NA} \cdot T_{obj} \cdot T_{fc} \cdot T_{TL} \cdot T_{cw} \cdot Q_{CCD}, \qquad \textbf{Eq. 6.2}$$

where η_{NA} is the collection efficiency of the objective lens, which is proportional to the maximal collection angle, T_{obj} is the transmittance of the objective lens, T_{fc} is the transmittance of the filter cube (including beam splitter and emission filter), T_{TL} is the transmittance of the tube lens, T_{cw} is the transmittance of the camera window, and Q_{CCD} is the quantum efficiency of detection of the camera sensor [Kubitscheck *et al.*, 2000][Chiu *et al.*, 2001]. The total efficiency for the

present set-up for transmitting Alexa Fluor® 488 emission (peak wavelength, 519 nm) was evaluated to be approximately 10.5% using the C9100-13 camera for detection, and 6.3% using the C9100-02 camera.

Photon noise was added in the form of a random number drawn from a Poisson distribution with a mean equal to the pixel value in the absence of noise. Background noise arising from readout noise, dark current in the camera electronics, autofluorescence from the specimen and fluorescent dust on the microscope optics was assumed to obey a Gaussian distribution. Autofluorescence and fluorescent dust are the sources which actually have a Poisson distribution, since they are due to light emission; however, readout noise and dark current are Gaussian processes. The mean of the distribution was set to the average value in a region of a real data frame of a typical cellular specimen where no objects were apparent, with the signal obtained of the specimen with the illumination source switched off subtracted. In a typical measured STORM acquisition, the background level decreased by about 18 photons throughout the entire course of recording. In view of the constantly changing level of background encountered during acquisition, the static model of the background was given a mean value equal to the average of the background found in the first and last frame of the STORM frame sequence. The observed decrease in extraneous fluorescence with time can be attributed to the steady bleaching of autofluorescence from the cell. Biological compounds known to cause cellular fluorescence are, for instance, flavins and porphyrins [communication by J. A. Kiernan in Histonet Archive, http://www.histosearch.com/histonet.html].

The molecule was systematically moved along a regularly spaced 2D grid of 501 × 501 positions across the area of one pixel, and was localised after each position shift. An odd number of positions was chosen in order to evaluate the localisation precision at the exact centre of the pixel. The diffraction-limited spots were fitted consecutively and in an iterative manner as follows. First, a centroid algorithm was applied, which located the centre of intensity of the spot. Similar to finding the centre of mass of an object, except changing the physical quantity from mass to intensity, this algorithm works by calculating the average of the pixel coordinates, weighted by the pixel intensity:

$$\boldsymbol{r}_C = \begin{cases} x_C = \dfrac{\sum_{i=1}^{M} x_i I_i}{\sum_{i=1}^{M} I_i} \\ \\ y_C = \dfrac{\sum_{i=1}^{M} y_i I_i}{\sum_{i=1}^{M} I_i} \end{cases},$$

where (x_i, y_i) are the coordinates and I_i is the intensity of pixel i, and M is the total number of pixels included in the calculation (as will be explained in the next sentence). These coordinates

are subsequently input as the means for the *x*- and *y*-components of a 2D discretised Gaussian function which is then used as a Gaussian mask (**Fig. 6.2.1**), thereby selecting only a part of the image, with total number of pixels *M*. A discretised Gaussian mask is used in certain localisation algorithms to select the area of the image containing the photon burst from a single-molecule emitter (a procedure known as 'segmentation'), which is why it was used here. The Gaussian mask was assigned a fixed standard deviation and the centroiding routine iterated ten times, in order to improve the localisation precision as much as possible. The standard deviation of the Gaussian mask was initially set to s_{Airy}, believing it to be the optimal value; however, after some

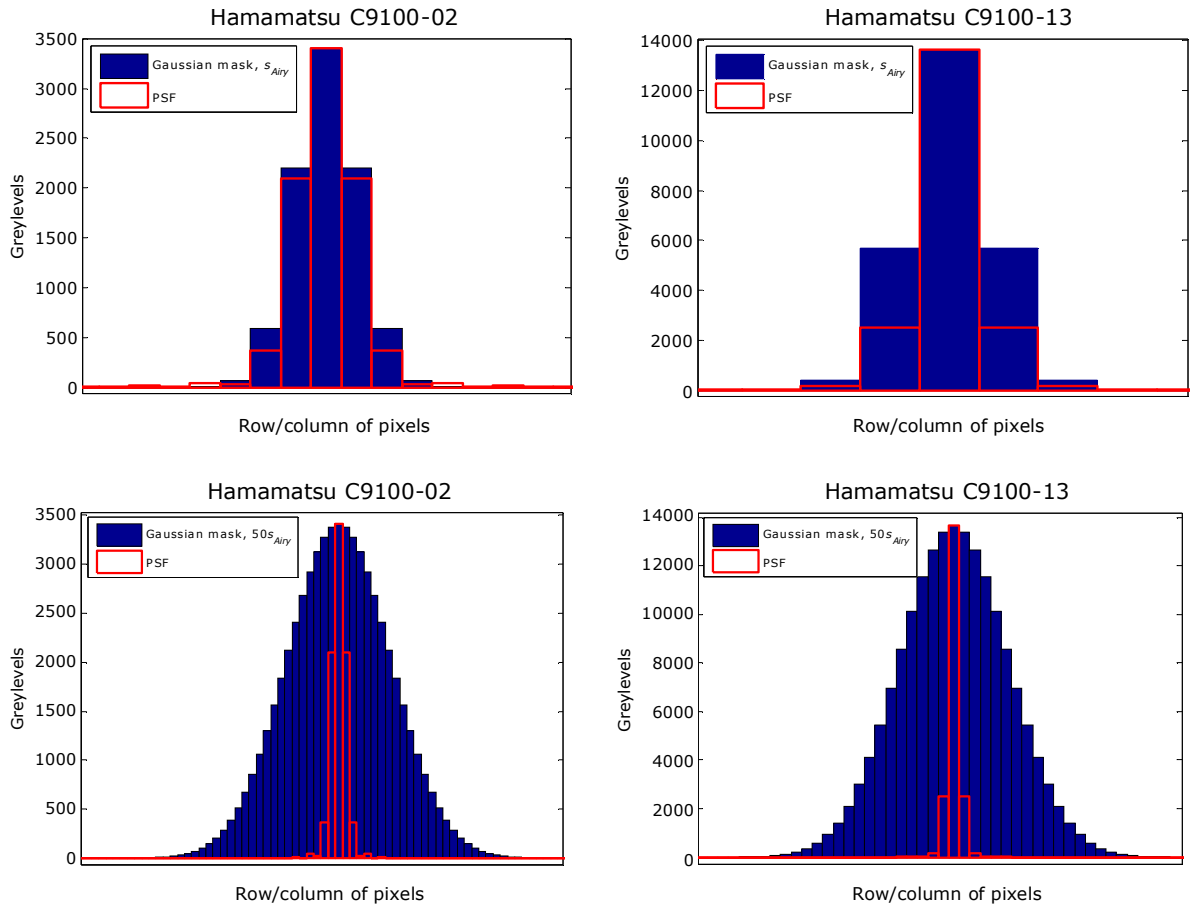

Figure 6.2.1. Computer-generated illustration of two different choices of Gaussian mask width used for determining the size of the selected region containing signal from a single molecule that is subsequently localised. The size of the mask has an impact on the accuracy of the localisation. The hollow red histograms exemplify the expected photon distribution from an Alexa Fluor® 488 molecule as would appear on the Hamamatsu C9100-02 (left) or C9100-13 (right) camera detectors. A Gaussian mask (blue bars) with a least-squares fit to the PSF is shown on the top row. Note the side lobes of the PSF, clearly visible in the C9100-02 image, remain unencompassed by this mask. The actual standard deviation of the Gaussian used in this work, which enabled the most precise localisation, was fifty times wider (bottom row). Inadvertent distortion of the shape of the PSF by noise in real-life situations has been neglected here for the sake of clarity.

trial and error, it was established that a standard deviation fifty times this width yielded the most precise localisation. For this reason, the Gaussian mask standard deviation was set to $50 \times s_{Airy}$. The cause of this unexpected finding is most likely that wider Gaussians include information contained in the first maximum of the PSF which is important for accurate localisation.

Naturally, a full Gaussian least-squares fit to a Gaussian distribution presents a more accurate localisation method than finding the centre of mass and overlaying the image with a fixed Gaussian mask. This is because, unlike the Gaussian mask, the least-squares minimisation algorithm is more flexible in dealing with photon-counting noise, since it allows for the proper weighting of the terms [Thompson *et al.*, 2002]. However, Gaussian least-squares fitting is more computationally expensive – especially in combination with the high sampling frequency employed to investigate faithfully the dependency of localisation accuracy on object position (as shall be explained further below). The latter becomes prohibitively time-consuming – hence settling on the Gaussian mask method instead.

A flowchart of the complete algorithm is shown in **Fig. 6.2.2**.

Fig. 6.2.3 and **Fig. 6.2.4** show that the localisation algorithm works correctly, since the localisation precision is very high (within10^{-12} and 5×10^{-4} nm, respectively, for the Hamamatsu C9100-02 and C9100-13 cameras.) The root-mean-square (RMS) error for C9100-02 is 0.41×10^{-12} nm, whereas for C9100-13 it is 0.345×10^{-3} nm. It is interesting to note that, despite C9100-13's superior quantum efficiency, the precision limit with this camera escalates nearly 10 magnitudes above that of its front-illuminated counterpart. This is most likely a purely numerical effect: in order to obtain the image on the large-pixel C9100-13 camera, unlike with the small-pixel C9100-02, there is an additional step of 2-by-2 binning that is carried out to simulate pixels with four times the area. This coarse-graining procedure possibly introduces an infinitesimal shift in the true position of the fluorophore, compared to its intended position. On the other hand, the worse performance of C9100-13 may be a direct consequence of the fact that the Nyquist criterion is not satisfied. In any case, since the localisation precision despite this perturbation is more than satisfactory (on the order of a pm), no attempt was made to seek out the true nature of the cause.

Another feature of interest in **Fig. 6.2.3** is the simple, repetitive localisation error pattern seen for C9100-13, in contrast to the highly complex localisation pattern for C9100-02. The existence of a pattern itself is due to the varying degrees of success in matching the pixelated PSF with the Gaussian localisation mask. Notably, the discrepancies are lowest in cases where the photons from the object are distributed symmetrically across the pixels – such as in the centre, corners and midway between the vertices of pixels. It was found that changing the sampling frequency (*i.e.* reducing the density of points in the grid) usually changed the peak and RMS error. The explanation for this may be that the underlying error pattern is considerably complex,

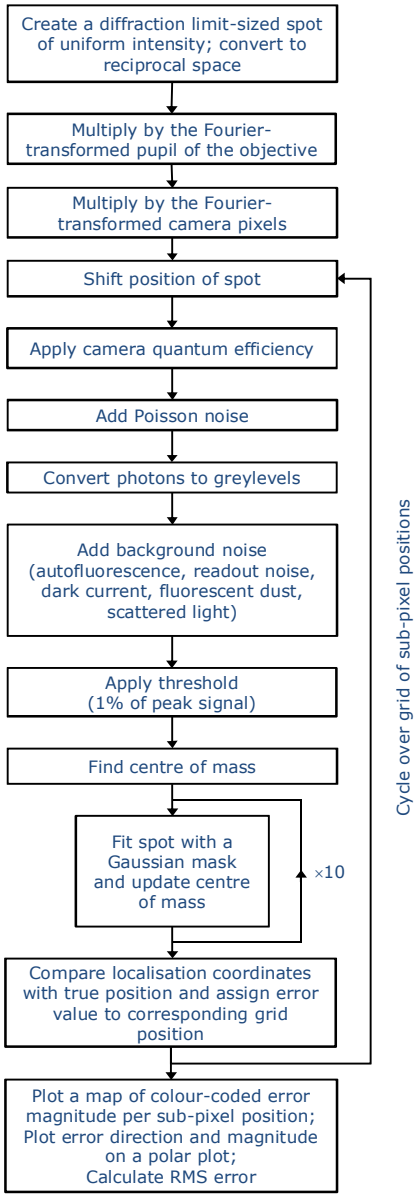

Figure 6.2.2. Flowchart of the algorithm used to decide which of two EMCCD camera candidates is more suitable for super-resolution imaging. The deciding factor is the magnitude of the localisation error. The algorithm begins by simulating an image of a point emitter separately on each camera chip, taking into account the intensity modulation of the objective and the integration of signal effected by the EMCCD pixel array. The emitter is centred on a known position of each camera chip. Next, the cameras' specific noise and quantum efficiency characteristics are imparted on the two separate images, together with statistical (Poisson) and ambient and measurement (background) noise. Pixels from the image above a certain threshold are then selected to locate the approximate origin of the photon burst, whereupon 10 iterative fits with a Gaussian mask pinpoint the coordinates of the emitter. The estimated coordinates are then compared with the emitter's true position, the difference recorded, and the process is repeated with the emitter moved to a different position. The routine stops once the emitter's position has been 'scanned' two-dimensionally and equidistantly across the face of one pixel. The collected error data are then plotted as a function of position (**Fig. 6.2.3** and **6.2.5**) and direction (**Fig. 6.2.4** and **6.2.6**). The overall RMS localisation error for each camera is also calculated (refer to main text).

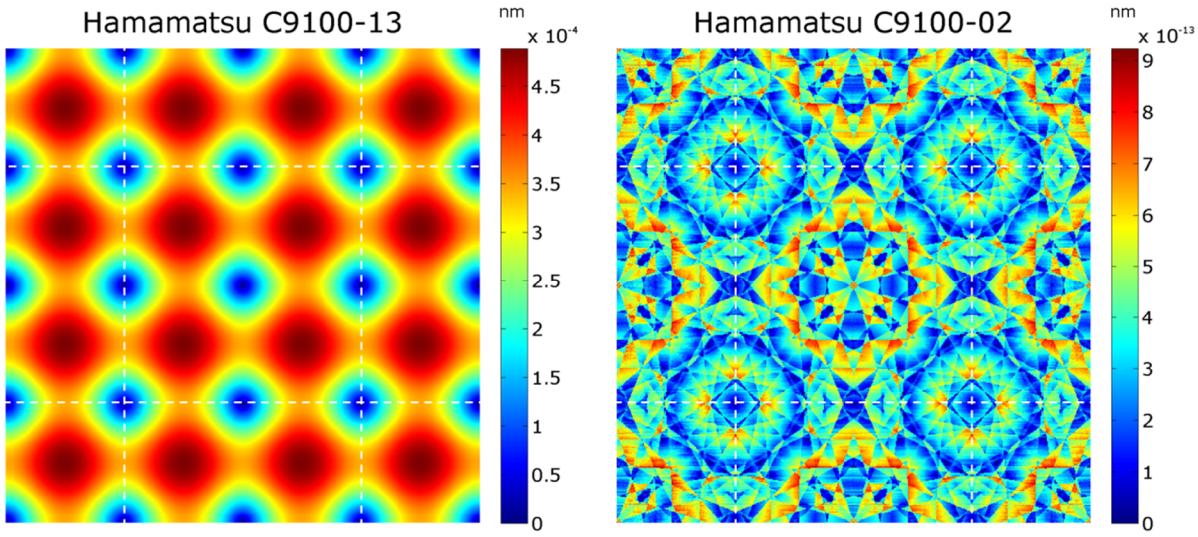

Figure 6.2.3. Localisation precision in the absence of noise sources. Depicted is part of the pixel array of candidate cameras for super-resolution imaging. The colour coding signifies the magnitude of the localisation error produced when a subdiffraction limit-sized object centred at the same location is localised, in the absence of signal distortion from various noise sources. Colour bar in units of nm. Dashed white lines demarcate the boundaries of individual pixels.

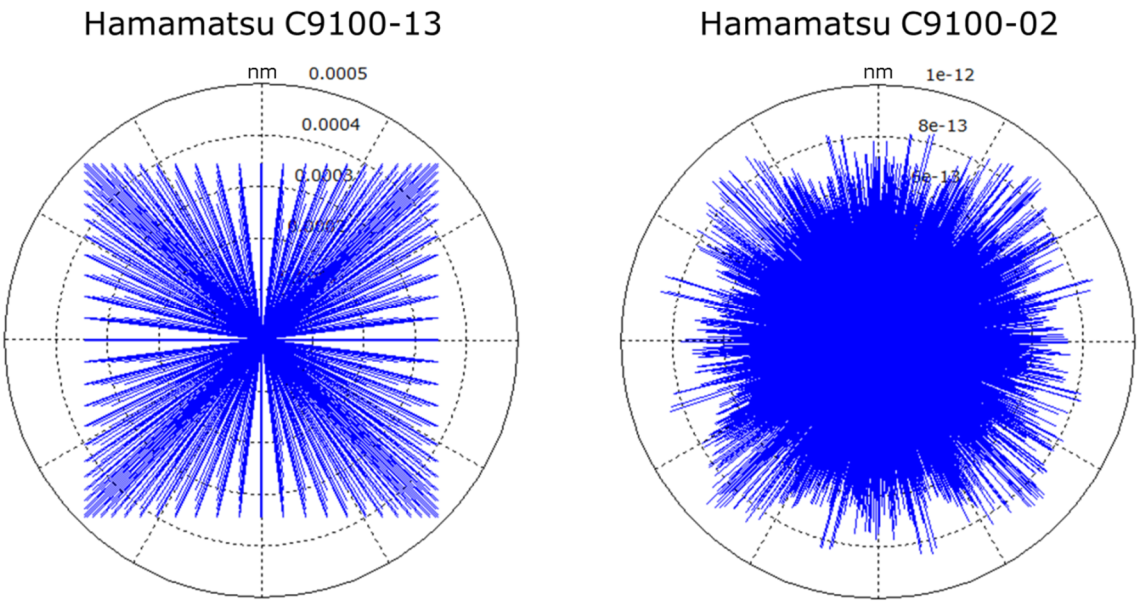

Figure 6.2.4. Localisation error distribution in the absence of noise sources. This figure depicts the magnitude and orientation of the localisation error plotted for all positions of a single-molecule object relative to a pixel. The patterned structure indicates that some positions preferentially lead to reduced or heightened localisation precision. This is a consequence of the finite size of the pixels. The plot on the right is not perfectly symmetrical due to the localisation precision approaching the precision limit of the floating point numbers used in the computer programme. Units are nm.

and that selecting a certain small subset of positions within the pixel would not fully explore the areas with relatively low or relatively high error, in order to give a true-to-life average. For this reason, the sampling frequency was increased as much as possible – within the limits of a reasonable timeframe for computational result delivery.

The patterns of localisation appear to be different; however, deliberately reducing the localisation precision of the C9100-02 to fall in the picometre range (similar to the C9100-13) by choosing a suboptimal standard deviation for the Gaussian mask (resulting in loss of information) yields a nearly identical mapping of the localisation error as that for C9100-13 in **Fig. 6.2.3** (data not shown). This suggests that pixel size is not involved in determining areas of low- or high-precision localisation within the pixel itself (although the choice of pixel size may affect the ratio of one to the other for a given imaging area.)

Confident that the localisation algorithm was correctly implemented, Poisson noise and background noise specific to each camera were added to the routine and the same localisation experiment run again. With approximately 47,000 photons per event, localisation with the C9100-02 camera yielded an RMS error of 2.3 nm, and the C9100-13, a slightly higher RMS error of 3.3 nm. These figures are averages obtained from at least three different simulation runs, since the numerical model of noise is random and generates a slightly different noise distribution each time. In agreement with these results, according to **Eq. 2.2.5.3**, the expected localisation precision would be 0.37 nm.

The pattern of localisation precision disappeared, apparently buried beneath the noise (**Fig. 6.2.5** and **Fig. 6.2.6**.) Visual analysis of plots of the directional error generated during each localisation (**Fig. 6.2.6**) indicated that the addition of noise had indeed obliterated the positional bias. Simultaneously, this observation serves as evidence that the localisation algorithm implemented here is devoid of systematic errors.

The simulation demonstrated that both cameras are suitable for super-resolution and capable of sub-nanometre localisation. Taking into account that a fluorescent emitter labelling a molecule of interest cannot occupy the same space as the molecule itself, and that therefore the molecule and emitter are separated by a finite distance (**Fig. 6.2.7**), a localisation precision of such magnitude is completely sufficient for the imminent task. The C9100-13 camera was selected for the super-resolution experiments for convenience, since C9100-02 was already part of another microscope set-up.

The figures obtained for the RMS localisation uncertainty are plotted together with the expected errors in **Fig. 6.2.8**. The theoretical prediction of the localisation error in **Eq. 2.2.5.3** was plotted twice, with the background profile and pixel-size characteristics of each camera.

Localisation of a point source using a Gaussian mask is associated with a 30% excess error, compared to the theoretical trend [Thompson *et al.*, 2002]. This deviation has been ascribed

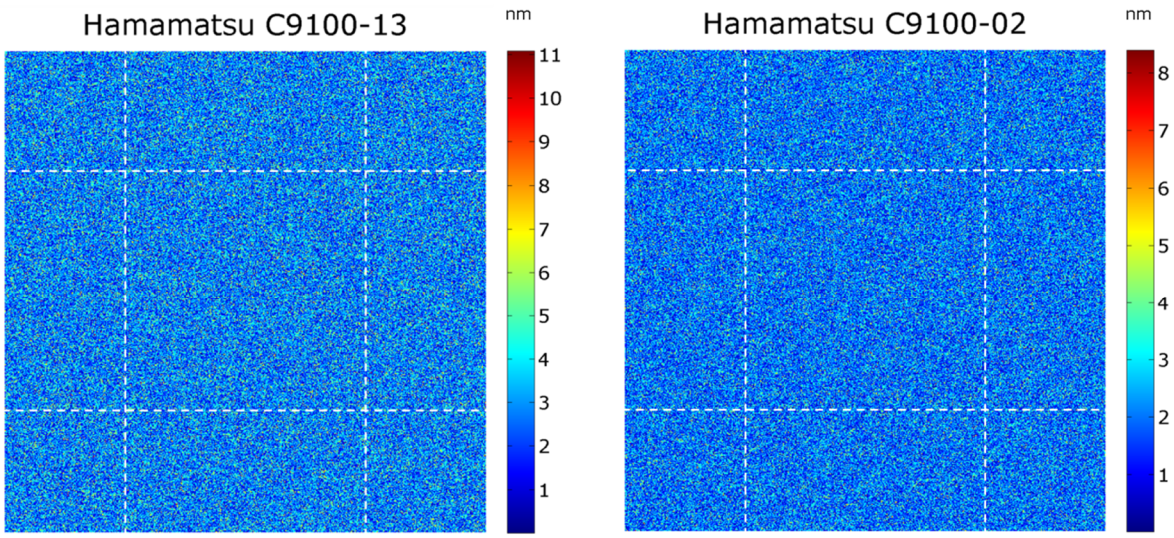

Figure 6.2.5. Localisation precision in the presence of noise sources. Depicted is part of the pixel array of candidate cameras for super-resolution imaging. The colour coding signifies the magnitude of the localisation error produced when a subdiffraction limit-sized object centred at the same location is localised, in the presence of signal distortion from various noise sources. Colour bar in units of nm; note the different colour scales. Dashed white lines delineate the boundaries of individual pixels.

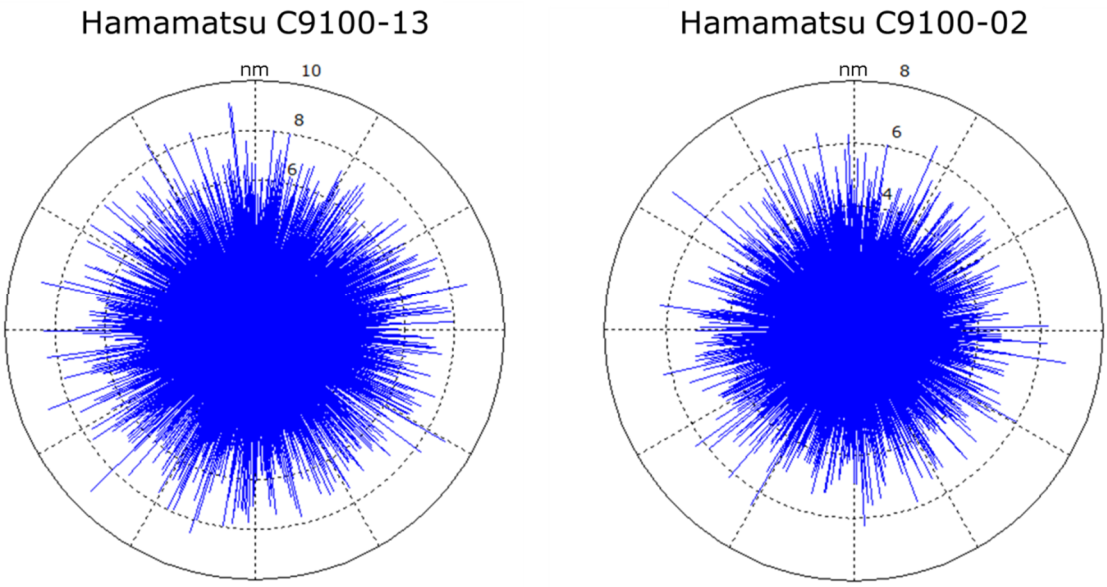

Figure 6.2.6. Localisation error distribution in the presence of noise. The plot shows the randomised nature of the localisation error produced with our own custom-written localisation algorithm. The lack of a distinctive pattern indicates that localisation precision is directionally unbiased.

by the authors of [Thompson *et al.*, 2002] to various imperfections in the model and fitting, including analytic interpolation between the photon-counting noise and background noise-defined limits, assumption of an infinitesimal pixel size and first-order approximations of the error, on the part of the theoretical expression, and disregard for photon-counting noise on the Gaussian mask fit's part.

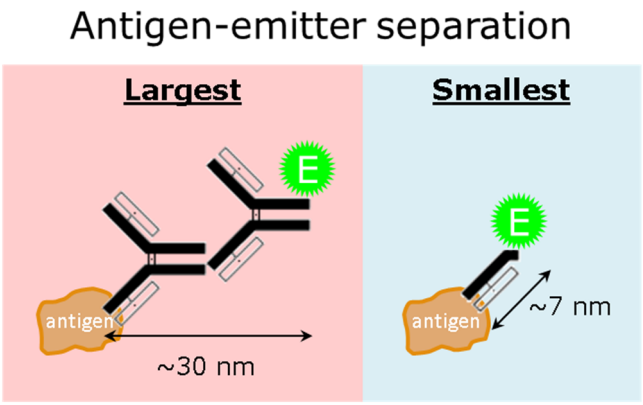

Figure 6.2.7. Separation distance between an antibody-conjugated fluorescent emitter and the antigen it represents. Immunolabelling of the antigen can be carried out in several different formats. Indirect labelling with primary and secondary antibodies leads to a large antigen-emitter separation distance, whereas direct labelling with a fluorophore-conjugated Fab fragment minimises this separation.

Disagreement between the outcome from the simulation (**Fig. 6.2.8**, asterisk data points) and the theoretical curve was observed, with a tendency of overestimation on the part of the computational results. The discrepancy cannot be attributed to stochasticity, since the simulation is a Monte Carlo experiment, and therefore any variability should have disappeared through repeated averaging. One plausible explanation, however, is the different optical gathering efficiency of the cameras: C9100-13 loses fewer photons to absorption, scattering and reflection. The theoretical model does not take this into account, hence resulting in a deviation from the trend line.

Another difference between the theoretical model and the numerical simulation described here is that in the former, the background is represented by an unwavering 'noise floor', whereas *in silico* it was given a Gaussian distribution with a certain variance (the variance measured in a dark frame). Running the simulation with constant background gives a substantially lower localisation precision (**Fig. 6.2.8**, circular data points). Largely consistent with these expectations, the computationally derived error for C9100-02 lay within 30% of the expected value, and for C9100-13, the deviation was 63% from the expected amount. This indicated that the additional fluctuation in the background evidently deteriorated the performance of the localisation algorithm immensely.

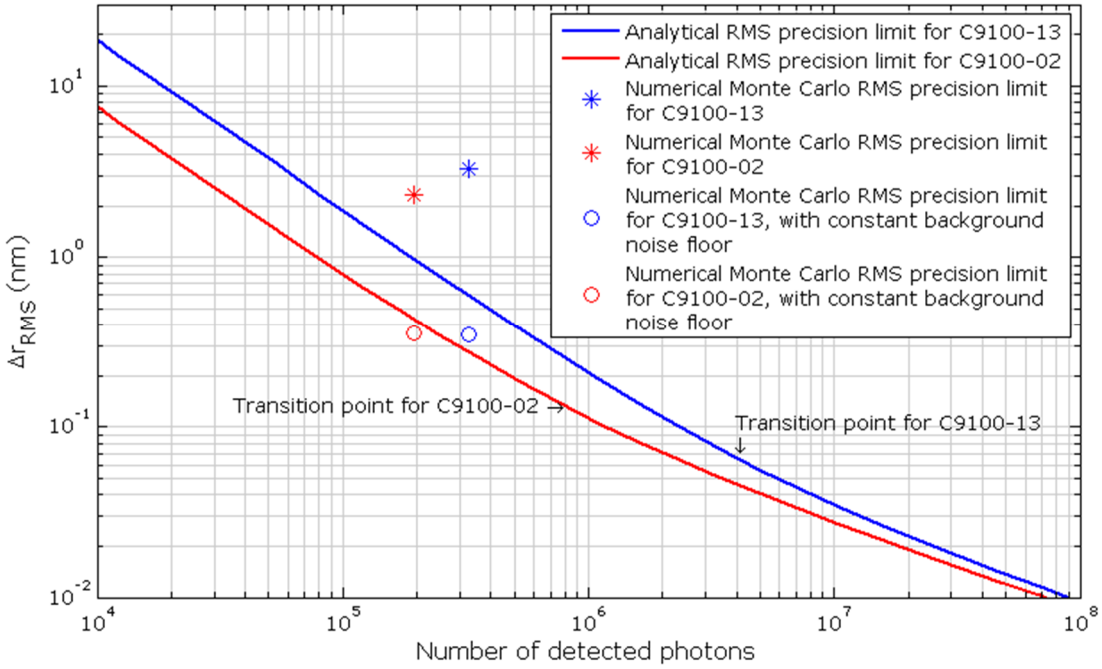

Figure 6.2.8. Analytical localisation precision as a function of detected photon number. This graph shows the theoretical prediction of the RMS localisation error, depending on the number of photons comprising the PSF of a single molecule. The theoretical closed-form expression was obtained from eq. (17) in [Thompson *et al.*, 2002] and was plotted with the parameters of the Hamamatsu C9100-02 and C9100-13 cameras. The lone data points indicate the localisation errors derived with the Monte Carlo simulations in the present work, obtained for the same number of incident photons. The impact of quantum efficiency of the cameras is not shown on this graph; however, given that this quantity is much lower for C9100-02, this puts it at an even deeper disadvantage, compared to C9100-13. The crossover points between the shot noise-limited case and the background noise-limited case are indicated with an arrow. Background fluctuation tends to be the major noise contributor in the low-photon case, whereas shot noise dominates at higher photon numbers.

6. 3. Assessment of PFA fixation on the cell permeabilisation state

It is important to stain only the Shh present on the exterior membrane of the cell and avoid Shh dwelling inside the cell body. For this reason, it was investigated whether PFA could permeabilise the cells.

A strain of HEK293 cells with improved adherence to glass, a quality selected for by cultivating the cells on glass coverslips, were indirectly immunostained for calnexin, as described in the Materials and Methods chapter. Calnexin is a transmembrane ER protein with a cytoplasmic C-terminal tail and a lumenal N-terminal domain; these termini were recognised by

rabbit pAb and mouse mAb, and detected with anti-rabbit IgG H + L Alexa Fluor® 555 and anti-mouse IgG1 Alexa Fluor 488®, respectively. Fluorescence imaging confirmed that the fixation process had not permeabilised the cells, as is evident by the lack of calnexin staining – both on the outer membrane and lumen of the ER (last row of **Fig. 6.3**). Triton X-100 treated cells served as controls to show that, if the cells were permeabilised, calnexin would indeed be detected (first row of **Fig. 6.3**). Triton permeabilises both the plasma membrane and ER membrane. A control for semi-permeabilisation was also conducted using digitonin. Treatment with the detergent digitonin, when used at an appropriately low concentration, selectively disrupts the cell membrane but spares the membrane of the ER to some extent [Le Gall *et al.*, 2004]. Consistent with the expectation, upon exposure to digitonin, C-terminal calnexin staining, but no N-terminal staining, was observed (**Fig. 6.3**, middle row).

6. 4. Validation of the STORM technique

Prior to embarking on an investigation of the biological question of Shh multimerisation, good practice dictates that the credibility of the outcome achieved with super-resolution be established first. Commonly, this involves carrying out super-resolution imaging on a well-characterised, predictable structure – for instance, microtubules or actin filaments [Heilemann *et al.*, 2009][Henriques *et al.*, 2010]. Consistent correspondence between the super-resolved image and the underlying structure in a conventional widefield snapshot effectively validates the technique and endorses the application of its principle on other, as yet uncharacterised, protein assemblies.

6. 4. 1. Optimisation of imaging conditions for STORM

Due to difficulties with handling HEK293 cells in preparation of super-resolution – in particular, losing the majority of the cell population through involuntary detachment – the model system was changed to COS-7 African green monkey kidney fibroblast cells, which withstood well the rigorous washing steps in between antibody incubations needed to minimise background fluorescence.

Microtubules in COS-7 cells were stained with anti-tubulin mAb coupled to an IgG1 Alexa Fluor® 488 secondary antibody, as described in the Materials and Methods chapter. Surprisingly, it was found that illumination intensities as low as at the threshold of lasing stability,

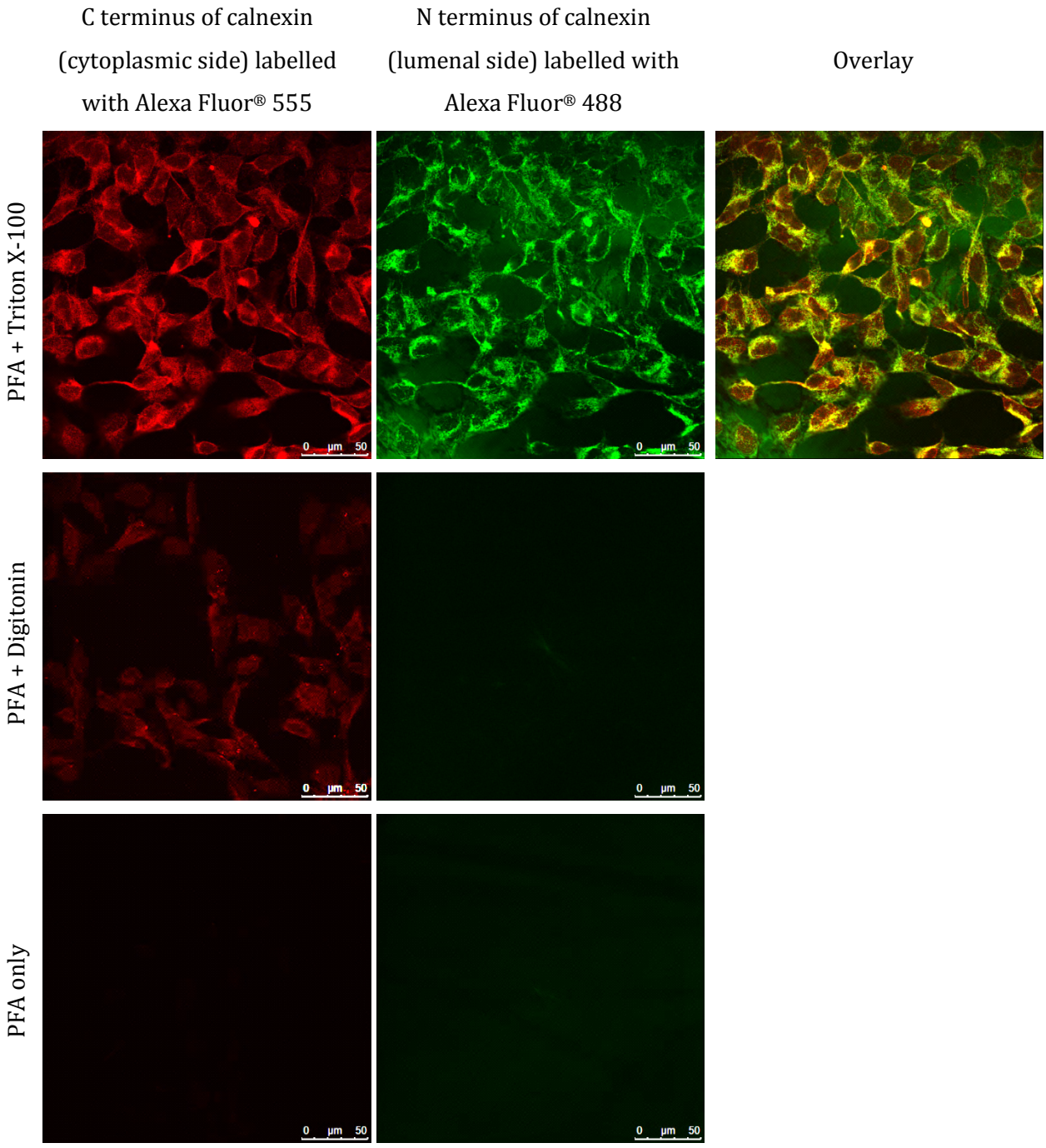

Figure 6.3. Paraformaldehyde (PFA) does not permeabilise the plasma membrane of the HEK293 cell line. Calnexin is an ER transmembrane protein with its N terminus located in the ER lumen and its C terminus in the cytoplasm. Indirect immunostaining of the N terminus with a mouse mAb, detected with Alexa Fluor® 488, and the C terminus with a rabbit pAb detected with Alexa Fluor® 555 indicates that paraformaldehyde leaves the plasma membrane intact. Triton X-100 fully permeabilises the plasma and ER membranes (top row). Digitonin selectively permeabilises the plasma membrane only (middle row). PFA alone does not permeabilise either membrane (bottom row). All micrographs were taken with the same microscope settings (including gain and offset), and their display brightness is increased here by 40% for the sake of improving their visibility.

in the presence of the redox imaging buffer, were sufficient to induce photoswitching – at least in Alexa Fluor® 488. No clear correlation between laser power and the quality of the STORM frames and reconstruction was observed (**Fig. 6.4.1.1**), contrary to the expectation that stronger photon stimulation would produce a better SNR. The choice of containment of the sample, however, appeared to make a distinct difference: MatTek® glass-bottomed dishes contributed less background (**Fig. 6.4.1.1**) and enabled prolonged switching, compared to glass coverslips. The latter is easily explained by the observation that larger volumes of imaging buffer, as can be accommodated by a MatTek® dish but not entrapped between microscope slide and coverglass, affords the correct stoichiometry for the reactants to engage with the fluorophores within the sample.

Reconstructions were carried out with the open-source software packages *QuickPALM* and *rapidSTORM* [Henriques *et al.*, 2010][Wolter *et al.*, 2012].

QuickPALM operates as follows:

1) The amount of noise in the image is estimated by calculating the standard deviation within a region of 13 × 13 pixels centred on the minimum-intensity pixel in the image. An assumption is made that, due to the stochastic, low-density photoswitching of the molecules, the probability of an activated molecule being present within the boundaries of this square is low.

2) A band-pass filter is applied, which simultaneously reduces stochastic noise and corrects for background intensity. The band-pass filtering is executed by removing intensity fluctuation occurring on a scale smaller than the size of the image pixels by convolving the original image with a Gaussian kernel of standard deviation 0.5 pixels, and subtracting from it the result of a convolution of the original with a Gaussian kernel of standard deviation twice the FWHM entered by the user, in order to remove baseline fluorescence.

3) An iterative procedure follows, known as the Högbom 'CLEAN' method [Högbom, 1974], whereby the maximum-intensity pixel in the image is selected, together with its neighbours within a square window of size twice the user-input FWHM, only if their values exceed a minimum-intensity threshold relative to the local peak intensity.

4) The spot is tested for several conditions, before it is accepted. The SNR of the spot should exceed the minimum SNR imposed by the user; SNR is calculated as the ratio of the mean intensity of the selected pixels and the standard deviation of the noise. The spot is rejected if its intensity profile is truncated by an image edge, if any saturation of the pixel values is detected, if it does not satisfy the symmetry assigned by the user, or if an already analysed region of interest overlaps with the pending region [Henriques *et al.*, 2010, Supplementary Note 1].

Localisations performed by *rapidSTORM* follow the protocol below:

1) Input images are smoothed to reduce noise.

2) Local maxima are registered and stored as potential spot candidates.

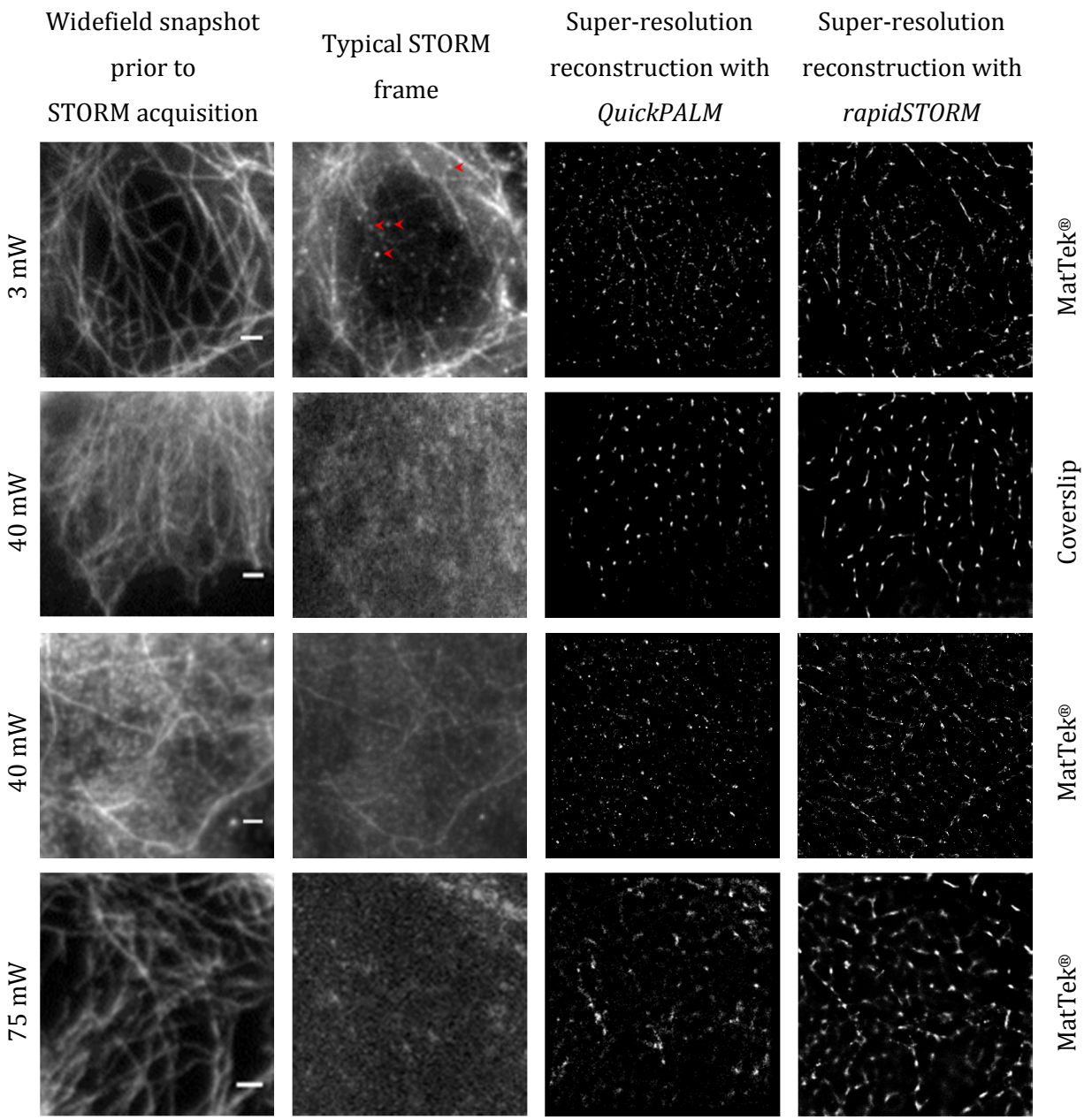

Figure 6.4.1.1. STORM reconstruction dependence on laser power and method of sample containment. Laser illumination intensity appears to have little effect on the quality of reconstructions of Alexa Fluor® 488-labelled microtubules in COS-7 cells. However, mass fluorophore inactivation with incremental increase of laser power is clearly evident. MatTek® glass-bottom dishes guarantee lower noise contamination of the fluorescence signal, compared to coverslip mounting. Reconstructions were carried out using open-source software *QuickPALM* [Henriques *et al.*, 2010] and *rapidSTORM* [Wolter *et al.*, 2010][Wolter *et al.*, 2012]. All imaging was performed with the sample immersed in a buffer of phosphate buffered saline (PBS) with 100 mM β-mercaptoethylamine (MEA), as prescribed in [Heilemann *et al.*, 2008]. Red arrowheads indicate photoswitched molecules. Scale bar: 2 μm.

3) The list of candidates is interrogated, beginning with the brightest value, whereupon the candidate is fitted non-linearly with a PSF model. The PSF model consists of a two-dimensional Gaussian function elevated over a pedestal of background signal. The parameters fitted by the algorithm are the amplitude, background signal and centre position.
4) Attempts to fit successive candidates cease in the event of failure of three consecutive candidates to satisfy the fitting requirements.

RapidSTORM assembles a super-resolution image by forming a localisation density map on a lattice of a user-defined pixel size through linearly interpolating the accumulated localisations, weighted according to their amplitude. During the generation process, the localisation density map is rendered in a quantitative, high dynamic-range format. After localisation is completed, the image is converted to a non-quantitative display range using weighted histogram equalisation (equivalent to gamma correction). This feature is meant to improve contrast and visibility of fainter features, which are often obscured by intensely bright structures in the linear display mode [*rapidSTORM* manual].

In general, the software seemed to have a propensity for detecting molecules at points of filament overlap, whilst often ignoring molecules along uninterrupted fibres; concurrently with this, bright features could be seen in the reconstruction that were not visible in the pre-acquisition widefield snapshot. Overall, on this basis it was judged that the SNR was likely not high enough, and that probably as a result of this, the switching events gathered were not sufficient. Alternatively, the fast decline in fluorescent scintillations could be a sign of imbalanced redox buffer conditions, whereby the dark-state lifetime is disproportionately long, compared to the bright-state lifetime, or that the fluorophores bleach prematurely, or that there is a *z*-drift in the system, shifting the objective downwards and moving the focal plane away from the specimen. There could also be an issue with the stability of the TIRF illumination angle, which may drift gradually towards the epifluorescent regime during the course of acquisition, thus bringing into view new features situated deeper into the sample.

A series of optimisation assessments were carried out next, in order to address the myriad of potential sources of the problem. The concentration of MEA and glucose was systematically and independently varied in a sample of COS-7 cells stained for tubulin with Alexa Fluor® 488. The concentration of glucose was increased or diminished in two-fold steps from the recommended value in [Heilemann *et al.*, 2008], whilst keeping the MEA and glucose oxidase enzyme (GlOx) at the recommended concentration, *i.e.* 100 mM and 0.5 mg/mL, respectively [van de Linde *et al.*, 2010] (**Fig. 6.4.1.2**). Similarly, the MEA concentration was varied in two-fold intervals around the recommended value of 100 mM, whilst keeping a constant GlOx and glucose concentration, *i.e.* 10% w/v glucose and 0.5 mg/mL GlOx, recommended in [van de Linde *et al.*, 2010] (**Fig. 6.4.1.3**).

Separating STORM frame sequences into batches and reconstructing them individually indicated that optimal fluorophore switching took place in the first ~3,000 frames – hence, a STORM time-series of 3,000 frames was collected for each condition. This was followed by super-resolution reconstruction of the time-series using *QuickPALM*, which emerged as the speedier, albeit less responsive, of the two programmes utilised in **Fig. 6.4.1.1**, with respect to detecting potential single-molecule events.

The optimal glucose concentration appears to be around 20% (or perhaps greater). This redox buffer concentration optimisation established that the most appropriate imaging buffer composition consists of 20% glucose and 100 mM MEA, in addition to the default 0.5 mg/mL of the enzyme GlOx. Concentrations of glucose greater than 20% w/v of the buffer content were not tested because it was thought that such disproportionate quantities of glucose may obstruct the free diffusion of the imaging buffer, and therefore compromise the efficient switching of the fluorophores.

These measures, however, still did not resolve the omission of sections of microtubules in the reconstructions – even when *rapidSTORM* was applied (**Fig. 6.4.1.2**, far right). This result prompted the exploration of other publicly available software, with a spot-finding and image-rendering capacity better suited to our data.

6. 4. 2. Optimising super-resolution reconstructions

Octane [Niu *et al.*, 2008][Tatavarty *et al.*, 2009] and *ThreeB* (standing for Bayesian analysis of Blinking and Bleaching) [Cox *et al.*, 2012][Rosten *et al.*, 2013] are both released as ImageJ plugins. *ThreeB* is designed to tackle high-density, overlapping molecule activation, and is formulated on the principle of Bayesian statistics and Bayes' Rule. The latter is a method of inferring the probability of a specific hypothesis, given a collection of evidence. The hypothesis being proved or disproved in this case is the number and locations of the fluorophores, and the evidence the hypothesis is compared against is the STORM data volume.

In brief, the algorithm functions by modelling the entire population of fluorophores appearing throughout the course of a STORM time-series as a certain spatial distribution of fluorophores in either an emitting, dark or bleached state at any given time [Cox *et al.*, 2012]. Activating and deactivating events, as well as instances of bleaching, are utilised to identify the presence and location of the emitters. Contrary to algorithms which do not track molecule behaviour from one frame to another (such as is believed to be the case with *QuickPALM* and *rapidSTORM*), reappearance of individual molecules in *ThreeB* contributes to the improvement of their localisation, and does not merely lead to the addition of a new point source. Overall, the theoret-

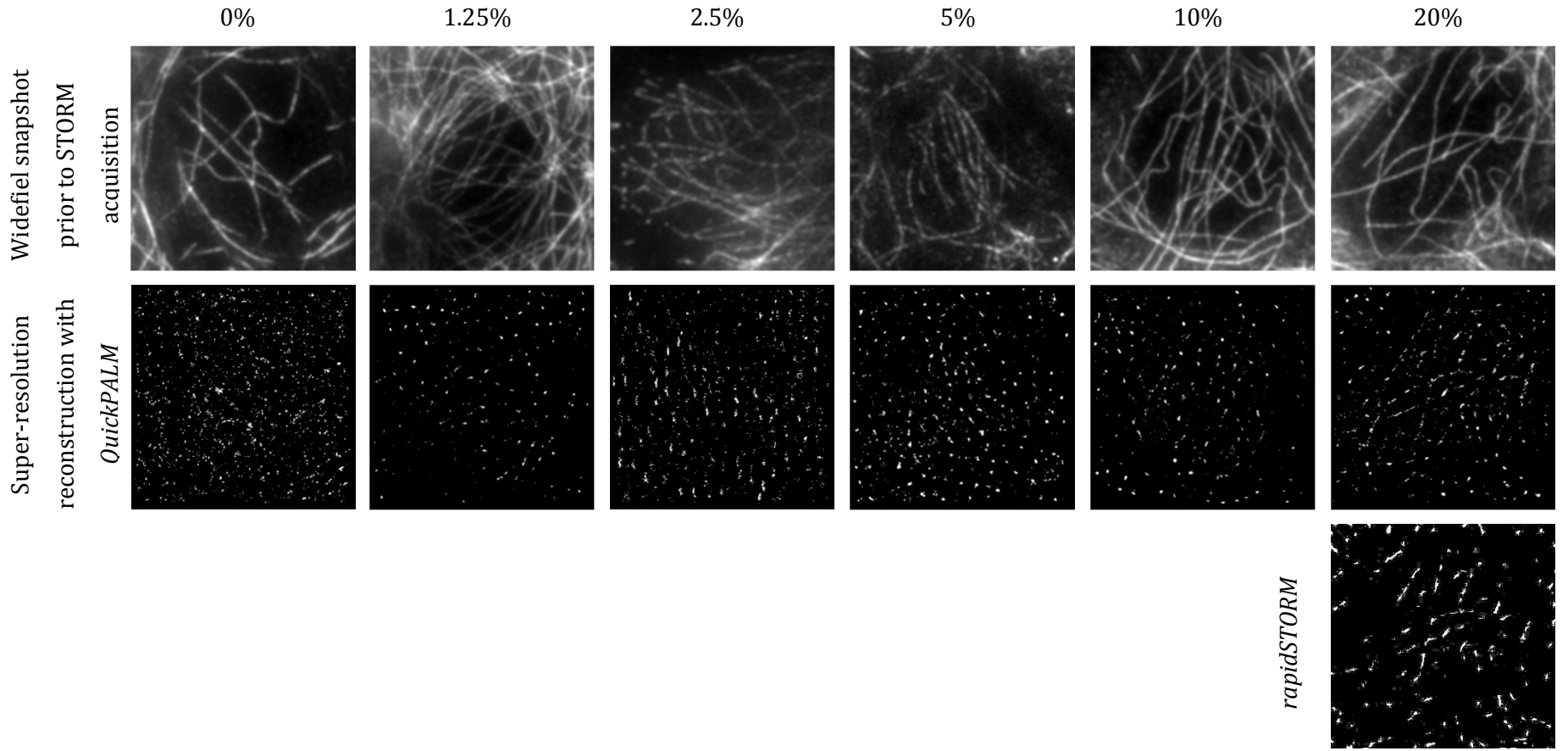

Figure 6.4.1.2. Determination of the optimal glucose (oxygen scavenger substrate) concentration for carrying out STORM. COS-7 cells were immunostained indirectly for α-tubulin with Alexa Fluor® 488. A widefield snapshot of the field of view was obtained (top row) prior to commencement of STORM data acquisition, whereby a set of short STORM frame sequences (~3000 frames each) was obtained upon immersing the sample in switching buffers with different glucose concentration. The latter was varied systematically from 0 to 20%, whilst keeping the concentration of glucose oxidase (0.5 mg/mL) and MEA (100 mM) constant. A qualitative assessment of the reconstruction of each data set with *QuickPALM* (middle row) and *rapidSTORM* (bottom right) and fidelity to the structure captured in the widefield snapshot permitted to identify the optimal glucose concentration (20%). Note that, in the absence of glucose, the reconstruction is particularly poor, indicating that MEA may not be sufficient to guarantee the appropriate conditions for STORM – contrary to guidelines in [Heilemann *et al.*, 2009]. Note, also, that some lateral drift can be observed in the reconstruction image for the 2.5% glucose condition.

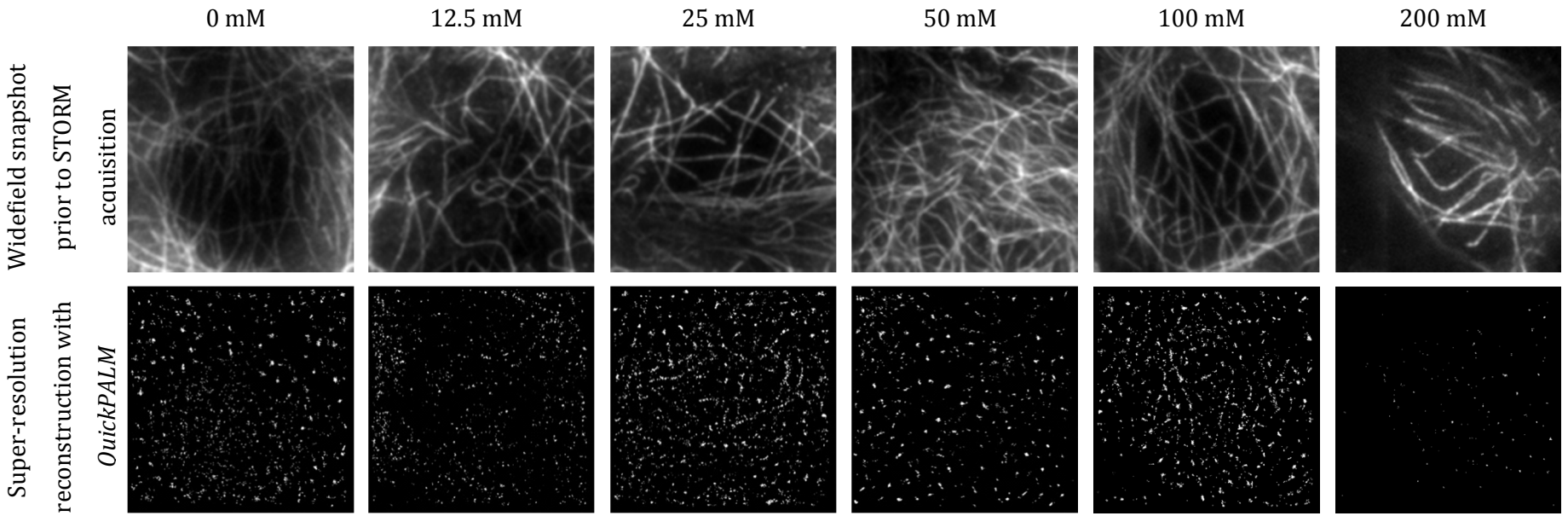

Figure 6.4.1.3. Determination of the optimal β-mercaptoethylamine (MEA) concentration for carrying out STORM. COS-7 cells were immunostained indirectly for α-tubulin with Alexa Fluor® 488. A widefield snapshot of the field of view was obtained (top row) prior to commencement of STORM data acquisition, whereby a set of short STORM frame sequences (~3000 frames each) was obtained upon immersing the sample in switching buffers with different MEA concentration. The latter was varied systematically from 0 to 200 mM, whilst keeping the concentration of glucose oxidase (0.5 mg/mL) and glucose (10% w/v) constant. A qualitative assessment of the reconstruction of each data set with *QuickPALM* (middle row) and fidelity to the structure captured in the widefield snapshot permitted to identify the optimal MEA concentration (100 mM). 100 mM of MEA appears to aid the reconstruction process to the highest degree, compared to all other concentrations which were tested here. Note that 200 mM MEA tends to quench the dye.

ical framework of *ThreeB* therefore makes it a highly reliable and robust algorithm.

In simplified terms, the *ThreeB* routine executes approximately the following steps:

1) Propose an initial distribution of fluorophores.

2) Make local, iterative adjustments of fluorophores' positions along the four major compass directions, one fluorophore and one direction at a time.

3) Introduce a new fluorophore or take away an existing one at random; re-adjust fluorophores' positions for optimal agreement with the data.

4) Compare the likelihood that the model matches the data before and after adding or deleting a fluorophore and select the more plausible model.

5) Repeat from step 2) onwards several hundred times, until significant changes in the reconstructed image can no longer be observed. The reconstruction of the super-resolution image takes place as follows: the estimated fluorophore density is mapped to a high-resolution image, quantising positions to the nearest pixel. Each fluorophore is then assigned a brightness according to the magnitude of its probability; thus, brighter molecules reflect more confident localisations than dimmer ones. Subsequently, the high-resolution image is blurred with a Gaussian kernel and sub-sampled by a factor of two [Cox *et al.*, 2012].

Although no official documentation of the algorithm is published for *Octane*, some operational features could be deduced from the Java source code and correspondence with the author. Particle localisation is executed through a full 2D Gaussian least-squares minimisation fit, and data are prepared for display by sorting into a histogram of bin size equal to the pixel size defined by the user. Having been designated for live-cell imaging, the programme offers the option of plotting only the initial, final or averaged particle positions. During the visualisation stage, all molecules are attributed the same intensity, and a Gaussian blur whose width is decided by the user. Thus, the user has control over both the final pixel resolution and localisation precision, decided by the Gaussian blur.

Subsequently, all four software packages were applied to data with the insofar most favourable parameters for STORM. Actin filaments instead of microtubules were dually labelled with phalloidin conjugated to either ATTO 565 or Alexa Fluor® 488. The reason for switching to actin was the laboratory materials available at the time, and ATTO 565 only being available in a form directly coupled to phalloidin, rather than to a secondary antibody.

The same area of sample was imaged first with ATTO 565, whose excitation was performed with the 561-nm laser, then with Alexa Fluor® 488, which was excited with the 491-nm laser. Reconstructions of samples labelled with Alexa Fluor® 488 yielded different, and consistently better, results with each software package. An additional reconstruction result with the software *SOFI*, courtesy of Ricardo Henriques, is included for Alexa Fluor® 488. *SOFI* is an acronym for Super-resolution Optical Fluctuation Imaging and incorporates an algorithm that anal-

yses the temporal fluctuations of densely spaced emitters. Similar to *ThreeB*, *SOFI* inspects inter-frame correlation, but differs from *ThreeB* in that it determines the locations of fluorophores using a cumulant correlation function, rather than by computing prior probabilities [Dertinger *et al.*, 2009, 2012a and 2012b]. Likewise, *SOFI* assigns brightness to the particles proportional to their correlation strength.

Prior to acquisition of these data, in order to accommodate both lasers, the TIRF condenser was adjusted to a position intermediate between the optimum focus for the 491-nm and 561-nm lasers. This is thought to be the reason why the Alexa Fluor® 488 dye in particular did not exhibit any blinking. In fact, throughout the recording, the specimen underwent bleaching at a steady rate, similar to a conventional widefield time-series. As a result, sparse localisation analysis software, such as *rapidSTORM*, failed to capture any information from the images; this is in contrast to *QuickPALM* which, surprisingly, performed much better than *rapidSTORM* for both dyes. The display settings, such as final pixel size and kernel size of the artificially applied Gaussian blur, were assessed through trial and error, and the settings deemed best were those which produced the smoothest, most continuous filaments.

The best performance was given by *ThreeB* and *Octane* with Alexa Fluor® 488. The *ThreeB* reconstructions depicted in **Fig. 6.4.2.1** and **Fig. 6.4.2.2**, in particular, are the outcomes of only 120 iterations each (as opposed to the recommended minimum of 200), due to the extreme computational intensity of the algorithm which could not be matched by our computer resources. It is possible that, had the data been processed further, accumulating the recommended number of iterative improvements, the *ThreeB* reconstruction quality would have been on a par with, or even surpassed, *Octane*.

Notwithstanding, moderately reliable reconstructions were achieved with both software programmes. To quantify the localisation precision, line profiles were drawn perpendicularly to randomly selected filaments in the super-resolved images, and their FWHM was measured. Representative examples are shown in **Fig. 6.4.2.3**. The average FWHM for *Octane* was 109 nm, and for *ThreeB* it was 75 nm. This assumes that the filaments resolved in super-resolution are all individual strands. By comparison, the actual diameter of an individual filament of actin (F-actin) fibre is 7 nm [Cooper, 2000].

The average resolution of the reconstructed images can be calculated as $2\sqrt{2}\,\Delta r_{rms}$ [Rees *et al.*, 2012], where Δr_{rms} is **Eq. 2.2.5.3**. The aforementioned equation predicts a localisation precision of 20 nm; using this figure, the expected resolution is calculated to be ~57 nm. If, on the other hand, one heuristically assumes the localisation precision to be reflected in the thickness of the filaments reconstructed with each software (with the real thickness subtracted), then assuming that the reconstructed fibres represent individual filaments, and since FWHM = $2\sqrt{2\,ln2}\,s$ ($s \equiv$ standard deviation), the expected resolution is FWHM/$\sqrt{ln2} \approx 122$ nm for *Oc-*

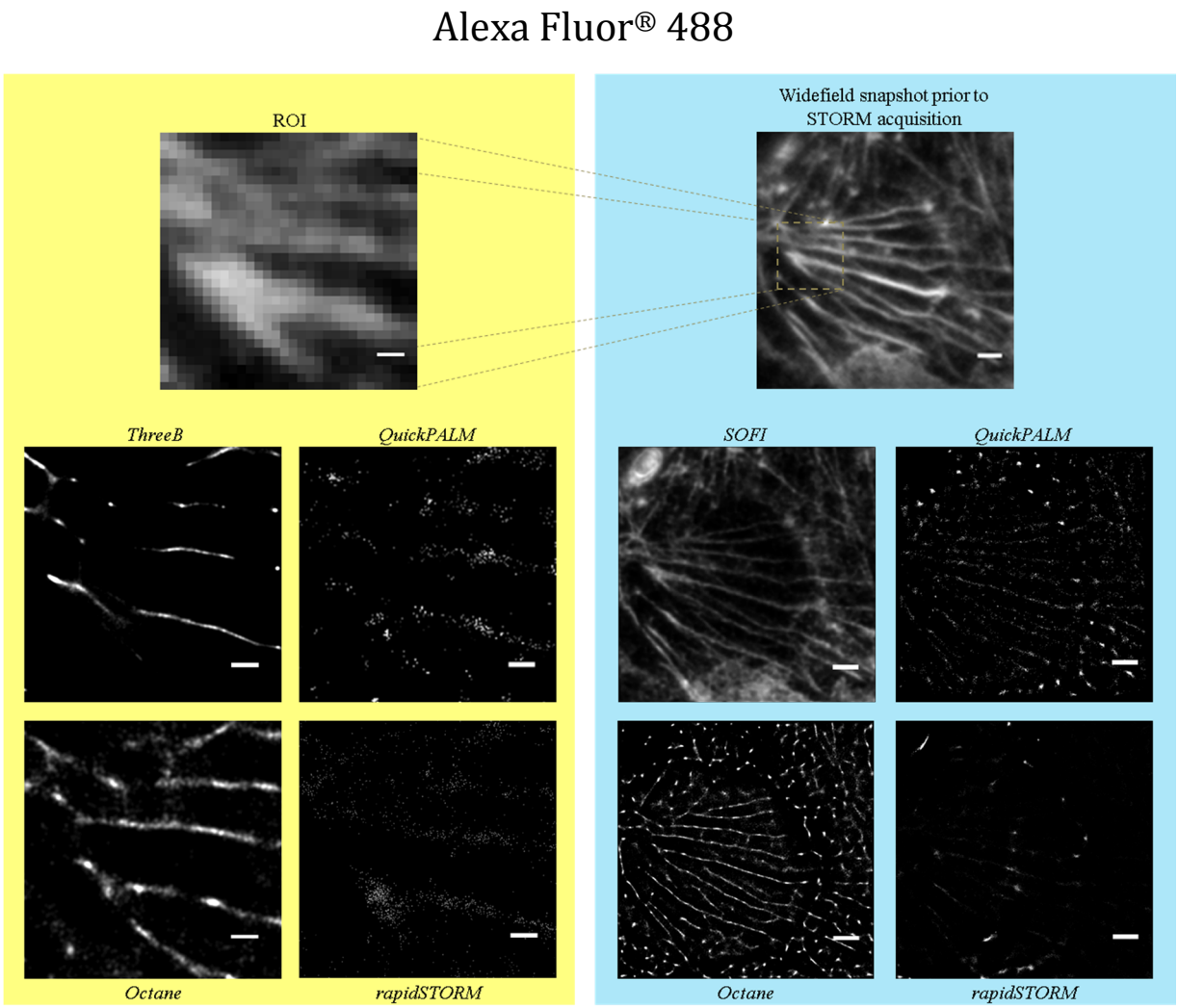

Figure 6.4.2.1. Testing of various open-source software packages *via* super-resolution reconstruction of actin filaments. Detection of F-actin was realised with Alexa Fluor® 488 conjugated to phalloidin. The left-hand panel shows reconstructions of the magnified region of interest (ROI), top left. The right-hand panel portrays the entire image (top right) in super-resolution. Note that *ThreeB* cannot process raw data of more than ~900 pixels, hence no full-view reconstruction is available with this software. For this reason, a *SOFI* reconstruction, which provides a resolution similar to a confocal image, is shown instead. Scale bars on images overlaid on yellow panel: 500 nm; scale bars on images within blue panel: 2 μm.

tane and 82 nm for *ThreeB*.

It is worth noting that **Eq. 2.2.5.3**, as before, is not entirely correct. In more detail, it was already shown earlier that a non-constant background can severely deteriorate the localisation precision. On the other hand, the above resolution expression is pessimistic, since it assumes that a fluorophore is localised only once in the entire STORM sequence. In fact, it is estimated as

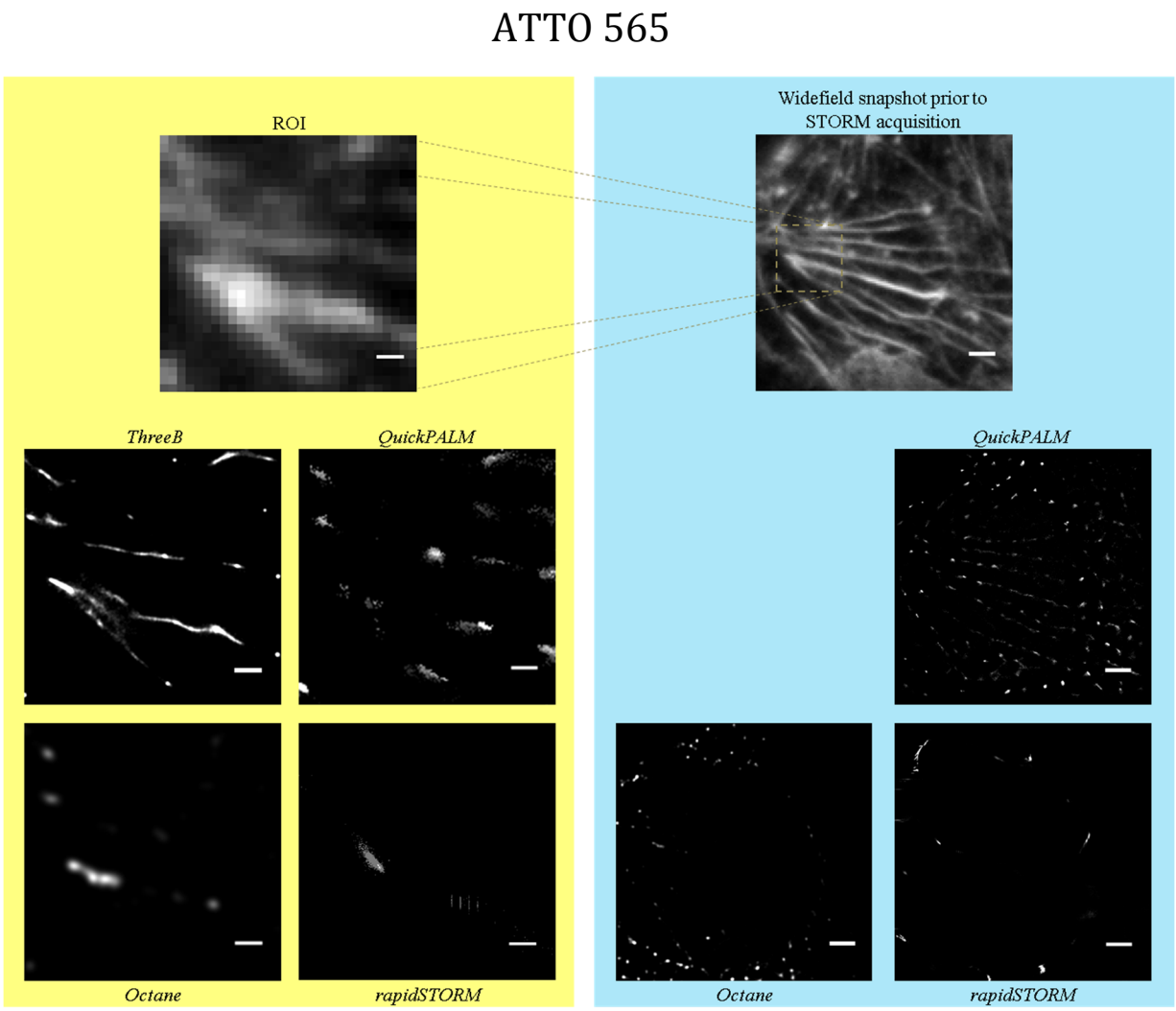

Figure 6.4.2.2. Testing of various open-source software packages *via* super-resolution reconstruction of actin filaments. Detection of F-actin was carried out with ATTO 565 conjugated to phalloidin. The left-hand panel shows reconstructions of the magnified ROI, top left. The right-hand panel portrays the entire image (top right) in super-resolution. Note that no super-resolution image with the software *SOFI* is available for this dye. Scale bars on images overlaid on yellow panel: 500 nm; scale bars on images within blue panel: 2 µm.

shall be expanded on in the next section that each fluorophore in the entire fluorophore population undergoes approximately 34 activation-deactivation cycles within the acquisition timeframe in this specific case, thus boosting the localisation precision and therefore resolution. A more realistic estimate of the resolution, therefore, lies between the precision limit, as defined by the Sparrow limit, $2\Delta r_{rms}$, and the single-localisation case, $2\sqrt{2}\Delta r_{rms}$.

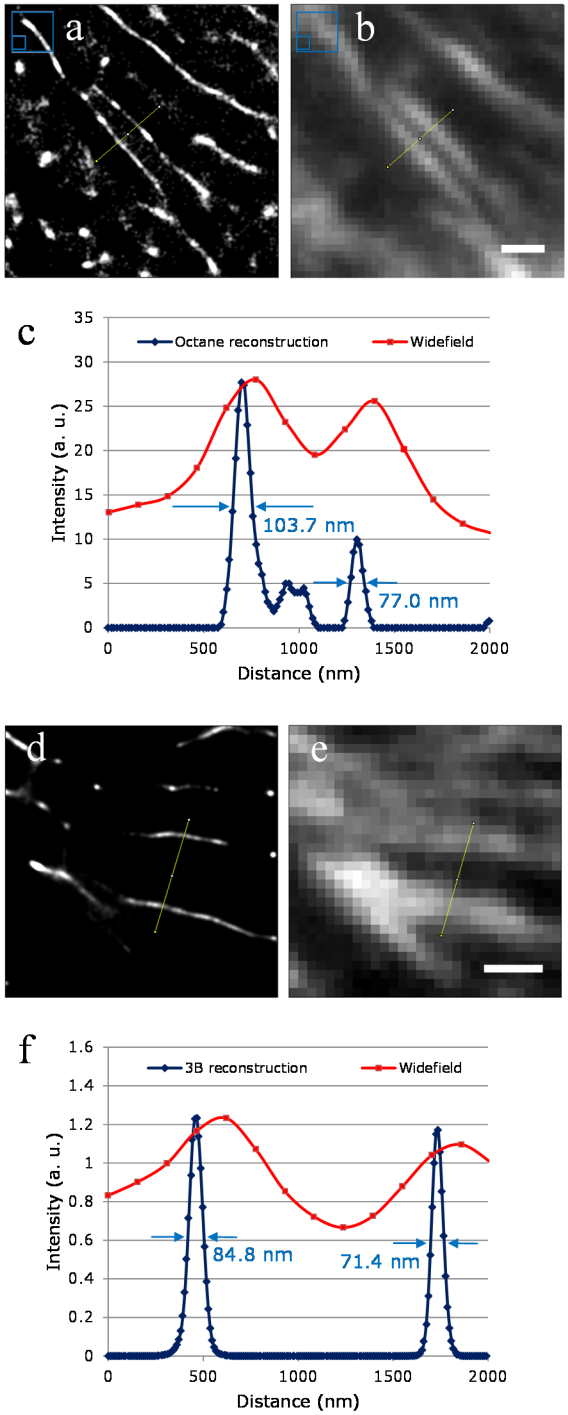

Figure 6.4.2.3. Direct assessment of the typical localisation precision of *Octane* and *ThreeB* super-resolution reconstruction software. The image data displayed here are a zoom-in of the *Octane* reconstruction in **Fig. 6.4.2.1** (a) and the corresponding area of the specimen in widefield (b); (d) is identical to the *ThreeB* reconstruction in **Fig. 6.4.2.1** and (e) to the corresponding widefield ROI. (c) and (f) are representative examples of pre- and post-reconstruction measurement of the line profiles of the actin filaments labelled with phalloidin-Alexa Fluor® 488 along the lines indicated in (a)/(b) and (d)/(e), respectively. Full-width at half-maxima (FWHM) as narrow as ~70 nm could be measured in both *Octane* and *ThreeB* reconstructions. The actual width of actin filaments is 7 nm. Scale bars: 1 µm.

6. 5. Characterisation of open-source super-resolution software performance and efficiency

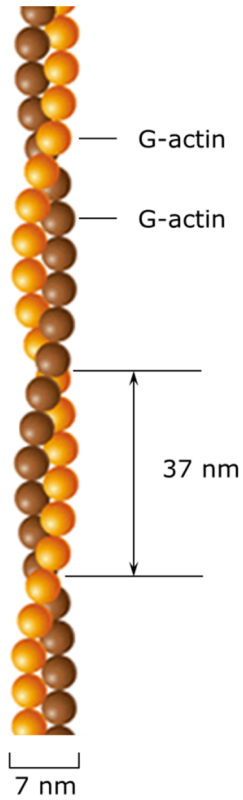

Figure 6.5.1. Filamentous actin (F-actin) architecture. Two actin protofilaments (shown in different colours) intertwine to create F-actin. The strands are coloured differently for clarity. Each strand is composed of a repetition of the same basic ingredient, G-actin. Figure adapted from [Haramoto *et al.*, 2010].

In order to assess the suitability of available open-source software specifically for reconstruction of my data, and to evaluate the software's limits, synthetic STORM image sequences were simulated and subsequently reconstructed with the super-resolution software packages *Octane* and *ThreeB*.

A pair of mutually parallel F-actin fibres was modelled traversing the field of view perfectly horizontally. Despite choosing a very specific and unnatural layout of the fibres, an effort was made to simulate F-actin as realistically as possible. F-actin is a part of the cytoskeleton and lends the cell structural stability, mobility, and serves as a network of 'tracks' for intracellular transport [Ming *et al.*, 2003]. The fibres are double-stranded helical polymers of the monomer G-actin. G-actin in non-muscle cells, such as COS-7, has two isoforms (β and γ) of identical sizes. Phalloidin binds specifically to F-actin at the interface between the G-actin subunits [Vandekerckhove *et al.*, 1985].

F-actin's architecture (**Fig. 6.5.1**) consists of a helix of two long polymers (termed protofilaments) assembled from actin monomers, entwined around each other. The protofilaments are staggered longitudinally. Every 13 subunits (74 nm) a complete turn around the helix axis is effected. The geometry of actin was incorporated into a routine written in Matlab (Actin simulation, Appendix B). It was posited that the quantity of fluorescently coupled phalloidin saturated the binding sites, such that no intermolecular binding site was left unoccupied. This was not directly investigated, however it was convenient to implement in computer code. Akin to the simulation described earlier in this chapter, all molecules were captured in their best focus in the image plane. This meant that the 3D double helix was orthographically projected onto a 2D plane, yielding a pair of out-of-phase sinusoids (**Fig. 6.6.2**). Ignoring the depth of the filaments causes a deviation from reality; however, it is unlikely that this reduces the soundness of the model, since the filaments are so thin that defocus would be negligible (the depth of field of a high-magnification, high-*NA* objective is several hundred nm). In

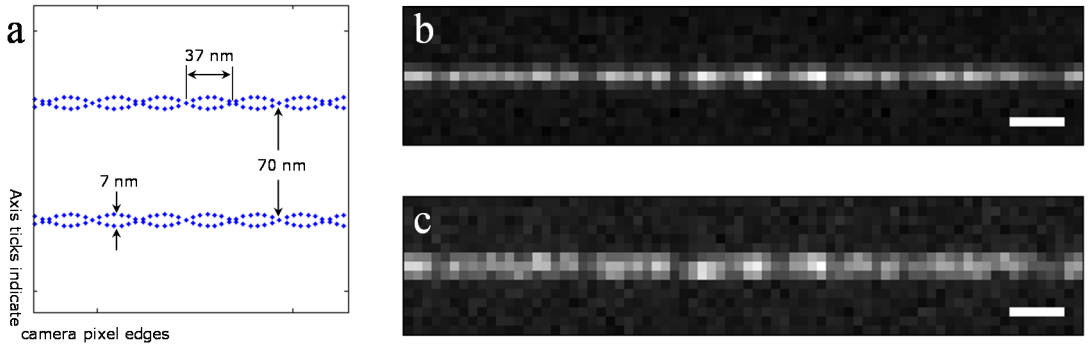

Figure 6.5.2. Simulation of actin filaments. (a) Depiction of the ultrastructure of a pair of simulated actin filaments. The separation between the longitudinal axes of the filaments is 70 nm. This figure is intended to provide insight into the relative size of the actin ultrastructure, compared to the size of the camera pixels. (b) A single frame from a simulated sequence of images, with a fluorophore activation density similar to that encountered in real data of F-actin. The filament separation here is 70 nm. (c) Same as (b), except the filament separation has been increased to 120 nm. Scale bar: 1 µm.

view of the theoretical resolution obtained in the previous section, the separation of the filaments was set to 125 nm; thus, *ThreeB* should be capable of resolving the filaments with relative ease, whereas *Octane* is expected to just be able to hint at the presence of two separate filaments.

The simulations determined that *Octane* attained a resolution of 170 nm (**Fig. 6.5.3**). The empirically obtained resolution was much poorer than expected. By and large, resolution can be improved by increasing the number of collected frames and raising the SNR. The SNR in the actin STORM stack in **Fig. 6.4.2.1** was identical to the one in the simulations, as was the total number of frames. On other occasions it was possible to collect at least 3,000 frames per acquisition run (data not shown), which is up to 3.8 times more than in **Fig. 6.4.2.1**, where bleaching interrupted the acquisition process comparatively early. Thus, the resolution may be improved from 170 nm, provided that more frames are collected. Surprisingly, *ThreeB* completely failed to resolve the filaments below a separation of about 190 nm. Henceforth I therefore concentrated solely on the *Octane* software.

Next, the localisation precision of *Octane* was investigated empirically as another means of assessing the software's performance (**Fig. 6.5.4**). During the generation of the synthetic actin fibre STORM frame stack, a list of the molecule coordinates was assembled. The tolerance with which *Octane* recovered molecular positions was assessed by comparing the coordinates of identified particles with the true coordinates of the simulated actin molecules, and the differences between them, representing the individual localisation errors, were calculated. The most optimistic situation possible was assumed – that is, that each localisation in a given frame was

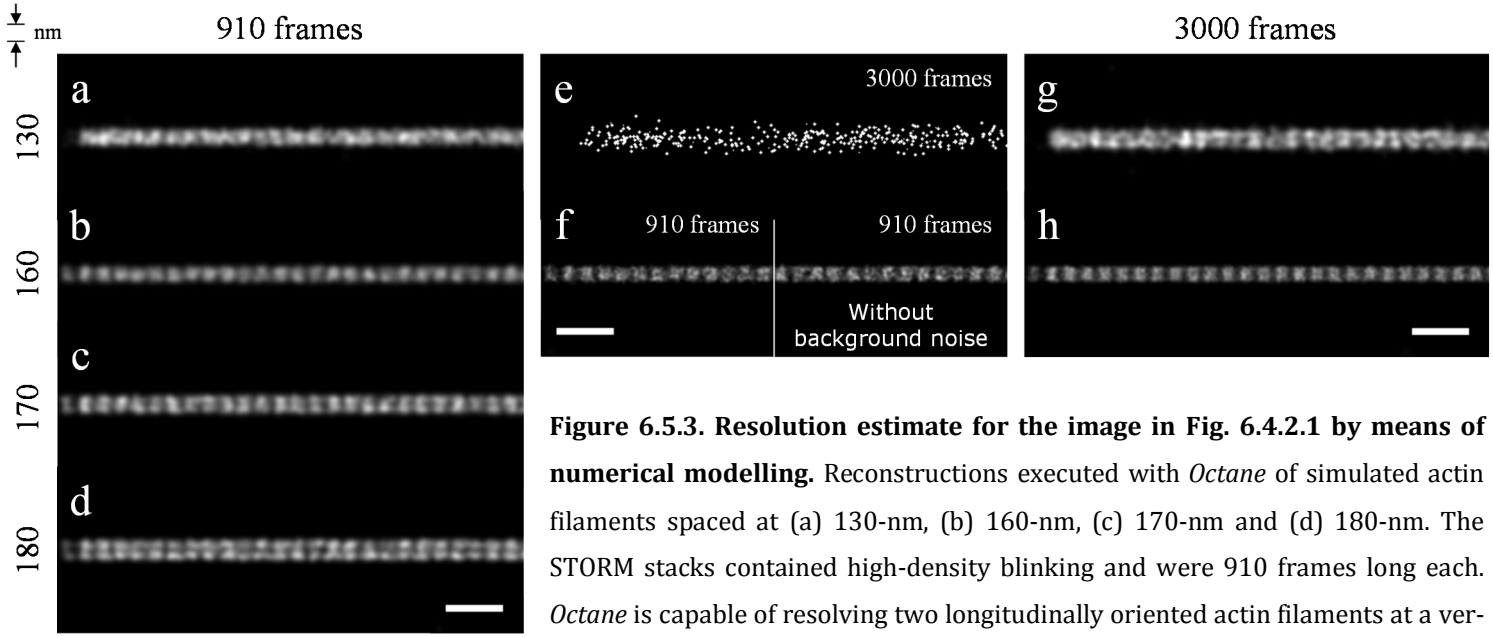

Figure 6.5.3. Resolution estimate for the image in Fig. 6.4.2.1 by means of numerical modelling. Reconstructions executed with *Octane* of simulated actin filaments spaced at (a) 130-nm, (b) 160-nm, (c) 170-nm and (d) 180-nm. The STORM stacks contained high-density blinking and were 910 frames long each. *Octane* is capable of resolving two longitudinally oriented actin filaments at a vertical separation of 170 nm, but not at 160 nm. Localised point sources were blurred with a Gaussian kernel of 60-nm standard deviation, in order to mask the pointillism of the image. The choice of its size was influenced by the RMS localisation precision [Rees *et al.*, 2012] which is ~53 nm. An intriguing beating frequency is observed in all *Octane* reconstructions; this effect indicates that this software may have a tendency to create localisations by averaging the position of several activated molecules. (e) Reconstruction with *QuickPALM*, where the synthetic STORM data were modified to contain much fewer activations per frame (<1 molecule per diffraction-limited area), spread over 3,000 frames. (f) Same as (b), except a Gaussian kernel of 30-nm standard deviation is applied, in order to show that the size of the smoothing blur is not the limiting factor in resolving the filaments. Curiously, removing background noise from the simulation (right-hand side) does not enhance the resolution either. (g) Reconstruction with *Octane* of non-overlapping molecule activations, as in (e). This time the software is able to resolve the filaments at a spacing of 130 nm. (h) Same as (f) with background noise, except with a stack containing 3,000 frames. Scale bars: 500 nm.

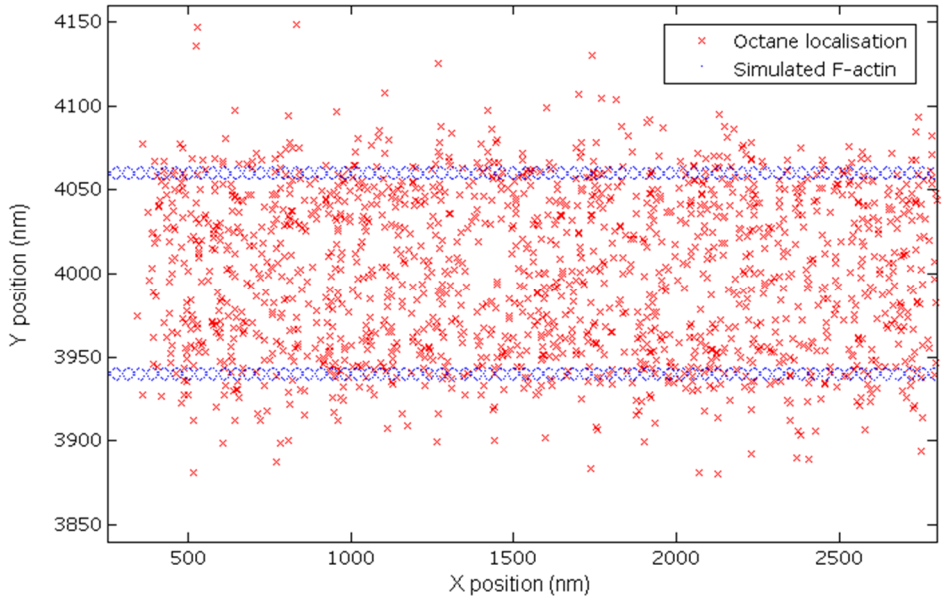

Figure 6.5.4. Alternative means of measuring the localisation precision of *Octane*. The localisations produced by *Octane* (red crosses) were compared with the true molecule positions (blue dots) as a means of directly measuring the error margin. Some assumptions apply, as outlined in the text. Also, some localisations (further than 100 nm in the *y*-direction from the outside of the filament pair) were removed from the calculation, as I believed that they arose because of background fluctuations wrongly identified as molecular events. An RMS localisation precision of 34 nm in the *x*- and 30 nm in the *y*-direction was found.

matched to the nearest activated fluorophore in the same frame of the image sequence. The radial distances between the localisation coordinates and actual fluorophore positions were then determined for each matched pair. All localisations further than 100 nm in the *y*-direction from the outside of the filament pair (outlined by the top and bottom boundaries of the graph) were discarded because they likely represented false positives stimulated by momentary random surges in the background. The localisation precision was thus calculated to be 45 nm on average in any direction in the transverse plane, or 34 nm in the *x*- and 30 nm in the *y*-direction. Given ~12,000 photons per localisation event, the localisation precision expected from **Eq. 2.2.5.3** would be sub-nanometre; however, since there is considerable overlap of activated molecules, this equation does not apply in this case. The overall detection efficiency, *i.e.* the ratio of the total number of molecules detected against the total number of simulated spots, was 4.6%. The poor localisation precision, together with the low spot identification score that the software achieved (caused in part – but not entirely, as shall be discussed shortly – by the poor SNR ratio), justifies the deficient resolution.

Interestingly, there appears to be a localisation bias towards the space between the fi-

bres; this is another indication of *Octane*'s alleged tendency to average particles' positions. Naturally, the software is expected to malfunction, since it was not explicitly designed for high-density blinking.

With my experimental conditions and materials, **Fig. 6.5.3** indicates that high-density molecule imaging is capable of resolving features up to 170 nm apart; single-molecule imaging (*i.e.* one molecule per diffraction-limited area) on the other hand can improve the resolution to 130 nm. Although not as high as anticipated, a resolution of 130 nm is below the diffraction limit and considerably outside the domain of confocal microscopy (without post-processing with deconvolution). These results justified proceeding towards visualising Shh with super-resolution imaging.

Considering that the size of the fluorescent detection system used here can be found anywhere within a radius of 30 nm from the antigen (due to the flexibility of the hinged regions on primary and secondary antibodies), the final resolution may deteriorate to as much as 180 nm, and including the effect of drift can bring it out of the sub-diffraction domain altogether. One means of preventing this is to select a smaller probe, for example, an FP tag.

6. 6. Super-resolution imaging of cell-surface Shh multimolecular complexes

The original intention was to transfect cells with wild-type and mutant Shh and immunostain them for the morphogen with an antibody linked to Alexa Fluor® 488. However, a transient impediment involving lack of success in transfecting the plasmids (which was eventually solved and traced to the transfection reagents), compelled me to find a workaround. An acquired construct, murine Shh::EGFP constituting a gift from Prof. Andrew P. McMahon, Harvard University, USA, transfected successfully and was therefore used instead.

Contrary to many other proteins, genetically fusing an FP tag to the *Shh* protein is not straightforward due to the fact that Shh undergoes double post-translational modifications. The FP cannot be encoded at either end of the *Shh* gene because it would either prevent palmitoylation, or the tag would be cleaved off as soon as the protein undergoes cholesteroylation. One solution is to insert the tag somewhere within the N-terminal domain. Murine Shh::EGFP [Chamberlain *et al.*, 2008] has the EGFP gene engineered into the DNA sequence straight after the signalling domain (Cys^{594}), followed again by the last 21 amino acids of the signalling domain and the rest of the *Shh* sequence. It should be noted, however, that modifying a gene in this way increases the molecular weight of the gene product and can impact its mobility. In addition, tampering with the protein can hinder its proper folding which can cause partial or total loss of function, or aberrant molecular interactions. The researchers who synthesised the construct report that it

does not undergo efficient cholesteroylation [Chamberlain *et al.*, 2008] and that it has been found to have reduced bioactivity compared to wild-type Shh. The latter is thought to be caused by the inefficient autoprocessing of the protein. However, it does show substantial biological activity, so must be sufficiently well folded to provide partial functionality.

The satisfactory folding is probably due to the fact that the linker peptides contain an abundance of glycine residues. Glycine is unique amongst amino acids in that it endows the protein structure with conformational flexibility. Glycine may therefore reside in locations which other amino acids with more restrictive topology may not. This is due to the presence of a hydrogen atom in place of a more elaborate carbon side-chain found in all other amino acids. The presence of glycine further favours the folding of the signalling domain, integrated EGFP and autocatalytic domain independently of each other – *i.e.* if one domain misfolds, it should not affect the folding of the others.

Standard, non-photoswitchable FPs have been known to exhibit spontaneous scintillating behaviour [Dickson *et al.*, 1997][Garcia-Parajo *et al.*, 2000][Chiu *et al.*, 2001][Lee *et al.*, 2011], even when exposed to illumination from non-laser sources [Cox *et al.*, 2012]. This makes it possible to carry out PALM/STORM on the Shh::EGFP construct. However, since the gene product is fluorescently detectable from the moment the folding of the β-barrel and chromophore is complete, the protein is traceable throughout the entire cell, as well as the surface of the membrane. In the context of this project, this is undesirable since only cell-surface Shh clusters are of interest. In an attempt to purge intracellular Shh::EGFP to the cell exterior, 24 hours after transient transfection with Shh::EGFP, COS-7 cells were treated with cycloheximide, an inhibitor of protein biosynthesis. One half of the cell population was exposed to 25 μM; the other was exposed to double the concentration – *i.e.* 50 μM. The cells were then incubated for 2 hours at 37°C, whereupon they were fixed and immunostained for Shh with pAb anti-Shh coupled to Alexa Fluor® 555 according to the standard protocol. A *z*-stack acquired on a confocal microscope (inverted Leica SP5) indicated that the pharmacological treatment had had little to no effect on removing intracellular Shh::EGFP (**Fig. 6.6.1**).

The result in **Fig. 6.6.1** indicated that the length of treatment and/or concentration needed to be increased significantly. However, unfortunately due to time constraints, further fine-tuning of the experiment was not possible.

Using **Eq. 2.2.3.3.1**, **2.2.4.1.1** and **2.2.4.1.7**, the minimum penetration depth of the TIRF field for this set-up can be calculated to be 71.5 nm. By contrast, the lipid bilayer of the plasma membrane has an average thickness of 5 nm [Lodish *et al.*, 2000]. Most mammalian cells, however, possess a network of glycoproteins and polysaccharides embedded in the outer leaflet of the lipid bilayer which adds additional thickness to the membrane [Vorbrodt *et al.*, 1969]. Simian virus 40 (SV40)-transformed cells, such as the COS-7 cell line, produce a particularly thick layer of

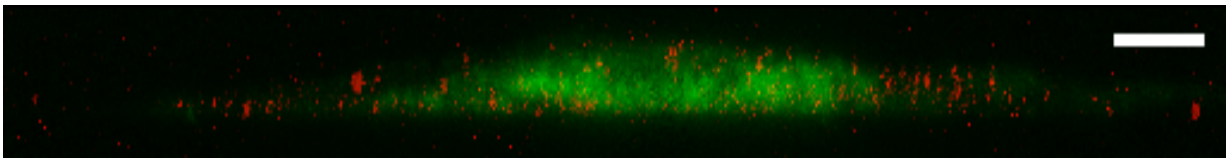

Figure 6.6.1. Cycloheximide treatment is unsuccessful in chasing Shh::EGFP out to the extracellular membrane leaflet. The micrograph is a confocal *x-z* section of a Shh::EGFP-expressing, unpermeabilised COS-7 cell (green) immunostained for Shh with anti-Shh pAb conjugated to a secondary Alexa Fluor® 555-tagged antibody (red). The cell shown here was treated with 25 μM cycloheximide protein synthesis inhibitor for 2 hours before fixing. If the cells had responded to the pharmacological treatment, the EGFP distribution would have coincided with that of Alexa Fluor® 555; instead, plenty of EGFP fluorescence is still observable within the body of the cell. Scale bar: 5 μm.

these long molecules, ranging from 8 to 19.2 nm and with a mean thickness of 13.6 nm [Vorbrodt *et al.*, 1969]. This means that the TIRF field penetrates at least an additional 52.9 nm into the cell interior and is capable of exciting any Shh::EGFP molecules which have not been secreted to the surface. Such molecules could be situated in the ER, or could reside in exocytic vesicles in preparation for fusion with the membrane, or in endocytic vesicles, or alternatively, if Shh::EGFP has not folded properly, it could be captured by the ER-associated degradation (ERAD) pathway and be in the process of being degraded.

Intracellular Shh is not known to form Shh multimers. For this reason, intracellular Shh::EGFP is not useful for our purposes of assessing the oligomerisation state of Shh::EGFP. I therefore resorted back to immunostaining. Since labelling Shh::EGFP with Alexa Fluor® 488 is not feasible due to the similarity of the fluorescent absorption and emission spectra of EGFP and Alexa Fluor® 488, STORM imaging with Alexa Fluor® 555 was attempted. **Fig. 6.6.2** shows that the signal from the fluorescent dye was not contaminated with non-specific excitation from the FP. Besides this, the redshifted dye moved the signal detection window away from the autofluorescence zone, providing an additional advantage over Alexa Fluor® 488.

COS-7 cells were transfected with *Shh::EGFP* DNA and subsequently stained with anti-Shh pAb coupled to a secondary antibody labelled with Alexa Fluor® 555, as described in the Materials and Methods chapter. The sample was immersed in the previously optimised photoswitching buffer and a time series was acquired until photoswitching into the bright state was no longer observable. The image stack was then reconstructed with *Octane* (**Fig. 6.6.3d**).

The integrated optical efficiency along the optical train falls from 10.5% for Alexa Fluor® 488 to 3.7% with Alexa Fluor® 555, owing to the non-ideal match of fluorophore to filter set components. The low photon collection rate, however, was deliberately offset by a much longer camera exposure time during data acquisition. Taking into account the latter fluorophore's molar ex-

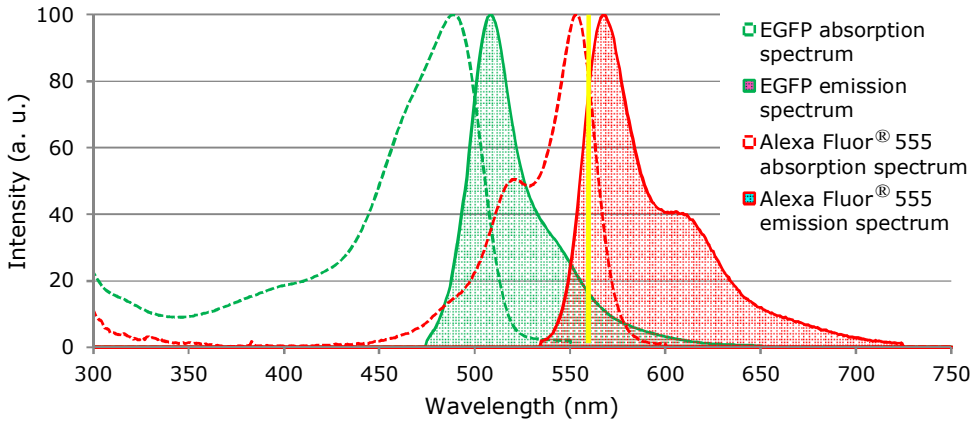

Figure 6.6.2. Normalised absorption and emission spectra of EGFP and Alexa Fluor® 555. The yellow line indicates the 561-nm laser line. Clearly, the 561-nm laser does not excite EGFP, therefore no crosstalk from EGFP should be expected in the Alexa Fluor® 555 imaging channel. Data source: Fluorescence SpectraViewer (probes.invitrogen.com/resources/spectraviewer).

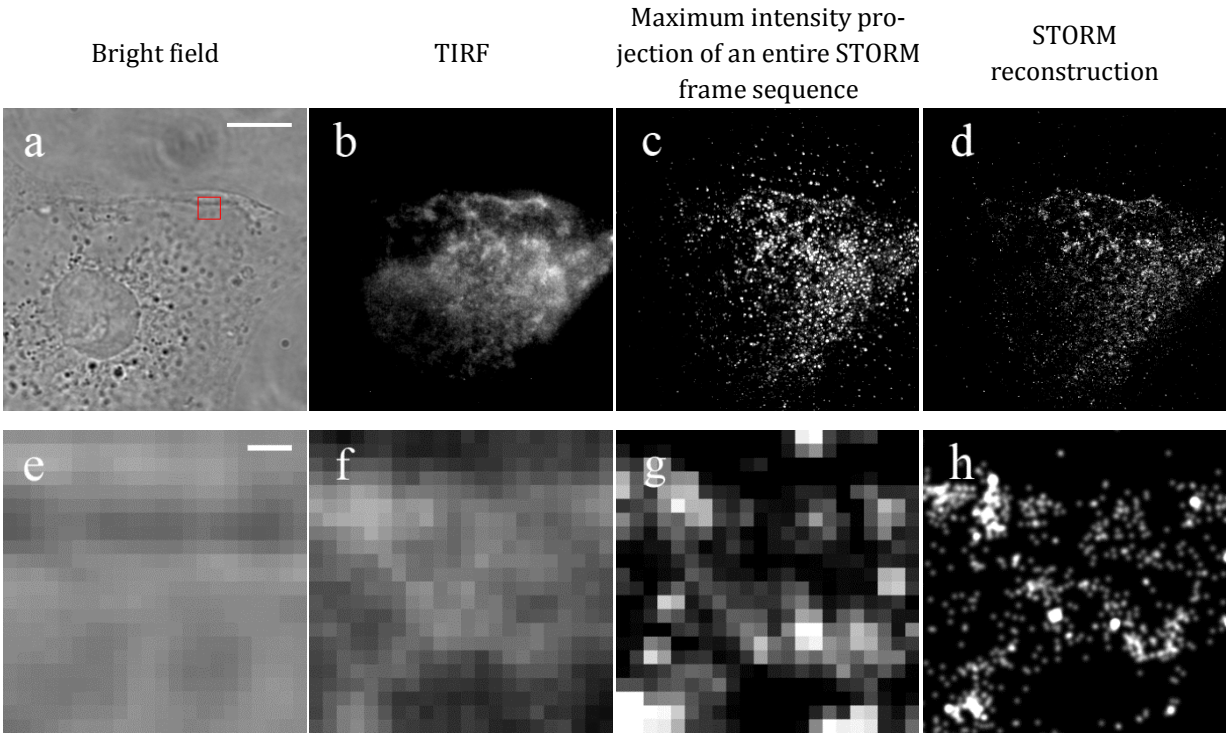

Figure 6.6.3. Super-resolution imaging of Shh using STORM. Here is demonstrated a COS-7 cell, transfected with *Shh::EGFP* and stained with anti-Shh pAb detected with a secondary Alexa Fluor® 555-conjugated antibody. This experiment is representative of one cell only due to the extremely low cellular transfection survivability. All panels in the same row display the same field of view, albeit visualised using different forms of imaging. (a)–(d) The cell in low magnification, scale bar: 10 μm, and (e)–(h) high magnification of the region in the red box in (a), scale bar: 500 nm; the dark shadow in (e) is the edge of a lamellipodium. (a), (e) Bright field; (b), (f) TIRF illumination; (c), (g) Superposition of the entire series of STORM raw data requisite for achieving super-resolution. (d), (h) STORM reconstruction from the same set of images as (c) and (g), respectively.

tinction coefficient and quantum yield, together with its corresponding optical efficiency, as well as the camera settings used during the STORM image sequence acquisition (*e.g.* exposure time, EM gain), laser power, total number of frames gathered and fluorophore blinking density, the numerical model of F-actin I had created previously was altered accordingly.

Surprisingly, reconstructions of the synthetic STORM stack demonstrated that *Octane* is capable of resolving Alexa Fluor® 555-labelled features down to a distance of 15 nm. The drastic improvement in resolution, compared to that evaluated for Alexa Fluor® 488, is most likely due to the vastly extended exposure time (ten-fold). Naturally, this figure does not encompass deterioration in resolution due to drift and the finite-sized probe; if those factors were taken into account, the resolution would approach 135 nm in the worst case.

Furthermore, interestingly, the redshifted dye photobleached slower than its green counterpart and permitted the acquisition of more than twice the number of frames. The F-actin simulations indicated that the surplus frames did not dramatically affect the resolution, but filled the gaps in between the rarefied localisations (**Fig. 6.6.4**).

Finally, the super-resolved features in **Fig. 6.6.3d** were analysed with *Volocity* 3D image analysis software (PerkinElmer, USA). The parameters which were assessed were cluster cross-sectional area, intensity and shape factor (degree of symmetry). The results from the analysis are displayed in **Fig. 6.6.5**. Using the conclusions drawn from the simulations, the lower limit of resolution in the cross-sectional area measurements is around 0.018 μm^2 in the worst case (*i.e.* maximum drift and maximal displacement between dye and antigen).

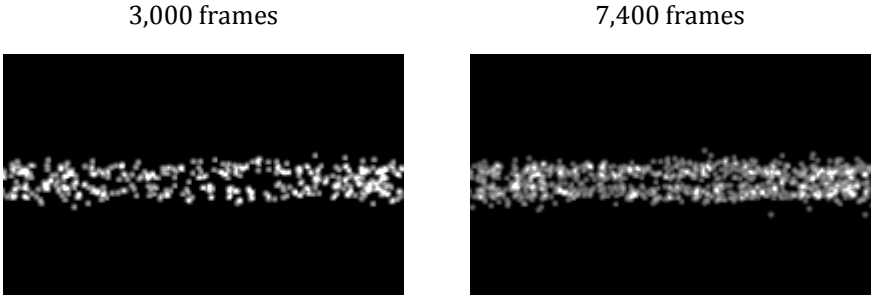

Figure 6.6.4. Evident superior photostability of Alexa Fluor® 555, compared to Alexa Fluor® 488, permits better definition of the underlying structure. The figure shows reconstructions of the same section of simulated actin filaments at a separation of 15 nm for a stack volume of 3,000 and 7,400 frames, corresponding to the empirically established maximum photostability lifetime of Alexa Fluor® 488 and 555, respectively. A larger number of gathered frames clearly results in a more complete mapping of the ultrastructure, as well as better definition and continuity of the filaments.

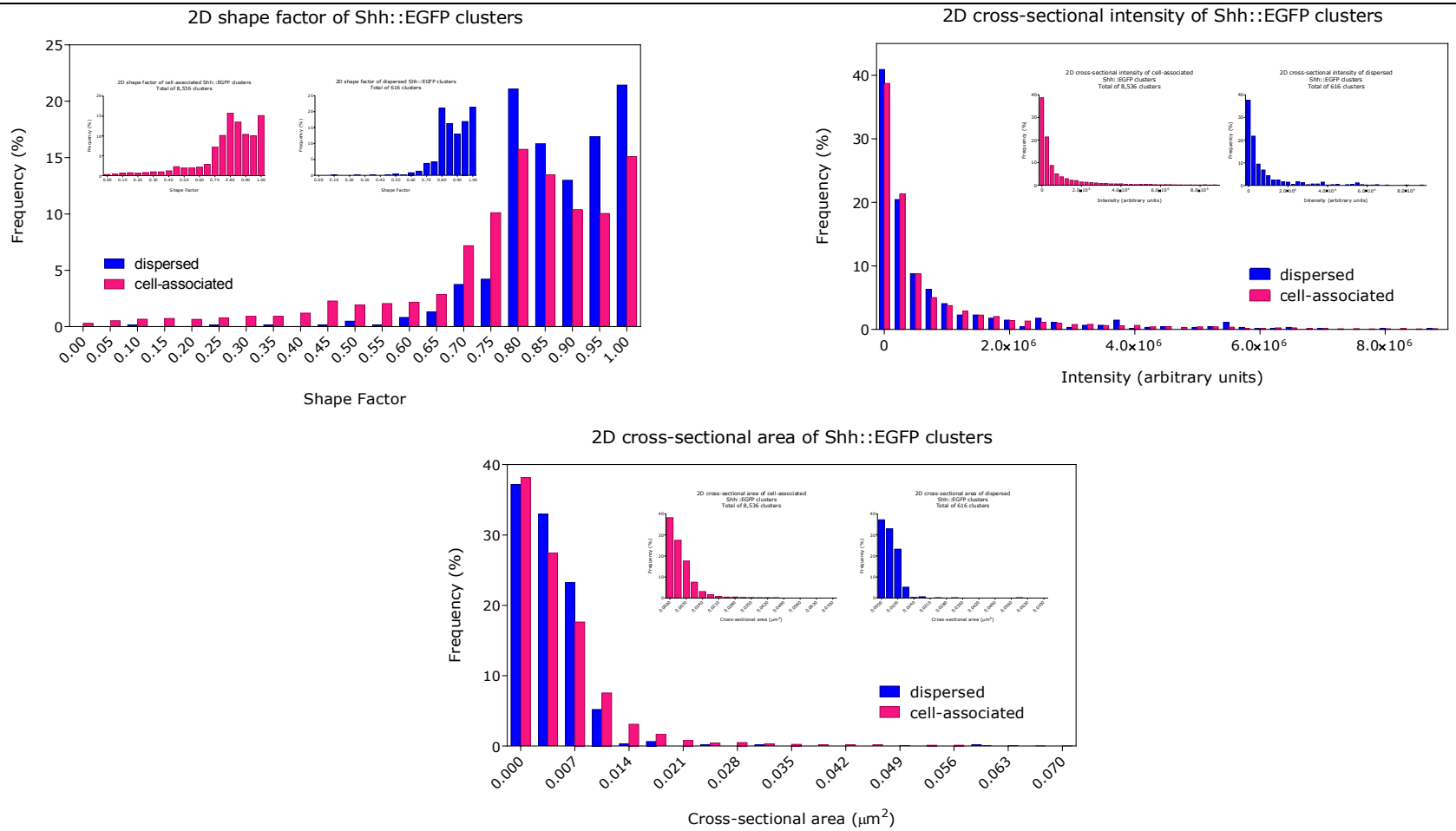

Figure 6.6.5. Tentative quantitation of several spatial attributes of Shh::EGFP clusters. Data presented here are extracted from a single COS-7 cell (shown in **Fig. 6.6.3**), which was transfected with *Shh::EGFP* and stained with anti-Shh pAb detected with a secondary Alexa Fluor® 555-conjugated antibody. The graphs are frequency histograms of the cross-sectional area, shape factor and intensity distributions of individual super-resolved clusters of EGFP-tagged Shh, based on fluorescence detected from Alexa Fluor® 555 which, unlike EGFP, labels only the extracellular protein. Based on findings in the subsequent chapter, particles found scattered around the cell are considered as clusters released by the cell (annotated in the graphs as 'dispersed') and have been plotted separately from those found residing on the membrane (annotated as 'cell-associated'). 'Shape factor' is a measure of shape regularity; 1 indicates perfect symmetry, *i.e.* a circle, whereas shape factors of diminishing values represent objects with progressively lower symmetry, *e.g.* long, thin objects. The cluster intensity is inextricably linked to the cross-sectional area and was thus used as a corroborative measure for the latter (refer to main text for details).

Taking into account that the detection of the clusters is executed with antibodies, which presumably bind only to the surface of the clusters but not within them, it is expected that a direct proportionality relationship should exist between the intensity and cross-sectional area measurements. Indeed, this appears to be the case, except for measurements below the expected resolution limit. This may be caused by the way different types of data are handled in *Volocity*: cross-sectional area is calculated using an algorithm called 'Marching Cubes', whereas intensity data are not. Performing the Marching cubes algorithm on the intensity information is not possible at present because it employs a mask and therefore does not contain information about the real intensity values. When assessing the surface covered by an object of interest of only a few pixels in size, simply counting the number of pixels it covers would lead to a large percentage error, due to pixelation. The Marching Cubes algorithm [Lorensen *et al.*, 1987] mitigates this error by identifying which pixel vertices are within the object and which are on the exterior, then draws a line that passes halfway between them. This line estimates the true boundary of the object more accurately.

In general, cluster sizes seem to follow an exponentially decaying trend, with larger clusters becoming exceedingly rare. In terms of the shape, there seems to be a tendency towards formation of round clusters, compared to elongated ones (shape factor of 1 signifies a perfect circle). These findings will have to be confirmed *via* an independent method, such as confocal microscopy in conjunction with deconvolution for improved resolution.

6. 7. Discussion

6. 7. 1. Summary of results

The main objective of this chapter was to study the nanoscale organisation of Shh on the surface of producing cells using the super-resolution technique, STORM. In pursuit of the objective, the following output was achieved:

- A TIRF-enabled pointillist super-resolution (PALM and STORM) microscope system, the first of its kind in Imperial College, laying the foundations for future super-resolution-mediated discoveries at the College;

- A semi-optimised protocol for carrying out direct STORM (*d*STORM) with two antibody-conjugated organic synthetic fluorophores, namely Alexa Fluor® 488 and 555;

- Characterisation and quantitation of the feasibility of two camera detectors for application to single-molecule imaging, and evaluation of the resolution power and localisation precision of super-resolution reconstruction software, given the present instruments, conditions and materials. All of this work was underpinned by rigorous mathematical and custom-written computational modelling.

- First attempt at quantitation of the physical attributes of cell-surface Shh oligomers.

6. 7. 2. Conclusions

The quality of super-resolution reconstructions achieved in this work suggested that it may not be sufficient to obtain reliable topological information about Shh in the sub-diffraction limit. This conclusion was drawn from a number of observations. For instance, the STORM validation experiments on filamentous proteins that were conducted yielded discontinuous filaments, a sign of an insufficient number of localisations. This deficiency would be translated as incomplete and potentially misleading Shh ultrastructure.

In some cases (*e.g.* **Fig. 6.4.1.1**), the background level during acquisition was high, adversely affecting the SNR. This background pollution may have been caused by unbound fluorescent antibody diffusing across the field of view. During the course of STORM series acquisition, some fluorescent signal originated from around the cell (**Fig. 6.6.3c**, **g**), which was picked up by the reconstruction software (**Fig. 6.6.3h**). Note that these outlier molecules cannot be observed in ensemble imaging (**Fig. 6.6.3b**), because they are too dim. Adjusting the software reconstruction settings in an attempt to discriminate against extracellular signal by increasing the signal threshold for molecular recognition did not remove this signal without also removing genuine signal from within the cell. This indicates that the extracellular fluorescence was emitted by the Alexa dye, and that the dye was more or less stationary (if it were not, it would be much dimmer and would contribute to building a background fuzz). The dye was therefore either bound to Shh, or it was non-specifically adsorbed to the coverslip. As will be shown in the next chapter, the former statement is likely to be true. Nevertheless, this emphasises the importance of rigorous washing for antibody-mediated STORM.

Utilising the sister technique PALM appears naturally to remove this encumbrance, since with genetically encoded fluorescent tags the detected fluorescence is virtually always specific. A secondary advantage of FPs – especially monomeric FPs – is that they do not have a proclivity for crosslinking and precipitation, a consequence of the multivalency of antibodies, and hence there is no danger of artificially clustering the proteins they highlight.

Nevertheless, genetic fusion of FPs, as already outlined above, is not always possible, and if nonetheless successful can have a perturbative effect on the function of the protein and on the overall metabolic state of the cell. Indeed, transfection with *Shh::EGFP* of the COS-7 cells used in this study caused a moderate rate of mortality. Another argument against genetically engineering FPs, specifically with relevance to the study of extracellular membrane-dwelling Shh, is that the intracellular fraction cannot be easily distinguished from that residing on the extracellular surface.

Fortunately, new biochemical technologies are being developed which give hope to finding a solution to this problem. A class of biosensors called fluorogen-activating proteins (FAPs) [Szent-Gyorgyi *et al.*, 2008] are a novel fluorescent detection system. FAPs are short peptide sequences of single-chain antibody fragments which have a strong affinity for exogenous fluorophores, called fluorogens. The fluorogens are specially designed dyes which are activated upon binding to FAPs, but remain dark otherwise. By genetically targeting the FAPs to the protein of interest and complementing them with membrane-impermeant fluorogens mixed into the liquid embedding medium, a suitable detection system of cell-surface proteins is devised. Any unbound fluorogens would be invisible and so would not interfere with the specific signal. Moreover, splicing a short peptide sequence (the FAP) to a gene would have a much smaller chance of perturbing the protein's normal dynamics, interactions and signalling activity, compared to an FP.

In spite of the difficulties encountered, super-resolution imaging was nevertheless carried out on Shh, as a proof of concept. The findings suggested that Shh did not preferentially assemble into clusters of any particular size, but the probability of forming larger clusters decreased dramatically according to what appeared to be an exponential decay law. Analysis of the dimensions of the structures indicated that the clusters tended to be predominantly round.

At the current juvenile stage that super-resolution is at, it is evidently more suited to qualitative, rather than quantitative, applications; this claim is consistently underpinned by the results in this chapter. It was reasoned that confocal imaging in tandem with deconvolution may yield a more reliable quantitative result, free of the concerns enumerated above, hence the next chapter is devoted to a deconvolution-aided conventional microscopy study of Shh nanoscale organisation in 2D and 3D.

Quantifying 2D images of 3D objects, such as cell-surface multimolecular clusters, imposes certain caveats. Undulation of the membrane may cause artificial clustering of proteins residing on the membrane when projected in 2D on the detector. This is particularly problematic in areas of high gradient, *i.e.* where the local membrane subtends a large angle with the substrate. A solution to a similar problem was offered recently [Owen *et al.*, 2013] by taking the membrane topology into consideration whilst analysing the degree of clustering of membrane

proteins. The method involves membrane staining with the dye DiI in order to capture the membrane's variation in depth in relation to the coverslip, whereupon the information is converted to a gradient map. A similar approach could be undertaken here to correct for potentially overestimated Shh cluster sizes.

The super-resolution branch of fluorescence microscopy nevertheless holds great impetus for the molecular and cellular biology research community. In the coming years, it can be foreseen that super-resolution image rendering will become more reliable and less susceptible to spurious noise; fluorescence marking will become more compact and the localisation uncertainty will be confined to the domain of the chemical bonds.

Recently, localisation precision to below 1 nm was achieved using single-particle averaging of the finite-sized fluorescent probes [Szymborska *et al.*, 2013]. The necessity for complex averaging of large volumes of super-resolution data to reduce position uncertainties may be eliminated with the recent development of a label-free methodology, documented in [Wang *et al.*, 2013], to visualise nanostructures lacking fluorescent properties (such as would be the case for most biological molecules under scrutiny). The STED-like optical scheme, termed Saturated Transient Absorption Microscopy (STAM), saturates electronic absorption in well-defined, sub diffraction-limit regions; the perturbed charge carrier density modulates the transmission of a second field, called the probe, which is the actuator of the imaging process. As with other techniques of the STED family, the illumination intensities involved are almost forbiddingly high for biological samples, alive or fixed (around 33 MW/cm^2 for the depletion beam alone is used in the Photonics Division, Imperial College). Therefore certain advances need to occur before the principle of STAM can be applied as an investigative tool in the biological sciences.

Novel scientific complementary metal-oxide semiconductor (sCMOS) detection technology has the potential to accelerate dramatically the rate of data acquisition, as well as enlarge the field of view [Huang *et al.*, 2013]. Historically, CMOS cameras have had relatively low quantum efficiency, making them unsuitable for single-molecule imaging. With recent progress in improving the detection efficiency, in combination with algorithmic tackling of the sCMOS-intrinsic, pixel-dependent readout noise, highly sensitive sCMOS cameras, such as the Hamamatsu Orca-Flash 4.0 V2, have been applied successfully to stochastic localisation imaging [Huang *et al.*, 2013]. This heralds the forthcoming widespread adoption of sCMOS into super-resolution applications.

7. Role of lipid modifications in the organisation and distribution of Shh clusters

The significance of Shh's post-translational covalent attachments is unresolved, and evidently remains out of grasp of the purely biochemical approach, such as collective use of precipitation, purification, fractionation, gel filtration and other techniques of this class. In a narrower sense, this traditional system of methods for studying biomolecules is virtually blind to the morphological and topological aspects of proteins, which may be key to unravelling this mystery.

This chapter is concerned with utilising deconvolved confocal optical sections to characterise the insofar unknown organisation of high molecular-weight Shh oligomers on the cell surface of producing cells, and the precise influence that the cholesterol and palmitate moieties each bestow on these properties. For this purpose, wild-type Shh, as well as three other artificial Shh constructs, devoid of either or both lipid attachments, were used throughout the experiments.

7. 1. Assessment of plasmid expression and relative protein expression levels

The protein expression levels of the Shh mutants and wild type were first assayed using a western blot (**Fig. 7.1**). All four plasmids were a gift from Dr Marta Świerczyńska, Max Planck Institute of Molecular Cell Biology and Genetics, Germany. The Shh sequence is human, and the mutants have been modified by: point-mutation of cysteine 24 to serine (Shh-C24S) to inhibit palmitoylation; inserting a stop codon after the signalling domain, thereby truncating the autocatalytic domain (Shh-N) and preventing cholesteroylation; or carrying out both manipulations on the same gene (Shh-NC24S). Upon receipt, the plasmid sequences were verified by re-sequencing.

The population of cells used in the western blot is the same as that used to prepare samples for immunostaining. Thus, the protein expression levels found in the western blot are indicative of those in the fixed and stained cells that were subsequently imaged.

The abundance of Shh expression was compared against a positive control (HEK293 cells stably transfected with Shh) and two negative controls: HEK293 and COS-7 cells subjected to the same transfection protocol, except without adding DNA. **Fig. 7.1** shows that the wild-type and mutant forms of Shh (Shh-FL and Shh-NC24S, Shh-N, Shh-C24S, respectively) are expressing

to a similar level (loading control shown below blot). Quantitation using ImageJ (U. S. National Institutes of Health, USA) indicates that the relative abundance of all Shh fractions (precursor and processed) in lanes 2 to 7 in **Fig. 7.1**, normalised first with respect to GAPDH, then to stably transfected Shh levels (lane 2), is 1 : 0.96 : 1.35 : 1.19 : 1.21 : 1.28. Quantifying specifically the processed Shh variety, the relative ratios – in the same order as above – are 1 : 0.78 : 1.62 : 1.40

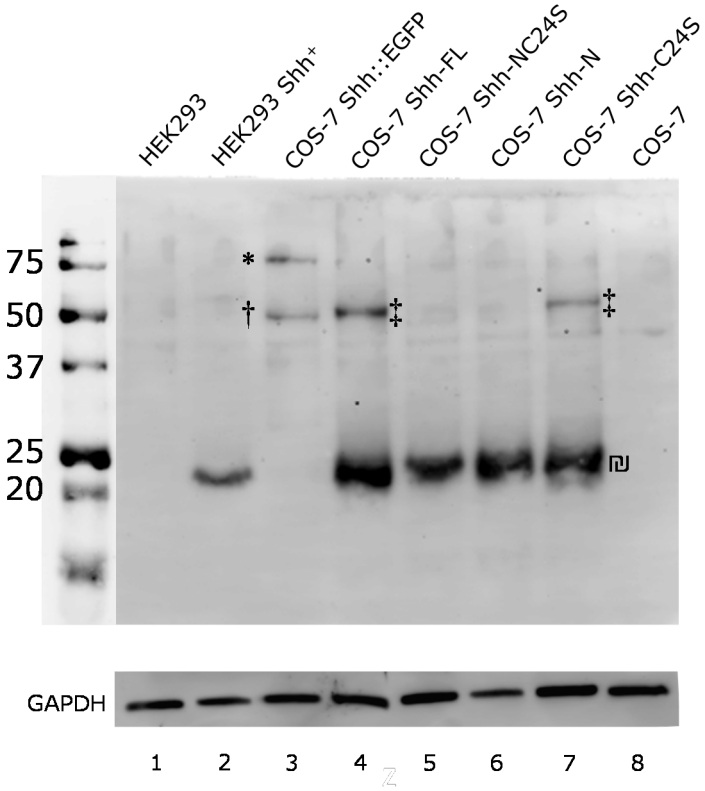

Figure 7.1. Western blot of Sonic hedgehog wild-type and mutant protein expression. Before commencing microscopy analysis of cluster characteristics, a western blot was carried out to verify that the mutant and wild-type Shh proteins were expressing equally, and to ensure a subsequent fair visual comparison. Cell lysate in this experiment was normalised for protein concentration and loaded volume. Lanes 1 and 8 display negative controls; HEK293 and COS-7 cells do not naturally express detectable Shh. Stable transfection of HEK293 cells with Shh serves as a positive control in lane 2. Note that, out of the wild type and Shh mutants, only the truncated proteins (lanes 5 and 6) lack the band at ~50 kDa normally occupied by the full-length precursor form of Shh. The bands observed near the 20 kDa level are the processed, active forms of Shh. Expression of Shh::EGFP fusion protein is also shown on this blot. Note that the band at ~50 kDa in this lane (lane 3) is not the precursor; the precursor is displaced upwards from the native ~50 kDa by the size of the fluorescent tag (25.9 kDa), so that it appears close to the 75 kDa mark, and processed Shh has correspondingly shifted upwards into the precursor's usual place. Key: * Shh::EGFP full-length protein; † Shh-N::EGFP; ‡ Shh full-length protein; ₪ Shh-N. GAPDH, with a molecular weight of ~37 kDa, was used as a loading control.

: 1.48 : 1.54. Since most reports in the literature note that the majority of acylated and cholesterol-modified Shh is localised to the plasma membrane [Grover *et al.*, 2011][Creanga *et al.*, 2012][Palm *et al.*, 2013], the figure suggests that the cells most likely produce similar quantities of Shh wild type and mutants on the cell surface. Shh-N (lane 6), however, may be very similar in substance to Shh-NC24S (lane 5), since mammalian cells which over-express a protein do not tend to palmitoylate it efficiently [Pepinsky *et al.*, 1998][Baker *et al.*, 2007].

7. 2. Deconvolution of serial optical sections

In order to be able to view the multimeric structures in more spatial detail, it was necessary to obtain a series of optical sections of the cells using a confocal microscope, and deconvolve them afterwards. Deconvolution must be performed with caution since improper application of deconvolution may lead to the introduction of diverse artefacts and spurious objects into the image, rendering a quantitation analysis of the resulting image meaningless. The following few sections describe the technical preparatory details of the deconvolution process and explain the careful selection of the deconvolution parameters, in order to avoid pitfalls.

7. 2. 1. Determining the Instrument's Point-Spread Function (PSF)

Deconvolution on a dataset can be carried out either with a theoretical PSF, calculated using electromagnetic diffraction theory based on the physical parameters of the microscope (NA, λ_{exc}, λ_{em}, n), or using an empirically derived PSF. The theoretical calculation of the PSF can either be made with a paraxial approximation or with widefield integrals [Pawley, 2006][van der Voort, 1990]. Numerical predictions, however, do not take into account misalignments and shortcomings of the optical components, therefore real PSFs are wider (typically by >20%) and more asymmetric. In principle, the empirical PSF is capable of producing the highest-quality deconvolution results. However, experience reveals that moderately aberrated PSFs in fact perform worse than ideal PSFs calculated in optimal imaging conditions [Parton *et al.*, 2006]. Overall, treatises on the deconvolution technique recommend determining the method that delivers the best results for a particular data type through a trial-and-error approach. Following this guideline, both the theoretical and measured PSFs were applied to the data, and the better method was selected based on the perceived success and integrity of the restored data, as will be described below.

The Huygens Essential software package (Scientific Volume Imaging, The Netherlands)

permits to 'distil' empirical PSF data from 3D images of sub-resolution microspheres. It achieves this by registering and averaging multiple microspheres, and correcting for their finite size. The exact procedure and materials for acquiring the PSF data are described in section 5. 2. 3. of the Materials and Methods chapter. The data set was then processed with the PSF distillation tool of Huygens Essential and the microscope PSF obtained (**Fig. 7.2.1**, right).

Although the optical density, and thus presence of aberration sources, varies across the image in both lateral and axial direction, the deconvolution software assumes a bilaterally symmetric depth-dependent, but radially invariant, PSF. Measurement of the PSF's full width at half-maximum (FWHM) yielded an average width in the *x-y* plane of 278 nm and in the axial direction of 519 nm. By comparison, the corresponding theoretical values for the same excitation wavelength (488 nm) and objective *NA* (1.4) are 178 and 455 nm [Cole *et al.*, 2011], and the computer-generated ideal PSF shown on the left of **Fig. 7.2.1** measured 205 nm in the *x-y* plane, and 614 nm on average in the *x-z* and *y-z* plane. The differing theoretical FWHMs depend on the method of calculation, as already stated earlier in this section.

Asymmetry in the axial direction is commonly a consequence of spherical aberration, caused by refractive index mismatch between the objective, immersion oil, embedding medium and/or sample, or varying coverslip thickness [Pawley, 2006]. Radial asymmetry can be expected from misaligned (decentred) or tilted optical components with regard to the z-axis. The reason for the much wider lateral-plane PSF (almost 100 nm wider than expected) in this case, however, is due to a differential interference contrast (DIC) prism and analyser being present in the detection path, splitting the incoming fluorescence light into two closely spaced beams.

The DIC configuration was intentionally selected for the high contrast that it generates in order to detect the boundaries of the cells, after it was discovered that Shh protein released in the extracellular environment by the cells while they were alive, had remained intact on the surface of the coverslips. It was reasoned that this was indeed Shh, and not some form of contaminant, since the fluorescent signal in the intercellular space was observed only in Shh-transfected (all four variants) and not in mock-transfected or in negatively stained specimens.

The unenvisaged, but attractive, notion of studying potential differences between differently localised Shh multimeric forms spurred the decision to collect information about the two Shh populations separately from each other. Thus, by highlighting the cells clearly, the DIC transmitted-light imaging configuration offered a convenient way of differentiating between Shh present on the cell membrane and that on the substratum. Regardless, the aberration this incurred on the fluorescence channel signal, which was gathered alternately with the white-light DIC channel while the birefringent prism was kept continuously in place, compelled the need to determine and apply a method for its correction.

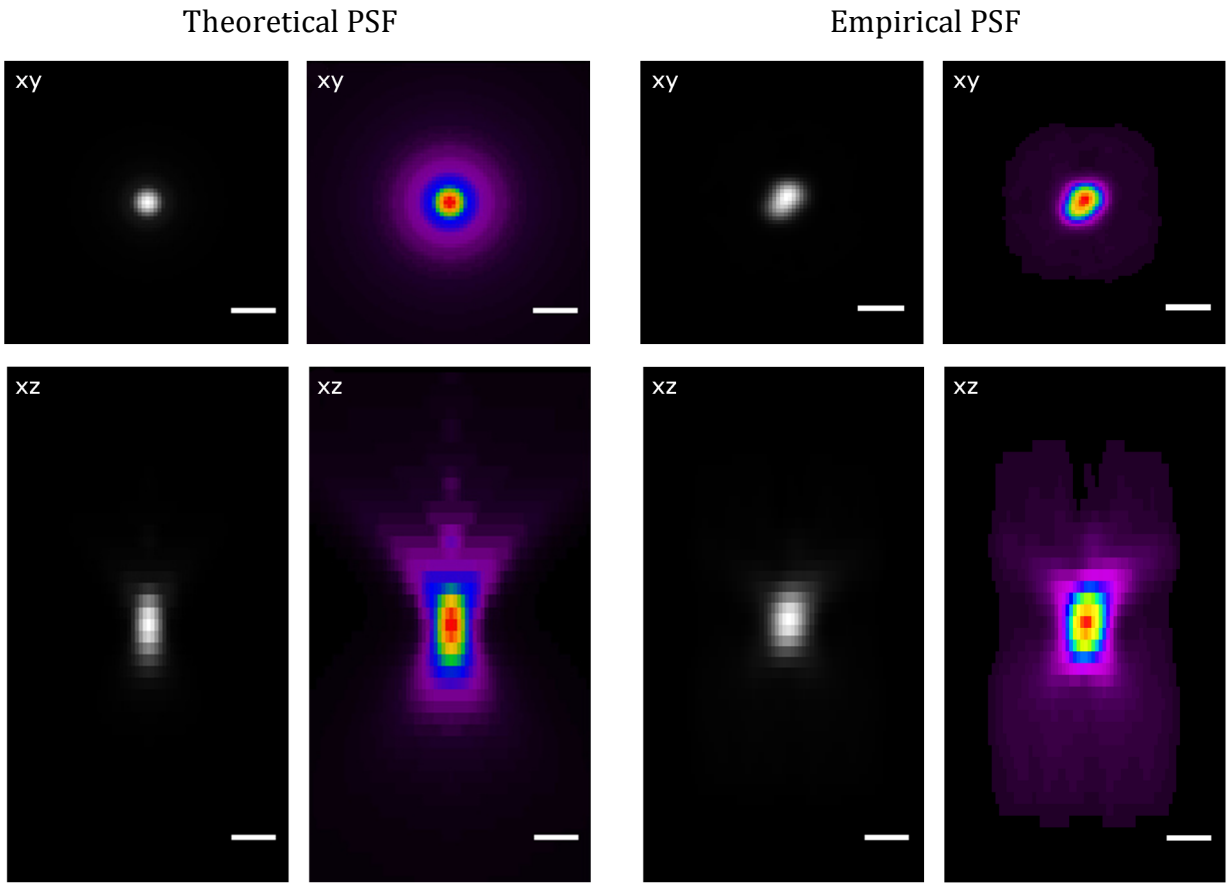

Figure 7.2.1. Theoretical and measured point-spread functions (PSF) for the imaging system used in this chapter. The theoretical PSF was determined using the online PSF Calculator tool, http://www.svi.nl/NyquistCalculator, which employs electromagnetic diffraction theory for the calculation. In the false-colour images, a gamma correction factor of 1.7 was applied to boost lower intensities and emphasise the overall shape of the PSFs. Scale bar: 500 nm.

7. 2. 2. Correction of DIC prism-incurred aberration

The origin of the radially oriented inhomogeneity lies in the unintentional distortion of the fluorescence image, caused by passing of emitted fluorescence light through the DIC prism of the objective, effectively creating a 'double' image.

One means of reversing this effect is to apply Fourier theory of deconvolution (Background and Theory chapter) to 'subtract' the second image. In order to do this, three parameters have to be determined: the orientation of the shear, the shear distance and the relative brightness of one image with respect to the other. The first two can be measured with some degree of accuracy from the Fourier transform of the sub-resolution microspheres used to characterise

the microscope's PSF (**Fig. 7.2.2.1**). The third parameter requires an initial guess, based on a qualitative judgement.

The measurement, nevertheless, is not exact and therefore introduces unavoidable noise into the image, which is aggravated by dividing the original image by this estimate [Russ, 1998], leading to an output image greatly hampered by artefacts. In order to overcome this, it is possible to perform a parameter search in the vicinity of the initial estimates to arrive at an optimal result. Such an iterative algorithm was written and implemented in a Matlab routine by me (DIC correction, Appendix B), and the numerous corrected outcomes were subsequently inspected visually. Overall, three parameter combinations – one of which was the original measurement itself – were found to render images as close as possible to what was expected (perfectly round microspheres). The circularity of the microspheres was measured as the ratio of the vertical FWHM and the horizontal FWHM. Magnified views of the topmost microsphere (**Fig. 7.2.2.1a**) in the images corrected with these parameters, as well as examples of the artefacts produced by ill-fitting parameters, are shown in **Fig. 7.2.2.2**.

Following the retrieval of the three best correction parameters, the aberrated *z*-stack of microspheres was corrected and deconvolved with either the theoretical or measured PSF.

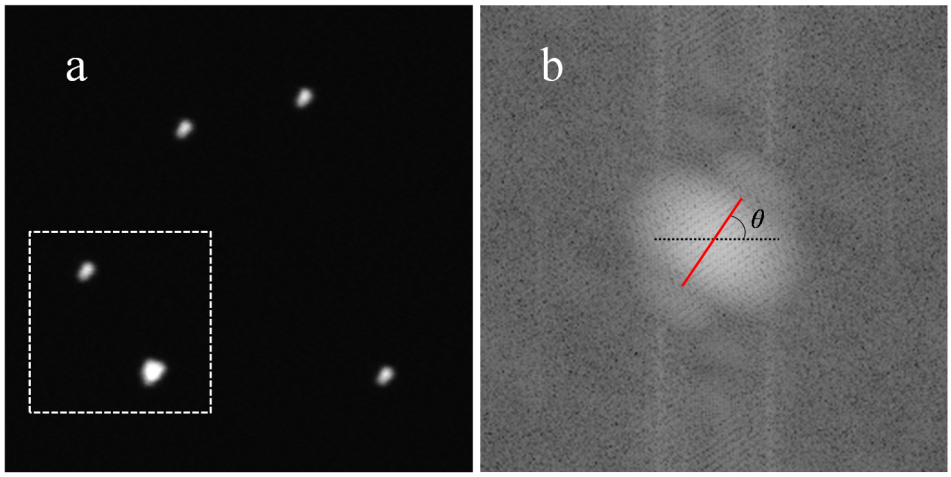

Figure 7.2.2.1. Method for correcting image duplication incurred by DIC optics inserted in the imaging path. (a) In-focus slice of the *z*-stack of sub-resolution microspheres used to measure the microscope PSF. (b) Logarithmic display of the power spectrum Fourier-domain representation of the image in (a). Working with the image in Fourier space allows for a much more accurate measurement of the differential interference contrast (DIC) shear magnitude and direction. In frequency space, the latter are given, respectively, by the red line, measuring the separation of the zero values arranged in parallel, oblique straight lines, and the angle θ. These quantities can then be converted into real space to obtain their spatial-domain equivalents.

Then, starting from the original stack, the same steps were repeated in reverse order. Thus, all possible ways of combining optimal parameters, sequence of events and PSFs were tried and the one arriving at the most plausible answer was selected. **Fig. 7.2.2.3** shows the systematic trial-and-error method for the correction parameter that conveyed the overall best result (bottom right corner). On the grounds of this result, it also became clear that the theoretical PSF presented the better option in this case than the empirical PSF, so it was used to deconvolve all subsequent image data.

The correction reduced the FWHM of the PSF in the imaging plane from 278 to 235 nm.

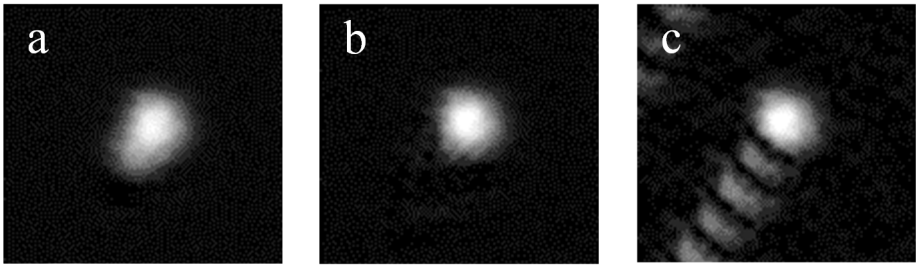

Figure 7.2.2.2. Compensation for differential interference contrast prism aberration. Magnification of the topmost microsphere in Fig. 7.2.2.1a. Ill-corrected versions, arisen from non-optimal correction parameter choices, are shown in (a) and (c). The optimal correction, substantiated by the near perfect roundness of the object, is shown in (b). All micrographs in this figure have been oversampled (interpolated) by a factor of 4, in order to allow the reader a better perception of the object's shape, and are shown prior to deconvolution.

7. 2. 3. Choosing the optimal deconvolution parameters

7. 2. 3. 1. Choosing the Restoration Method

From a choice of several deconvolution algorithms offered by the Huygens Essential suite, the one best suited to the character of the image data was chosen. This was the Quick Maximum Likelihood Estimation (QMLE) method. The iterations of the QMLE are approximately five times more efficient than the Classical Maximum Likelihood Estimation Method (CMLE) and are more economical in time. For high SNR cases, such as this, both methods converge to the same result, although the QMLE arrives at the result after much fewer iterations.

The MLE procedure is based on the idea of optimising the likelihood of an estimate of the object, given the measured image and the PSF. It is a non-linear iterative method and it al-

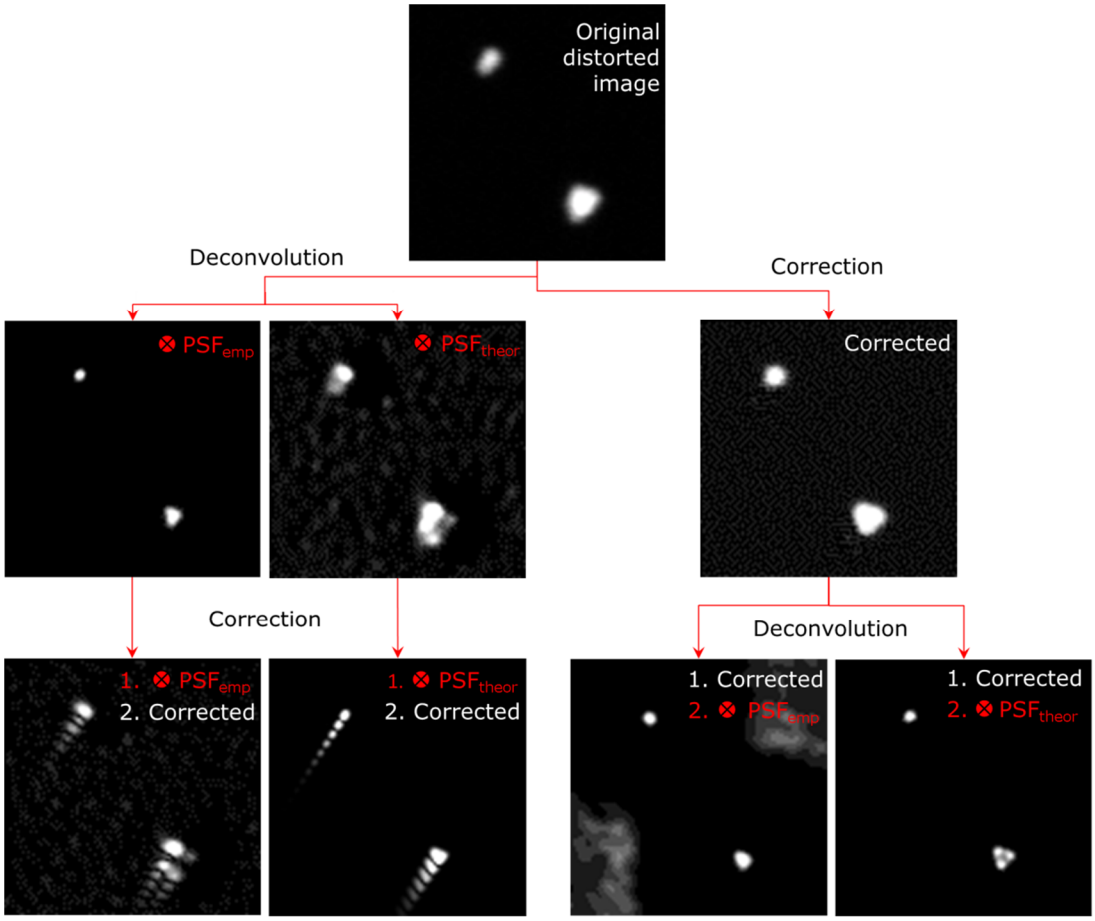

Figure 7.2.2.3. Confirmation of the validity of the differential interference contrast correction method. All panels show a magnification of the microspheres, of diameter 175 nm, in the boxed region of **Fig. 7.2.2.1**. The bottom right panel demonstrates that, by correcting the raw images for differential interference contrast (DIC) aberration first, the underlying features are correctly resolved upon deconvolution (a cluster of three microspheres is revealed). This is not the case if the raw images are unaltered prior to deconvolution (two panels on the left in the middle row), or if they are DIC-corrected post deconvolution (two leftmost panels in the bottom row). Note that, in this case, using a theoretical PSF is more appropriate than the empirical PSF: deconvolving the empirical PSF out of the image causes the microspheres to appear as a monolithic object (third panel from left to right in the bottom row). Key: ⊗ denotes deconvolution; PSF_{emp}, empirical PSF; PSF_{theor}, theoretical PSF.

lows for the recovery of some lost information. The likelihood is computed by a variable called the 'quality criterion' under the assumption that the noise in the image is governed by Poisson statistics. The quality criterion is a measure of the quality of the estimate, which is gradually improved with every iteration. It is directly derived from the concept of Maximum Likelihood, and is based on the I-divergence [Csiszár I., 1991], also known as relative entropy and Kullback-

Leibler distance. It is a global value computed over the entire image and is used as a stop criterion to terminate the deconvolution iterations.

In other words, the quality criterion is an optimal measure for quantifying the difference between two non-negative images with a single number. It was developed with an in-built mechanism of escaping misleading solutions to the deconvolution problem. The quality factor reported by the Huygens Essential software is the ratio of the I-divergence between the first image estimate and the measured image, divided by the I-divergence between the current image estimate and the measured image.

7. 2. 3. 2. Choosing the optimal signal-to-noise ratio

In confocal microscopy images, the low light levels that are being detected during acquisition mean that the SNR is a function of photon counting noise. The SNR is often easier to estimate for low-SNR confocal images. One method involves detecting single-photon events in the background, which manifest themselves as isolated 'spikes'. The value of the spike roughly indicates the number of grey levels that correspond to one photon. Obtaining an estimate of the SNR is then straightforward, since it is equal to the quotient of the maximum intensity in the image and the single-photon grey level value. However, the failure to spot any clear, single-photon events in the background of the raw images implied that the SNR of the recordings was probably quite high. A different approach for estimating the SNR was therefore adopted.

In order to ensure that the SNR selected for deconvolution matched that of the raw images, this parameter was estimated in three independent ways. The first method was centred around an iterative improvement of the deconvolved dataset, based on a well-informed initial guess of the SNR. The SNR parameter was initially set to 20, a rule-of-thumb value expected for an average confocal microscopy image. After inspecting the resultant restored image and verifying that no undesired effects had been introduced by the process, the SNR was increased. If the background had not been removed effectively, the average background estimate was elevated. This procedure was repeated until the highest SNR value was found that did not create artefacts by enhancing noise, and there was minimal background residue. This strategy of arriving at the optimal SNR, however, suffered from an inextricable user dependence and therefore bias. Indeed, due to the complexity of the image data, qualitative assessment of the restorations led to ambiguous conclusions. It was felt that the selection process was therefore too overshadowed by the possibility of human error, and for this reason alternative, more reliable estimation methods were sought.

The second method employed the 'Huygens Remote Manager' (http://hrm.svi.nl/) 'SNR

estimator' feature, a web-based extension of the Huygens software. The programme provided more accurate guidance for determining the real SNR, through creating synthetic images with added known noise level, subsequently comparing the array of artificially generated images with the real dataset and selecting the one which most closely matched the dataset.

The third and final approach was an experimental measurement of SNR, which was undertaken as follows. In the first place, the SNR of an image is expressed as the average intensity, divided by the standard deviation:

$$SNR = \frac{\bar{I}}{s}. \qquad \textbf{Eq. 7.1}$$

The SNR can be estimated by determining s around the strongest signal in the image (deemed to be the signal we are interested in recording). To obtain a true value for s, it is necessary to perform this measurement on a homogeneous sample consisting of a uniform, high-intensity plateau so that, in the absence of any experimental artefacts, any noise present in the image of this slide would be solely due to the shot noise, s An autofluorescent Chroma plastic slide approximates such a perfectly uniform surface.

The intensity in a digital image is usually recorded in terms of greylevels, not intrinsic numbers of photons. The two quantities are related by an arbitrary constant, called the conversion factor. Since we assume that the presence of noise is solely due to Poisson statistics of the photon detection events, then if $\overline{N}$ is the average number of photons, $\bar{I} = c \cdot \overline{N}$, $s = c \cdot \sqrt{\overline{N}}$. Invoking **Eq. 7.1** therefore yields SNR = $\sqrt{\overline{N}}$.

A yellow and a green autofluorescent Chroma slide were used for the measurement. A snapshot of each slide was taken with all microscope acquisition parameters preserved exactly as when the biological data were acquired (this, amongst others, included laser power, laser gain and offset, detector resolution, zoom, excitation and emission bands, and pinhole size.) The green fluorescent slide produced a signal-to-noise measurement of 34.5, whereas the yellow slide gave a similar reading of 31.7. This was reassuringly close to the suggested value of the Huygens Remote Manager's SNR estimator, which was 30. The MLE restoration algorithm of Huygens Essential does not require a very precise establishment of the SNR, therefore no further effort was made to fine-tune the SNR parameter.

7. 2. 3. 3. Background estimation

The background is estimated automatically by the software; it is the average background level.

The software-generated estimate was nevertheless verified manually by probing the intensity values in dark areas where any signal of importance was evidently absent.

7. 3. Processing and quantitation of the deconvolved data

7. 3. 1. Assessment of the deconvolution outcome

All of the deconvolved files were individually examined visually for artefacts, prior to being subjected to quantitation. Files with features unwarranted by the corresponding pre-deconvolution file were excluded from further analysis. Discarded files contained, for example, visible data only along straight lines spanning the entire image, which was indicative of the recording process having been corrupted, or a uniform random pattern throughout the entire stack of optical sections – even in planes above and below the cells – which was assumed to be noise that the deconvolution algorithm had failed to suppress.

True restorative deconvolution algorithms, such as the one used in Huygens Essential, attempt to relocate light back to the correct point in space; therefore the total fluorescence signal is conserved. In spite of this, in certain circumstances, this conservation may be violated – for example, during reassignment of distant, dim light, where the SNR is low and noise is dominant, and during evaluation and removal of noise. As a means of verification, intensity comparisons between deconvolved data should therefore be analysed together with the raw (non-deconvolved) data. Structural and morphological information, on the other hand, is independent of absolute intensity values, and volumetric analysis can be performed with a high degree of confidence. Since one is interested only in the physical traits, and not in the absolute intensity itself, it was deemed unnecessary to quantify raw images side by side with the deconvolved ones.

An example of the image improvement after deconvolution is shown in **Fig. 7.3.1**. It should be noted that the software automatically removes any objects smaller than the PSF, as such an object could not have, in practice, been detected by the microscope.

The deconvolution process grants a certain resolution improvement – both in-plane and axially. This is usually not inferable straightforwardly from the data. **Fig. 7.2.2.3** provides evidence that deconvolution on its own can achieve a lateral distance discrimination of at least 175 nm (this is deduced from the apparent success in resolving three adjacent microspheres of size 175 nm in the bottom right corner). In order to determine more precisely the resolution capabilities of deconvolution on our data, a *z*-stack of 20-nm nanodiamonds (kindly provided by Hugo Sinclair, Department of Physics) was obtained (without the DIC analyser obstructing the path

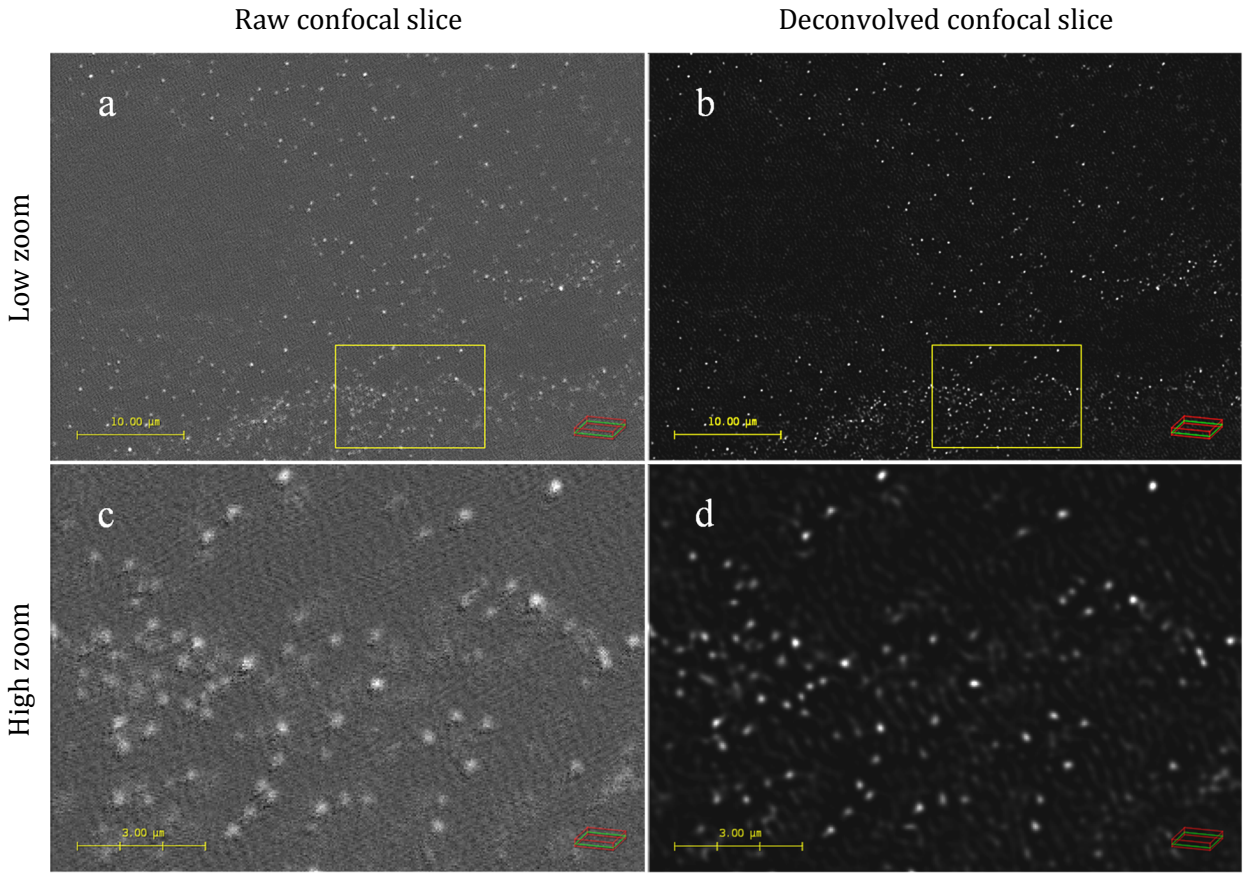

Figure 7.3.1. Comparison of a typical deconvolution outcome with raw image data. The panels show a single image plane cutting through the middle of a cell, immunostained for full-length Shh with anti-Shh pAb detected with a secondary Alexa Fluor® 488-conjugated antibody. (a) and (b) are, respectively, unprocessed and deconvolved confocal images. The area on the left-hand side where Shh is scarce is where the cell nucleus is situated. (c) and (d) are magnifications of the region outlined by the yellow boxes in (a) and (b) respectively. The deconvolved images clearly seem superior to the raw image data. Note that the wave-like pattern present throughout the raw image and particularly visible in high magnification (c), is not a consequence of the DIC correction procedure, since it is also present prior to applying the DIC correction (data not shown). It is possible that the faint filiform clusters visible in (d) are artefacts, whereby the deconvolution algorithm has allowed the wave-like noise pattern in (c) to propagate into the deconvolution result. In any case, these do not affect subsequent cluster quantitation, since their intensity falls approximately five times below the intensity threshold which was applied prior to cluster approval for quantitation.

of imaging) and subsequently deconvolved with the usual parameters. The dimensions of isolated nanodiamonds were measured in all three dimensions, before and after deconvolution.

Prior to deconvolution (and after DIC correction), their measurements were 257 nm in *x*, 247 nm in *y* and 1,021 nm in *z*, on average. After deconvolution, they were 157, 152 and 487

nm, in *x*, *y* and *z*, respectively. The resolution improvement is therefore 1.6 in *x*, 1.6 in *y*, and nearly 2.1 in *z*.

7. 3. 2. Cluster measurement strategy

Shh clusters situated on the cell membrane were measured separately from those occurring in the extracellular space. Presumably, clusters found in spaces where cells were absent were released by the cells prior to being fixed; a plausible explanation for their presence is that they had become adsorbed to the glass substrate, thus escaping being washed away with the culture medium, before the formaldehyde solution was applied.

Each three-dimensional image stack was analysed two-fold: regions of the field of view covered with cells (**Fig. 7.3.2b**) were queried for cluster volume, intensity, surface area and shape factor (clarified below); regions where cells were lacking (**Fig. 7.3.2c**) were assessed for the same parameters, albeit keeping the figures in a separate record. Ambiguous areas where this distinction could not be made with confidence were excluded from the measurement, in order to avoid mixing the populations' characteristics. As well as in three dimensions (*x*, *y*, *z*), the clusters were examined in two dimensions (*x*, *y*) to remove any distortion effects caused by the inherent differential resolution in the transverse and axial directions.

The shape factor is a numerical indication of how closely a 2D object resembles a circle, or a 3D object a sphere. The shape factor is 1 for a perfect circle or sphere and decreases for more irregular shapes. In 2D, the shape factor is expressed with the formula

$$S.F._{2D} = 4\pi \frac{A}{P^2}, \qquad \textbf{Eq. 7.2}$$

where A is the object area and P the object perimeter. In three dimensions, the shape factor is the ratio of the surface area of a sphere, having the same volume as the object, and the surface area of the object itself. The expression becomes

$$S.F._{3D} = \frac{\pi^{\frac{1}{3}}(6V)^{\frac{2}{3}}}{A'}, \qquad \textbf{Eq. 7.3}$$

where V is the volume of the object and A' is its surface area.

Collecting a large enough sample size is important, if one is to avoid drawing an incorrect inference from the data. To ensure that the statistical samples gathered were of sufficient

statistical power, a total of 122 Shh-FL, 130 Shh-C24S, 163 Shh-N and 87 Shh-NC24S partial or whole cells were analysed.

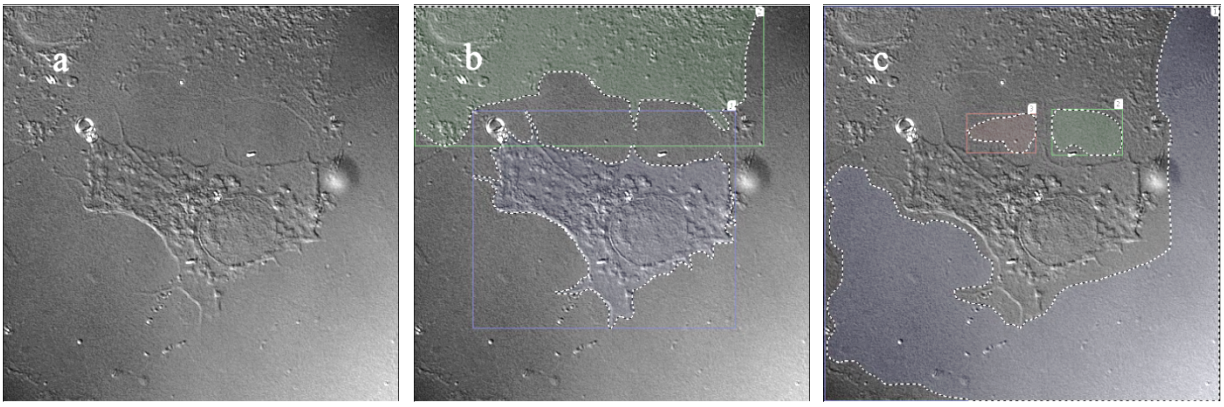

Figure 7.3.2. Selection of cellular and extracellular regions for cluster quantitation using the software package *Volocity*. Regions of cell membrane-bound Shh multimers were quantified separately from regions not in direct contact with the cells. The areas were drawn by hand in a qualitative manner. To minimise misidentification of free-space clusters as membrane-bound, and *vice versa*, only areas that could clearly be distinguished as one or the other were isolated for the quantitation. (a) DIC transmitted light image. (b) Selected regions of interest for quantitation of membrane-bound Sonic hedgehog clusters. (c) Selected regions of interest for quantitation of extracellular (dispersed) clusters.

7. 4. Two- and three-dimensional characterisation of the dimensional properties of Shh multimers

7. 4. 1. Data presentation format and resolution considerations

Fig. 7.4.1.1–5 depict the spatial data obtained in the previous section, in histogram format. It was recognised that the choice of binning was vital for visualising the correct shape of the underlying distribution. Therefore time was dedicated to trying different histogram bin sizes and discerning which one most likely brought out the true distribution profile.

Switching from fine binning, showing very high columns next to empty ones, to coarser, rendering a more dynamic filling of the columns, suggested that the coarser was more appropriate. On the other hand, too coarse a binning would cause some of the subtleties of the distribution to disappear. By observing the changes in the histogram appearance by making small increments, and replicating this strategy over the histograms of all physical attributes concerned,

it was arrived at the most plausible distributions shown in the figures below.

Note that, without deconvolution and the Marching Cubes algorithm, confocal microscopy would have imposed a resolution cut-off at 0.04 μm^3 for the volume measurements, 0.73 μm^2 for the surface area, and 0.08 μm^2 for the cross-sectional area, rendering it impossible to visualise the distributions' pattern. According to measurements of the resolution improvement with deconvolution, in combination with measurements of the (corrected) PSF, the final resolution expected here is 147 nm in the *x*-*y* plane and 247 nm in the *z*-direction. Therefore, the expected minimal volume resolution is 0.005 μm^3, minimal surface area is 0.19 μm^2 and minimal cross-sectional area is 0.02 μm^2.

These figures, however, do not incorporate the enhancing effect of the Marching Cubes algorithm, which contributes additional spatial precision. Most of the advantage of the algorithm actually consists of undoing the pixelation of the clusters being measured, and refining their boundaries. Unable to obtain a quantitative report on the non-standard version of the algorithm employed by *Volocity*, the precise refinement that the Marching Cubes algorithm provides remains presently unknown.

However, judging by the fact that there are yet smaller features to be found in the histograms, combined with the fact that the FWHM is only an approximate measure of resolution, it was estimated that features up to five times smaller in volume, ten times smaller in surface area and seven times smaller in cross-sectional area could be detected than was expected. Translated into directional resolution, that equates to 53 nm in *x* and *y*, and 62 nm in *z*, assuming that the smallest resolvable structure is a parallelepiped with equal resolution in the *x*-*y* plane. Since the FWHM is not a real indicator of the resolution capability of the microscope (as explained in section 2. 2. 3. 3. 2.), and actually underestimates it, I believe that the resolution improvements found by *Volocity* are real.

7. 4. 2. Comparison of wild-type and mutant Shh multimerisation tendencies

An interesting question is whether the cell-tethered protein structures bear the same physical characteristics as their counterparts which were released into the extracellular environment. Answering this question would glean insight into whether any rearrangements take place on the surface of the cell prior to multimer release.

Comparing the magenta columns against the blue in the histograms seems to suggest that all Shh variants, bar the Shh-C24S mutant, have very similar physical characteristics both on and off the cells. In order to determine whether the cell-surface and extracellular clusters' surface area, volume and shape factor distributions belong to the same parent distribution (*i.e.*

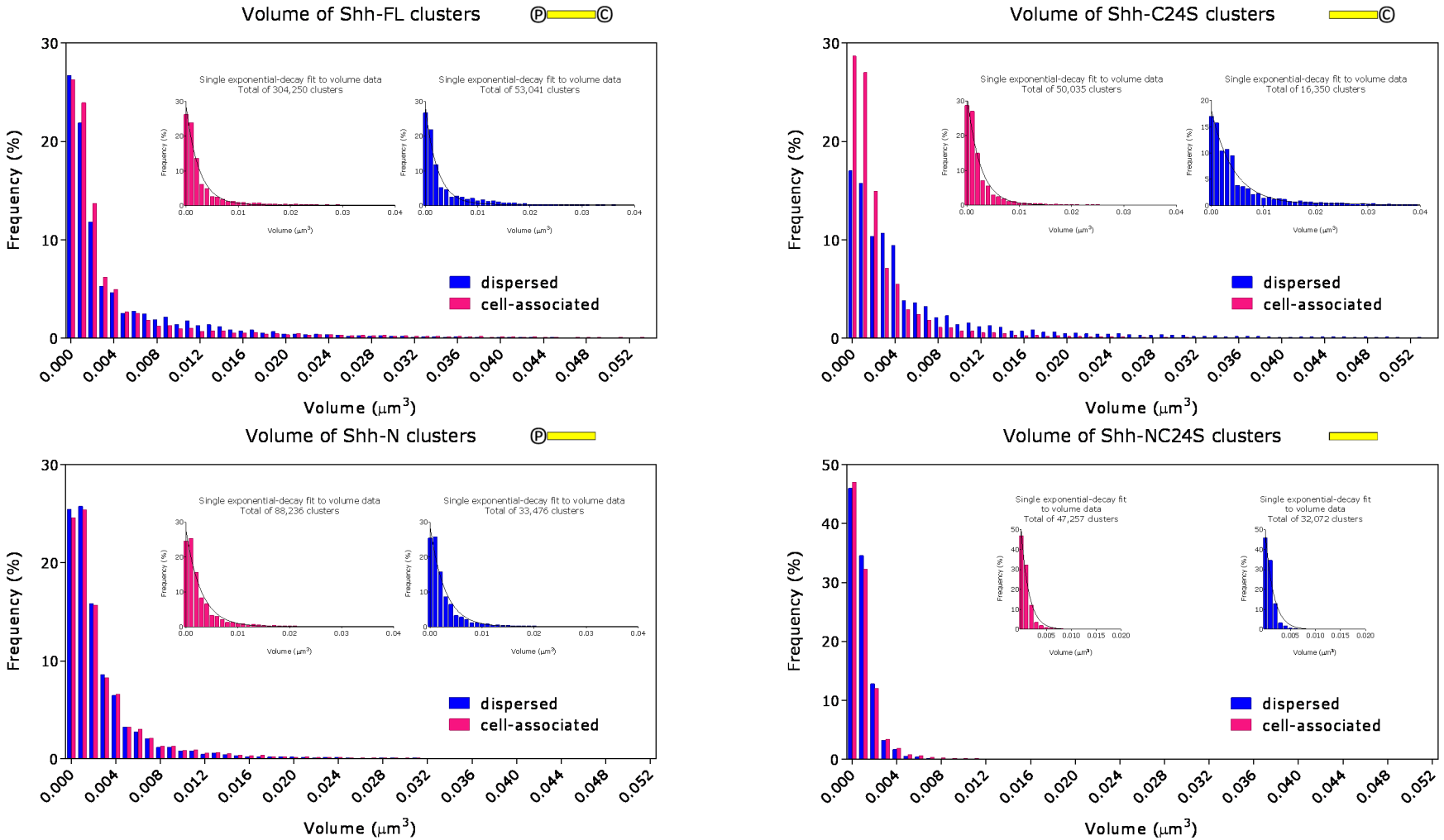

Figure 7.4.1.1. Frequency distribution histogram of the volume of individual cell-associated and dispersed clusters from all four Shh variants. The clusters were generated by COS-7 cells transiently transfected with wild-type (Shh-FL) or any one of three other lipid modification mutants: Shh-C24S (lacking palmitate), Shh-N (lacking cholesterol) and Shh-NC24S (missing both lipid moieties). Ⓟ denotes palmitate, © – cholesterol. The cell-associated and dispersed cluster data are plotted together (separately, inset). They appear to decrease monotonically, thus they have been fitted tentatively with a monoexponential decay curve (black), throughout giving a goodness-of-fit, $R^2 > 0.96$. The fit parameters are summarised in **Table 7.4.2**. Note that the unlipidated mutant outputs higher amounts of small clusters, as well as smaller clusters on average, in contrast to the other variants. Data are representative of 122 Shh-FL-, 130 Shh-C24S-, 163 Shh-N- and 87 Shh-NC24S-expressing cells from two transfection experiments.

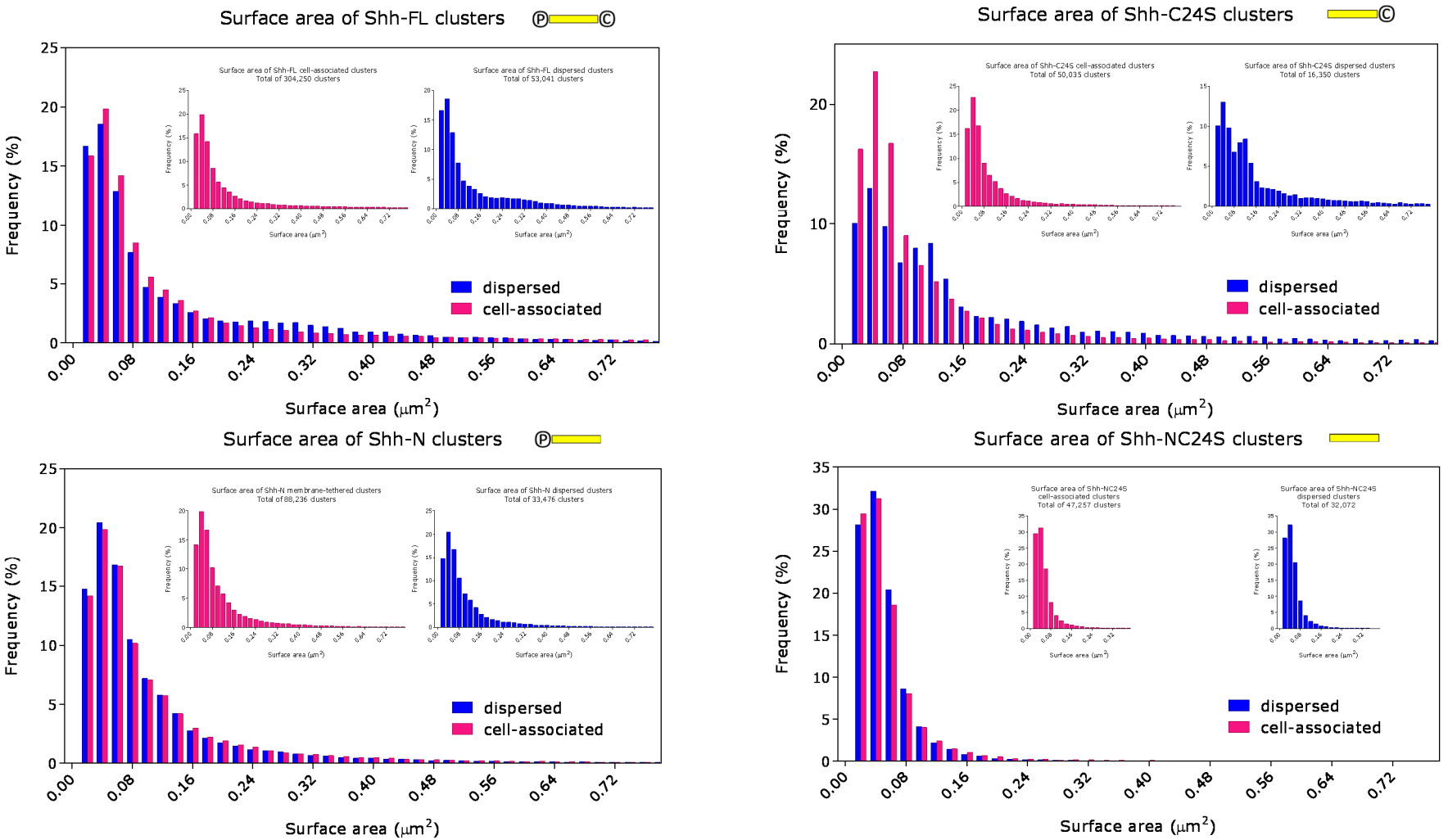

Figure 7.4.1.2. Frequency distribution histogram of the surface area of individual cell-associated and dispersed clusters from all four Shh variants. The clusters were generated by COS-7 cells transiently transfected with wild-type (Shh-FL) or any one of three other lipid modification mutants: Shh-C24S (lacking palmitate), Shh-N (lacking cholesterol) and Shh-NC24S (missing both lipid moieties). Ⓟ denotes the palmitate adduct, © – cholesterol. The cell-associated and dispersed cluster data are plotted together (separately, inset). As in **Fig. 7.4.1.1**, all Shh variants, except for the Shh-C24S, exhibit similar cluster size distributions on and off the cell. The Shh-C24S mutant appears to release larger clusters preferentially to smaller ones; this may be due to altered kinetics of the clusters – an effect realised by the cholesterol moiety acting on its own. Data are representative of 122 Shh-FL-, 130 Shh-C24S-, 163 Shh-N- and 87 Shh-NC24S-expressing cells from two transfection experiments.

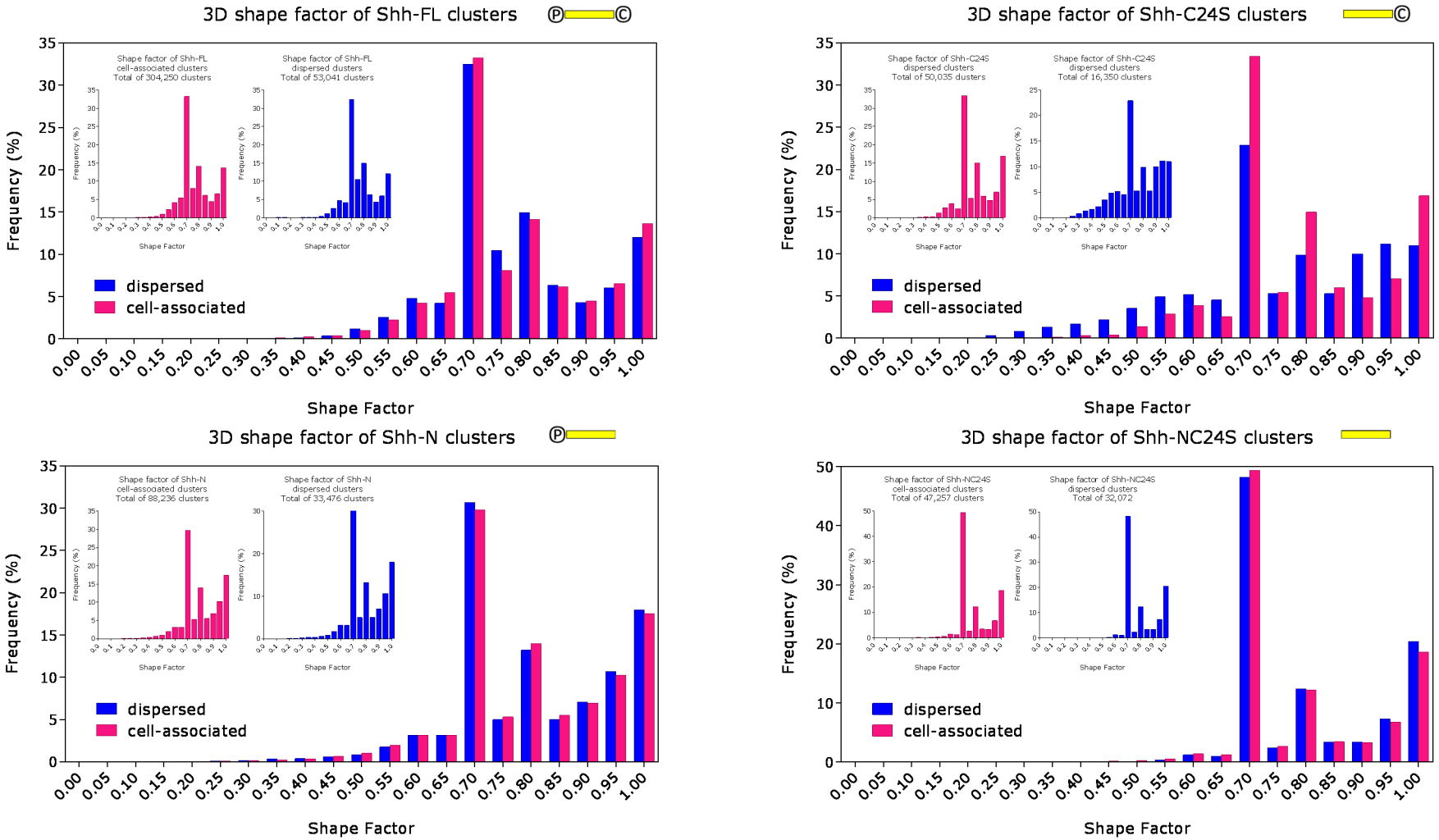

Figure 7.4.1.3. Frequency distribution histogram of the 3D shape factor of individual cell-associated and dispersed clusters from all four Shh variants. The clusters were generated by COS-7 cells transiently transfected with wild-type (Shh-FL) or any one of three other lipid modification mutants: Shh-C24S (lacking palmitate), Shh-N (lacking cholesterol) and Shh-NC24S (missing both lipid moieties). Ⓟ denotes palmitate, © – cholesterol. The cell-associated and dispersed cluster data are plotted together (separately, inset). Compared to the wild type, the Shh-C24S mutant exhibits a broadening of the range of cluster shapes. Conversely, the Shh-NC24S mutant appears to favour an elliptical cluster shape factor of 0.7. It should be brought into attention that, owing to the low axial resolution, the shape factors may have been underestimated (refer to main text for an elaboration). Data are representative of 122 Shh-FL-, 130 Shh-C24S-, 163 Shh-N- and 87 Shh-NC24S-expressing cells from two transfection experiments.

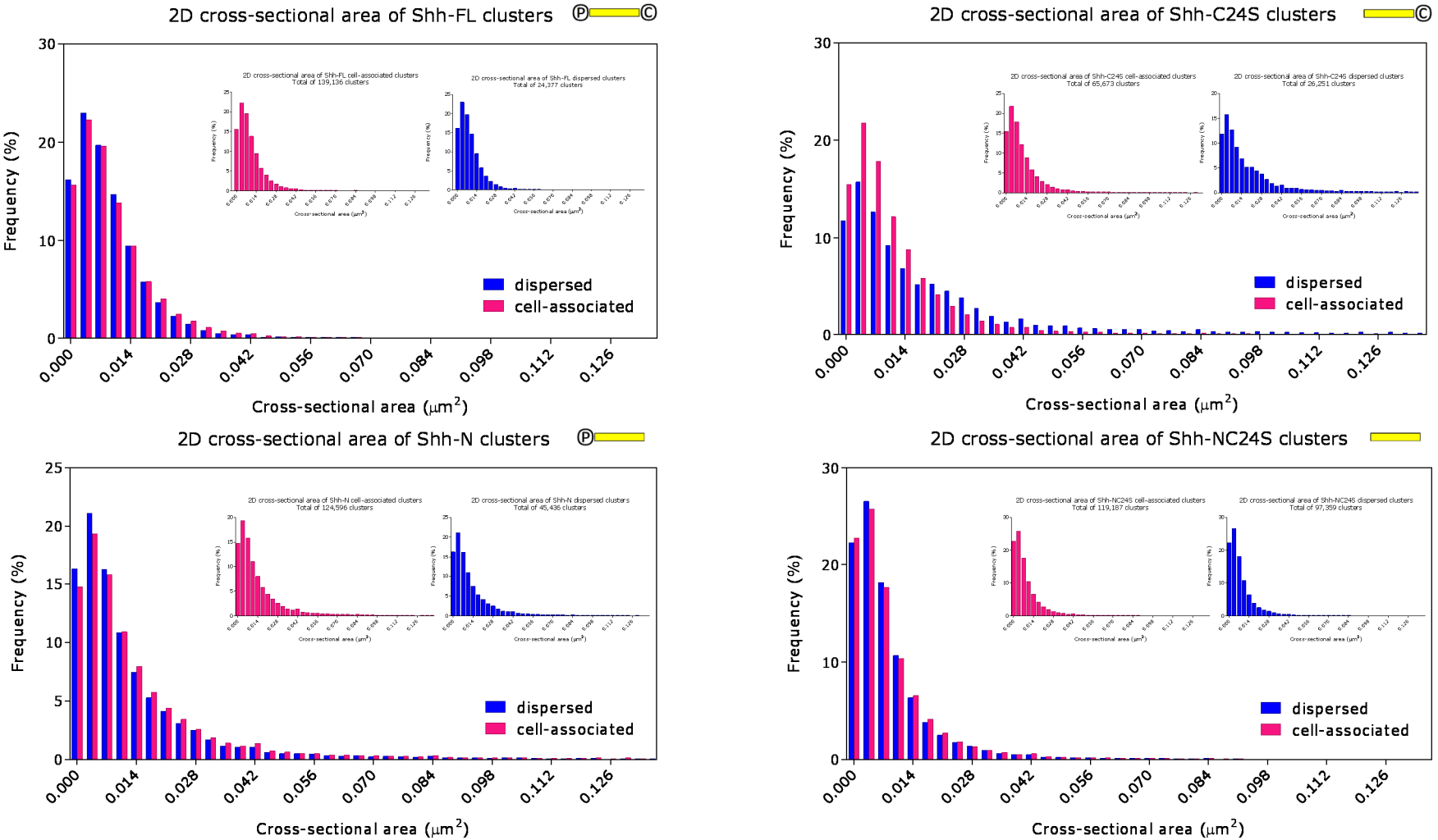

Figure 7.4.1.4. Frequency distribution histogram of the cross-sectional area of cell-associated and dispersed clusters from all four Shh variants. The clusters were generated by COS-7 cells transiently transfected with wild-type (Shh-FL) or any one of three other lipid modification mutants: Shh-C24S (lacking palmitate), Shh-N (lacking cholesterol) and Shh-NC24S (missing both lipid moieties). Ⓟ denotes palmitate, © – cholesterol. The cell-associated and dispersed cluster data are plotted together (separately, inset). The cross-sectional area was measured in the sample plane (*x*-*y*). Again, an upward shift in the cluster cross-section median is observed for dispersed, compared to the cell-associated, Shh-C24S clusters. Interestingly however, contrary to expectations from **Figs. 7.4.1.1–2**, the unlipidated mutant (Shh-NC24S) exhibits as large cross-sectional areas as the wild type. Data are representative of 122 Shh-FL-, 130 Shh-C24S-, 163 Shh-N- and 87 Shh-NC24S-expressing cells from two transfection experiments.

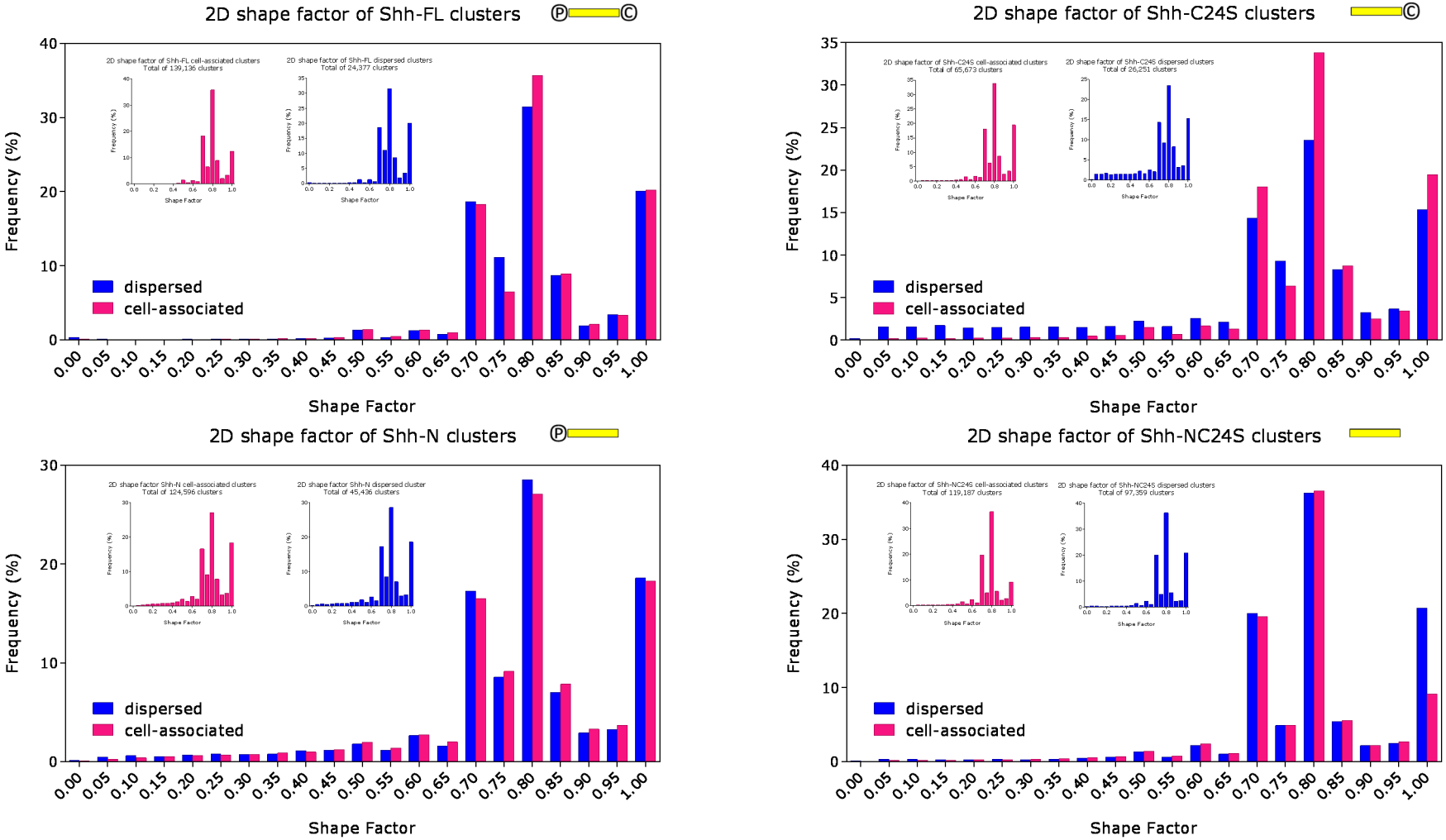

Figure 7.4.1.5. Frequency distribution histogram of the 2D Shape factor of cell-associated and dispersed clusters from all four Shh variants. The clusters were generated by COS-7 cells transiently transfected with wild-type (Shh-FL) or any one of three other lipid modification mutants: Shh-C24S (lacking palmitate), Shh-N (lacking cholesterol) and Shh-NC24S (missing both lipid moieties). Ⓟ denotes palmitate, © – cholesterol. The cell-associated and dispersed cluster data are plotted together (separately, inset). The 2D shape factor was measured in the sample plane (*x*-*y*) where resolution is isotropic (as in **Fig. 7.4.1.4**), thus there is no risk of distorting the shape factor values. Shape factor range broadening for Shh-C24S, and to a lesser extent Shh-N, with respect to the other Shh versions, is evident. Clearly, slightly oblong clusters (shape factor 0.8) are favoured by all variants. Data are representative of 122 Shh-FL-, 130 Shh-C24S-, 163 Shh-N- and 87 Shh-NC24S-expressing cells from 2 transfection experiments.

whether they were identical), a non-parametric, two-sample Kolmogorov-Smirnov test was carried out. Being non parametric, the test does not make any prior assumptions about the form of the distribution, *e.g.* whether it is Gaussian or exponential. The null hypothesis of the Kolmogorov-Smirnov test states that the distributions of the two variables are the same, without actually asserting their form. 'Two sided' (or two tailed) means that the test looks for differences between the distribution functions in both directions, as opposed to a 'one-sided' test, which looks for differences using an *a priori* assumption that a specified distribution will have a larger mean than the other.

Carrying out the statistical test on cluster populations from all four Shh variants revealed that the cell-associated portion most likely belongs to a distinct distribution to the dispersed portion, since the *p*-value in all cases came to be generally below 1×10^{-4}, with the exception of the Shh-N mutant which scored $p = 0.0028$ for the 3D shape factor, wild-type Shh (Shh-FL) with $p = 0.1963$ for the 2D shape factor and the Shh-NC24S mutant with $p = 0.0077$ for the 2D shape factor as well. A tabulated summary of the *p*-values is shown in **Table 7.4.2**. This means that for all, with the exception of the three cases enumerated above, there is less than 0.01% chance of observing a difference as large as was observed, even if the two populations were identical (*i.e.* the null hypothesis is true). On the other hand, for the cases with $p > 0.0001$, random sampling from identical populations would lead to finding the populations to be more dissimilar than was observed in, respectively, 0.28%, 19.63% and 0.77% of experiments. The first and the last results represent a relatively low probability, but the middle (2D shape factor of Shh-FL clusters) indicates a significant chance that the dimensions that Shh multimolecular structures assume are the same both on and off the cell. A further interpretation of this possibility is that, once released, the shape of Shh-FL clusters is not subject to change by proteins in suspension, such as HSPGs, which would certainly be released by the cells and are also likely to be present in the FCS component of the growth medium.

7. 4. 2. 1. Volume, surface area and cross-sectional area

Indeed, from the volume and surface-area quantitation in **Fig. 7.4.1.1** and **Fig. 7.4.1.2** it is clear that Shh-FL, and especially Shh-C24S, multimers undergo a shift from a smaller to a larger size. Interestingly, for the cholesterol-lacking mutants (Shh-N and Shh-NC24S), the same cannot be deduced from the figures: the shift from smaller to larger clusters in the dispersed population is not evident, implying that cholesterol plays an important part in mega-multimerisation (*i.e.* augmenting the size of the already existing small multimers). The more pronounced 'mega-multimerisation' in Shh-C24S, compared to the wild type, moreover, suggests that palmitate acts

to restrict the size of the clusters, since removing this adduct, whilst simultaneously keeping the molecule's capacity to multimerise by retaining the cholesterol moiety, results in a consistent aggrandisement of the clusters. This alludes to the curious conclusion that cholesterol and palmitate are mutually antagonistic, and that they strike a careful balance, producing a unique multimer output profile.

Table 7.4.2. Summary of *p*-values and fit parameters. The *p*-values which were calculated using the two-sided Kolmogorov-Smirnov test assess whether the cell-associated and dispersed clusters of each Shh variant are identical in size and shape. The physical parameters describing the size and shape of the clusters are the surface area, volume, cross-sectional area, 2D and 3D shape factors. The fit parameters used for curve-fitting the cluster volume histogram distributions in **Fig. 7.4.1.1** are also shown on the right of the table. Key: y_0, y-intercept, in units of %; τ, constant of exponential decay, in units of μm^3.

	p-Values				*Cluster Volume Fit Parameters*	
Shh Variant	*Surface Area/ Cross-sectional Area/ Volume*	*2D Shape Factor*	*3D Shape Factor*		*Cell-associated*	*Dispersed*
Shh-FL	$< 1 \times 10^{-4}$	0.1963	$< 1 \times 10^{-4}$	y_0:	28.64	28.07
				τ:	0.002485	0.002319
Shh-C24S	$< 1 \times 10^{-4}$	$< 1 \times 10^{-4}$	$< 1 \times 10^{-4}$	y_0:	31.59	18.13
				τ:	0.002521	0.004248
Shh-N	$< 1 \times 10^{-4}$	$< 1 \times 10^{-4}$	0.0028	y_0:	27.92	28.75
				τ:	0.002948	0.002887
Shh-NC24S	$< 1 \times 10^{-4}$	0.0077	$< 1 \times 10^{-4}$	y_0:	49.20	48.92
				τ:	0.001563	0.001636

Upon considering the graphs of Shh-NC24S, however, this theory seems to be at odds with these data: if the theory expounded above were true, then one would expect the lack of mutually antagonistic lipid modifications to restore a profile similar to that of Shh-FL. Quite to the contrary, removal of the lipid modifications causes an even greater attenuation of the cluster sizes (**Fig. 7.4.1.1** and **Fig. 7.4.1.2**). In fact, this result endorses the commonly held opinion in the research community that the Shh-NC24S mutant has an impaired ability to form multimers. At this point, it should be mentioned that during the experiments it was observed that Shh-NC24S scattered outside the cells was found in great abundance, and at a high ratio with respect

to that found associated with the cells, which was rather scarce compared to that of the other Shh variants. To accommodate all of these findings, therefore, it seems logical to posit that the lipid modifications may serve to associate wild-type Shh to the cell surface for some time during which the multimerisation process takes place. Following this argument, Shh-NC24S which is devoid of any lipid anchors, is not able to remain on the surface for long, and as a consequence is not multimerised to as high a degree as the other variants. This model does not, however, directly reconcile the anomalous behaviour of Shh-C24S, which appears to over-stimulate multimer assembly; it is thus possible that other, extracellular molecules, too, influence the multimerisation process.

Finally, the two-dimensional graphs of the cross-sectional area (**Fig. 7.4.1.4**) do not portray a noticeable difference between the wild-type and Shh-NC24S distributions. This leads to the suggestion that the lipid adducts are important for the growth in height of the clusters from the cell surface.

7. 4. 2. 2. Shape factor

Fig. 7.4.1.3 displays the three-dimensional shape factor of the clusters. All four graphs in this figure are dominated by a spike at ~0.7 (a slightly oblong shape). Given that the shape of the voxels building up the image data are oblong themselves (due to the poorer resolution in the *z* direction), with a shape factor of 0.71, there certainly may be a systematic error corrupting the measurements. The systematic error may be underestimating the sphericity of the clusters (*i.e.* introducing a bias to the left of the graph); however, it should be noted that the shape factor distribution pattern itself is likely to be correct. If the predominance of the shape factor of 0.7 is indeed due to the non-cubical nature of the voxels, then to obtain the actual distribution, one simply needs to displace the graph to the right by 0.29 points so that the peak acquires the shape factor value for perfect symmetry, 1, and all other columns previously greater than 0.71 would also need to be stacked on top of this column. The interpretation of the outcome would then be that Shh has a preference for making highly symmetrical clusters.

A 2D version of the shape factor evaluation (**Fig. 7.4.1.5**) conducted in the plane of imaging, where the *x* and *y* dimensions have equal resolution, is free of the aforementioned bias, and indicates a preference for assembling into mildly oblong shapes (shape factor 0.8). The second most popular configuration is a perfect circle and a slightly less symmetrical shape (shape factor 0.7). String-like formations and/or complicated shapes (*i.e.* small shape factors), on the other hand, appear to be rare. In conjunction with the earlier observation that Shh-C24S generates larger-than-normal clusters due to lack of palmitate competition for the multimerisation

process, both 3D and 2D shape factor graphs (**Fig. 7.4.1.3** and **Fig. 7.4.1.5**) insinuate that palmitoylation may have the additional purpose of maintaining the globularity of the clusters and possibly preventing 'chain'-multimerisation. Exercising strict control over the multimers' compactness may be necessary to ensure unimpeded transit through the intracellular environment and/or an efficient interaction between the receptor Ptc and the multimeric ligand.

It should be borne in mind that it is possible that some of the quantitation data – including the shape factor – may be corrupted by general resolution limitations (aside from considerations of directional variation in resolution mentioned above). Thus, for example, the irregular Shh shapes indicated by the low shape factor may in fact be densely situated monomers which, in an image with limited distance discrimination, may appear to be joined together. Both large and small clusters can succumb to this artefact, since comparatively large clusters may also lie very close by each other.

7. 4. 2. 3. Corroboration of the nature of the cluster volume distribution

The conjecture that the cluster volume distribution obeyed a monoexponential decay was ascertained, by drawing up quantile-quantile plots (also known as Q-Q plots.) A Q-Q plot is a type of probability plot and a useful visual statistical tool for checking the validity of a distributional assumption for a particular data set. By quantile, it is meant a point below which a fraction (or percentage) of the data lies. For example, the 10% quantile is the point at which 10% of the data can be found below and 90% above this particular point. The aim is to compute the expected value of every data point, given the distribution in question. If the data indeed follow the surmised distribution, then the points will fall approximately on a straight line; any deviations from it would indicate an imperfect match, and the greater the departure from the reference line, the more dubious the supposed distribution.

The volume data from all four Shh variants was plotted against an exponential distribution with the corresponding best-fit parameters, as in **Fig. 7.4.1.1**. The outcome is shown in **Fig. 7.4.2.3**. Overall, the agreement with an exponential distribution was quite good for all Shh-FL clusters and for the cell-bound group of mutant clusters – except for a few outliers towards the right (representing large values). This indicates that these large values may, in fact, be suspect, and that they may, for example, be the result of merging of clusters in the image due to the inevitable resolution limit. Q-Q plots for the other parameters (**Fig. 7.4.1.2–5**) were not plotted because none of those exhibited a clear monotonic decrease in values.

If the volume distribution is indeed an exponential function, it is interesting to speculate on what the generating process can be. One possibility is that it is the law of mass action – if it

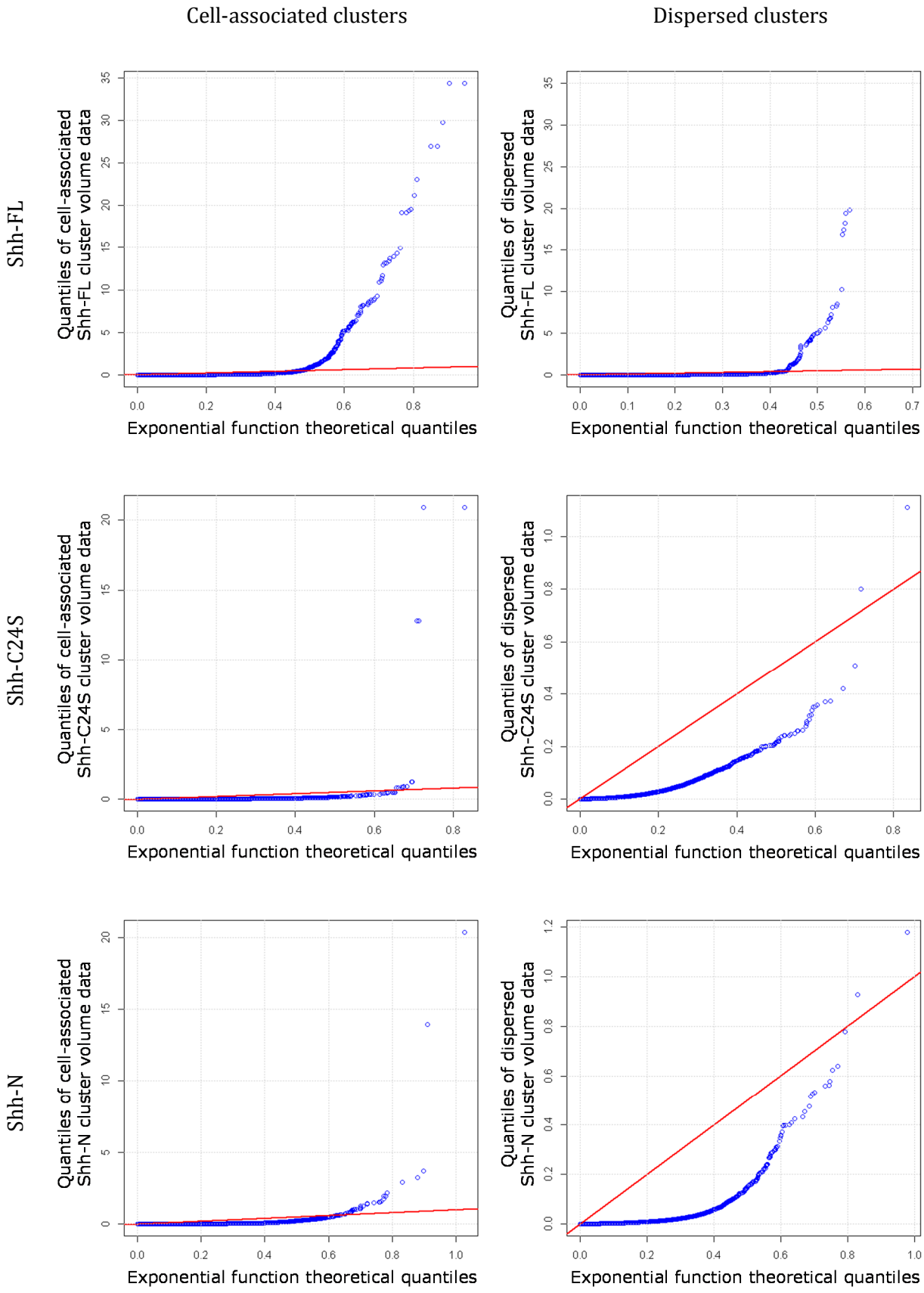
Cell-associated clusters
Dispersed clusters
Shh-FL
Shh-C24S
Shh-N
Quantiles of cell-associated Shh-FL cluster volume data
Quantiles of dispersed Shh-FL cluster volume data
Quantiles of cell-associated Shh-C24S cluster volume data
Quantiles of dispersed Shh-C24S cluster volume data
Quantiles of cell-associated Shh-N cluster volume data
Quantiles of dispersed Shh-N cluster volume data
Exponential function theoretical quantiles

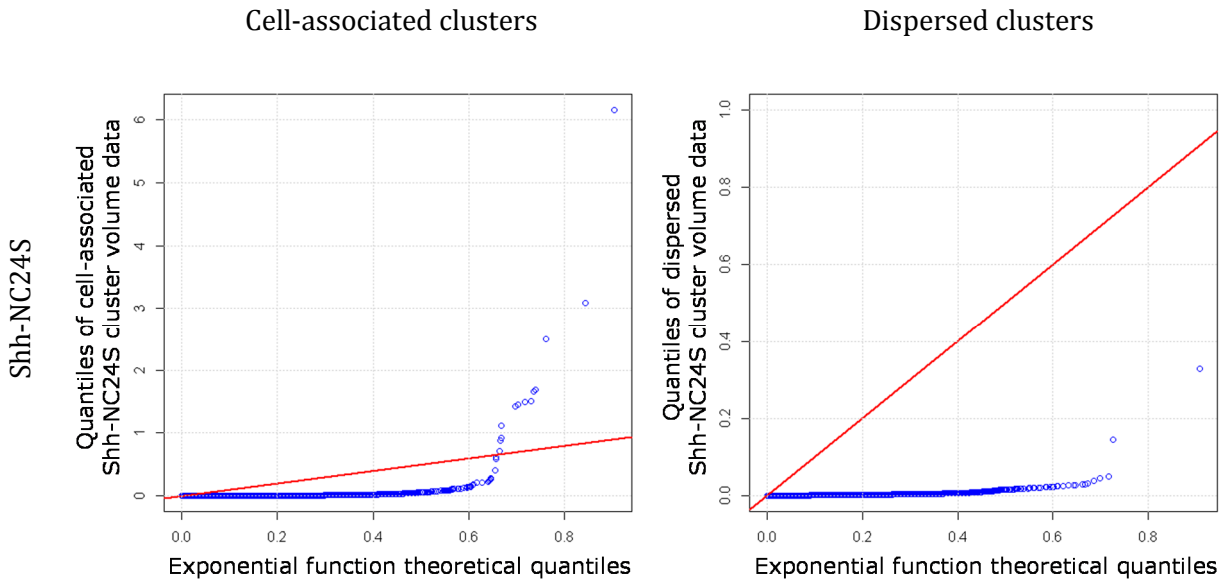

Figure 7.4.2.3. Quantile-quantile plots graphically exploring the likelihood that the volume distribution of cell-surface and dispatched cluster populations from all Shh lipid modification variants obey a monoexponential decay distribution. Quantiles of the unknown empirically derived cluster distributions (blue circles) on the ordinate are plotted against quantiles on the abscissa of the suspected form of the distributions (red line) – in this case, monoexponential decay functions with best-fit parameters as shown in **Fig. 7.4.1.1**. The quantiles are equally sized subsets of the total number of data points. Because the plot has been set up as a function of the quantiles of the exponential distribution, the latter appears as a straight line $y = x$. Thus, if the posited distribution is correct, the blue circles will adhere closely to the straight red lines; conversely, if the guess is wrong, there will be a strong deviation between the blue and red trajectories. Quantile-quantile plots for each individual Shh variant (shown on dedicated rows) have been generated separately for the cell-tethered (left panels) and freed (right panels) cluster states. Judging from this graphical statistical analysis, the likelihood of the distributions following an exponential trend is considerably high for small to medium values in all cases, except for the released Shh mutants (right panels of the rows labelled Shh-C24S, Shh-N and Shh-NC24S). The breakdown in the trend to the right (high values) could be an artefact due to working with limited resolution and the concomitant merging of clusters below this resolution limit, resulting in detected structures which are larger than expected.

can be assumed that the Shh ligands bind to other Shh ligands in a reversible manner, with a certain rate of association and dissociation. Thus, when brought into close proximity, and given that the ligands are in the correct orientation and carry enough energy, they will be expected to bind together. After some stochastic period of time, they will dissociate again. A steady state is reached when the rate of new ligand-ligand complexes formed equals the rate of complex dissociation. The law of mass action predicts that the fraction of the ligand population engaged with a partner at equilibrium is a function of the ligand concentration; in particular, the ligand occu-

pancy follows an exponential relationship, whereby association becomes increasingly inefficient as the concentration is augmented.

With application to Shh, this can be interpreted to mean that the local concentration of Shh on the extracellular membrane leaflet – whether released by Disp (the transmembrane protein mediating Shh's externalisation) or exocytosed *via* the secretory pathway, or even another mechanism – determines the local size of the clusters. If the local concentration released on the surface has an equal probability throughout its entire range, then the size distribution of clusters observed on the surface will be an exponential decay.

To address why the mutant dispersed clusters do not conform to an exponential decay, one can consider the fact that the law of mass action breaks down when the ligand is modified in some way upon binding and/or dissociation. This indirectly implies that the mutants undergo conformational changes or become somehow chemically modified when interacting to form clusters, whereas the wild-type does not. Keeping this thread of reasoning in mind, one arrives at a conflict with the Grobe group's stance [Ohlig *et al.*, 2011] that the cholesterol and palmitate moieties are removed upon correct multimerisation of the protein. If any de-lipidation does occur on the extracellular cell surface at all, our data suggest that it is the inappropriately post-translationally modified Shh versions that undergo it, not the native, fully functioning protein. Turning the same argument around also implies that the formation of larger-than-normal clusters by Shh-C24S could be a result of an irreversible modification which prevents its dissociation from the surface, thus driving up the assembly of the multimers.

7. 5. Assessment of the primary antibody dependency of the data

In order to establish whether the specificity of the primary antibody used to detect Shh has any consequence on the data presented in the previous section, an independent set of data for the Shh-FL variant was obtained using a different primary antibody, namely a monoclonal rabbit C9C5 (Cell Signaling Technology, USA). Unlike the polyclonal rabbit H-160 antibody used thus far, C9C5 was raised against a specific peptide sequence of Shh. The exact sequence is proprietary and cannot be stated here explicitly; however it can at least be revealed that the sequence is completely contained within the binding site of the H-160, and is less than 15% of the H-160 binding site length. Measurements in 3D and 2D, in the style of **Fig. 7.4.1.1**–**5**, were carried out and are displayed on **Fig. 7.5**. The number of cells assessed was 53, with a collective number of 14,641 cell-associated and 810 dispersed clusters.

The various distributions obtained with the two antibodies largely agree with each oth-

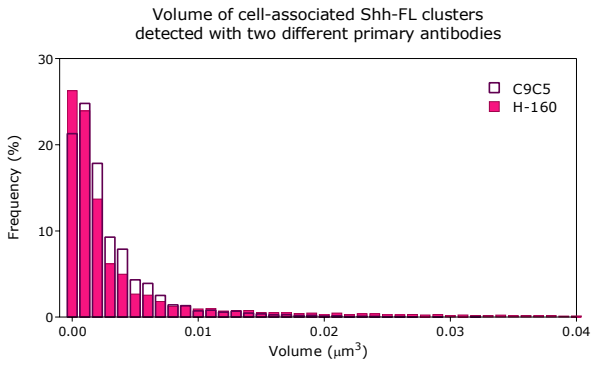
Volume of cell-associated Shh-FL clusters
detected with two different primary antibodies
C9C5
H-160
Frequency (%)
Volume (μm3)

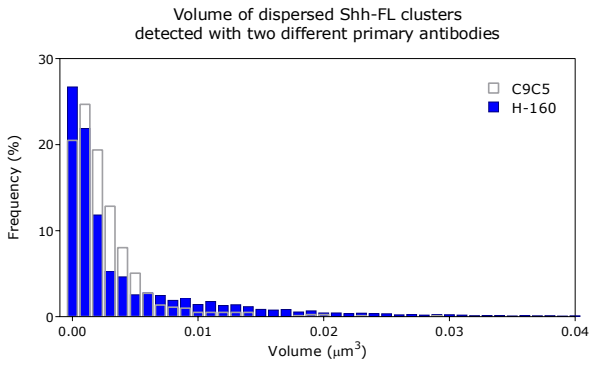
Volume of dispersed Shh-FL clusters
detected with two different primary antibodies
C9C5
H-160
Frequency (%)
Volume (μm3)

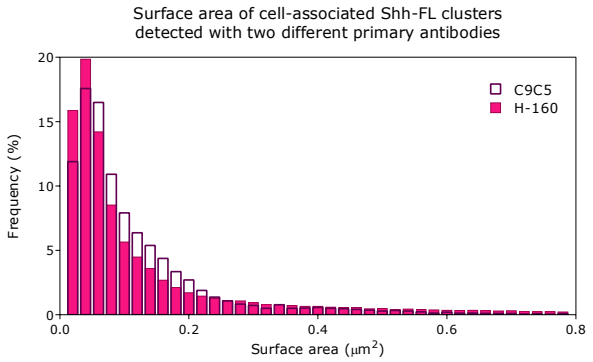
Surface area of cell-associated Shh-FL clusters
detected with two different primary antibodies
C9C5
H-160
Frequency (%)
Surface area (μm2)

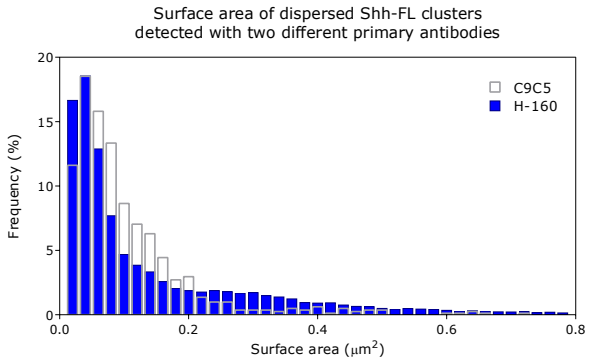
Surface area of dispersed Shh-FL clusters
detected with two different primary antibodies
C9C5
H-160
Frequency (%)
Surface area (μm2)

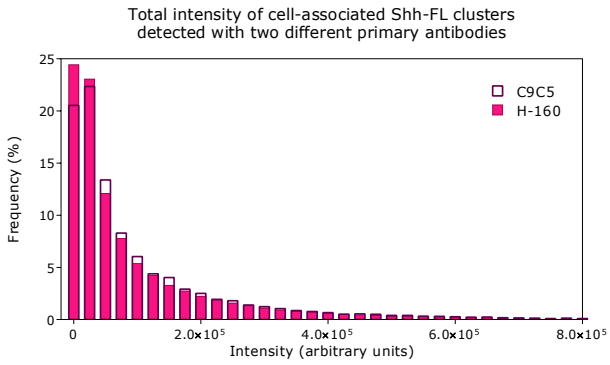
Total intensity of cell-associated Shh-FL clusters
detected with two different primary antibodies
C9C5
H-160
Frequency (%)
Intensity (arbitrary units)

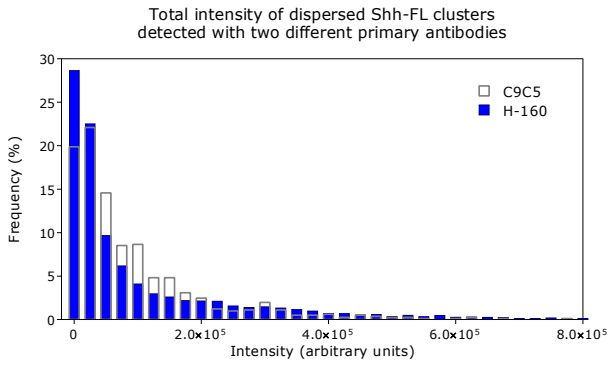
Total intensity of dispersed Shh-FL clusters
detected with two different primary antibodies
C9C5
H-160
Frequency (%)
Intensity (arbitrary units)

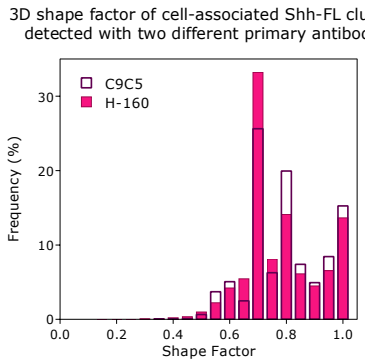
3D shape factor of cell-associated Shh-FL clusters
detected with two different primary antibodies
C9C5
H-160
Frequency (%)
Shape Factor

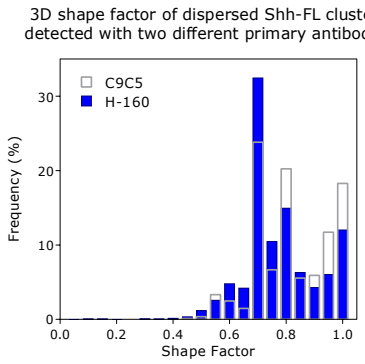
3D shape factor of dispersed Shh-FL clusters
detected with two different primary antibodies
C9C5
H-160
Frequency (%)
Shape Factor

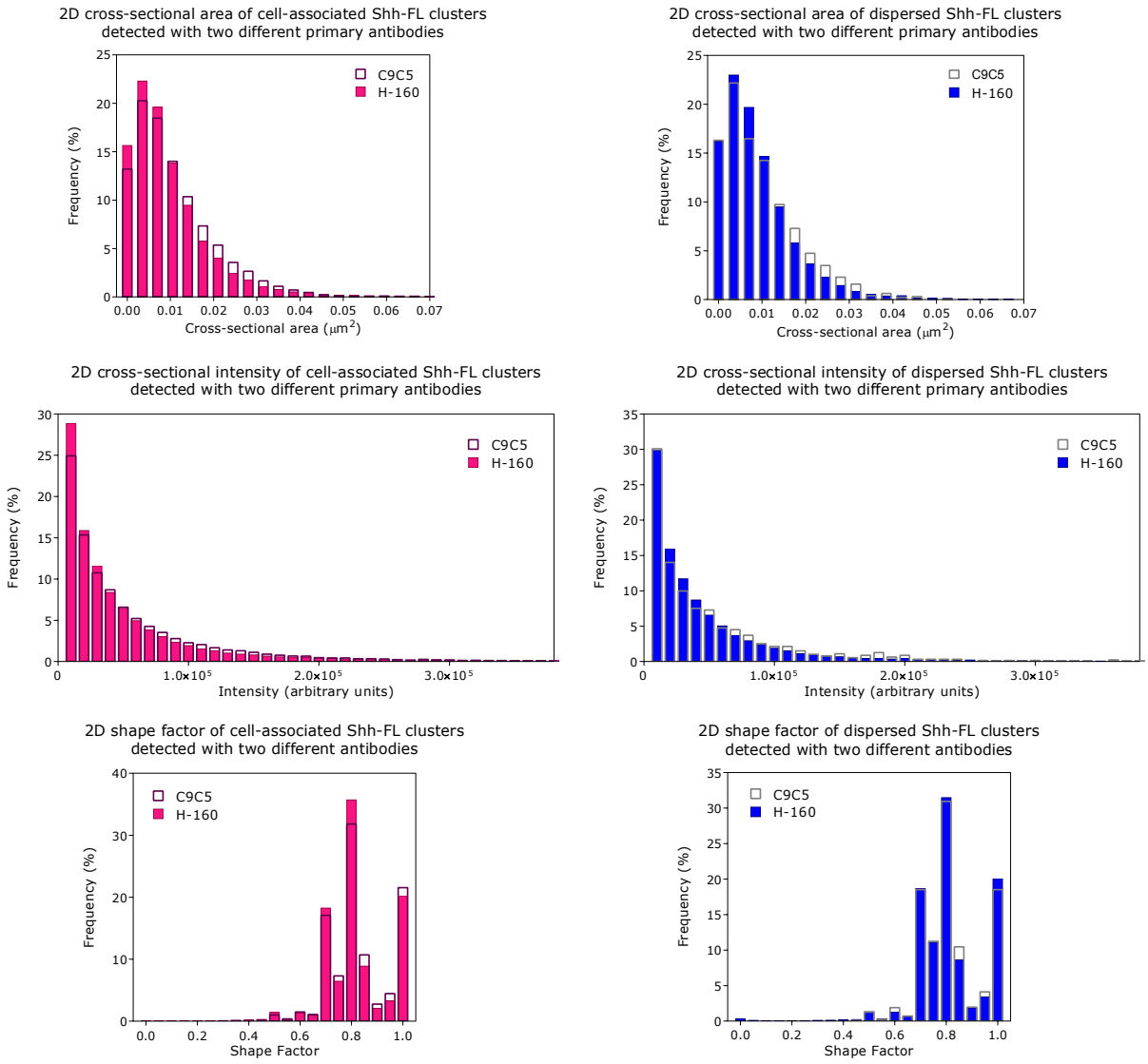

Figure 7.5. 3D and 2D quantitation of Shh cluster dimensionality and morphology with an alternative primary antibody. In order to corroborate the results in **Fig. 7.4.1.1–5** obtained with the anti-Shh pAb, H-160, the same Shh cluster parameters were investigated with the anti-Shh mAb, C9C5 for the case of Shh-FL only. C9C5 data are coded by empty histogram bars overlaid on top of the corresponding H-160 data, represented with filled bars. The colour scheme is the same as that used in the above figures: magenta signifies cell-associated clusters, blue denotes dispersed clusters. The graphs of total and cross-sectional intensity were intended as a corroborative measure on the surface area and cross-sectional area measurements. The surface area measurement is directly mappable, *via* some constant of proportionality, onto the total intensity measurement, due to the immunological detection method employed here. The cross-sectional area is related to the cross-sectional intensity in a more complex way, with a rough dependence on the average radius of the clusters.

er, indicating that the antibodies are specific to Shh, and that the distributions are real. It was expected that the C9C5, being monoclonal, and therefore more specific, would produce more accurate results; however, its biochemical superiority was ultimately hampered by the fact that, due to the lower number of antibodies binding per Shh molecule (the binding sequence on Shh is much shorter for C9C5), the resulting fluorescent signal effected by the secondary antibodies was weaker, compared to that of H-160. With confocal microscopy, this can be problematic, since, as already outlined in the Background and Theory chapter, this type of microscope discards substantial amounts of light, and its detector efficiency is not particularly high, therefore a strong signal is imperative.

7. 6. Discussion

7. 6. 1. Summary of results

The goal of the present chapter was to attest the tentative results obtained with super-resolution of the two-dimensional nanoscale organisation of Shh multimers in the previous chapter, and to expand the survey into three dimensions.

The main achievements are:

- Provision of, to our knowledge, unprecedented insight into the size and morphology of Shh multimolecular complexes using high-resolution optical microscopy;

- New evidence about the role of Shh lipid modifications in the assembly of the multimolecular complexes, including

    - confirmation of cholesterol's involvement in multimerisation;

    - evidence for palmitate's involvement in multimerisation;

    - evidence for multimer shape regularisation by palmitate;

    - confirmation of the existence of small oligomeric structures thought to precede multimer maturation;

- tentative contention to the theory of palmitate and cholesterol cleavage upon cluster release.

7. 6. 2. Conclusions

Before embarking on discussing the main findings of this chapter, it is instructive to revisit the shortcomings of the experimental method. On this subject, it is understood that complete confidence in the determination of the physical characteristics of Shh clusters is not possible. One of the major obstacles in this endeavour was the inherent resolution barrier (albeit an improvement on conventional microscopy resolution, by courtesy of deconvolution), which should ideally be lowered sufficiently in order to be able to distinguish single Shh proteins (~4 nm). The inability to discriminate features below a certain limit can lead to the misinterpretation of sub-resolution clusters into an agglomeration of totally different proportions. One concrete allusion to the existence of such unnatural agglomerations is the sudden deviation from the theoretical exponential function in the Q-Q plots in **Fig. 7.4.2.3**. It is also important to note that the use of indirect immunolabelling introduced a systematic error of consistent over-estimation by approximately 30 nm at each cluster boundary.

Another culprit is the necessity to separate unwanted background fluorescence from true Shh signal. Besides owing to superior adherence to the glass coverslips, the COS-7 cell line was chosen over the HEK293 cell line as an expression system because of reduced levels of autofluorescence. Despite these measures, residual fluorescence was still detectable and, with the intention of minimising its detrimental effects, during selection of clusters for quantitation it was decided to impose a minimum intensity threshold. This, in turn, poses the possibility that Shh clusters – whole or partial – have been inevitably omitted from the quantitation process. At this point, the researcher is faced with two choices, each coupled to its own disadvantage: 1) to eliminate false positive cases (*i.e.* background signal wrongly identified as originating from Shh), at the expense of generating more false negative cases (a few Shh molecules – or sparsely immunolabelled Shh clusters – emitting a number of photons comparable to or less than general autofluorescence or non-specific secondary antibody binding), or 2) of consciously admitting more fluorescence contamination from non-Shh sources into the quantitation, with the compensating benefit of gathering more specific Shh information. Alternatively, it is possible – as was already resorted to in the previous chapter – to select a fluorescent dye with a longer wavelength, in order to escape the zone of autofluorescence. Taking such a decision, however, would hinder the advance in resolution which deconvolution is providing, due to the associated increase in the PSF size for longer wavelengths.

Other minor issues with the accuracy of the quantitation are the risk of bifurcating the clusters while drawing cell boundaries – despite best efforts, and despite selecting a transmitted-light technique with the best edge definition for this application (DIC). Inexactitude in the hand-drawing of the boundaries, whereby areas of the image are assigned as definitively occupied by a cell or free of cell coverage, could have inevitably been committed, although the impact of such errors is likely to be minimal.

Bearing this in mind, and notwithstanding, several inferences can be made from the conducted experiments. First, the sterol and acyl moieties of Shh appear to be involved in the large-scale polymerisation of pre-existing small oligomers. This finding is in harmony with previous reports in the literature. The small oligomers themselves were first reported by [Vyas *et al.*, 2008], where they were claimed to be of sub-optical resolution. It is thought that cholesterol promotes electrostatic interactions between the Shh monomers by concentrating and immobilising them into membrane microdomains [Chen *et al.*, 2004][Dierker *et al.*, 2009a][Dierker *et al.*, 2009b][Ryan *et al.*, 2012] (the residues participating in the electrostatic interactions are thought to be Glu^{72}, Arg^{73} and Lys^{75} [Ohlig *et al.*, 2011]). Furthermore, my data seem to suggest that the formation of the small oligomers is independent of either post-translational modification; this is implied by the fact that the double mutant, Shh-NC24S, manages to produce small multimers – presumably the same structures mentioned in the publications listed above. Notably, the experiments which I have conducted with this mutant indicate that a much larger proportion, compared to the other Shh variants, is released in the extracellular environment than is retained on the cell surface.

In summary, we therefore put forward the following theory: both the fatty-acid and cholesterol modification serve, at least in part, to anchor Shh to the cell surface in order to increase its concentration which, recalling the law of mass action, stimulates the formation of large multimeric structures. In this model, Shh is entirely self-sufficient in driving its own multimerisation. In any case, we cannot rule out input from other molecules – for example, HSPGs in the extracellular environment – which might be necessary for stabilisation of the multimeric structures during their intercellular transit. In *Drosophila*, Hh and glypican HSPGs have been observed to localise to lipid rafts, membrane areas with high abundance of embedded cholesterol [Rietveld *et al.*, 1999]. However, the imaging was carried out with diffraction-limited confocal microscopy, implying that the proximity of the molecules was anywhere up to ~200 nm – a resolution insufficient to state confidently that the molecules were indeed interacting. Future colocalisation studies of Shh and HSPGs in super-resolution may be helpful and illuminating in this respect.

The two-dimensional cross-sectional area and volume information that was extracted hints that the small oligomers may in fact be a thin, or even a single, layer of Shh which is subse-

quently built upon vertically. This, however, does not seem to tally with the 3D shape factor measurements (**Fig. 7.4.1.3**), which would be expected to shift to the left for the Shh-NC24S mutant (even after correcting for the oblong voxels), since thin, flat structures deviate further from an ideal sphere than structures with more balanced dimensions. More information needs to be collected to understand and reconcile these data.

Conclusions could also be drawn on the role that palmitate takes in multimer assembly. As with cholesterol, albeit to a lesser extent, palmitate on its own appears to raise the fraction of multimers with larger sizes – both on clusters manifested on the surface and those which are already disengaged. Additionally, it appears to regularise the clusters' shape, counteracting the formation of chain-like and/or elaborate shapes. As a mild surprise comes the observation that a collaboration between cholesterol and palmitate emerges not as amplification, but as moderation of the cluster sizes. Why there should be a redundancy in the function of the lipids could be explained by first reiterating that each moiety *per se* promotes a cluster size distribution with a different median. In each other's presence, the cluster distribution acquires a profile with a median intermediate between those two. Therefore, the moieties could act in a synergistic manner towards sculpting a size distribution with a well-defined, precise profile that may be important in regulating the potency of the physiological signal being relayed by Shh upon binding to Ptc, its receptor.

Finally, robust statistical evidence was found that the volume distribution on the cell surface, for all Shh variants, and that of the dispersed Shh-FL cluster only, follow an exponential decay law. This could be due to the law of mass action which postulates that the degree of binding of monomers will increase exponentially, dependent on the abundance of Shh monomers delivered on the extracellular membrane leaflet. Importantly, the law only holds if there are no chemical modifications or changes in conformation involved, otherwise the trend breaks down. This indirectly conveys the possibility that Shh-FL clusters do not, in fact, undergo any cleavage by proteases on the surface – in stark contrast to the findings in [Ohlig *et al.*, 2011] – although this claim needs to be substantiated (or rejected) in a more rigorous way. In fact, the evidence laid out by the Grobe group in [Ohlig *et al.*, 2011] appears to be unconvincing. For example, they make hasty conclusions about the identity of the Shh variant in a pull-down assay, without being able to substantiate them. Moreover, their experiments claim that wild-type Shh cannot be immunoprecipitated with the Shh antibody 5E1, which is in stark contrast to the experience in the Magee laboratory. Together with inadequate controls and other ambiguous data presented by the Grobe group, it is therefore not surprising that their theory is put to question.

The method of scrutinising Shh's assembly into high molecular-weight structures presented here constitutes a novel way of approaching the long-standing problem of Shh packaging and release, and contributes a new angle to the catalogue of knowledge collected so far. Remov-

ing the ambiguity in the three-dimensional data, and any large objects that may be suspect, should increase the credibility of the data. Neither of those targets seems achievable with deconvolution at present, since this technique is not powerful enough to transcend two orders of magnitude in resolution. In that respect, super-resolution is a much better candidate – if the problems surrounding the technique could be solved.

8. Estimation of the number of Shh subunits comprising multimolecular Shh complexes

One of the celebrated advantages of the fluorescence tagging technique of genetically targeted fluorescent proteins is its supreme labelling specificity. Another is that, unlike immunostaining, fluorescence labelling of the antigen is not reliant on the diffusivity of the probe to reach its intended target. A third, still, is that there is a precise one-to-one correspondence between the number of antigens labelled and the intensity of the fluorescence signal. All of these particulars make genetically encoded proteins ideal for studying the number of a molecular species in a multimolecular complex.

Shh complexes extracted from the supernatant of tissue culture cells span a range of ~150 to 4,000 kDa (as suggested by gel filtration experiments), equivalent to between roughly 8 and 210 monomers [Zeng *et al.*, 2001][Chen *et al.*, 2004][Eaton, 2008]. Whether those are entirely comprised of Shh molecules, or whether they contain other proteins also, is presently unknown. Enumerating the number of molecules in the clusters therefore has the potential of shedding light on this question.

8. 1. Selection of the imaging configuration

The Shh::EGFP construct, described in chapter 6, was utilised for these experiments. This construct, as already highlighted before, is fluorescent from the moment of maturation. It therefore emits a fluorescent signal even before reaching the cell surface.

In order to image the surface multimolecular complexes selectively, one could consider using the total internal reflection fluorescence (TIRF) configuration. However, having established that the theoretical minimum penetration depth of the TIRF field, determined by the optics and materials in the set-up, is 71.5 nm, and that the COS-7 cell membrane is displaced only by about 18.6 nm from the substrate [Lodish *et al.*, 2000] [Vorbrodt *et al.*, 1969], then a slice of at least a 52.9-nm thickness beyond the cell membrane would also be visible. Considering that, to emerge eventually on the extraneous surface, the Shh protein forges its way through the endoplasmic reticulum (ER) which permeates the bulk of the cell, it is very possible that one would also involuntarily detect Shh travelling through elements of the ER close to the plasma membrane.

Nonetheless the technique of TIRF was selected for this study, for lack of a more suitable

option. It was reasoned that, since Shh clusters do not occupy the entirety of the cell surface, there would be patches free of Shh clusters that would contain only diffuse signal from the cell interior (emanating from Shh monomers in the secretory pathway). Thus, the unwanted fluorescence could be removed by subtracting the intensity of neighbouring 'empty' regions from the cluster of interest.

8. 2. Single-molecule bleaching as a means of molecule enumeration

If epi-fluorescence were used, then finding out the molecular count in a particular cluster would be as simple as measuring the total signal from a cluster and dividing it by the intensity of a single EGFP molecule. With TIRF, however, this is not possible, since the intensity profile of the TIRF field is not constant with depth into the specimen (in fact, it falls exponentially: **Eq. 2.2.4.1.5**), and the detected fluorescence follows an even more complicated pattern, as shall be explained later in this chapter. In consequence, applying the above method to determine the molecular count would lead to an erroneous result.

A different approach was therefore adopted: a time-series was obtained of the specimen and the imaging continued until all EGFP molecules in the field of view were completely bleached. The time-series therefore recorded (uneven) steps symbolising single-molecule bleaching events. Summing the individual steps was then expected to amount to the total number of Shh subunits present. A mathematical algorithm, termed the Chung-Kennedy filter [Chung *et al.*, 1991] (described in the Appendix C), implemented in a Matlab routine [Reuel *et al.*, 2012] was intended to be used to reduce the background noise and uncover the underlying steps of interest.

8. 3. Unmasking single-molecule bleaching events obscured by noise

Briefly, the signal-processing algorithm – unlike low-pass filtering – is an edge-preserving filter which weights the predictions of a forwards- and a backwards-heading averaging function situated on either side of a data point, and estimates the signal at that point with predominant influence from whichever function exhibits less variability.

Attention should be drawn to the fact that, during acquisition of the data, the imaging intensity was carefully selected so as to prolong the viability of the EGFP molecules and to raise their chances of being detected by the Chung-Kennedy filter, since the latter cannot recover

multiple features in exceedingly rapid succession. For reference, a single EGFP bleaching event observed with laser-based microscopes (with illumination intensity of about 93 W/cm^2, in this case) can be expected to have a lifetime within the range of 100-500 ms [Kubitscheck *et al.*, 2000][Chiu *et al.*, 2001].

The Chung-Kennedy algorithm was originally devised for and tested on electrical signals issuing from ion channels and synaptic signalling. The Matlab routine proffered by [Reuel *et al.*, 2012], however, is an adaptation for visual, fluorescence signals. It has been given the name NoRSE (noise reduction and state evaluator) by the authors.

8. 3. 1. Logical basis for locating steps in the data

In order to find sudden drops or leaps in the data, NoRSE arranges the data points in a histogram and flags the position of any distinct peaks. To qualify as a peak at the outset, the histogram bin being evaluated must score a higher frequency count than the bins adjacent to it [Reuel *et al.*, 2012, Supplemental Text].

The second assessment stage is a pairwise comparison of the peaks. Based on the vertical extent of the valley between a peak pair, the peaks can be categorised as either: 1) a unique and significant peak, 2) an insignificant peak, or 3) significant peak candidate for averaging with the next. The sorting is executed with respect to a reference point of 50% of the average frequency response. The average frequency response is the average number of counts per bin, and is calculated as the total number of data points divided by the number of bins in the histogram, then divided further by the size of the averaging window. Thus, peaks falling into category 1) have an average-frequency count difference between the peak and both valleys on either side greater than 50% of the average frequency response. If the distances to the valleys are both smaller than this point of reference, the peaks are sorted into the second category, and if the valley distance on one side of the peak is above the cut-off, whilst the one on the other side is below it, the peak is catalogued into the category 3), whereby it is scrutinised further to determine whether to discard it or merge it with an adjacent peak [Reuel *et al.*, 2012, Supplemental Text].

In the final stage, another threshold is used to determine the fate of category 3) peaks. This horizontal threshold is a distance of 2.5% of the total bin count (obtained as the total number of data points divided by the number of histogram bins). If the separation of the bins of the peaks is below the specified threshold, the peaks are merged – but only if a significant vertical valley distance is found; otherwise the next peak is considered for merging, too. If the first case is true, the new valley distances after combining the peaks are calculated. If the frequency count is less than the vertical reference point specified above, the combined peak is ignored. This

strategy is particularly useful for eliminating purported peaks cropping up on the rising side of a genuine peak, or in the valley between two peaks [Reuel *et al.*, 2012, Supplemental Text].

8. 3. 2. Choosing the optimal noise reduction parameters

NoRSE has a slightly different set of free parameters open to modification by the user than the basic Chung-Kennedy filter (for more information, the reader is referred to Appendix C). It keeps the *p* parameter as defined in the original publication [Chung *et al.*, 1991], but splits the *M* parameter into two sub-parameters, one of which is a redefinition of *M* as the number of points to be used as centre points for the array of analysis windows contained in the second sub-parameter, *N*. The NoRSE *M* therefore serves to expand the segments of data involved in generating an estimate.

As the actual shape of the time-varying intensity is of no consequence here, though potential fast signal transients must be safeguarded against, the free parameter *p* and the number of iterations were set to reasonably high values. Predictors of a broad range of analysis windows were added (embodied by the variable *N* in **Eq. B.3**) to cater for as many different intervals between photobleaching events as possible, since the time constant of photobleaching of EGFP was not known originally. The NoRSE variable *M* was set to its optimum, 1. When aiming to extract the time constant of photobleaching, *p* was kept low since, according to [Chung *et al.*, 1991], this choice of *p* permitted a more faithful evaluation of the lifetime.

8. 4. Enumeration of Shh molecule content within individual clusters

8. 4. 1. Pre-treatment of the image data

The illumination of the sample was, in fact, not homogeneous, due to the Gaussian TEM_{00} profile of the laser (*i.e.* the Gaussian-distributed pattern of radiation measured in a plane transverse to the laser beam propagation direction), and the widefield imaging configuration. Moreover, the uneven effect is aggravated by the additional optics installed at the TIRF condenser (Materials and Methods chapter), which decrease the laser spot size at the object plane. Correcting for this unevenness was mandatory, because removing the autofluorescence component from the data requires uniformity in the field. This is in spite of the fact that neither the absolute intensity of the clusters, nor the relative intensity of one cluster with respect to another, was important for the task at hand. For this reason, the images were flattened as follows.

First, the image stack was duplicated and one copy convolved with a Gaussian filter of kernel size 100 pixels. The size of the kernel was carefully chosen so as to smooth low-frequency variations in the image, yet leave high-frequency features, such as the clusters of interest, virtually untouched. This effectively produced an image of the laser illumination cross-sectional profile.

The next step involved subtracting the blurred version of the stack (or the 'local mean intensity'), frame by frame from the original stack. Finally, the decrease in intensity resulting from this manipulation was compensated for by adding the 'global mean' value of each frame of the laser illumination profile to each pixel in the data stack.

8. 4. 2. Selection of sub-optical resolution clusters

With the aid of the software *ImageJ* and its plug-in, *Time Series Analyser*, clusters targeted for quantitation were manually encircled in a region of interest, **Fig. 8.4.2b**, together with a closely positioned partner ROI containing the 'background signal' for reference. The exact positioning of the background reference ROI was decided so as to match as closely as possible the amount of diffuse signal immediately surrounding the cluster of interest. To provide a degree of assurance that the clusters visualised in normal lateral optical resolution were not, in fact, multiple smaller ones very close together, super-resolution imaging on the clusters was used in a qualitative sense, **Fig. 8.4.2c**.

8. 4. 3. *In silico* simulation of the cluster bleaching time course

Building a simulation of the data was intended to fine-tune the performance of the NoRSE algorithm. More precisely, the numerical model would aid in determining a free parameter detailing the number of bins across which the data points are spread, which is crucially related to resolving individual steps; an inappropriate choice can lead to either over-zealous or too grudging step discrimination. This parameter is not deducible *a priori*, so it needs to be tailored to the data.

In order to determine the best value for the number of bins, a simulation was written in Matlab (Stepwise bleaching, Appendix B) modelling the stepwise bleaching of a collection of EGFP molecules excited with polarised light and undergoing imaging in TIRF mode.

The probability of absorption of linearly polarised light by an absorption dipole oriented

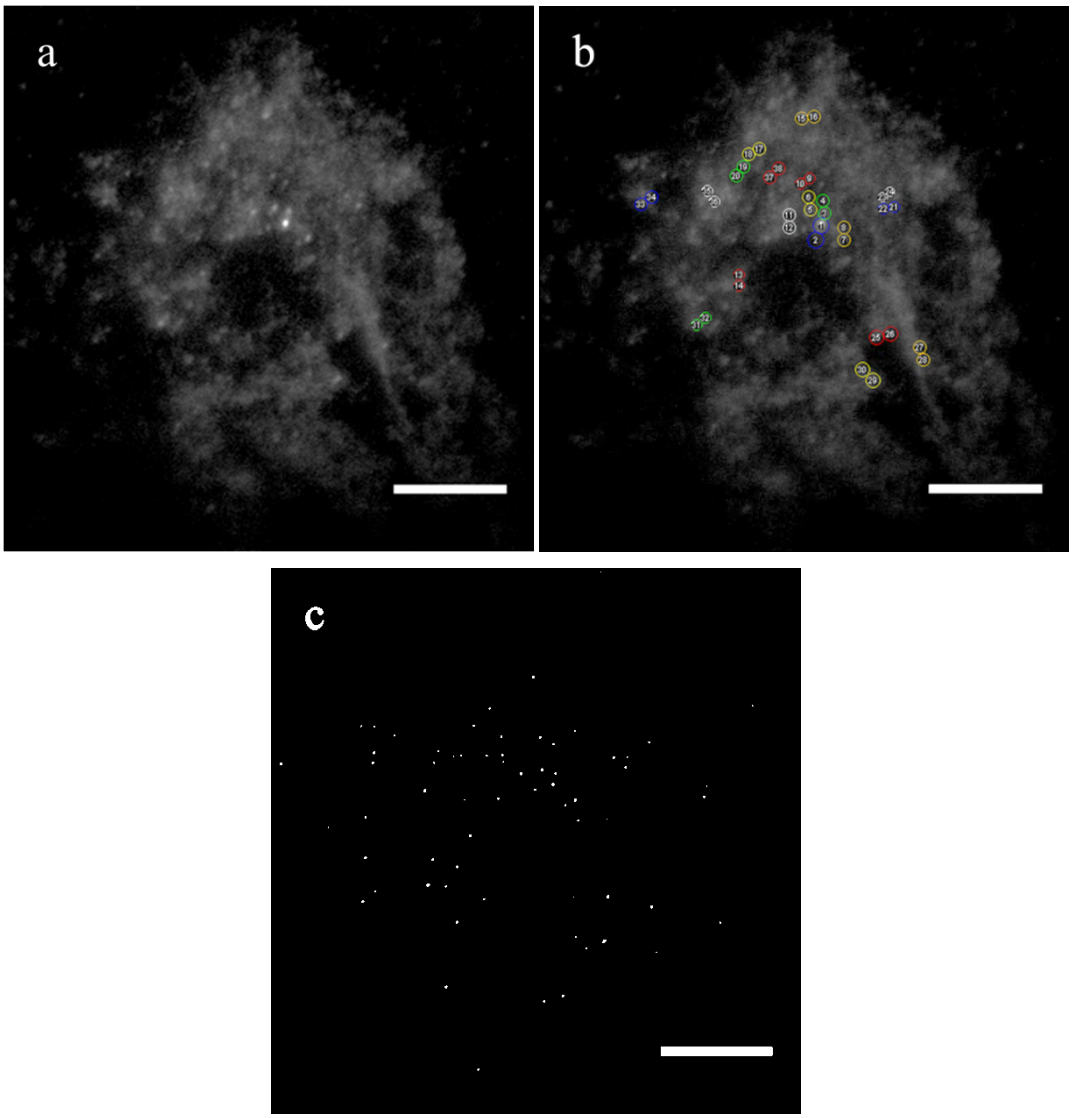

Figure 8.4.2. Method of selectively extracting individual Shh cluster signal from the cell-surface stratum. (a) Widefield snapshot of the cell in TIRF mode, before bleaching commenced. (b) The annotated ROIs which were evaluated. Adjacent ROIs with the same colour were processed in pairs: odd numbers indicate the ROIs containing clusters, even numbers represent the corresponding ROIs with 'background Shh::EGFP' situated inside the cell. (c) Super-resolution reconstruction with *Octane* software. Scale bars: 10 μm.

at polar and azimuthal angles θ_a and ϕ_a is $\sin^2\theta_a \cos\phi_a$. By analogy to the excitation case, the intensity registered by the detector depends in part on the projection of the emission dipole on the plane of the detector [Leuba *et al.*, 2001]. However, due to gathering the emitted light with an objective, some NA effects become prominent; collimating the light captured by the large solid angle spanned by the high-NA objective means that some small proportion of the dipoles orthogonal to the detection plane will also be detected. The mixing of polarisations and the resultant impact on the detected intensity can be expressed with the aid of three coefficients, C_1, C_2

and C_3 – one for each spatial direction [Child *et al.*, 1989]. Thus, for a high-*NA* objective, the detected intensity per unit time is:

$$\mathbb{F} \propto C_1 \sin^2\theta_e \cos^2\phi_e + C_2 \sin^2\theta_e \sin^2\phi_e + C_3 \cos^2\theta_e,$$

where θ_e and ϕ_e are the polar and azimuthal angles of the emission dipole, and the constant of proportionality equating the left- to the right-hand side incorporates the optical efficiency of the system, the laser power and the attributes of the fluorophore (absorption cross-section, *etc*.) [Leuba *et al.*, 2001].

Scaling empirically derived data linearly to coincide with the intensities used here, one obtains between 7.42×10^4 and 7.97×10^4 photons/s (the values are corrected for optical loss within the microscope system and were originally obtained in epi-illumination mode) [Chiu *et al.*, 2001]. Therefore, since the system's optical efficiency can be worked out, this multiplicative factor is known, and to complete the model of a single molecule's bleaching time course, one only needs to modulate the intensity with an exponential decay characteristic to TIRF excitation, **Eq. 2.2.4.1.5**, and add a factor acknowledging the increase in intensity at the TIRF interface:

$$\mathbb{F} = \Phi_{EGFP}\, k\, \eta_{total}(C_1 \sin^2\theta_e \cos^2\phi_e + C_2 \sin^2\theta_e \sin^2\phi_e + C_3 \cos^2\theta_e)\, e^{-\frac{z}{d}}, \qquad \textbf{Eq. 8.1}$$

where Φ_{EGFP} (the photon flux per EGFP molecule per second) is taken to be 76,950 photons/s, the mean photon flux found in [Chiu *et al.*, 2001], k = 1.51 is the jump in intensity at the substrate-specimen boundary (for more information on how the value of k was calculated, the reader should consult section 2. 2. 4. 2. 2. of the Background and Theory chapter), η_{total} is the total optical efficiency of the microscope, C_1 = 0.757, C_2 = 0.013, C_3 = 0.230, and d, the penetration depth, is 71.5 nm. Note that $\mathbb{F}$ is in units of photons/s.

The autofluorescence of the cells was characterised from mock-transfected cells; it is shown in **Fig. 8.4.3.1a**. To determine its precise behaviour in time, mono-, dual and triple exponential decay curves were fitted. The curve yielding the highest R square value (the goodness of fit). which was in excess of 0.998, was the triple-phase decay. The curve was subsequently subtracted from all of the collected image data. The signal from the cluster in ROI 1 is shown in **Fig. 8.4.3.1b**, and that of the corresponding 'background' (ROI 2) in **Fig. 8.4.3.1c**. Separating the signal of ER-localised Shh from that of cluster-incorporated Shh would generate additional noise [Leake *et al.*, 2006], hence the two traces were not subtracted from each other. Upon inspection of the curves, it became clear that, although the specimen had appeared to have been bleached at the end of the imaging, a large fraction of the molecules had remained unbleached.

Fitting the signals in **Fig. 8.4.3.1b** and **Fig. 8.4.3.1c** with a triple-phase exponential func-

tion with nearly identical fast, medium and slow lifetimes confirmed that they were both generated by the same type of fluorophore, as expected. Additionally, and reassuringly, this result rejected the possibility that the Shh::EGFP component within the ER of the unpermeabilised cells was diffusing around and exchanging bleached for unbleached molecules. Thus, these decay rates were henceforth used to simulate the bleaching rate of all of the data.

By assigning the initial intensity in **Fig. 8.4.3.1b** to the simulated cluster, a computer model of ROI 1 was generated (**Fig. 8.4.3.2**). The synthetic trace was subsequently queried with the step-finding algorithm, NoRSE. The initial value for the number of histogram bins was chosen at random, then adjusted iteratively until optimised, taking cue from the findings in the previous trial.

Repeating the same procedure on the remainder of the ROIs demonstrated no clear relationship between the best-suited histogram binning and the particulars of the traces in question. Worryingly, the NoRSE algorithm produced values close to the ground truth most often with unreasonably high number of bins – for example, higher than the total number of data points. It was concluded therefore that NoRSE was defeated by the sheer brevity of the bleaching events (or the insufficient sampling frequency in time), and that its performance was unpredictable, as it varied from ROI to ROI. As an example, an appraisal of the bleaching curve of ROI

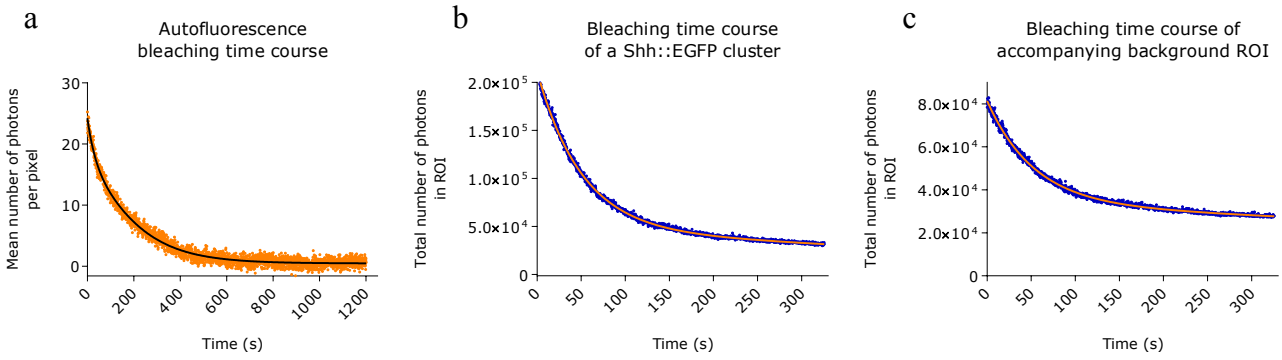

Figure 8.4.3.1. Characterisation of autofluorescence and intracellular Shh::EGFP contribution to the total signal measured from a cluster. (a) Autofluorescence trace (orange) from a mock-transfected cell, fitted with a triple-phase exponential function (black). (b) Bleaching curve (blue) of the largest cluster in **Fig. 8.4.2**, ROI 1, with the autofluorescence contribution, smoothed as the fit in (a), subtracted, and fitted with its own triple-lifetime exponential (orange). (c) Signal originating from ROI 2 (blue) in **Fig. 8.4.2**, with the fit in (a) subtracted from it. This ROI does not contain signal from multimeric Shh::EGFP, but contains contributions from intracellular monomeric Shh::EGFP. The three lifetimes used in the fit here (orange) agree excellently with those found in (b), confirming that the nature of the molecules present in the cluster and endogenously are the same, and that there are no contaminants in the signal (or, alternatively, that the same hypothetical contaminant was present in both).

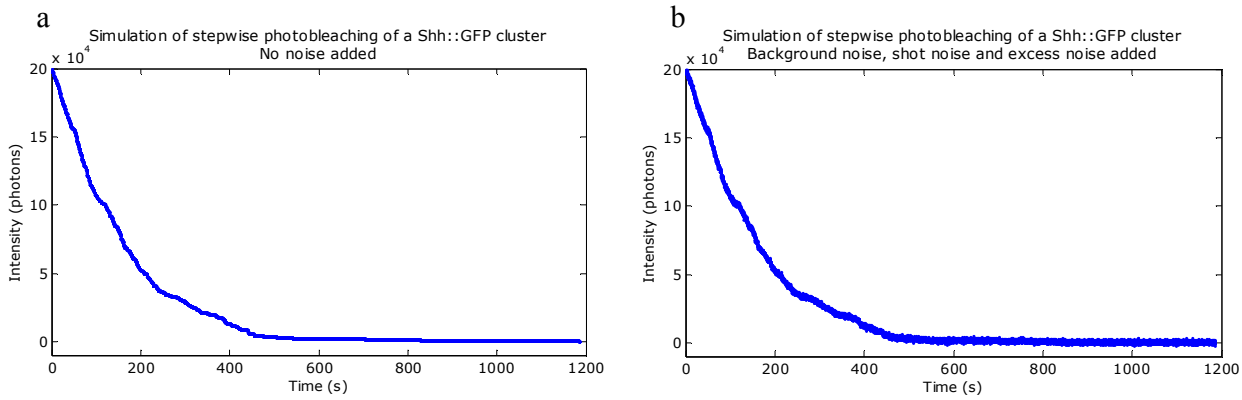

Figure 8.4.3.2. Simulated bleaching traces. These curves are modelled on the data in **Fig. 8.4.3.1b**, which correspond to ROI 1 in **Fig. 8.4.2**. (a) Noiseless simulation showing the precise transitions. (b) Realistic curve incorporating all noise sources. The time course of bleaching was constructed using **Eq. 8.1** and the triple-lifetime exponential decay curve of the real signal fitted in **Fig. 8.4.3.1**. These traces represent 488 bleaching events, i.e. 488 EGFP molecules.

1 with a Monte Carlo simulation (~10 repetitions), after calibration of the binning parameter against another ROI, demonstrated it to contain only about 44% ± 2% of the molecules that the simulation predicted, whereas the average detection rate of NoRSE for this ROI was estimated to be 92% ± 7% with optimum binning. NoRSE's questionable performance in the circumstances, coupled with the incomplete bleaching of the ROIs, called for an abandonment of this method.

Arguably, however, the number of molecules could be derived from the computational model, with the initial intensity of the empirical time series as the only input parameter. Running a Monte Carlo simulation (1,000 repetitions) of each ROI permitted estimating a likely average number of molecules, and the error associated with that estimate (**Fig. 8.4.3.3**).

A frequency distribution of the abundance of Shh::EGFP (**Fig. 8.4.3.3b**) is reminiscent of that already obtained for the cross-sectional area with super-resolution (**Fig. 6.5.5**), and the volume, surface area and cross-sectional area distributions discovered with deconvolution of confocal images (**Fig. 7.4.1.1**, **Fig. 7.4.1.2** and **Fig. 7.4.1.4**), reinforcing the credibility of the data. All bar one of the clusters fall within the expected range of Shh content. The cluster with 323 molecules exceeds the expected upper limit by over 50%, possibly casting doubt over *Octane*'s confidence in resolving sub-optical resolution objects. On the other hand, this cluster may have been correctly resolved, and the oversized agglomeration may have been stimulated by EGFP's predilection for dimerisation at high concentrations [Phillips, 1997][Chiu *et al.*, 2001]. In fact, suspicions of oligomerisation of Shh::EGFP have been openly expressed in [Chamberlain *et al.*, 2008], where this very construct was used. The homodimer dissociation constant of GFP is es-

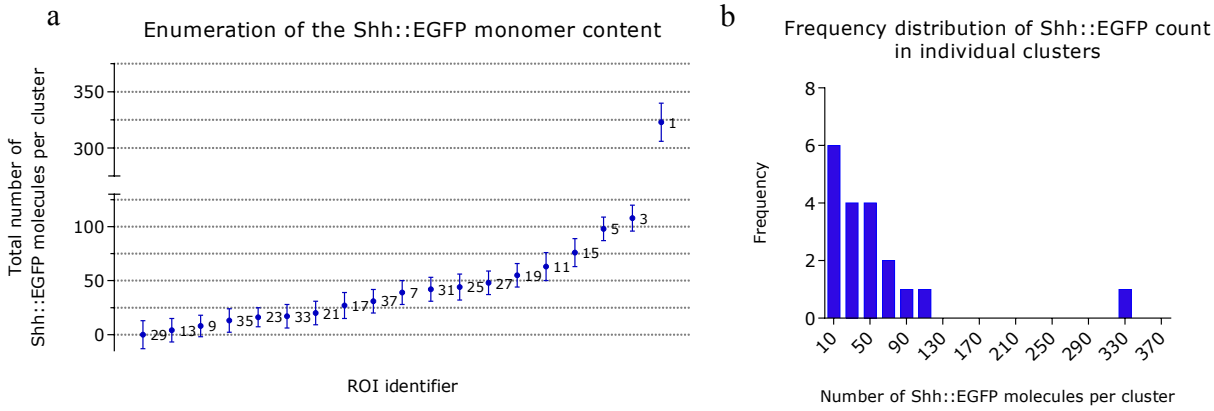

Figure 8.4.3.3. Characterisation of the number and distribution of Shh::EGFP molecules found within clusters. (a) Mean number of molecules and their associated standard deviation, as evaluated by 1,000 Monte Carlo simulations run on each individual cluster. The indices refer to clusters numbered in **Fig. 8.4.2**. (b) The clusters in (a) grouped according to size.

timated to be 100 μM [Phillips, 1997][Chiu *et al.*, 2001][Zacharias *et al.*, 2002]; the concentration of Shh::EGFP within the clusters may be over this limit, thus causing unwanted oligomerisation.

8. 5. Discussion

8. 5. 1. Summary of results

The objective was to make an assessment of the Shh subunit count in cell-surface multimolecular Shh complexes. Originally, the problem was approached with the idea to count the consecutive intensity steps of a real cluster being bleached over time. Due to suboptimal parameters – in particular, long exposure time or high illumination intensity – or perhaps due to unsuitability of the step-finding algorithm, NoRSE, for this type of data, it was necessary to seek an alternative approach. It was thus settled on the following solution: utilising the initial intensity of the cluster (*i.e.* before bleaching commenced) as a starting point for simulating the expected bleaching curve, given the particular conditions of imaging and the expected properties of the fluorophore. This led to the following outcomes:

- Development of a computational model for molecule counting;

- Enumeration of Shh::EGFP using the computational model;

- Specification of prerequisites for following up these results with counting of stepwise bleaching.

8. 5. 2. Conclusions

Investigating the organisation, absolute abundance and stoichiometry of the participating molecular species in multimolecular complexes is essential for grasping their function. Counting fluorophores by stepwise bleaching for enumerating EGFP-tagged molecules in biological complexes with the aid of a TIRF field has been carried out before [Leake *et al.*, 2006]. However, the complexes in question did not pose a significant problem, by virtue of the fact that they were confined in the plane of imaging. Intensity variability arising from the inhomogeneous strength of TIRF illumination with depth causes complications to stepwise counting in an object with axial extent: a deviation from a predictable step size induces ambiguity (one step = one molecule, or several simultaneously decaying molecules?), as well as diminishes the odds of detecting faraway, unfavourably oriented molecules.

Notwithstanding, accurate computational modelling of the system, coupled with a Monte Carlo-style method, can transcend these shortcomings by working out the most likely answer. The method presented here is quasi-dependent on the accuracy of the EGFP photon yield per unit time estimated by other research groups [Chiu *et al.*, 2001]. To add to this, it also assumes random orientation of the EGFP moieties, and therefore Shh monomers, too, which may not be very reasonable if the clusters are comparatively dense. Nonetheless, since no prior information about the orientation of Shh is at one's disposal yet, it seems rational to assume the simplest possible case, rather than more biased orientations.

Using this method, quantitation of a single cell revealed that clusters typically tended to contain a few dozen Shh::EGFP molecules, with larger clusters becoming increasingly rare, having a cut-off at around 120 molecules. It is believed that the cluster of ~323 molecules is some kind of artefact, perhaps owing to resolution limitations or dimerisation of EGFP. Alternatively, it could be a very rare, true phenomenon, with a probability inversely proportional to the number of molecules incorporated into it.

These findings hark back to the observations made in the previous two chapters – that smaller Shh clusters are preferential. That is, if the data in **Fig. 8.4.3.3** are interpreted so as to mean that the size of the cluster scales up with the number of Shh molecules occupying it – which may not necessarily be the case.

Although casual imaging for exploration of optimal areas was performed at minimal intensities and without unnecessary lingering, in order to prevent premature bleaching and subsequent underestimation of the number of molecules, neutral-density filters could be used for preliminary observations. At incident intensities of < 4 W/cm^2, for example, the rate constant of bleaching is stretched to ~30 s [Chiu *et al.*, 2001], allowing just enough time to adjust the focus and field of view, without sacrificing the integrity of subsequent measurements.

Fluorescence anisotropy due to the linear polarisation of the laser excitation source may also have compromised the measurements. If the Shh monomers were randomly oriented and immobilised (it is expected that their degrees of freedom have been reduced by assembling into a dense structure, such as a cluster), then those oriented with their transition dipole moment (TDM) parallel to the oscillation of the field would have been excited efficiently, whereas those in an unfavourable orientation would have emitted few to no fluorescent photons. This leaves the possibility that far-displaced Shh molecules with TDMs perpendicular to the TIRF interface would have remained completely undetected. In order to investigate the polarisation effect on the excitation and emission of the fluorophores, a series of images, taken in quick succession whilst switching the polarisation alternately between *s*- and *p*- upon each exposure, can be acquired and the differences in intensity of the clusters in each set of frames compared. If the polarisation effect is significant, and the molecules are indeed rotationally constrained, the trace that alternate switching of the polarisation would describe in time would include periodic increases in fluorescence, coincident precisely with the polarisation switching [Leake *et al*, 2006, Supplementary Information].

In hindsight, using the Polychrome unpolarised light source (Materials and Methods chapter) may have been a better choice, although confining it to a sufficiently narrow chromatic bandwidth could have posed a problem, since high-quality TIRF requires a highly monochromatic beam of light. An excitation filter would need to be installed.

Förster resonance energy transfer (FRET) is known to occur between GFP molecules in multimeric membrane proteins [Siegel *et al.*, 1997]. Homo-FRET involves the transfer of emitted energy from one molecule (the donor) to another of the same kind in close proximity (the acceptor), where appreciable strength is observed for separation distances of less than 10 nm [Krishnan *et al.*, 2001][Clegg, 2009]. Homo-FRET could have had a confounding effect on our experiments, owing to the quenching that it causes, and the concomitant decline in visibility of the FRET donor (the degree of which depends on the separation between the molecules). The FRET effect is further complicated by the fact that direct contact between GFP molecules can result in conformational change, altering the FRET efficiency [De Angelis *et al.*, 1998]. Quenching through homo-FRET should be addressed in future experiments, for instance, by using an

EGFP mutant with non-overlapping absorption and emission spectra, or by imaging with an embedding buffer at a pH or ionic strength which inhibits FRET [Tsien, 1998][Chiu *et al.*, 2001].

A monomeric version of EGFP, as synthesised by [Zacharias *et al.*, 2002] involving three alternative point-mutations to positively charged residues A206K, L221K or F223R, would be suitable for preventing clustering of Shh for non-physiological reasons. Alternatively, the novel fluorogen-activating protein (FAP) biosensors [Szent-Gyorgyi *et al.*, 2008], mentioned at the end of Chapter 6, would present a high SNR detection system with specific targeting of extracellular proteins – although the degree of efficiency of the fluorogens to permeate and bind molecules within the clusters has not yet been characterised, and therefore the feasibility of FAPs in this problem is not yet established.

Improperly folded proteins are identified and segregated for ER-associated degradation (ERAD) or autophagy [Cao *et al.*, 2012]. Despite the flexible linker joining EGFP to Shh in the Shh::EGFP mutant used here, the folding efficiency of the EGFP moiety may have been reduced. A F64L mutant, described in [Cormack *et al.*, 1996], which folds 30 times more efficiently than the wild type at 37°C could ensure that Shh::EGFP clusters are not abnormally small due to insufficient flux of Shh::EGFP to the cell surface.

Repeating the quantitation by resolving steps in the bleaching curve with NoRSE could provide useful backup to the results obtained with the simulations. Since the measurements are independent of the magnitude of the steps (on the condition that they still remain resolvable), factors such as the orientation of the chromophores which affect the amount of light received from the molecule, are irrelevant.

When acquiring the data, full bleaching of the clusters must be ensured (this would require an uninterrupted acquisition of at least 1200 s at an illumination intensity of 93 W/cm^2, as predicted by the simulations), and an exposure time of around 10 ms would be preferable, in order to resolve individual photodestruction events more clearly. Additionally, quantifying more cells – in spite of the high cell death rate upon transfection with the Shh::EGFP plasmid – could reduce the errors associated with the measurements.

The data provided here do not address whether Shh is the sole ingredient of Shh multimolecular complexes. If the Shh monomer has dimensions of 3.45, 3.54 and 2.40 nm (crystal structure 3M1N of the N-terminal domain [Pepinsky *et al.*, 2000], measured with the *Jmol* molecule viewer in the Protein Data Bank repository), the largest homomultimer contains 210 molecules (as stated in the literature), one assumes that the cluster is spherical and that the molecules are tightly packed, then the expected extent of the cluster in any of the three spatial dimensions is ~22 nm. This spatial scale is currently unobtainable by deconvolution, and the super-resolution capabilities achieved in this work. However, combined use of genetic or FAP tagging and powerful super-resolution on the order of the nanometre could hold the key to an-

swering the long-standing question of homomultimeric versus heteromultimeric Shh. Dual-colour STORM imaging of Shh in tandem with some of the most eligible candidates for involvement in multimerisation – namely HSPGs – is likely to be able to elucidate this.

9. Concluding remarks and outlook

9. 1. Preface

The preceding three chapters have described quantitative and qualitative analyses of Shh multimolecular complexes, and the significance of the Shh sterol and fatty-acid covalent modifications in determining their properties. The investigation was carried out with a range of imaging techniques: STORM, confocal imaging coupled with deconvolution for post-acquisition resolution enhancement, and single-molecule imaging.

This chapter begins by summarising the course of the work carried out in this thesis, in order to highlight the logical basis and reasoning behind the work undertaken. Next, the key results from the previous three chapters are recapitulated and the impact of the findings on the understanding of the multimerisation process of Shh discussed. Furthermore, work in this thesis is put into context with past reports in the literature, and agreement or contradiction with individual reports is identified. Future directions for cell and molecular biology investigations, as well as areas for further instrumentation development, are also suggested from the point of view of unravelling the Shh multimerisation mechanism.

9. 2. Summary of work progression

Contrary to our expectations, optimisation of the conditions for STORM imaging with the small organic dye Alexa Fluor® 488 did not yield a sufficiently high quality of super-resolution reconstructions. This conclusion was reached after critically assessing the fidelity with which well-characterised structural elements of the cell, such as microtubules and F-actin, were rendered with super-resolution software, and subsequently observing many discontinuities. Suspecting that such 'gaps' can seriously affect the density and perceived dimensions of the clusters in an unpredictable way, STORM imaging of Shh was exchanged for a more traditional – yet high-resolution – mode of imaging, *i.e.* deconvolution of confocal optical sections. The apparent underperformance of STORM may be traced to the dye and it can be speculated that its chemical reactivity and/or photophysical properties are simply not permissive for controlled manipulation with the STORM redox buffer. In support of this, Alexa Fluor® 555 proved to be much more photostable under the imaging conditions, a property translated into more continuous filaments, as my simulations showed. Provided that, to our knowledge, Alexa Fluor® 555 had not been reported as suitable for STORM until very recently [Kasuboski *et al.*, 2012][Olivier *et al.*,

2013], this came as a surprise. Alexa Fluor® 555 was subsequently used to obtain super-resolution images of Shh::EGFP complexes tethered to the cell surface.

Although also not guaranteeing complete confidence in the deconvolved output, such as would otherwise nearly always be afforded by direct widefield or confocal imaging, deconvolution does not suffer from pointillism-induced artefacts, therefore it was expected to provide more reliable topological data. In addition, optical sectioning through the specimen permitted gathering volumetric data, which was not possible with STORM, given that no components facilitating 3D STORM imaging had been incorporated into the microscope. Despite concerns over the credibility of the STORM data, measurements of the cross-sectional area of the clusters in the *x*-*y* plane (extending perpendicularly to the optic axis) with STORM largely agreed with those of deconvolution – at least in the overall profile of the distributions – thereby affirming the integrity of the findings. Differences in the 2D shape factors, however, reflected possible discretisation of the Shh structures with STORM (a tendency towards perfect circularity is expected for isolated PSFs), and/or merging of discrete structures (expected to yield more complicated shapes – hence lower shape factors) with deconvolution-aided confocal microscopy. Differential drift (not measured on the confocal microscope) and resultant differences in the afforded resolution by each technique could also be responsible for the observed dichotomy. The resolution attained with deconvolution was ~50 nm in the *x* and *y* directions and ~60 nm in *z*, whereas with STORM, that was ~135 nm in the *x*-*y* plane.

Reports in the literature have shown that, compared to the monomeric protein, Shh macromolecules possess increased signalling potency. Whether there is a relationship of direct proportionality between the number of Shh monomers incorporated into the signalling complex and strength of the signal elicited at the receiving cell, and whether the complex size scales directly with Shh number continue to be as yet unanswered questions. In an attempt to establish the range of Shh monomer content in the clusters, a presently relatively seldom-used technique involving steady bleaching of individual molecules over time was employed. This technique, along with STORM conducted earlier, was performed with recombinant Shh::EGFP, which was transfected into the cells with low rates of success as it appeared to be highly cytotoxic; consequently, very few cells expressed the construct to a level that was easily distinguishable from basal autofluorescence. This permitted only one cell to be quantitated as a viable example with each technique. It is difficult, therefore, to determine whether the data collected from a singular cell represent typical Shh organisation, or whether they contain large statistical deviations away from the true mean values. In any case, experience with plotting single-cell data from the deconvolved batch of acquisitions has shown that single-cell data plots resemble ensemble plots of dozens of cells very closely, meaning that cluster data obtained from a single cell is already statistically representative. To be sure of this, however, data from more cells will need to be col-

lected.

9. 3. Significance of the results and future directions

To my knowledge, this is the first instance that direct dimensional characterisation of Shh multimolecular complexes has been performed. Previously, data of the physical size of Shh existed only for the signalling fragment of Shh, which was obtained using x-ray crystallography [Pepinsky *et al.*, 2000]. The studies I have conducted with four variants of Shh – namely full-length wild type, a cholesterol-deficient, a palmitate-deficient, and an unlipidated mutant – show that it is possible that Shh drives its own multimerisation by the law of mass action, and that its lipid modifications may serve to associate it with the cell surface in order to stimulate the assembly of larger clusters. The involvement of the law of mass action was suggested by the exponential decay-like distribution of the volume of the clusters (to some extent also observable in the surface area and cross-sectional area graphs). The law states that the local concentration of a ligand (in this case, Shh) determines the rate of binding to neighbouring ligands. Thus, a low local concentration of Shh accelerates the rate of multimer assembly, whereas a high local concentration (presumably realised through anchoring of the protein to the plasma membrane with its lipid adducts) slows the rate of formation of high molecular-weight complexes.

This model is generally in good agreement with the data; however, it does not address why the absence of palmitate prompts a significant decrease in the number of small clusters (and possibly a concomitant increase in the large ones) released from the cell surface. My speculation is that there may be other molecules involved in modulating the release of Shh, such as for example HSPGs. HSPGs, binding to Shh *via* the CW motif and other more recently discovered amino acids in the N-terminal domain [Chang *et al.*, 2011], have now for a long time been suspected to be implicated in Shh signalling – not only on the sending side, but also on the receiving end, where they are thought to facilitate reception of the Shh signal [Wilson *et al.*, 2006]. Future studies should therefore focus on establishing the spatial relationship between Shh and HSPGs and investigate the co-distribution of these molecules in high resolution, *e.g.* powerful super-resolution imaging with single-molecule discrimination capabilities, in order to provide an unambiguous answer to the question of whether colocalisation of the two molecules is close enough to indicate intermolecular interaction. FRET studies on this topic could also be helpful in this respect. In addition, co-distribution of Shh with other extracellular proteins, *e.g.* fibronectin, should also be investigated with these methods in the future, since intercellular space is the most plausible transport route of Shh, and the morphogen is very likely to interact with ECM molecules.

The single-molecule measurements conducted with the Shh::EGFP construct showed that the number of Shh::EGFP monomers was mostly under 125. As imaging was performed in the TIRF mode with a penetration depth reaching well into the interior of the cell, where Shh::EGFP could be visualised within the secretory pathway of the ER, it was necessary to remove signal contributions from intracellular Shh::EGFP in order not to over-estimate the multimer sizes. Having to subtract an estimate for the number of background-contributing Shh::EGFP molecules introduced an additional source of error. This could be avoided by using fluorogen-activating proteins (FAPs) in tandem with fluorogens (*i.e.* specially designed small molecules which bind to FAPs). FAPs in conjunction with fluorogens are a novel detection system that is capable of selectively detecting proteins localised to the outer membrane leaflet, and may be small enough to permeate multimolecular complexes in order to bind each of the participating subunits. This method guarantees no intracellular background contribution (except for autofluorescence), and simultaneously may ensure direct proportionality between the detected intensity and the number of labelled Shh molecules. In any case, the degree of success in fluorogen permeabilisation and binding of subunits in multimolecular clusters requires to be characterised first.

An unambiguous correlation between multimer size (obtained with STORM and deconvolution) and number of molecules (obtained with single-molecule bleaching) cannot be made at present. This is because both measurements were not performed simultaneously on one and the same cluster. Performing such a measurement in the future, perhaps with a 3D STORM technique, could be an effective way of answering the question of whether the multimolecular cluster grows in size with increase in Shh subunits, or whether the extra volume in large clusters is filled in with other molecules.

Overall, the results in this thesis have revealed important new implications about the mechanism of multimerisation of Shh and the purpose of the lipid modifications – both subjects of heated debate in the molecular and developmental biology arena. Importantly, the use of a completely unlipidated mutant of Shh, as well as the two semi-lipidated variants and the wild type, has proved very insightful with respect to the exact individual impact of the lipid modifications on multimerisation. My key results agree with [Vyas *et al.*, 2008][Farshi *et al.*, 2011], who claim that electrostatic interactions between certain amino acids could be at the heart of small-scale oligomerisation. At the same time, findings in this thesis directly contradict [Dierker 2009b] and [Ohlig, 2011] who find that uncholesteroylated Shh cannot form multimers. Further, they also indirectly disagree with their claim that Shh multimers are proteolytically processed prior to release.

To conclude, the aim of fully comprehending the sequence of events that takes place on the cell's outer leaflet during multimerisation, and the identity of and manner that Shh lipid

moieties and other molecules are potentially involved in this process, will most likely have to be pursued using 3D multicolour super-resolution imaging on the single-molecule scale.

Bibliography

Abbe, E. Beiträge zur Theorie des Mikroskops und der mikroskopischen Wahrnehmung. *Arch. Mikrosk. Anat.* **9,** 413–8 (1873).

Aitken, C. E., Marshall, R. A. & Puglisi, J. D. An oxygen scavenging system for improvement of dye stability in single-molecule fluorescence experiments. *Biophys. J.* **94,** 1826–35 (2008).

Allen, B. L., Tenzen, T. & McMahon, A. P. The Hedgehog-binding proteins Gas1 and Cdo cooperate to positively regulate Shh signaling during mouse development. *Gene. Dev.* **21,** 1244–57 (2007).

Alvarez, J. I. *et al.* The Hedgehog pathway promotes blood-brain barrier integrity and CNS immune quiescence. *Science* **334,** 1727–31 (2011).

Amankulor, N. M. *et al.* Sonic hedgehog pathway activation is induced by acute brain injury and regulated by injury-related inflammation. *J. Neurosci.* **29,** 10299–308 (2009).

Axelrod, D. Chapter 7: Total internal reflection fluorescence microscopy. *Method. Cell Biol.* **89**, 169–221 (2008).

Axelrod, D. Evanescent Excitation and Emission in Fluorescence Microscopy. *Biophys. J.* **104**, 1401–9 (2013).

Axelrod, D., Thompson, N. L. & Burghardt, T. P. Total internal inflection fluorescent microscopy. *J. Microsc.* **129,** 19–28 (1983).

Baker, D. P., Taylor, F. R. & Pepinsky, R. B. Purifying the hedgehog protein and its variants. *Methods Mol. Biol.* **397**, 1–22 (2007).

Bates, M., Huang, B., Dempsey, G. T. & Zhuang, X. Multicolor super-resolution imaging with photo-switchable fluorescent probes. *Science* **317,** 1749–53 (2007).

Beachy, P. A., Hymowitz, S. G., Lazarus, R. A., Leahy, D. J. & Siebold, C. Interactions between Hedgehog proteins and their binding partners come into view. *Gene. Dev.* **24**, 2001–12 (2010).

Bellaiche, Y., The, I. & Perrimon, N. Tout-velu is a Drosophila homologue of the putative tumour suppressor EXT-1 and is needed for Hh diffusion. *Nature* **394**, 85–8 (1998).

Berman, D. M. *et al.* Widespread requirement for Hedgehog ligand stimulation in growth of digestive tract tumours. *Nature* **425**, 846–51 (2003).

Betzig, E. *et al.* Imaging intracellular fluorescent proteins at nanometer resolution. *Science* **313,** 1642–5 (2006).

Bishop, B. *et al.* Structural insights into hedgehog ligand sequestration by the human hedgehog-interacting protein HHIP. *Nature Struct. Mol. Biol.* **16**, 698–703 (2009).

Bosanac, I. *et al.* The structure of SHH in complex with HHIP reveals a recognition role for the Shh pseudo active site in signaling. *Nature Struct. Mol. Biol.* **16**, 691–7 (2009).

Brown, A. C. N. *et al.* Remodelling of cortical actin where lytic granules dock at natural killer cell immune synapses revealed by super-resolution microscopy. *PLoS Biol.* **9,** e1001152 (2011).

Buglino, J. A. & Resh, M. D. Hhat is a palmitoylacyltransferase with specificity for N-palmitoylation of Sonic Hedgehog. *J. Biol. Chem.* **283**, 22076–88 (2008).

Bürglin, T. R. The Hedgehog protein family. *Genome Biol.* **9,** 241.1–9 (2008).

Burke, R. *et al.* Dispatched, a novel sterol-sensing domain protein dedicated to the release of cholesterol-modified hedgehog from signaling cells. *Cell* **99**, 803–15 (1999).

Cao, S. S. & Kaufman, R. J. Unfolded protein response. *Curr. Biol.* **22,** R622–6 (2012).

Chalfie, M., Tu, Y., Euskirchen, G., Ward, W. W. & Prasher, D. C. Green fluorescent protein as a marker for gene expression. *Science* **263,** 802–5 (1994).

Chamberlain, C. E., Jeong, J., Guo, C., Allen, B. L. & McMahon, A. P. Notochord-derived Shh concentrates in close association with the apically positioned basal body in neural target cells and forms a dynamic gradient during neural patterning. *Development* **135,** 1097–106 (2008).

Chang, S.-C., Mulloy, B., Magee, A. I. & Couchman, J. R. Two distinct sites in sonic Hedgehog combine for heparan sulfate interactions and cell signaling functions. *J. Biol. Chem.* **286,** 44391–402 (2011).

Chen, M.-H. *et al.* Cilium-independent regulation of Gli protein function by Sufu in Hedgehog signaling is evolutionarily conserved. *Genes Dev.* **23**, 1910–28 (2009).

Chen, M.-H., Li, Y.-J., Kawakami, T., Xu, S.-M. & Chuang, P.-T. Palmitoylation is required for the production of a soluble multimeric Hedgehog protein complex and long-range signaling in vertebrates. *Genes Dev.* **18**, 641–59 (2004).

Chen, M.-H., Wilson, C. W. & Chuang, P.-T. SnapShot: hedgehog signaling pathway. *Cell* **130,** 386–386.e2 (2007).

Chen, X. *et al.* Processing and turnover of the Hedgehog protein in the endoplasmic reticulum. *J. Cell Biol.* **192,** 825–38 (2011).

Chen, Y. & Struhl, G. Dual roles for patched in sequestering and transducing Hedgehog. *Cell* **87,** 553–63 (1996).

Child, J., Taylor, D. L., Wang, Y.-L. (ed.) *Methods in Cell Biology: Fluorescence Microscopy of Living Cells in Culture, Part B*. 503 (Academic Press, 1989).

Chiu, C. S., Kartalov, E., Unger, M., Quake, S. & Lester, H. A. Single-molecule measurements calibrate green fluorescent protein surface densities on transparent beads for use with "knock-in" animals and other expression systems. *J. Neurosci. Meth.* **105,** 55–63 (2001).

Chuang, P. T. & McMahon, A. P. Vertebrate Hedgehog signalling modulated by induction of a Hedgehog-binding protein. *Nature* **397,** 617–21 (1999).

Chung, S. H. & Kennedy, R. A. Forward-backward non-linear filtering technique for extracting small biological signals from noise. *J. Neurosci. Meth.* **40,** 71–86 (1991).

Clegg, R. M. Fret and Flim Techniques. *Laboratory Techniques in Biochemistry and Molecular Biology* **33,** 534 (Elsevier, 2009).

Cole, R. W., Jinadasa, T. & Brown, C. M. Measuring and interpreting point spread functions to determine confocal microscope resolution and ensure quality control. *Nat. Protoc.* **6**, 1929–41 (2011).

Cooper, G. M. *The Cell: A Molecular Approach*. 689 (ASM Press, 2000).

Corbit, K. C. *et al.* Vertebrate Smoothened functions at the primary cilium. *Nature* **437**, 1018–21 (2005).

Cormack, B. P., Valdivia, R. H. & Falkow, S. FACS-optimized mutants of the green fluorescent protein (GFP). *Gene* **173,** 33–8 (1996).

Cox, S. *et al.* Bayesian localization microscopy reveals nanoscale podosome dynamics. *Nat. Methods* **9,** 195–200 (2012).

Creanga, A. *et al.* Scube/You activity mediates release of dually lipid-modified Hedgehog signal in soluble form. *Gene. Dev.* **26,** 1312–25 (2012).

Cremer, C. & Masters, B. R. Resolution enhancement techniques in microscopy. *Eur. Phys. J. H* **38,** 281–344 (2013).

Csiszár, I. Why Least Squares and Maximum Entropy? An Axiomatic Approach to Inference for Linear Inverse Problems. *Ann. Stat.* **19,** 2032–66 (1991).

De Angelis, D. A., Miesenböck, G., Zemelman, B. V & Rothman, J. E. PRIM: proximity imaging of green fluorescent protein-tagged polypeptides. *Proc. Natl. Acad. Sci. USA* **95,** 12312–6 (1998).

Dertinger, T., Colyer, R., Iyer, G., Weiss, S. & Enderlein, J. Fast, background-free, 3D super-resolution optical fluctuation imaging (SOFI). *Proc. Natl. Acad. Sci. USA* **106,** 22287–92 (2009).

Dertinger, T., Xu, J., Naini, O., Vogel, R. & Weiss, S. SOFI-based 3D superresolution sectioning with a widefield microscope. *Opt. Nanoscopy* **1,** 2 (2012a).

Dertinger, T. *et al.* Superresolution optical fluctuation imaging (SOFI). *Adv. Exp. Med. Biol.* **733,** 17–21 (2012b).

Desbordes, S. C. & Sanson, B. The glypican Dally-like is required for Hedgehog signalling in the embryonic epidermis of Drosophila. *Development* **130**, 6245–55 (2003).

Dickson, R. M., Cubitt, A. B., Tsien, R. Y. & Moerner, W. E. On/off blinking and switching behaviour of single molecules of green fluorescent protein. *Nature* **388,** 355–8 (1997).

Dierker, T., Dreier, R., Migone, M., Hamer, S. & Grobe, K. Heparan sulfate and transglutaminase activity are required for the formation of covalently cross-linked hedgehog oligomers. *J. Biol. Chem.* **284**, 32562–71 (2009b).

Dierker, T., Dreier, R., Petersen, A., Bordych, C. & Grobe, K. Heparan sulfate-modulated, metalloprotease-mediated sonic hedgehog release from producing cells. *J. Biol. Chem.* **284**, 8013–22 (2009a).

Donnert, G. *et al.* Macromolecular-scale resolution in biological fluorescence microscopy. *Proc. Natl. Acad. Sci. U. S. A.* **103,** 11440–5 (2006).

Donnert, G. *et al.* Two-color far-field fluorescence nanoscopy. *Biophys. J.* **92,** L67–9 (2007).

Ducuing, A., Mollereau, B., Axelrod, J. D. & Vincent, S. Absolute requirement of cholesterol binding for Hedgehog gradient formation in Drosophila. *Open Biol.* **2,** 596–604 (2013).

Duncan, T., Kutty, G., Chader, G. J. & Wiggert, B. A glycoprotein binding retinoids and fatty acids is present in Drosophila. *Arch. Biochem. Biophys.* **312**, 158–66 (1994).

Eaton, S. Multiple roles for lipids in the Hedgehog signalling pathway. *Nat. Rev. Mol. Cell Biol.* **9,** 437–45 (2008).

Eaton, S. Release and trafficking of lipid-linked morphogens. *Curr. Opin. Genet. Dev.* **16**, 17–22 (2006).

Eggenschwiler, J. T. & Anderson, K. V. Cilia and developmental signaling. *Annu. Rev. Cell Dev. Biol.* **23,** 345–73 (2007).

Farshi, P. *et al.* Dual roles of the Cardin-Weintraub motif in multimeric Sonic hedgehog. *J. Biol. Chem.* **286**, 23608–19 (2011).

Franch-Marro, X. *et al.* Glypicans shunt the Wingless signal between local signalling and further transport. *Development* **132**, 659–66 (2005).

Gallet, A., Staccini-Lavenant, L. & Thérond, P. P. Cellular trafficking of the glypican Dally-like is required for full-strength Hedgehog signaling and wingless transcytosis. *Dev. Cell* **14**, 712–25 (2008).

Garcia-Parajo, M. F., Segers-Nolten, G. M., Veerman, J. A., Greve, J. & van Hulst, N. F. Real-time light-driven dynamics of the fluorescence emission in single green fluorescent protein molecules. *Proc. Natl. Acad. Sci. USA* **97,** 7237–42 (2000).

Goetz, J. A., Singh, S., Suber, L. M., Kull, F. J. & Robbins, D. J. A highly conserved amino-terminal region of sonic hedgehog is required for the formation of its freely diffusible multimeric form. *J. Biol. Chem.* **281**, 4087–93 (2006).

Goodrich, L. V, Johnson, R. L., Milenković, L., McMahon, J. A. & Scott, M. P. Conservation of the hedgehog/patched signaling pathway from flies to mice: induction of a mouse patched gene by Hedgehog. *Gene. Dev.* **10**, 301–12 (1996).

Grobe, K. *et al.* Cerebral hypoplasia and craniofacial defects in mice lacking heparan sulfate Ndst1 gene function. *Development* **132**, 3777–86 (2005).

Grover, V. K., Valadez, J. G., Bowman, A. B. & Cooper, M. K. Lipid modifications of Sonic hedgehog ligand dictate cellular reception and signal response. *PLoS ONE* **6,** e21353 (2011).

Gustafsson, M. G. L. Extended resolution fluorescence microscopy. *Curr. Opin. Struct. Biol.* **9,** 627–34 (1999).

Gustafsson, M. G. L. Surpassing the lateral resolution limit by a factor of two using structured illumination microscopy. *J. Microsc.* **198,** 82–7 (2000).

Gustafsson, M. G. L. Nonlinear structured-illumination microscopy: wide-field fluorescence imaging with theoretically unlimited resolution. *Proc. Natl. Acad. Sci. USA* **102,** 13081–6 (2005).

Gustafsson, M. G. L., Agard, D. A. & Sedat, J. W. Sevenfold improvement of axial resolution in 3D wide-field microscopy using two objective lenses. *J. Opt. Soc. Am. A* **9**, 147–156 (1995).

Han, C., Belenkaya, T. Y., Wang, B. & Lin, X. Drosophila glypicans control the cell-to-cell movement of Hedgehog by a dynamin-independent process. *Development* **131**, 601–11 (2004).

Han, C., Yan, D., Belenkaya, T. Y. & Lin, X. Drosophila glypicans Dally and Dally-like shape the extracellular Wingless morphogen gradient in the wing disc. *Development* **132**, 667–79 (2005).

Haramoto, Y. *et al.* (ed.) *Life Science*. (University of Tokyo: Tokyo, 2010).

Heilemann, M. *et al.* Subdiffraction-resolution fluorescence imaging with conventional fluorescent probes. *Angew. Chem. Int. Edit.* **47,** 6172–6 (2008).

Heilemann, M., van de Linde, S., Mukherjee, A. & Sauer, M. Super-resolution imaging with small organic fluorophores. *Angew. Chem. Int. Edit.* **48**, 6903–8 (2009).

Heim, R., Cubitt, A. B. & Tsien, R. Y. Improved green fluorescence. *Nature* **373,** 663–4 (1995).

Hein, B., Willig, K. I. & Hell, S. W. Stimulated emission depletion (STED) nanoscopy of a fluorescent protein-labeled organelle inside a living cell. *Proc. Natl. Acad. Sci. USA* **105,** 14271–6 (2008).

Heintzmann, R. & Cremer, C. G. Lateral modulated excitation microscopy: Improvement of resolution by using a diffraction grating. *Proc. SPIE* **356,** 185–196 (1999).

Heintzmann, R., Münch, H. & Cremer, C. High-precision Distance Measurements in Epifluorescent Microscopy-Simulation and Experiment. In *Cell Vision, 3D image processing in microscopy. International conference; 10th, 3D image processing in microscopy* **4,** 252–3 (1997).

Hell, S. W. Far-field optical nanoscopy. *Science* **316,** 1153–8 (2007).

Hell, S. & Stelzer, E. H. K. Properties of a 4Pi confocal fluorescence microscope. *J. Opt. Soc. Am. A* **9,** 2159–66 (1992).

Hell, S. W. & Wichmann, J. Breaking the diffraction resolution limit by stimulated emission: stimulated-emission-depletion fluorescence microscopy. *Opt. Lett.* **19,** 780–2 (1994).

Henriques, R. *et al.* QuickPALM: 3D real-time photoactivation nanoscopy image processing in

ImageJ. *Nat. Methods* **7**, 339–40 (2010).

Hess, S. T., Girirajan, T. P. K. & Mason, M. D. Ultra-high resolution imaging by fluorescence photoactivation localization microscopy. *Biophys. J.* **91,** 4258–72 (2006).

Hinterdorfer, P. & van Oijen, A. (ed.) *Handbook of Single-Molecule Biophysics*. 626 (Springer: New York, 2009).

Hirvonen, L. M., Wicker, K., Mandula, O. & Heintzmann, R. Structured illumination microscopy of a living cell. *Eur. Biophys. J.* **38,** 807–12 (2009).

Högbom, J. Aperture Synthesis with a Non-Regular Distribution of Interferometer Baselines. *Astron. Astrophys. Suppl.* **15**, 417–26 (1974).

Huang, B., Wang, W., Bates, M. & Zhuang, X. Three-dimensional super-resolution imaging by stochastic optical reconstruction microscopy. *Science* **319,** 810–3 (2008).

Huang, F. *et al.* Video-rate nanoscopy using sCMOS camera-specific single-molecule localization algorithms. *Nat. Methods* **10,** 653–8 (2013).

Imamoto, Y. Evidence for Proton Transfer from Glu-46 to the Chromophore during the Photocycle of Photoactive Yellow Protein. *J. Biol. Chem.* **272,** 12905–8 (1997).

Incardona, J. P. *et al.* Receptor-mediated endocytosis of soluble and membrane-tethered Sonic hedgehog by Patched-1. *Proc. Natl. Acad. Sci. USA* **97**, 12044–9 (2000).

Ingham, P. W. & McMahon, A. P. Hedgehog signaling in animal development: paradigms and principles. *Gene. Dev.* **15**, 3059–87 (2001).

Jones, S. A., Shim, S.-H., He, J. & Zhuang, X. Fast, three-dimensional super-resolution imaging of live cells. *Nat. Methods* **8,** 499–508 (2011).

Juette, M. F. *et al.* Three-dimensional sub-100 nm resolution fluorescence microscopy of thick samples. *Nat. Methods* **5,** 527–9 (2008).

Kao, H. P. & Verkman, A. S. Tracking of single fluorescent particles in three dimensions: use of cylindrical optics to encode particle position. *Biophys. J.* **67,** 1291–300 (1994).

Kasuboski, J. M., Sigal, Y. J., Joens, M. S., Lillemeier, B. F. & Fitzpatrick, J. A. J. Super-resolution microscopy: a comparative treatment. *Current Protocols in Cytometry* **Chapter 2,** Unit2.17 (2012).

Khaliullina, H. *et al.* Patched regulates Smoothened trafficking using lipoprotein-derived lipids. *Development* **136,** 4111–21 (2009).

Kiernan, J. A. *Microscopy Today*, **00-1**, 8–12 (2000).

Kittel, R. J. *et al.* Bruchpilot promotes active zone assembly, Ca2+ channel clustering, and vesicle release. *Science* **312,** 1051–4 (2006).

Klar, T. A. & Hell, S. W. Subdiffraction resolution in far-field fluorescence microscopy. *Opt. Lett.* **24,** 954–6 (1999).

Kner, P., Chhun, B. B., Griffis, E. R., Winoto, L. & Gustafsson, M. G. L. Super-resolution video microscopy of live cells by structured illumination. *Nat. Methods* **6,** 339–42 (2009).

Kohtz, J. D. *et al.* N-terminal fatty-acylation of sonic hedgehog enhances the induction of rodent ventral forebrain neurons. *Development* **128,** 2351–63 (2001).

Kreuger, J., Perez, L., Giraldez, A. J. & Cohen, S. M. Opposing activities of Dally-like glypican at high and low levels of Wingless morphogen activity. *Dev. Cell* **7**, 503–12 (2004).

Krishnan, R. V., Varma, R. & Mayor, S. Fluorescence Methods to Probe Nanometer-Scale Organization of Molecules in Living Cell Membranes. *J. Fluoresc.* **11,** 211–26 (2001).

Kubitscheck, U., Kückmann, O., Kues, T. & Peters, R. Imaging and tracking of single GFP molecules in solution. *Biophys. J.* **78,** 2170–9 (2000).

Lakowicz, J. R. (ed.) *Topics in Fluorescence Spectroscopy - Volume 3: Biochemical Applications*. 390 (Springer: 1992).

Lakowicz, J. R. (ed.) *Principles of Fluorescence Spectroscopy*. 954 (Springer: 2006).

Le Gall, S., Neuhof, A. & Rapoport, T. The endoplasmic reticulum membrane is permeable to small molecules. *Mol. Biol. Cell* **15**, 447–55 (2004).

Leake, M. C. *et al.* Stoichiometry and turnover in single, functioning membrane protein complexes. *Nature* **443,** 355–8 (2006).

Lee, S. F., Thompson, M. A., Schwartz, M. A., Shapiro, L. & Moerner, W. E. Super-resolution imaging of the nucleoid-associated protein HU in Caulobacter crescentus. *Biophys. J.* **100,** L31–3 (2011).

Leuba, S. H., Zlatanova, J. (ed.) *Biology at the Single Molecule Level*. 284 (Pergamon Press, 2001).

Lewis, P. M. *et al.* Cholesterol modification of sonic hedgehog is required for long-range signaling activity and effective modulation of signaling by Ptc1. *Cell* **105,** 599–612 (2001).

Li, G., Zwick, H., Stuck, B. & Lund, D. J. On the use of schematic eye models to estimate retinal image quality. *J. Biomed. Opt.* **5,** 307–14 (2000).

Li, Y., Zhang, H., Litingtung, Y. & Chiang, C. Cholesterol modification restricts the spread of Shh gradient in the limb bud. *Proc. Natl. Acad. Sci. USA* **103,** 6548–53 (2006).

Liem, K. F., He, M., Ocbina, P. J. R. & Anderson, K. V. Mouse Kif7/Costal2 is a cilia-associated protein that regulates Sonic hedgehog signaling. *Proc. Natl. Acad. Sci. USA* **106,** 13377–82 (2009).

Lodish, H. *et al. Molecular Cell Biology*. 1084 (W. H. Freeman: New York, 2000).

Lorensen, W. E. & Cline, H. E. Marching cubes: A high resolution 3D surface construction algorithm. In *SIGGRAPH-87* **21,** 163–9 (ACM Press, 1987).

Lucy, L. B. An iterative technique for the rectification of observed distributions. *Astron. J.* **79**, 745–54 (1974).

Ma, Y. *et al.* Hedgehog-mediated patterning of the mammalian embryo requires transporter-like function of dispatched. *Cell* **111**, 63–75 (2002).

Macias-Garza, F., Bovik, A. C., Diller, K. R., Aggarwal, S. J. & Aggarwal, J. K. The missing cone problem and low-pass distortion in optical serial sectioning microscopy. *ICASSP-88* 890–3 (1988).

Marigo, V., Davey, R. A., Zuo, Y., Cunningham, J. M. & Tabin, C. J. Biochemical evidence that patched is the Hedgehog receptor. *Nature* **384**, 176–9 (1996).

May, S. R. *et al.* Loss of the retrograde motor for IFT disrupts localization of Smo to cilia and prevents the expression of both activator and repressor functions of Gli. *Dev. Biol.* **287**, 378–89 (2005).

McLellan, J. S. *et al.* Structure of a heparin-dependent complex of Hedgehog and Ihog. *Proc. Natl. Acad. Sci. USA* **103**, 17208–13 (2006).

Milenković, L. & Scott, M. P. Not lost in space: trafficking in the hedgehog signaling pathway. *Sci. Signal.* **3,** pe14 (2010).

Ming, D., Kong, Y., Wu, Y. & Ma, J. Simulation of F-actin filaments of several microns. *Biophys. J.* **85,** 27–35 (2003).

Miura, H. *et al.* Shh and Ptc are associated with taste bud maintenance in the adult mouse. *Mech. Develop.* **106,** 143–5 (2001).

Miyaji, T. *et al.* Expression and distribution of transcripts for sonic hedgehog in the early phase of fracture repair. *Histochem. Cell Biol.* **119,** 233–7 (2003).

Mukhopadhyay, S. *et al.* The ciliary G-protein-coupled receptor Gpr161 negatively regulates the Sonic hedgehog pathway *via* cAMP signaling. *Cell* **152**, 210–23 (2013).

Naora, H. Microspectrophotometry and cytochemical analysis of nucleic acids. *Science* **114,** 279–80 (1951).

Niu, L. & Yu, J. Investigating intracellular dynamics of FtsZ cytoskeleton with photoactivation single-molecule tracking. *Biophys. J.* **95,** 2009–16 (2008).

Nüsslein-Volhard, C. & Wieschaus, E. Mutations affecting segment number and polarity in Drosophila. *Nature* **287**, 795–801 (1980).

Ohlig, S. *et al.* Sonic hedgehog shedding results in functional activation of the solubilized protein. *Dev. Cell* **20**, 764–74 (2011).

Olivier, N., Keller, D., Rajan, V. S., Gönczy, P. & Manley, S. Simple buffers for 3D STORM microscopy. *Biomed. Opt. Express* **4,** 885–99 (2013).

Owen, D. M. *et al.* Quantitative Analysis of Three-Dimensional Fluorescence Localization Microscopy Data. *Biophys. J.* **105,** L05–7 (2013).

Palm, W. *et al.* Secretion and Signaling Activities of Lipoprotein-Associated Hedgehog and Non-Sterol-Modified Hedgehog in Flies and Mammals. *PLoS Biol.* **11**, e1001505 (2013).

Panáková, D., Sprong, H., Marois, E., Thiele, C. & Eaton, S. Lipoprotein particles are required for Hedgehog and Wingless signalling. *Nature* **435**, 58–65 (2005).

Park, Y. *et al.* Drosophila Perlecan modulates FGF and Hedgehog signals to activate neural stem cell division. *Dev. Biol.* **253**, 247–57 (2003).

Parton, R. M. & Davis, I. *Cell biology: a laboratory handbook*. 187–200 (2006).

Paschotta, R. *Encyclopedia of Laser Physics and Technology*. 844 (Wiley-VCH: Berlin, 2008).

Pavani, S. R. P. & Piestun, R. Three dimensional tracking of fluorescent microparticles using a photon-limited double-helix response system. *Opt. Express* **16,** 22048–57 (2008).

Pawley, J. B. (ed.) *Handbook of Biological Confocal Microscopy*. 988 (Springer: New York, 2006).

Peart, J. R. *et al.* Ubiquitin ligase-associated protein SGT1 is required for host and nonhost disease resistance in plants. *Proc. Natl. Acad. Sci. USA* **99**, 10865–9 (2002).

Pepinsky, R. B. *et al.* Identification of a palmitic acid-modified form of human Sonic hedgehog. *J. Biol Chem.* **273**, 14037–45 (1998).

Pepinsky, R. B. *et al.* Mapping sonic hedgehog-receptor interactions by steric interference. *J. Biol Chem.* **275**, 10995–11001 (2000).

Phillips, G. N. Structure and dynamics of green fluorescent protein. *Curr. Opin. Struc. Biol.* **7,** 821–7 (1997).

Poher, V. Y. J. Microscopic Imaging and Photo-stimulation using Micro-structured Light Emitting Diodes. 200 (Imperial College London: 2008).

Porter, J. A., Young, K. E. & Beachy, P. A. Cholesterol modification of hedgehog signaling proteins in animal development. *Science* **274**, 255–9 (1996).

Prasher, D. C., Eckenrode, V. K., Ward, W. W., Prendergast, F. G. & Cormier, M. J. Primary structure of the *Aequorea victoria* green-fluorescent protein. *Gene* **111,** 229–33 (1992).

Rees, E. J. *et al.* Blind assessment of localisation microscope image resolution. *Opt. Nanoscopy* **1,** 12 (2012).

Resh, M. D. Covalent lipid modifications of proteins. *Curr. Biol.* **23**, R431–5 (2013).

Reuel, N. F. *et al.* NoRSE: noise reduction and state evaluator for high-frequency single event traces. *Bioinformatics* **28,** 296–7 (2012).

Richardson, W. H. Bayesian-Based Iterative Method of Image Restoration. *J. Opt. Soc. Am.* **62**, 55–9 (1972).

Rietveld, A., Neutz, S., Simons, K. & Eaton, S. Association of sterol- and glycosylphosphatidylinositol-linked proteins with Drosophila raft lipid microdomains. *J. Biol. Chem.* **274**, 12049–54 (1999).

Robbins, D. J., Fei, D. L. & Riobo, N. A. The hedgehog signal transduction network. *Sci. Signal.* **5**, 1–13 (2012).

Rosten, E., Jones, G. E. & Cox, S. ImageJ plug-in for Bayesian analysis of blinking and bleaching. *Nat. Methods* **10,** 97–8 (2013).

Rubin, J. B., Choi, Y. & Segal, R. A. Cerebellar proteoglycans regulate sonic hedgehog responses during development. *Development* **129,** 2223–32 (2002).

Russ, J. C. *The image processing handbook*. 771 (CRC Press: 1998).

Rust, M. J., Bates, M. & Zhuang, X. Sub-diffraction-limit imaging by stochastic optical reconstruc-

tion microscopy (STORM). *Nat. Methods* **3,** 793–5 (2006).

Ryan, K. E. & Chiang, C. Hedgehog secretion and signal transduction in vertebrates. *J. Biol. Chem.* **287**, 17905–13 (2012).

Sanders, T. A., Llagostera, E. & Barna, M. Specialized filopodia direct long-range transport of SHH during vertebrate tissue patterning. *Nature* **497,** 628–32 (2013).

Sauer, M., Hofkens, J. & Enderlein, J. *Handbook of Fluorescence Spectroscopy and Imaging: From Ensemble to Single Molecules*. 290 (Wiley-VCH: Weinheim, 2011).

Schermelleh, L., Heintzmann, R. & Leonhardt, H. A guide to super-resolution fluorescence microscopy. *J. Cell Biol.* **190,** 165–75 (2010).

Schröder, J., Benink, H., Dyba, M. & Los, G. V. In vivo labeling method using a genetic construct for nanoscale resolution microscopy. *Biophys. J.* **96,** L01–3 (2009).

Sheppard, C. J. R. The spatial frequency cut-off in three-dimensional imaging. *Optik* **72,** 131–3 (1986a).

Sheppard, C. J. R. The spatial frequency cut-off in three-dimensional imaging II. *Optik* **74,** 128 – 9 (1986b).

Sheppard, C. J. R., Choudhury, A. & Gannaway, J. Electromagnetic field near the focus of wide-angular lens and mirror systems. *Microwave Opt. Acoust.* **1,** 129–32 (1977).

Sheppard, G. J. R. & Matthews, H. J. Imaging in high-aperture optical systems. *J. Opt. Soc. Am. A* **4**, 1354 (1987).

Shimomura, O., Johnson, F. H. & Saiga, Y. Extraction, Purification and Properties of Aequorin, a Bioluminescent Protein from the Luminous Hydromedusan, Aequorea. *J. Cell. Compar. Physl.* **59,** 223–39 (1962).

Shroff, H. *et al.* Dual-color superresolution imaging of genetically expressed probes within individual adhesion complexes. *Proc. Natl. Acad. Sci. USA* **104,** 20308–13 (2007).

Shroff, H., Galbraith, C. G., Galbraith, J. A. & Betzig, E. Live-cell photoactivated localization microscopy of nanoscale adhesion dynamics. *Nat. Methods* **5,** 417–23 (2008).

Shtengel, G. *et al.* Interferometric fluorescent super-resolution microscopy resolves 3D cellular ultrastructure. *Proc. Natl. Acad. Sci. USA* **106,** 3125–30 (2009).

Sieber, J. J., Willig, K. I., Heintzmann, R., Hell, S. W. & Lang, T. The SNARE motif is essential for the formation of syntaxin clusters in the plasma membrane. *Biophys. J.* **90,** 2843–51 (2006).

Siegel, M. S. & Isacoff, E. Y. A genetically encoded optical probe of membrane voltage. *Neuron* **19,** 735–41 (1997).

Sparrow, C. M. On Spectroscopic Resolving Power. *Astrophys. J.* **44,** 76–87 (1916).

St-Jacques, B. *et al.* Sonic hedgehog signaling is essential for hair development. *Curr. Biol.* **8,** 1058–68 (1998).

Stebel, M. *et al.* The growth suppressing gas1 product is a GPI-linked protein. *FEBS Lett.* **481,** 152–8 (2000).

Szent-Gyorgyi, C. *et al.* Fluorogen-activating single-chain antibodies for imaging cell surface proteins. *Nat. Biotechnol.* **26**, 235–40 (2008).

Szymborska, A. *et al.* Nuclear Pore Scaffold Structure Analyzed by Super-Resolution Microscopy and Particle Averaging. *Science*, 1240672 (2013).

Tanaka, Y., Okada, Y. & Hirokawa, N. FGF-induced vesicular release of Sonic hedgehog and retinoic acid in leftward nodal flow is critical for left-right determination. *Nature* **435**, 172–7 (2005).

Tatavarty, V., Kim, E.-J., Rodionov, V. & Yu, J. Investigating sub-spine actin dynamics in rat hippocampal neurons with super-resolution optical imaging. *PLoS ONE* **4,** e7724 (2009).

Thayer, S. P. *et al.* Hedgehog is an early and late mediator of pancreatic cancer tumorigenesis. *Nature* **425**, 851–6 (2003).

Thompson, R. E., Larson, D. R. & Webb, W. W. Precise nanometer localization analysis for individual fluorescent probes. *Biophys. J.* **82**, 2775–83 (2002).

Tian, H., Jeong, J., Harfe, B. D., Tabin, C. J. & McMahon, A. P. Mouse Disp1 is required in sonic hedgehog-expressing cells for paracrine activity of the cholesterol-modified ligand. *Development* **132,** 133–42 (2005).

Tokhunts, R. *et al.* The full-length unprocessed hedgehog protein is an active signaling molecule. *The J. Biol. Chem.* **285,** 2562–8 (2010).

Tsien, R. Y. The green fluorescent protein. *Annu. Rev. Biochem.* **67,** 509–44 (1998).

van de Linde, S. *et al.* Multicolor photoswitching microscopy for subdiffraction-resolution fluorescence imaging. *Photoch. Photobio. Sci.* **8**, 465–9 (2009).

van de Linde, S. *et al.* Photoinduced formation of reversible dye radicals and their impact on super-resolution imaging. *Photoch. Photobio. Sci.* **10,** 499–506 (2011).

van de Linde, S., Wolter, S., Heilemann, M. & Sauer, M. The effect of photoswitching kinetics and labeling densities on super-resolution fluorescence imaging. *J. Biotechnol.* **149**, 260–6 (2010).

van den Brink, G. R. Hedgehog signaling in development and homeostasis of the gastrointestinal tract. *Physiol. Rev.* **87,** 1343–75 (2007).

van der Voort, H. T. M. & Brakenhoff, G. J. 3-D image formation in high-aperture fluorescence confocal microscopy: a numerical analysis. *J. Microsc.* **158**, 43–54 (1990).

Vandekerckhove, J., Deboben, A., Nassal, M. & Wieland, T. The phalloidin binding site of F-actin. *EMBO J.* **4,** 2815–8 (1985).

Vorbrodt, A. & Koprowski, H. Ruthenium red-stained coat of normal and simian virus 40-transformed cells. *J. Natl. Cancer I.* **43,** 1241–8 (1969).

Vyas, N. *et al.* Nanoscale organization of hedgehog is essential for long-range signaling. *Cell* **133**, 1214–27 (2008).

Walker, J. M. & Rapley, R. (ed.) *Molecular Biomethods Handbook*. 1124 (Humana Press, 2008).

Wang, P. *et al.* Far-field imaging of non-fluorescent species with subdiffraction resolution. *Nat. Photonics* **7**, 449–53 (2013).

Warren, M. M. *et al.* Ground-state proton transfer in the photoswitching reactions of the fluorescent protein Dronpa. *Nat. Commun.* **4,** 1461 (2013).

Watkins, D. N. *et al.* Hedgehog signalling within airway epithelial progenitors and in small-cell lung cancer. *Nature* **422,** 313–7 (2003).

Westphal, V. & Hell, S. Nanoscale Resolution in the Focal Plane of an Optical Microscope. *Phys. Rev. Lett.* **94,** 143903 (2005).

Wilhelm, S., Gröbler, B., Gluch, M. & Heinz, H. *Confocal laser scanning microscopy principles*. 29 at <http://zeiss-campus.magnet.fsu.edu/referencelibrary/pdfs/ZeissConfocalPrinciples.pdf> (2008)

Willig, K. I., Rizzoli, S. O., Westphal, V., Jahn, R. & Hell, S. W. STED microscopy reveals that synaptotagmin remains clustered after synaptic vesicle exocytosis. *Nature* **440,** 935–9 (2006).

Wilson, C. W. & Chuang, P.-T. New "Hogs" in Hedgehog Transport and Signal Reception. *Cell* **125,** 435–8 (2006).

Wolter, S. *et al.* rapidSTORM: accurate, fast open-source software for localization microscopy. *Nat. Methods* **9,** 1040–1 (2012).

Wolter, S. *et al.* Real-time computation of subdiffraction-resolution fluorescence images. *J. Microsc.* **237,** 12–22 (2010).

Yan, D. & Lin, X. Shaping morphogen gradients by proteoglycans. *Cold Spring Harb. Perspect. Biol.* **1,** a002493 (2009).

Zacharias, D. A., Violin, J. D., Newton, A. C. & Tsien, R. Y. Partitioning of lipid-modified monomeric GFPs into membrane microdomains of live cells. *Science* **296,** 913–6 (2002).

Zarogoulidis, P. *et al.* Hedgehog signaling pathway: the must, the maybe and the unknown. *J. Thorac. Dis.* **5**, 195–7 (2013).

Zeng, X. *et al.* A freely diffusible form of Sonic hedgehog mediates long-range signalling. *Nature* **411**, 716–20 (2001).

Zhang, B., Zerubia, J. & Olivo-Marin, J.-C. A study of Gaussian approximations of fluorescence microscopy PSF models. *SPIE Proc. Ser.* **6090**, 60900K–60900K–11 (2006).

Zhang, B., Zerubia, J. & Olivo-Marin, J.-C. Gaussian approximations of fluorescence microscope point-spread function models. *Appl. Optics* **46**, 1819–29 (2007).

Appendix A – The origin of the singlet and triplet energy states

The nomenclature 'singlet' and 'triplet' stems from quantum mechanics, and in particular, the quantum-mechanical property of spin multiplicity – as shall be explained shortly.

Electrons possess a certain quantum-mechanical angular momentum, called 'spin'. Each electron can either have a spin up or spin down (in shorthand denoted by ↑ or ↓, respectively, and amounting to ½ in magnitude). Depending on how the electrons are distributed among different orbitals, and how their spins are oriented, the vector sums of the spins will be different. Not all combinations of electron orbitals and spins are possible since, according to the Pauli Exclusion Principle (PEP), no two electrons with the same spin can co-exist in a single energy level.

Spin multiplicity is the total number of different possible vector spin additions. With *singlet* states, summing the electrons' spins always results in only *one* value (although there are many ways of combining the spins whilst observing the PEP), and that is invariably zero. The spin multiplicity of singlet states is therefore one. Similarly, with *triplet* states, *three* different outcomes are possible: a total spin of either –1, 0 or 1. The spin multiplicity of triplet states is therefore three.

The fluorophore normally resides in the singlet state. On occasion, however, the singlet excited state can become a triplet state in the course of the quantum-mechanical evolution that results after excitation. Vibration or rotation of all or part of the molecule can lead to this inter-system crossing. Once in the triplet excited state, decay back to the ground state is not spontaneous. Direct transition from a triplet state to a singlet is not allowed; the electron in the triplet-state orbital has the same spin orientation as that in the ground state, hence the PEP forbids transition to the ground state. A time-dependent 'evolution' of the quantum-mechanical properties of the system must occur, where the excited electron eventually experiences a spin flip and is allowed to decay into the singlet ground state again. Absorption of a photon cannot change the spin state by itself – hence photon absorption of a singlet ground state will yield a singlet excited state. A spin flip can only be achieved *via* coupling to the environment. This is a relatively time-consuming process and as a result, this transition, called phosphorescence, takes several orders of magnitude longer to occur than that of fluorescence.

Appendix B – Computer programmes

All of the routines below were written in the Matlab language on versions R2010a to R2012a, and are all executable in version R2012a.

DIC correction

```
clear all; close all;
delete('deconv_175nm_PS-Speck_5beads_red_emitting_in_green_cluster_DIC-corrected.tif');
%--------------------------------------------------------------------------
disp_x = 5;
disp_y = 5;
c = 1.0;
%--------------------------------------------------------------------------
fname = 'deconv_175nm_PS-Speck_5beads_red_emitting_in_green_cluster.tif';
fcorr = 'deconv_175nm_PS-Speck_5beads_red_emitting_in_green_cluster_DIC-corrected.tif';
info = imfinfo( fname );
num_images = numel( info );
B = imread( fname, 14 );
figure; imshow( B ); title( 'Original deconvolved image, with DIC aberration' );
size_x = size( B, 2 );
size_y = size( B, 1 );
[x y] = meshgrid( 1 : size_x, 1 : size_y );
kx = size_x ./ x;
ky = size_y ./ y;
for k = 14
   A = imread( fname, k );
   shift = ( c / sqrt( size_x * size_y ) ) * exp( -2 * 1i * pi * ( ( disp_x * kx ) + ( disp_y * ky ) ) );
   A = fftshift( fft2( A ) );
   A = A / ( eye( size_y, size_x ) + shift );
   A = abs( ifft2( fftshift( A ) ) );
   figure; imshow( A, [] );
   A = uint16( A );
   imwrite( A, 'deconv_175nm_PS-Speck_5beads_red_emitting_in_green_cluster_DIC-corrected.tif', 'tif',
'compression', 'none', 'writemode', 'append' );
end
C = imread( fcorr, 14 );
figure; imshow( C ); title( 'Deconvolved image, where DIC aberration has been corrected' ); zoomcenter(
82, 45, 8 );
disp( isequal( B, C ) );
```

x-y drift estimation

```
clear all; close all;
fname='cropped_bead_bleach-correct_oversampled.tif'; %_bleach-correct
floc='trackresult.txt';
info=imfinfo(fname);
fr=numel(info);
width=info.Width;
height=info.Height;
```

```
[x,y]=meshgrid(1:width,1:height);
sigma=0.548;
px=155/2;
Loc=zeros(fr,3);
A=imread(fname,1);
Gauss=zeros(4,1);
[xx,yy]=find(A==max(A(:)));
Ampl=double(max(max(A)));
Gauss(3)=xx(1);
Gauss(4)=yy(1);
% mask=0.2*Ampl;
for k=1:fr
   A=imread(fname, k);
   a=x(:);
   b=y(:);
   c=double(A(:));
   % Define a function which finds the residual between the image and a Gaussian distribution
   Residual = @( params ) ( params(1) / ( 2 * pi * params(2)^2 ) * exp( -( ( a - params(3) ).^2 + ( b -
params(4) ).^2 ) / ( 2 * params(2)^2 ) ) ) - c;
   Ampl=double(max(max(A)));
   InitialParams = [Ampl, sigma, Gauss(3), Gauss(4)];
   % Choose manner of display of optimised parameters
   opts = optimset('Display', 'Final', 'TolX', 1e-10, 'TolFun', 1e-10, 'MaxFunEval', 1e8, 'MaxIter', 1e3);
   % Non-linear least squares fit of Gaussian over image data
   Gauss = lsqnonlin( Residual, InitialParams, [], [], opts );
   Loc(k,:)=[k Gauss(3)*px Gauss(4)*px]; % in nm
end
dlmwrite(floc, Loc, '\t');
```

Single-molecule localisation

```
clear all; close all;
matlabpool open
profile on
tic;
% VARIABLES-------------------------------------------------------------
mesh = 256;
subpix = 501;
CoarseCF = 5.8;
FineCF   = 4.4;
pxSizeF = 80;
pxSizeC = 160;
QEcoarse = 0.153;
QEfine = 0.0916;
EMgainC = 4.0;
EMgainF = 4.0;
analogue_gainC = 1;
analogue_gainF = 1;
exposC = 0.031;
exposF = 0.031;
[x, y] = meshgrid( -1 : 2/mesh : 1-2/mesh, -1 : 2/mesh : 1-2/mesh
xF = mesh/2 * x;
yF = mesh/2 * y;
xC = 0.5 * xF( 1 : 2 : end, 1 : 2 : end );
yC = 0.5 * yF( 1 : 2 : end, 1 : 2 : end );
```

```
dr  = linspace( -2.0, 2.0, subpix );
drC = 0.5 * dr;
CentrerrFX  = zeros( subpix );
CentrerrFY  = zeros( subpix );
CentrerrFXN = zeros( subpix );
CentrerrFYN = zeros( subpix );
CentrerrCX  = zeros( subpix );
CentrerrCY  = zeros( subpix );
CentrerrCXN = zeros( subpix );
CentrerrCYN = zeros( subpix );
CentrerrF   = zeros( subpix );
CentrerrFN  = zeros( subpix );
CentrerrC   = zeros( subpix );
CentrerrCN  = zeros( subpix );
% GENERATE A POINT SOURCE FROM MICROSCOPE OBJECTIVE APERTURE----------
rd = sqrt( x.^2 + y.^2 );
rn = rd / ( 0.5 * 0.08 / 0.0895 );
ps = ( rn < 2 ) .* ( 2 / pi * ( acos( rn / 2 ) - rn / 2 .* sqrt( 1 - ( rn / 2 ) .^ 2 ) ) );
% CONVOLVE IMAGE WITH CORRESPONDING CAMERA PIXELS----------
psPupil_funcx  = sinc( x/2 );
psPupil_funcy  = sinc( y/2 );
psCPupil_funcx = sinc( x );
psCPupil_funcy = sinc( y );
planck = 6.62606957e-34; % Planck's constant, in m^2.kg/s
speed_of_light = 299792458; % in m/s
lambda = 519e-9; % peak emission wavelength of the dye, in m
avogadro = 6.02214129e23; % Avogadro's number, in mol^-1
epsilon = 71e6; % molar extinction coefficient (or absorptivity) of the dye, in cm^2/mol
QY = 0.92; % quantum yield of the dye
LP = 2330; % laser intensity, in W/cm^2
En = planck * speed_of_light / lambda;
crsec = 1000 * log(10) * epsilon / avogadro;
Alx488flux = QY * LP * crsec / En;
NA = 1.45;
Gauss_s = 0.255 * lambda / NA;
radC = 26.76;
radF = 52.00;
fIOTF = psPupil_funcx  .* psPupil_funcy  .* ps;
cIOTF = psCPupil_funcx .* psCPupil_funcy .* ps;
% SHIFT THE POINT SOURCE ACROSS THE AREA OF A PIXEL----------
CamImgFine = fIOTF;
CamImgFine = real( fftshift( ifft2( fftshift( CamImgFine ) ) ) );
CamImgCoarse = cIOTF;
CamImgCoarse = real( fftshift( ifft2( fftshift( CamImgCoarse ) ) ) );
CamImgCoarse = CamImgCoarse( 1 : 2 : end, 1 : 2 : end );
% ASSIGN CHARACTERISTICS OF ALEXA 488 DYE----------
CamImgFine   = CamImgFine   * Alx488flux * exposC / sum( sum( CamImgFine   ) );
CamImgCoarse = CamImgCoarse * Alx488flux * exposF / sum( sum( CamImgCoarse ) );
% APPLY QE OF DETECTOR AND CONVERT TO GREYLEVELS----------
CamImgFine   = CamImgFine   * EMgainF * analogue_gainF * QEfine   / FineCF; % 0.55 is the QE of the
C9100-02 camera at lambda = 520 nm
CamImgCoarse = CamImgCoarse * EMgainC * analogue_gainC * QEcoarse / CoarseCF; % 0.92 is the QE of
the C9100-13 camera at lambda = 520 nm
AmplC = max(max(CamImgCoarse));
AmplF = max(max(CamImgFine));
threshC = 0.01 * AmplC;
threshF = 0.01 * AmplF;
parfor i = 1 : subpix
   for j = 1 : subpix
```

```
    % SHIFT THE POINT SOURCE ACROSS THE AREA OF A PIXEL----------
    shift = exp( 1i * pi * ( x *-dr(i) + y *-dr(j) ) );

    CamImgFine = fIOTF .* shift;
    CamImgFine = real( fftshift( ifft2( fftshift( CamImgFine ) ) ) );
    CamImgCoarse = cIOTF .* shift;
    CamImgCoarse = real( fftshift( ifft2( fftshift( CamImgCoarse ) ) ) );
    CamImgCoarse = CamImgCoarse( 1 : 2 : end, 1 : 2 : end );
    % ASSIGN CHARACTERISTICS OF ALEXA 488 DYE----------
    CamImgFine   = CamImgFine   * Alx488flux * exposC / sum( sum( CamImgFine   ) );
    CamImgCoarse = CamImgCoarse * Alx488flux * exposF / sum( sum( CamImgCoarse ) );
    % APPLY QE OF DETECTOR----------
    CamImgFine   = CamImgFine  * QEfine;
    CamImgCoarse = CamImgCoarse * QEcoarse;
    % ADD PHOTON-COUNTING NOISE----------
    CamImgFineN   = CamImgFine; % N = noiseless
    CamImgFine    = poissrnd( CamImgFine   );
    CamImgCoarseN = CamImgCoarse;
    CamImgCoarse  = poissrnd( CamImgCoarse );
        % CONVERT TO GREYLEVELS----------    ----------
    CamImgFine = CamImgFine * EMgainF * analogue_gainF / FineCF; %       CamImgCoarse =
CamImgCoarse * EMgainC * analogue_gainC / CoarseCF;
    BgrNoiseC    = 624.512;
    CamImgCoarse = CamImgCoarse + abs( BgrNoiseC );

    BgrNoiseF  = 166.071;
    CamImgFine = CamImgFine + abs( BgrNoiseF );
    maskF  = CamImgFine   > threshF;
    maskC  = CamImgCoarse  > threshC;
    maskFN = CamImgFineN   > threshF;
    maskCN = CamImgCoarseN > threshC;

    xlocF = 0;
    ylocF = 0;
    xlocFN = 0;
    ylocFN = 0;
    xlocC = 0;
    ylocC = 0;
    xlocCN = 0;
    ylocCN = 0;

    % FIND CENTROID OF THE PARTICLE (CENTRE OF MASS)----------
    for k = 1 : 10

      % summed total of the product of intensity and x position
      sumMXF  = sum( sum( CamImgFine   .* maskF  .* xF ) );
      sumMXFN = sum( sum( CamImgFineN  .* maskFN .* xF ) );
      sumMXC  = sum( sum( CamImgCoarse .* maskC  .* xC ) );
      sumMXCN = sum( sum( CamImgCoarseN .* maskCN .* xC ) );

      % summed total of the product of intensity and y position
      sumMYF  = sum( sum( CamImgFine   .* maskF  .* yF ) );
      sumMYFN = sum( sum( CamImgFineN  .* maskFN .* yF ) );
      sumMYC  = sum( sum( CamImgCoarse .* maskC  .* yC ) );
      sumMYCN = sum( sum( CamImgCoarseN .* maskCN .* yC ) );

      % total intensity of the masked image
      sumMF  = sum( sum( CamImgFine   .* maskF  ) );
```

```
        sumMFN = sum( sum( CamImgFineN   .* maskFN ) );
        sumMC  = sum( sum( CamImgCoarse  .* maskC  ) );
        sumMCN = sum( sum( CamImgCoarseN .* maskCN ) );

        xlocF  = sumMXF  / sumMF;
        xlocFN = sumMXFN / sumMFN;
        xlocC  = sumMXC  / sumMC;
        xlocCN = sumMXCN / sumMCN;

        ylocF  = sumMYF  / sumMF;
        ylocFN = sumMYFN / sumMFN;
        ylocC  = sumMYC  / sumMC;
        ylocCN = sumMYCN / sumMCN;

        % GAUSSIAN MASK FITTING METHOD
        maskF  = AmplF * exp( -( ( xF - xlocF  ).^2 + ( yF - ylocF  ).^2 ) / 2 / radF ); % was
max(max(CamImgFine))
        maskC  = AmplC * exp( -( ( xC - xlocC  ).^2 + ( yC - ylocC  ).^2 ) / 2 / radC ); % was
max(max(CamImgCoarse))
        maskFN = AmplF * exp( -( ( xF - xlocFN ).^2 + ( yF - ylocFN ).^2 ) / 2 / radF ); %
max(max(CamImgFineN))
        maskCN = AmplC * exp( -( ( xC - xlocCN ).^2 + ( yC - ylocCN ).^2 ) / 2 / radC ); %
max(max(CamImgCoarseN))

    end
    % CALCULATION OF ERRORS FROM CENTROID-FINDING METHOD
        % CENTROIDING----------------------------------------------
        CentrerrFX(  i, j ) = ( dr(i)  - xlocF  ) * pxSizeF;
        CentrerrFY(  i, j ) = ( dr(j)  - ylocF  ) * pxSizeF;
        CentrerrFXN( i, j ) = ( dr(i)  - xlocFN ) * pxSizeF;
        CentrerrFYN( i, j ) = ( dr(j)  - ylocFN ) * pxSizeF;
        CentrerrCX(  i, j ) = ( drC(i) - xlocC  ) * pxSizeC;
        CentrerrCY(  i, j ) = ( drC(j) - ylocC  ) * pxSizeC;
        CentrerrCXN( i, j ) = ( drC(i) - xlocCN ) * pxSizeC;
        CentrerrCYN( i, j ) = ( drC(j) - ylocCN ) * pxSizeC;
        CentrerrF ( i, j ) = pxSizeF * sqrt( ( dr(i)  - xlocF  )^2 + ( dr(j)  - ylocF  )^2 );
        CentrerrFN( i, j ) = pxSizeF * sqrt( ( dr(i)  - xlocFN )^2 + ( dr(j)  - ylocFN )^2 );
        CentrerrC ( i, j ) = pxSizeC * sqrt( ( drC(i) - xlocC  )^2 + ( drC(j) - ylocC  )^2 );
        CentrerrCN( i, j ) = pxSizeC * sqrt( ( drC(i) - xlocCN )^2 + ( drC(j) - ylocCN )^2 );
  end
  i
end
% calculate RMS (root-mean-squared) error for centroiding method
CentrrmsFX  = sqrt( sum( sum( CentrerrFX.^2  ) ) / subpix^2 );
CentrrmsFY  = sqrt( sum( sum( CentrerrFY.^2  ) ) / subpix^2 );
CentrrmsFXN = sqrt( sum( sum( CentrerrFXN.^2 ) ) / subpix^2 );
CentrrmsFYN = sqrt( sum( sum( CentrerrFYN.^2 ) ) / subpix^2 );
CentrrmsCX  = sqrt( sum( sum( CentrerrCX.^2  ) ) / subpix^2 );
CentrrmsCY  = sqrt( sum( sum( CentrerrCY.^2  ) ) / subpix^2 );
CentrrmsCXN = sqrt( sum( sum( CentrerrCXN.^2 ) ) / subpix^2 );
CentrrmsCYN = sqrt( sum( sum( CentrerrCYN.^2 ) ) / subpix^2 );
CentrrmsF  = sqrt( CentrrmsFX^2  + CentrrmsFY^2 );
CentrrmsFN = sqrt( CentrrmsFXN^2 + CentrrmsFYN^2 );
CentrrmsC  = sqrt( CentrrmsCX^2  + CentrrmsCY^2 );
CentrrmsCN = sqrt( CentrrmsCXN^2 + CentrrmsCYN^2 );
matlabpool close
toc;
```

Actin simulation

```
clear all, close all
profile on
matlabpool open
tic;
% VARIABLES-----------------------------------------------------------------
C = 910; % total number of acquired STORM frames, e.g. 6,000
mu = 300; % mean number of stochastic activations per frame
sigma = 10; % standard deviation of the Gaussian distribution determining the number of stochastic
events per frame
mesh = 148;
sep = 190; % choose separation of filaments (in nm)
% Camera parameters
CoarseCF = 5.8; % photon-to-electron count conversion factor for large-pixel camera, i.e. 1 photon = 5.8
electrons
FineCF   = 4.4; % fine-pixel camera gain conversion factor
pxSizeF = 80; % effective size of the pixels on the small-pixel camera is 80 nm
pxSizeC = 160; % " " " " " " " large-" " " 160 nm
px = 155; % measured size (not theoretical!) of C9100-13 camera pixels, with 100x objective
QEcoarse = 0.153; % total optical efficiency of the microscope
QEfine = 0.55;
EMgainC = 51.0; % equivalent to sensgain = 142
EMgainF = 4.0;
analogue_gainC = 1;
analogue_gainF = 1;
exposC = 0.00875; % length of exposure, in s, of large-pixel camera
exposF = 0.031;
planck = 6.62606957e-34; % Planck's constant, in m^2.kg/s
speed_of_light = 299792458; % in m/s
lambda = 519e-9; % peak emission wavelength of the dye, in m
avogadro = 6.02214129e23; % Avogadro's number, in mol^-1
epsilon = 71e6; % molar extinction coefficient (or absorptivity) of the dye, in cm^2/mol
QY = 0.92; % quantum yield of the dye
LP = 2330; % laser power, in W/cm^2
En = planck * speed_of_light / lambda; % energy of 1 photon, in J, or kg.m^2/s^2
crsec = 1000 * log(10) * epsilon / avogadro; % absorption cross-section of the dye, in cm^2
Alx488flux = QY * LP * crsec / En; % photons emitted per second by Alexa Fluor 488
R = mesh/2; % number of pixels in the x-dimension
r = 50; % number of pixels in the y-dimension
fil1_1 = 0.5*r - 0.5*sep/px + (3.5/px)*sin((37*2/13:37*2/13:37*2*px-37*2/13)*2*pi/37/2);
fil1_2 = 0.5*r - 0.5*sep/px - (3.5/px)*sin((37*2/13:37*2/13:37*2*px-37*2/13)*2*pi/37/2);
fil2_1 = 0.5*r + 0.5*sep/px + (3.5/px)*sin((37*2/13:37*2/13:37*2*px-37*2/13)*2*pi/37/2);
fil2_2 = 0.5*r + 0.5*sep/px - (3.5/px)*sin((37*2/13:37*2/13:37*2*px-37*2/13)*2*pi/37/2);
meshy = 2*r; % number of pixels in y-dimension of pre-coarsening mesh
[x, y] = meshgrid( -1 : 2/mesh : 1-2/mesh, -1 : 2/meshy : 1-2/meshy );
% convert grid to pixel coordinates with integer values
xF = mesh/2 * x;
yF = meshy/2 * y;
xC = 0.5 * xF( 1 : 2 : end, 1 : 2 : end );
yC = 0.5 * yF( 1 : 2 : end, 1 : 2 : end );
% GENERATE A POINT SOURCE FROM MICROSCOPE OBJECTIVE APERTURE----------------
rd = sqrt( x.^2 + y.^2 );
rn = rd / ( 0.5 * 0.08 / 0.0862 );
ps = ( rn < 2 ) .* ( 2 / pi * ( acos( rn / 2 ) - rn / 2 .* sqrt( 1 - ( rn / 2 ) .^ 2 ) ) );
% CONVOLVE IMAGE WITH CORRESPONDING CAMERA PIXELS--------------------------
```

```
psPupil_funcx  = sinc( x/2 );
psPupil_funcy  = sinc( y/2 );
psCPupil_funcx = sinc( x );
psCPupil_funcy = sinc( y );
fIOTF = psPupil_funcx  .* psPupil_funcy  .* ps;
cIOTF = psCPupil_funcx .* psCPupil_funcy .* ps;
i = (37*2/13:37*2/13:37*2*px-37*2/13)/px;
i = [i i i i];
j = [fil1_1, fil1_2, fil2_1, fil2_2];
[randx, randy] = RandStream.create('mrg32k3a','NumStreams',2);
tot_litups = 0; % total number of fluorophore activations since the beginning of the acquisitions
k = 1; % index that keeps track of the number of activated fluorophores
frame = zeros(r, R); % holds the activated fluorophores in a single switching cycle
frame_noiseless = zeros(r, R); % holds the activated fluorophores in a single switching cycle - without
noise
z_project = zeros(r,R);
z_project_noiseless = zeros(r,R);
STORMnoisy =
strcat('C:/Users/Megy/Documents/PhD/Matlab_files/STORM_actin_stack_2filam_',num2str(sep),'-
nm_sep_',num2str(R),'x',num2str(r),'res_',num2str(C),'cycles.tif');
STORMnoiseless =
strcat('C:/Users/Megy/Documents/PhD/Matlab_files/STORM_actin_stack_noiseless_2filam_',num2str(se
p),'-nm_sep_',num2str(R),'x',num2str(r),'res_',num2str(C),'cycles.tif');
fname = strcat('C:/Users/Megy/Documents/PhD/Matlab_files/True_locs_actin_2filam_',num2str(sep),'-
nm_sep_',num2str(R),'x',num2str(r),'res_',num2str(C),'cycles.txt');
delete(STORMnoisy); delete(STORMnoiseless);
% CREATE FILAMENTS-------------------------------------------------------------
for cyc = 1:C % cycling through the number of STORM frames
   cyc
   no_litup  = round( normrnd(mu, sigma) ); % generate a number of fluorophores to be lit up during each
cycle - modelled as obeying a Gaussian variance.
   % fluorophore chooser
   rr = randi(randx, length(i), [1 no_litup]); % generate random x coordinates from master list of fluoro-
phore positions
   locs(k:k+no_litup-1, 1) = i(rr);
   locs(k:k+no_litup-1, 2) = j(rr);
   locs(k:k+no_litup-1, 3) = cyc; % the number of the frame where the particle is localised
   tot_litups = tot_litups + no_litup;
   k = k + no_litup;
   parfor pos = 1:no_litup % cycling through the number of activated fluorophores
     % SHIFT THE POINT SOURCE ACROSS THE AREA OF A PIXEL-----------------
      shift = exp( 1i * pi * ( x * (R-(2*i(rr(pos))-2))+ y * (r-(2*j(rr(pos))-2))) );
      CamImgCoarse = cIOTF .* shift;
      CamImgCoarse = real( fftshift( ifft2( fftshift( CamImgCoarse ) ) ) );
      CamImgCoarse = CamImgCoarse( 1 : 2 : end, 1 : 2 : end );
      CamImgCoarse = CamImgCoarse * Alx488flux * exposC / sum( sum( CamImgCoarse ) );
      % ADD POISSON NOISE-----------------------------------------------
      CamImgCoarse = poissrnd( CamImgCoarse );
      CamImgCoarse = CamImgCoarse * EMgainC * analogue_gainC * QEcoarse / CoarseCF;
      frame_noiseless = frame_noiseless + CamImgCoarse;
      % COMPILE STORM STACK---------------------------------------------
      frame = frame + CamImgCoarse;
   end
   z_project_noiseless = z_project_noiseless + frame_noiseless; % superpose all frames on top of each other
   frame_noiseless = uint16(frame_noiseless);
   imwrite(frame_noiseless,STORMnoiseless,'tif','compression','none','writemode','append');
   z_project = z_project + frame; % superpose all frames on top of each other
   frame = uint16(frame);
   % ADD BACKGROUND NOISE-------------------------------------------------
```

```
    BgrNoiseC    = 7296.585 + 670 * randn( r, R ); actual measured values
    frame = abs(frame + uint16(BgrNoiseC));
    imwrite(frame,STORMnoisy,'tif','compression','none','writemode','append');
    frame_noiseless = zeros(r, R);
    frame = zeros(r, R);

end
toc;
dlmwrite(fname,locs,'\t');
matlabpool close
```

Stepwise bleaching

```
clear all; close all;
% FILE NAME----------------------------------------------------------------
[path, name, ext]=fileparts('C:/Users/Megy/Documents/PhD/Single-
molecule_imaging/Simulated_cluster1.csv');
fname = strcat(path, '/', name, ext);
fname_full = strcat( path, '/', name, '_full-length', ext );
% CONSTANTS----------------------------------------------------------------
EGFPmean = 7.695e4; % mean number of photons emitted in one second by EGFP, as measured by Chiu
et al., 2001.
k = 1.51; % fold increase in intensity at TIRF interface
QE = 0.096225958;
% Coefficients expressing mixing of polarisation detected, due to the NA of the objective
C1 = 0.756592;
C2 = 0.0134078;
C3 = 0.23;
d = 71.5; % penetration depth, in nm
expos = 0.1; % exposure time, in s
stdev = 833.2; % fluctuation in intensity, in number of photons
t_on = 0;
tot_intens = 0; % cumulative intensity
I_limit = 11650; % maximum intensity of the cluster, as found from my experimental data
i = 3256; % number of frames (data points) of real data
QY_photobleach = 1.6e5; % from [Kubitscheck et al., 2000], in photons
t1 = 1/0.04693 * 10; % 1/kfast
t2 = 1/0.019425 * 10; % 1/kmedium
t3 = 1/0.0003197 * 10; % 1/kslow
t_photobleach = t1*t2*t3/(t1*t3+t2*t3+t1*t2); % mean photobleaching lifetime, in seconds
for Monte=1:1000
    tot_intens = 0;
    CI = zeros(2,1); % cumulative intensity
    mol = 0; % molecule counter
    while ( tot_intens < I_limit )
        % VARIABLES-----------------------------------------------------
        phi = 2*pi * rand(1); % range 0 to 2*pi
        theta = pi * rand(1); % range 0 to pi
        z = d * rand(1); % depth into the sample, in nm; range 0 to d
        % STEP SIZE CALCULATION-----------------------------------------
                % The size of the steps depends on the orientation of the dipoles
        step_size = EGFPmean * expos * k * QE * ( C1 * (sin(theta))^2 * (cos(phi))^2 + C2 * (sin(theta))^2 *
(sin(phi))^2 + C3 * (cos(theta))^2 ) * exp(-z/d); % intensity over interval of time equal to the variable
'expos'
        % ASSEMBLE SERIES OF BLEACHING STEPS----------------------------
```

```
        t_on = random( 'exp', t_photobleach ) / expos; % draw a random number from an exponential distribution representing the probability of the duration of a switched 'on' interval;
        if t_on > length( CI )
           CI( length( CI ) + 1 : ceil(t_on) ) = 0;
        end
        t_on = uint8(t_on);
        CI( 1 : t_on ) = CI( 1 : t_on ) + step_size; % cumulative intensity; assumes all molecules start decaying together, not one after the other
        tot_intens = CI( 1 );
        mol = mol + 1;
    end
    CI( length( CI + 1 ) : length( CI + 1 ) + 10 ) = 0; % add on a dark period; was 1.66 s, the typical dark lifetime of EGFP according to literature
    X_end = length( CI );
    X =( expos : expos : X_end * expos );
    noiseless = CI;
    CI = poissrnd( CI );
    BCI = normrnd( 0, stdev, size( CI ) ); % background simulation
    noisy = CI + BCI; % noisy cumulative intensity.
    l = length(noisy);
    tot_mol(Monte)=mol;
    Monte
end
```

Appendix C – The Chung-Kennedy filter

The Chung-Kennedy filter is a mathematical signal-processing tool for reducing high-frequency noise and increasing the prominence of underlying signals – particularly those with fast transitions. Unlike the simple moving average, which removes high-frequency fluctuations by averaging adjacent values – yet likewise also erases real sudden changes in a stepped signal, the Chung-Kennedy filter preserves the meaningful jumps, whilst attenuating random noise. It was originally developed for visualising fast, transient signals from opening and closing ion channels and post-synaptic currents, overwhelmed by noise [Chung *et al.*, 1991]. The output of the filter consists of non-linear weighting of two predictors: one proceeding forward in time (causal) and one in reverse (anti-causal). A separate decision on the weights is made at every data point, depending on the outcome of the predictors. The rationale and theoretical framework of the filtering scheme are laid out below.

Given a time-varying signal, $x(t)$, and introducing unknown background noise or noise issuing from the measuring instrument itself, $n(t)$, the measured signal would assume the form

$$y(t) = x(t) + n(t).$$

A standard means of suppressing the noise and estimating the desired signal is to average the measurements over some arbitrary window of time (*e.g.* groups of three measurements, as shown below):

$$\hat{x}(t) = \frac{1}{3}[y(t-3) + y(t-2) + y(t-1)].$$

This sort of estimator, however, is effective only for smoothly varying functions and would blur any sharp edges that may be present. By recognising this fact and breaking the linearity of the scheme, one arrives at a satisfactory estimate of the real signal. First, the signal must be comparatively constant over the window of time – that is, $y(t-3) \approx y(t-2) \approx y(t-1)$, so that the measurements add constructively. Avoiding large differences between the terms ensures that the estimator, $\hat{x}(t)$, does not accidentally distort edges in the signal. After a second estimator is introduced – this time on the other side of the current point in time, t – there is now a forward and a backward predictor:

$$\hat{x}^f(t) \triangleq \frac{1}{3}[y(t-3) + y(t-2) + y(t-1)]$$

$$\hat{x}^b(t) \triangleq \frac{1}{3}[y(t+1) + y(t+2) + y(t+3)].$$

The predictors are unbiased because they are non overlapping. The final estimate is a combination of the two, with non-constant, time-varying coefficients, $f(t)$ and $b(t)$:

$$\hat{x}(t) = f(t)\hat{x}^f(t) + b(t)\hat{x}^b(t), \qquad \textbf{Eq. B.1}$$

where $0 \leq f(t) \leq 1$, $0 \leq b(t) \leq 1$ and $f(t) + b(t) = 1$. Hereon, the principle of operation is to choose automatically the forward predictor ($f(t) \approx 1$) if there is a sudden leap in the data ahead (*i.e.* $y(t)$, $y(t+1)$, $y(t+2)$, $y(t+3)$), or the backward predictor if the opposite is true. In the absence of any sudden leaps, both predictors will present reasonable estimates of the signal, and the weights would not be consequential.

In order to improve the accuracy of the estimate, instead of using single predictors in each direction, a 'bank' of predictors with different time windows is incorporated. This increases the performance of the filter, because fine features in the signal are estimated better by short time windows, whereas broad features are suited by longer windows.

Extrapolating **Eq. B.1** for a bank of predictors, the formula for obtaining the estimate becomes

$$\hat{x}(t) = \sum_{i=1}^{K}\left[f_i(t)\hat{x}_i^f(t) + b_i(t)\hat{x}_i^b(t)\right], \qquad \textbf{Eq. B.2}$$

where $f_i(t)$ and $b_i(t)$ are the weights, representing

$$f_i(t) \propto \pi_i \left\{\sum_{j=0}^{M-1}\left[y(t-j) - \hat{x}_i^f(t-j)\right]^2\right\}^{-p}$$
$$b_i(t) \propto \pi_i \left\{\sum_{j=0}^{M-1}\left[y(t+j) - \hat{x}_i^b(t+j)\right]^2\right\}^{-p}. \qquad \textbf{Eq. B.3}$$

The weights are normalised, *i.e.*

$$\sum_{i=1}^{T} f_i(t) + \sum_{i=1}^{T} b_i(t) = 1. \qquad \textbf{Eq. B.4}$$

M is the length of the window, over which the predictors are to be compared. M is usually confined to the range $4 \leq M \leq 20$, depending on the data. π_i is an optional parameter corresponding

to known prior probabilities. If some prior knowledge on the signal exists, this constant can be set to reflect it and skew the preference towards one of the predictors. To eliminate any subjectivity, however, π_i can be neutralised by setting it to $(2T)^{-1}$ for all i, where T is the length of the data segment. p is a weighting factor; higher values of p tend to improve the signal estimate. In essence, high values of p strongly exaggerate the weights of the predictor, thus giving unrivalled precedence to the prevalent predictor and suppressing the influence of the others. *In silico* simulations indicate that growing the value of p tackles noise less effectively, but preserves the amplitude and steepness of the edges. In addition, the signal processing can be applied repeatedly to diminish the noise. Many, as opposed to a few, iterations lead to gain in signal-to-noise ratio – at the expense of distorting the original shape of the signal.

The Chung-Kennedy filter is particularly valuable because it does not require an explicit model for the hidden signal. Therefore no prior knowledge of the characteristics of the signal is needed. The smallest feature that the algorithm can recover reliably is usually no less than 4 samples in duration [Chung *et al.*, 1991].